NUMERICAL INVESTIGATION OF ION TRANSPORT MECHANISMS IN ELECTROCHEMICAL ENERGY STORAGE DEVICES: SIMILARITY CORRELATION AND EXERGY DESTRUCTION ANALYSIS

BY

VENKAT PAVAN NEMANI

DISSERTATION

Submitted in partial fulfillment of the requirements
for the degree of Doctor of Philosophy in Mechanical Engineering
in the Graduate College of the
University of Illinois at Urbana-Champaign, 2019

Urbana, Illinois

Doctoral Committee:

Assistant Professor Kyle C. Smith, Chair and Director of Research
Associate Professor Randy H. Ewoldt
Professor Narayana R. Aluru
Professor Albert J. Valocchi

ABSTRACT

The shift towards renewable sources of energy requires the development of electrochemical energy storage solutions due to their scalability and ability to handle intermittency. In this thesis, the ion transport mechanisms are studied by modeling redox flow batteries (RFBs) and intercalation-based Li-ion batteries. Redox flow batteries are an emerging technology which allows independent scaling of energy and power density making them suitable candidates for grid-scale energy storage. In RFBs the redox active species is dissolved in electrolytes and stored in tanks. The electrolyte is pumped through the reactor where electrochemical reactions occur. Contemporary RFB research is focused around developing newer materials. However, the fundamental mechanisms causing polarization losses and energy inefficiencies that are inherent to the RFB design, and independent of chemistry, have received lesser attention in research. In this thesis, we present a transient multi-species RFB model using homogenized Poisson-Nernst-Planck formulation with hydrodynamic dispersion in porous media for the species transport. The RFBs modeled here can use either cost-effective non-selective separators or crossover reducing ion-exchange membranes. We also introduce Marcus-Hush-Chidsey kinetic theory based on microscopic electron transfer and solvent reorganization in modeling the redox reactions for RFBs instead of the most commonly used Butler Volmer empirical model. We detail the finite volume formulation with implicit time stepping along with a logarithmic transform of the concentration fields to solve the system of equations. A detailed stability analysis is conducted using the fixed-point iteration scheme for the two kinetic models to establish convergence.

For RFBs using non-selective separators, we use Damköhler numbers to classify three RFB operating regimes: redox shuttle limited, ohmic polarized, and sufficient supporting electrolyte. The sufficient supporting electrolyte regime ensures the least capacity fade due to crossover. In the case of RFBs using ion-exchange membranes, we perform comprehensive exergy destruction analysis, using the first and second laws of thermodynamics, to quantify the energy losses arising due to electron-conduction, pore-scale mass transfer, reaction kinetics, species transport, and electrolyte mixing in the tanks. Mapping of these exergy losses enables the identification of major sources of irreversibilities for designing more energy efficient RFBs. The non-dimensional nature of results presented in this study should find applicability towards designing efficient low-cost RFBs by modifying the flow conditions, reactor geometry, electrode morphology, and engineering the redox active species and the salt ions.

Li-ion batteries, in contrast with RFBs, operate on the principle of intercalation of lithium ions. The strong anisotropic behavior of graphite platelets restricts the transport of lithium ions through the electrode thickness limiting the thickness. However, thick Li-ion battery electrodes could enable batteries that cost less and have higher gravimetric and volumetric energy density. With the help of a porous electrode model with anisotropic transport processes, we propose and develop a design criterion for bi-tortuous graphite electrodes with electrolyte-rich macro-pores. Macro-pores with optimal aspect ratio spaced at short intervals enable maximum enhancement in Li-ion intercalation.

ACKNOWLEDGEMENTS

I would like to begin by thanking my advisor, Dr. Kyle C. Smith for working with me and providing guidance during my Ph.D. program at UIUC. He was always there to help me, evoking thoughtful questions and different perspectives to approach the research questions. Further, I would like to thank Professor Narayana Aluru, Professor Randy Ewoldt and Professor Albert Valocchi for serving on my thesis committee and offering valuable inputs on my project and career development.

I would also like to thank all my colleagues in the FLINT research group for helping me a lot by asking questions and making the lab a fun place to be in. Mr. Sizhe Liu, Mr. Aniruddh, Mr. Erik Reale, Mr. Hamid Abdul, Mr. Xia Shang, Mr. Vinay Iyer, Mr. Yite Wang, and Mr. Fan Kiat. Additionally, I would like to thank my collaborators Dr. Stephen J. Harris and JCESR electrolyte optimization sprint team for giving me valuable feedback on my modeling results. My special thanks to MechSE staff Mrs. Kathy Smith, Mrs. Ruthie Lubkeman and Glennys Mensing for being very helpful.

My special gratitude to my parents who showered all the love and support halfway across the globe. I am forever grateful to all teachers in my life who became my role models encouraging me to envision a better society and strive for it.

The research presented in the thesis is funded in part by the Joint Center for Energy Storage Research (JCESR) and by the Department of Mechanical Science and Engineering at UIUC. I also acknowledge the Abraham Lincoln Fellowship for funding me for my first year

Dedicated to my ever-loving parents and teachers

TABLE OF CONTENTS

LIST OF FIGURES

LIST OF TABLES

CHAPTER 1: Introduction

1.1 Electrochemical Energy Storage

The rapid growth of industrial societies in the past two hundred years has led to rapid exploitation of low-cost non-renewable fossil fuels. The demand in global energy demand almost doubled in the past 40 years[1]. The global production of electricity is about 25000 TWh in 2017 lead by China, United States and India[2]. Within the United States, about 60% of electricity in the USA was generated from fossil fuels whereas only ~10% was generated using renewable energy sources such as wind and solar[3]. However, the use of renewables (excluding hydropower) has grown by 15% in the USA over the past 10 years,[4] and it is projected that by 2050, 22% of total electricity generation in the USA will be accounted by wind and solar power plants[5]. Integration of the sources of energy with the grid is crucial for control and management of electricity distribution[6]. Lack of proper energy storage solutions can make the grid unstable if the demand exceeds 20% of the generated power[7]. Renewable energy sources such as solar and wind could complement traditional energy generation methods to stabilize power and load levelling. However, the dependence on climatic conditions make the renewable energy sources intermittent. The various energy storage solutions are characterized by storage capacity and response time. Durability and the ability to withstand many charge/ discharge cycles is crucial[8]. Pumped hydro energy storage (PHES)[9], which has high storage capacity but poor response time, is the most widely used. Other energy storage technologies, in decreasing order of capacity include compressed air[10], thermal[11], flywheel[12], electrochemical batteries and double layer capacitor[13]. Each of these energy storage technologies have specific features with pros and cons. For example, PHES systems have very high energy

storage capacity but fail to handle intermittency. Double layer capacitors, on the other hand, have very fast response time, the amount of energy stored is limited by the available area for forming the double layers. Integration with the grid, in the context of using renewable sources of energy, requires ability to store large quantities of energy and handle intermittency. In between the high capacity PHES and high power capacitors are the electrochemical energy storage (EES) systems. EES solutions can handle intermittency, have short-to-long time scale, be portable and have potential to increase energy storage capacity for application at the grid. Typically, in EES, energy is stored as chemical energy facilitated by oxidation or reduction of redox couples. EES comprises of electrochemical cells and each cell consists of a positive electrode, a negative electrode and an electrolyte. During discharge, the redox reactions within the electrodes generate a flow of electrons through an external circuit providing electricity. In most EES devices there is an inverse relationship between the specific power and energy density. Attempting to increase specific power or energy restricts the other. For example, increasing energy density in Li-ion batteries restricts fast ion transport limiting the power density. Redox flow batteries are a class of EES devices where independent scaling of power and energy densities is possible, making them attractive candidates for grid scale energy storage. The aim of this thesis work is to analyze the species/ ion transport mechanisms in two EES devices: lithium-ion batteries and redox flow batteries.

1.2 Lithium ion Batteries

Amongst the various energy storing devices available, Li-ion batteries have benefits of high gravimetric and volumetric energy-density[14–16]. Modern Li-ion battery electrodes are porous composites of solid-state active-material particles bound together by a conductive carbon-binder mixture, with an ion-conducting liquid electrolyte filling the pores. When a battery operates, electrons and ions are simultaneously transported to the surfaces of active-material particles, where electrochemical reactions take place. Figure 1.1 shows the working principle of a lithium cobalt oxide (LCO) and graphite Li-ion battery. During the charging process, lithium ions which are excess in LCO deintercalated from the LCO grains, transport through the electrolyte and be stored/ intercalated within the graphite layers. At the end of charging process, graphite electrode is rich in Li^+ whereas LCO is deficient in Li^+. During discharge process, the reverse mechanism occurs where Li^+ intercalates into LCO from graphite.

Figure 1.1

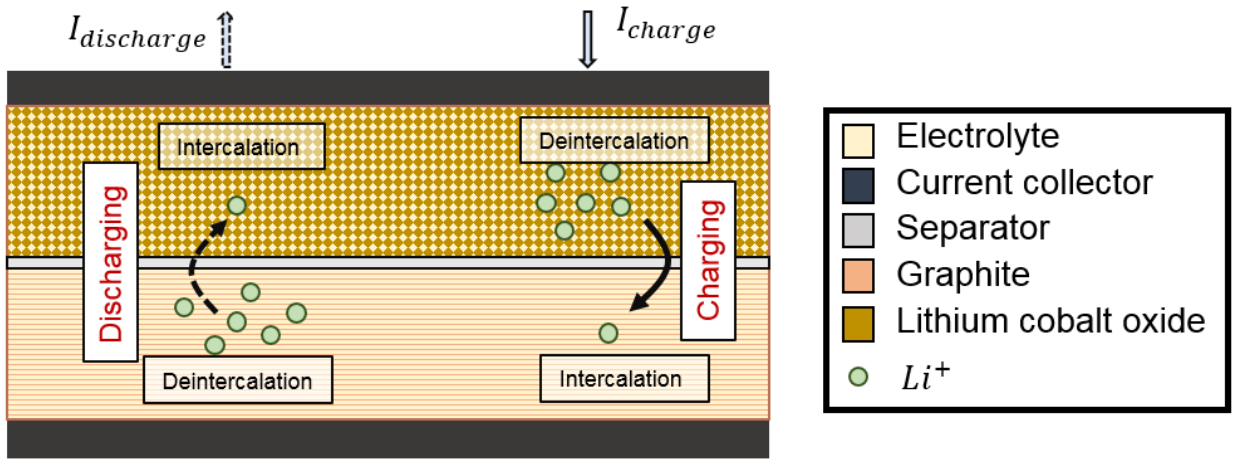

Figure 1.1 (cont.)

Figure 1.1: Working principle of a Li-ion battery.

The rates at which ions are transported depend on the microscopic structure of the composite electrodes through a parameter called tortuosity. The microstructure in an electrode results from the particular choice of material constituents and processes that are used to fabricate the electrodes. To maximize the energy density of a battery, we would like to have electrodes with low porosity (maximizing the density of active material) and high thickness, reducing the number of inactive components (separators, current collectors) that are required for a given amount of active material, saving considerable cost. Unfortunately, electrodes with low porosity generally have high tortuosity[17], making ion transport slow, an effect whose importance is magnified when electrodes are thick. Thus, techniques that produce thick, dense electrodes with enhanced ion transport could enable the development of batteries with high energy-density *and* high power density at a lower cost than is currently available[18].

It has recently been shown that the morphology of active particles and the processing conditions used affect the electrode microstructure. For example, electrodes composed of plate- or flake-shaped particles of $LiFePO_4$ (Ref. [19]) and graphite (Ref. [20]) exhibit ordered orientation (self-assembly) that affects the ability to transport Li ions when they are confined into a dense state. Also, it has been shown that the tortuosity itself can be heterogeneous[21], in addition to being anisotropic for electrodes comprised of non-spherical particles[20].

Novel approaches have been developed recently to enhance ion-transport in Li-ion batteries by controlling electrode microstructure. Chiang and co-workers[22] used a co-extrusion process to manufacture half-cells containing low-tortuosity macro-pores embedded in sintered, micro-porous $LiCoO_2$. Here, structured electrodes with tuned dimensions achieved greater capacity than homogeneous electrodes with the same average porosity[22]. The mechanism for this enhancement was attributed to the improved Li-ion transport provided by the low-tortuosity macro-pores. Similarly, Lu and Harris suggested that electrodes made with self-assembled particles could have low tortuosities in all direction[23].

High-fidelity models of electrochemical transport are needed to guide the design of complex, multi-scale electrodes. In Ref. [22] scaling analysis of 'effective' tortuosity was used to explain experimentally observed enhancements in capacity. Subsequently, Cobb and Blanco[24] analyzed half-cells containing similar bi-tortuous structures using porous-electrode theory. They found that co-extruded macro-pore dimensions on order of $25\mu m$ yielded the highest utilization of electroactive material for electrode thicknesses in the range of $150 - 300\mu m$[24].

1.3 Redox Flow Batteries

Redox flow batteries (RFBs) are attractive EES solutions because of their ability to independently scale energy capacity and power density. Decoupling energy and power, by altering the tank size and reactor design respectively, enables the stabilization of power, and application in load levelling and peak shaving with low environmental impact[8,25–28]. The commercialization of RFB technology at grid-scale is currently

challenged by high system prices[29,30]. Accordingly, the United States Department of Energy has set an aggressive target price of $120kW/h for the commercialization of RFB EES[31]. A typical RFB constitutes a reactor (electrode compartments separated by an electron insulating separator) and two tanks (electrolyte storehouse) connected through a network of pipes and pumps. Figure 1.2 depicts the reactor and tank arrangement of an RFB. Each tank consists of one set of redox couples $R1/O1$ and $R2/O2$ respectively.

Figure 1.2

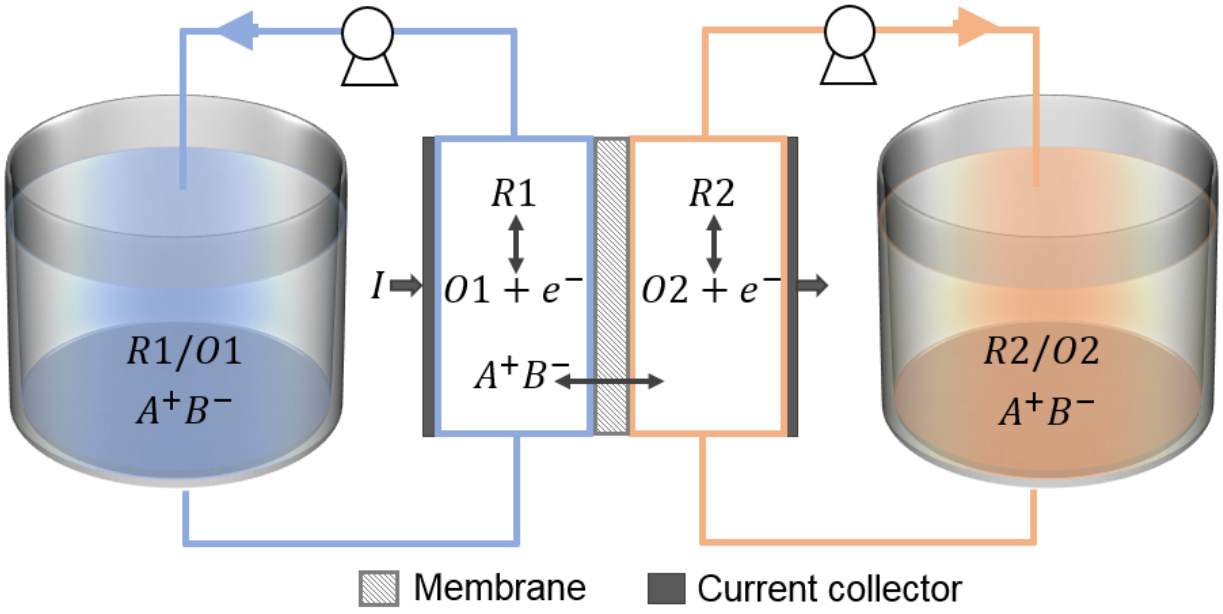

Figure 1.2: Design and working of an RFB

A variety of active compounds, inorganic (e.g. vanadium [32], polysulfide-bromine [33]) and organic/semi-organic (e.g. TEMPO[34], quinone[35], viologen based polymers[36]) have been explored for use in RFBs. Vanadium redox batteries [32] are the most common and widely studied aqueous redox flow batteries (AqRFBs). However, metal ions such as vanadium are not abundantly available and their high cost restricts their utility for large scale

systems[26,27]. The corrosive and toxic nature of some of the non-metallic materials, such as bromine, affects the pipes, pumps and tanks[37]. This motivated the development of AqRFBs with organic or semi-organic active species[35,38]. Such systems can be cheaper and safer, but the electrochemical stability window of aqueous based electrolytes impedes achievement of high energy density. On the other hand, nonaqueous redox flow batteries (NAqRFBs) provide a wider electrochemical stability window (hence high energy density)[39–42], while NAqRFBs tend to have lower ionic conductivity and higher electrolyte costs as compared to their aqueous counterparts[43].

Solutions containing macromolecular motifs, such as RAPs, show high viscosity with increasing redox-active species concentration,[36] potentially affecting mechanical design and pumping costs in scaled RFBs. Fluid distribution within the reactor, and consequently reaction distributions, can be affected by the electrolyte viscosity, in addition to the flow rate used. Therefore, understanding the impact of flow rate on cell performance is essential to establish optimized operating regimes and cell designs for RAP-based RFBs. Tailoring flow field design (serpentine, parallel, interdigitated and spiral flows) and electrode architecture is important to enhance mass transport in the reactor, thus achieving high power densities and limiting currents[47–49]. Systematic studies in this regard revealed that an interdigitated flow field (IDFF) paired with carbon paper electrodes gives the optimal performance with respect to electrochemical reactions and pressure drops[49]. Therefore, proper reactor design coupled with material selection[41,43,50] would significantly reduce the cost of the RFBs helping in their widespread commercialization[31]. Also, less conventional RFBs utilizing high-viscosity, shear-thinning suspensions of carbon black

and solid active compounds required the development of various flow-mode strategies to enable efficient operation in both aqueous and non-aqueous RFBs[51–55].

1.4 References

1. Moncada, L. G. G., Asdrubali, F. & Rotili, A. Influence of new fac tors on global energy prospects in the medium term: compar ison among the 2010, 2011 and 2012 editions of the IEA's World Energy Outlook reports. *ECONOMICS AND POLICY OF ENERGY AND THE ENVIRONMENT* (2013). doi:10.3280/EFE2013-003003
2. Electricity Production Data | World Electricity Statistics | Enerdata..
3. https://www.eia.gov
4. BP Statistical Review of World Energy 2017. 52
5. EIA - Annual Energy Outlook 2018.
6. Coster, E. J., Myrzik, J. M. A., Kruimer, B. & Kling, W. L. Integration Issues of Distributed Generation in Distribution Grids. *Proceedings of the IEEE* **99**, 28–39 (2011).
7. Vazquez, S. *et al.* Recent advances on Energy Storage Systems. in *IECON 2011 - 37th Annual Conference of the IEEE Industrial Electronics Society* 4636–4640 (2011). doi:10.1109/IECON.2011.6120075
8. Alotto, P., Guarnieri, M. & Moro, F. Redox flow batteries for the storage of renewable energy: A review. *Renewable and Sustainable Energy Reviews* **29**, 325–335 (2014).
9. Yang, C.-J. & Jackson, R. B. Opportunities and barriers to pumped-hydro energy storage in the United States. *Renewable and Sustainable Energy Reviews* **15**, 839–844 (2011).
10. Crotogino, F. & Leonhard, W. Compressed air storage-gas turbines-power plants to balance fluctuating wind energy production. in 431–438 (2004).

11. Oró, E., Gil, A., de Gracia, A., Boer, D. & Cabeza, L. F. Comparative life cycle assessment of thermal energy storage systems for solar power plants. *Renewable Energy* **44**, 166–173 (2012).

12. Lazarewicz, M. L. & Ryan, T. M. Integration of flywheel-based energy storage for frequency regulation in deregulated markets. in *IEEE PES General Meeting* 1–6 (2010). doi:10.1109/PES.2010.5589748

13. Sharma, P. & Bhatti, T. S. A review on electrochemical double-layer capacitors. *Energy Conversion and Management* **51**, 2901–2912 (2010).

14. Bruce, P. G., Freunberger, S. A., Hardwick, L. J. & Tarascon, J.-M. Li–O_2 and Li–S batteries with high energy storage. *Nature Materials* **11**, 19–29 (2012).

15. Li, Y., Song, J. & Yang, J. A review on structure model and energy system design of lithium-ion battery in renewable energy vehicle. *Renewable and Sustainable Energy Reviews* **37**, 627–633 (2014).

16. Armand, M. & Tarascon, J.-M. Building better batteries. *Nature* **451**, 652–657 (2008).

17. Zacharias, N. A. *et al.* Direct Measurements of Effective Ionic Transport in Porous Li-Ion Electrodes. *J. Electrochem. Soc.* **160**, A306–A311 (2013).

18. Zheng, H., Li, J., Song, X., Liu, G. & Battaglia, V. S. A comprehensive understanding of electrode thickness effects on the electrochemical performances of Li-ion battery cathodes. *Electrochimica Acta* **71**, 258–265 (2012).

19. Smith, K. C., Mukherjee, P. P. & Fisher, T. S. Columnar order in jammed LiFePO4 cathodes: ion transport catastrophe and its mitigation. *Phys. Chem. Chem. Phys.* **14**, 7040–7050 (2012).

20. Ebner, M., Chung, D.-W., García, R. E. & Wood, V. Tortuosity Anisotropy in Lithium-Ion Battery Electrodes. *Advanced Energy Materials* **4**, 1301278 (2014).

21. Kehrwald, D., Shearing, P. R., Brandon, N. P., Sinha, P. K. & Harris, S. J. Local Tortuosity Inhomogeneities in a Lithium Battery Composite Electrode. *J. Electrochem. Soc.* **158**, A1393–A1399 (2011).

22. Bae, C.-J., Erdonmez, C. K., Halloran, J. W. & Chiang, Y.-M. Design of Battery Electrodes with Dual-Scale Porosity to Minimize Tortuosity and Maximize Performance. *Advanced Materials* **25**, 1254–1258 (2013).

23. Harris, S. J. & Lu, P. Effects of Inhomogeneities—Nanoscale to Mesoscale—on the Durability of Li-Ion Batteries. *J. Phys. Chem. C* **117**, 6481–6492 (2013).

24. Cobb, C. L. & Blanco, M. Modeling mass and density distribution effects on the performance of co-extruded electrodes for high energy density lithium-ion batteries. *Journal of Power Sources* **249**, 357–366 (2014).

25. Weber, A. Z. *et al.* Redox flow batteries: a review. *J Appl Electrochem* **41**, 1137 (2011).

26. Skyllas-Kazacos, M., Chakrabarti, M. H., Hajimolana, S. A., Mjalli, F. S. & Saleem, M. Progress in Flow Battery Research and Development. *J. Electrochem. Soc.* **158**, R55–R79 (2011).

27. Leung, P. *et al.* Progress in redox flow batteries, remaining challenges and their applications in energy storage. *RSC Adv.* **2**, 10125–10156 (2012).

28. Wang, W. *et al.* Recent Progress in Redox Flow Battery Research and Development. *Adv. Funct. Mater.* **23**, 970–986 (2013).

29. Darling, R. M., Gallagher, K. G., Kowalski, J. A., Ha, S. & Brushett, F. R. Pathways to low-cost electrochemical energy storage: a comparison of aqueous and nonaqueous flow batteries. *Energy Environ. Sci.* **7**, 3459–3477 (2014).

30. Viswanathan, V. *et al.* Cost and performance model for redox flow batteries. *Journal of Power Sources* **247**, 1040–1051 (2014).

31. U. S. Department Of Energy, Energy Storage, Program Planning Document. (2011).

32. Rychcik, M. & Skyllas-Kazacos, M. Characteristics of a new all-vanadium redox flow battery. *Journal of Power Sources* **22**, 59–67 (1988).

33. Remick, R. J. & Ang, P. G. P. Electrically rechargeable anionically active reduction-oxidation electrical storage-supply system. (1984).

34. Li, Z. *et al.* Electrochemical Properties of an All-Organic Redox Flow Battery Using 2,2,6,6-Tetramethyl-1-Piperidinyloxy and N-Methylphthalimide. *Electrochem. Solid-State Lett.* **14**, A171–A173 (2011).

35. Huskinson, B. *et al.* A metal-free organic-inorganic aqueous flow battery. *Nature* **505**, 195–198 (2014).

36. Nagarjuna, G. *et al.* Impact of Redox-Active Polymer Molecular Weight on the Electrochemical Properties and Transport Across Porous Separators in Nonaqueous Solvents. *J. Am. Chem. Soc.* **136**, 16309–16316 (2014).

37. Yang, Z. *et al.* Electrochemical Energy Storage for Green Grid. *Chem. Rev.* **111**, 3577–3613 (2011).

38. Janoschka, T. *et al.* An aqueous, polymer-based redox-flow battery using non-corrosive, safe, and low-cost materials. *Nature* **527**, 78–81 (2015).

39. Wang, Y., He, P. & Zhou, H. Li-Redox Flow Batteries Based on Hybrid Electrolytes: At the Cross Road between Li-ion and Redox Flow Batteries. *Adv. Energy Mater.* **2**, 770–779 (2012).

40. Brushett, F. R., Vaughey, J. T. & Jansen, A. N. An All-Organic Non-aqueous Lithium-Ion Redox Flow Battery. *Adv. Energy Mater.* **2**, 1390–1396 (2012).

41. Darling, R. M., Gallagher, K. G., Kowalski, J. A., Ha, S. & Brushett, F. R. Pathways to low-cost electrochemical energy storage: a comparison of aqueous and nonaqueous flow batteries. *Energy Environ. Sci.* **7**, 3459–3477 (2014).

42. Wei, X. *et al.* A High-Current, Stable Nonaqueous Organic Redox Flow Battery. *ACS Energy Lett.* **1**, 705–711 (2016).

43. Dmello, R., Milshtein, J. D., Brushett, F. R. & Smith, K. C. Cost-driven materials selection criteria for redox flow battery electrolytes. *Journal of Power Sources* **330**, 261–272 (2016).

44. Zhang, H., Zhang, H., Li, X., Mai, Z. & Wei, W. Silica modified nanofiltration membranes with improved selectivity for redox flow battery application. *Energy & Environmental Science* **5**, 6299–6303 (2012).

45. Yuan, Z. *et al.* Advanced porous membranes with ultra-high selectivity and stability for vanadium flow batteries. *Energy Environ. Sci.* **9**, 441–447 (2016).

46. Montoto, E. C. *et al.* Redox Active Colloids as Discrete Energy Storage Carriers. *J. Am. Chem. Soc.* **138**, 13230–13237 (2016).

47. Aaron, D. S. *et al.* Dramatic performance gains in vanadium redox flow batteries through modified cell architecture. *Journal of Power Sources* **206**, 450–453 (2012).

48. Darling, R. M. & Perry, M. L. The Influence of Electrode and Channel Configurations on Flow Battery Performance. *J. Electrochem. Soc.* **161**, A1381–A1387 (2014).

49. Dennison, C. R., Agar, E., Akuzum, B. & Kumbur, E. C. Enhancing Mass Transport in Redox Flow Batteries by Tailoring Flow Field and Electrode Design. *J. Electrochem. Soc.* **163**, A5163–A5169 (2016).

50. Darling, R., Gallagher, K., Xie, W., Su, L. & Brushett, F. Transport Property Requirements for Flow Battery Separators. *J. Electrochem. Soc.* **163**, A5029–A5040 (2016).

51. Duduta, M. *et al.* Semi-Solid Lithium Rechargeable Flow Battery. *Adv. Energy Mater.* **1**, 511–516 (2011).

52. Fan, F. Y. *et al.* Polysulfide Flow Batteries Enabled by Percolating Nanoscale Conductor Networks. *Nano Lett.* **14**, 2210–2218 (2014).

53. Brunini, V. E., Chiang, Y.-M. & Carter, W. C. Modeling the hydrodynamic and electrochemical efficiency of semi-solid flow batteries. *Electrochimica Acta* **69**, 301–307 (2012).

54. Smith, K. C., Chiang, Y.-M. & Carter, W. C. Maximizing Energetic Efficiency in Flow Batteries Utilizing Non-Newtonian Fluids. *J. Electrochem. Soc.* **161**, A486–A496 (2014).

55. Smith, K. C., Brunini, V. E., Dong, Y., Chiang, Y.-M. & Carter, W. C. Electroactive-Zone Extension in Flow-Battery Stacks. *Electrochimica Acta* **147**, 460–469 (2014).

56. Lu, W., Li, X. & Zhang, H. The next generation vanadium flow batteries with high power density – a perspective. *Phys. Chem. Chem. Phys.* **20**, 23–35 (2017).

57. Milshtein, J. D. *et al.* Quantifying Mass Transfer Rates in Redox Flow Batteries. *J. Electrochem. Soc.* **164**, E3265–E3275 (2017).

58. Aaron, D., Tang, Z., Papandrew, A. B. & Zawodzinski, T. A. Polarization curve analysis of all-vanadium redox flow batteries. *J Appl Electrochem* **41**, 1175 (2011).

59. Bromberger, K., Kaunert, J. & Smolinka, T. A Model for All-Vanadium Redox Flow Batteries: Introducing Electrode-Compression Effects on Voltage Losses and Hydraulics. *Energy Technology* **2**, 64–76 (2014).

60. Wei, L., Zhao, T. S., Zhao, G., An, L. & Zeng, L. A high-performance carbon nanoparticle-decorated graphite felt electrode for vanadium redox flow batteries. *Applied Energy* **176**, 74–79 (2016).

61. Bhattarai, A. *et al.* Advanced porous electrodes with flow channels for vanadium redox flow battery. *Journal of Power Sources* **341**, 83–90 (2017).

62. Liu, Q. H. *et al.* High Performance Vanadium Redox Flow Batteries with Optimized Electrode Configuration and Membrane Selection. *J. Electrochem. Soc.* **159**, A1246–A1252 (2012).

63. Chang, T.-C., Zhang, J.-P. & Fuh, Y.-K. Electrical, mechanical and morphological properties of compressed carbon felt electrodes in vanadium redox flow battery. *Journal of Power Sources* **245**, 66–75 (2014).

64. Lin, K. *et al.* Alkaline quinone flow battery. *Science* **349**, 1529–1532 (2015).

65. Burgess, M. *et al.* Scanning Electrochemical Microscopy and Hydrodynamic Voltammetry Investigation of Charge Transfer Mechanisms on Redox Active Polymers. *J. Electrochem. Soc.* **163**, H3006–H3013 (2016).

66. Montoto, E. C., Nagarjuna, G., Moore, J. S. & Rodríguez-López, J. Redox Active Polymers for Non-Aqueous Redox Flow Batteries: Validation of the Size-Exclusion Approach. *J. Electrochem. Soc.* **164**, A1688–A1694 (2017).

67. Wei, X. *et al.* TEMPO-Based Catholyte for High-Energy Density Nonaqueous Redox Flow Batteries. *Adv. Mater.* **26**, 7649–7653 (2014).

68. Gong, K., Fang, Q., Gu, S., Yau Li, S. F. & Yan, Y. Nonaqueous redox-flow batteries: organic solvents, supporting electrolytes, and redox pairs. *Energy & Environmental Science* **8**, 3515–3530 (2015).

69. Zhou, X. L., Zhao, T. S., An, L., Zeng, Y. K. & Wei, L. Critical transport issues for improving the performance of aqueous redox flow batteries. *Journal of Power Sources* **339**, 1–12 (2017).

70. Nemani, V. P. & Smith, K. C. Uncovering the role of flow rate in redox-active polymer flow batteries: simulation of reaction distributions with simultaneous mixing in tanks. *Electrochimica Acta* **247**, 475–485 (2017).

71. Gaffney, B. J. & Drew, T. B. Mass Transfer from Packing to Organic Solvents in Single Phase Flow through a Column. *Ind. Eng. Chem.* **42**, 1120–1127 (1950).

72. Williamson, J. E., Bazaire, K. E. & Geankoplis, C. J. Liquid-Phase Mass Transfer at Low Reynolds Numbers. *Ind. Eng. Chem. Fund.* **2**, 126–129 (1963).

73. Wilson, E. J. & Geankoplis, C. J. Liquid Mass Transfer at Very Low Reynolds Numbers in Packed Beds. *Ind. Eng. Chem. Fund.* **5**, 9–14 (1966).

74. Lewis, W. K. & Whitman, W. G. Principles of Gas Absorption. *Ind. Eng. Chem.* **16**, 1215–1220 (1924).

75. Appel, P. W. & Newman, J. Application of the limiting current method to mass transfer in packed beds at very low reynolds numbers. *AIChE Journal* **22**, 979–984 (1976).

76. You, X., Ye, Q. & Cheng, P. The Dependence of Mass Transfer Coefficient on the Electrolyte Velocity in Carbon Felt Electrodes: Determination and Validation. *J. Electrochem. Soc.* **164**, E3386–E3394 (2017).

77. Schmal, D., Van Erkel, J. & Van Duin, P. J. Mass transfer at carbon fibre electrodes. *J Appl Electrochem* **16**, 422–430 (1986).

78. Whitaker, S. Diffusion and dispersion in porous media. *AIChE Journal* **13**, 420–427 (1967).

79. Sahimi, M., Hughes, B. D., Scriven, L. E. & Ted Davis, H. Dispersion in flow through porous media—I. One-phase flow. *Chemical Engineering Science* **41**, 2103–2122 (1986).

80. Daneyko, A., Hlushkou, D., Khirevich, S. & Tallarek, U. From random sphere packings to regular pillar arrays: Analysis of transverse dispersion. *Journal of Chromatography A* **1257**, 98–115 (2012).

81. Xu, A., Zhao, T. S., Shi, L. & Xu, J. B. Lattice Boltzmann Simulation of Mass Transfer Coefficients for Chemically Reactive Flows in Porous Media. *J. Heat Transfer* **140**, 052601-052601–8 (2018).

82. Kok, M. D. R. *et al.* Mass transfer in fibrous media with varying anisotropy for flow battery electrodes: Direct numerical simulations with 3D X-ray computed tomography. *Chemical Engineering Science* **196**, 104–115 (2019).

83. Spiegler, K. S. Polarization at ion exchange membrane-solution interfaces. *Desalination* **9**, 367–385 (1971).

84. Krol, J. J., Wessling, M. & Strathmann, H. Concentration polarization with monopolar ion exchange membranes: current–voltage curves and water dissociation. *Journal of Membrane Science* **162**, 145–154 (1999).

85. Tanaka, Y. Concentration polarization in ion-exchange membrane electrodialysis: The events arising in an unforced flowing solution in a desalting cell. *Journal of Membrane Science* **244**, 1–16 (2004).

CHAPTER 2: Porous Electrode Modeling of Li-ion Batteries

2.1 Bi-tortuous Electrodes: Porosity and Electroactive-material Distribution

A full-cell containing a $LiCoO_2$ cathode and a graphite anode is simulated, as shown in Fig. 2.1(a). Each of these electrodes is modeled as a two-dimensional continuum using porous-electrode theory. A heterogeneous distribution of electroactive material and electrolyte is incorporated with spatially dependent electroactive-material volume-fraction $v_s(x,y)$ and micro-porosity $\epsilon(x,y)$. Presently, we neglect the volume of conductive-carbon binder, in which case the local porosity and electroactive-material volume fraction are related by $v_s + \epsilon = 1$. As shown in previous work,[1] the orientation of particles inside heterogeneous, composite electrodes affects the ion transport rates. We assume that graphite and $LiCoO_2$ particles orient parallel to the respective current collectors on which they are cast and calendered. Accordingly, in Fig. 2.1(a) horizontal-line pattern is used to represent the orientation of graphite platelets in the anode, while a cross-hatch pattern is used for oblate $LiCoO_2$ particles in the cathode (because electrodes containing oblate $LiCoO_2$ particles produce more isotropic microstructures than pressed graphite platelets[1]).

Figure 2.1

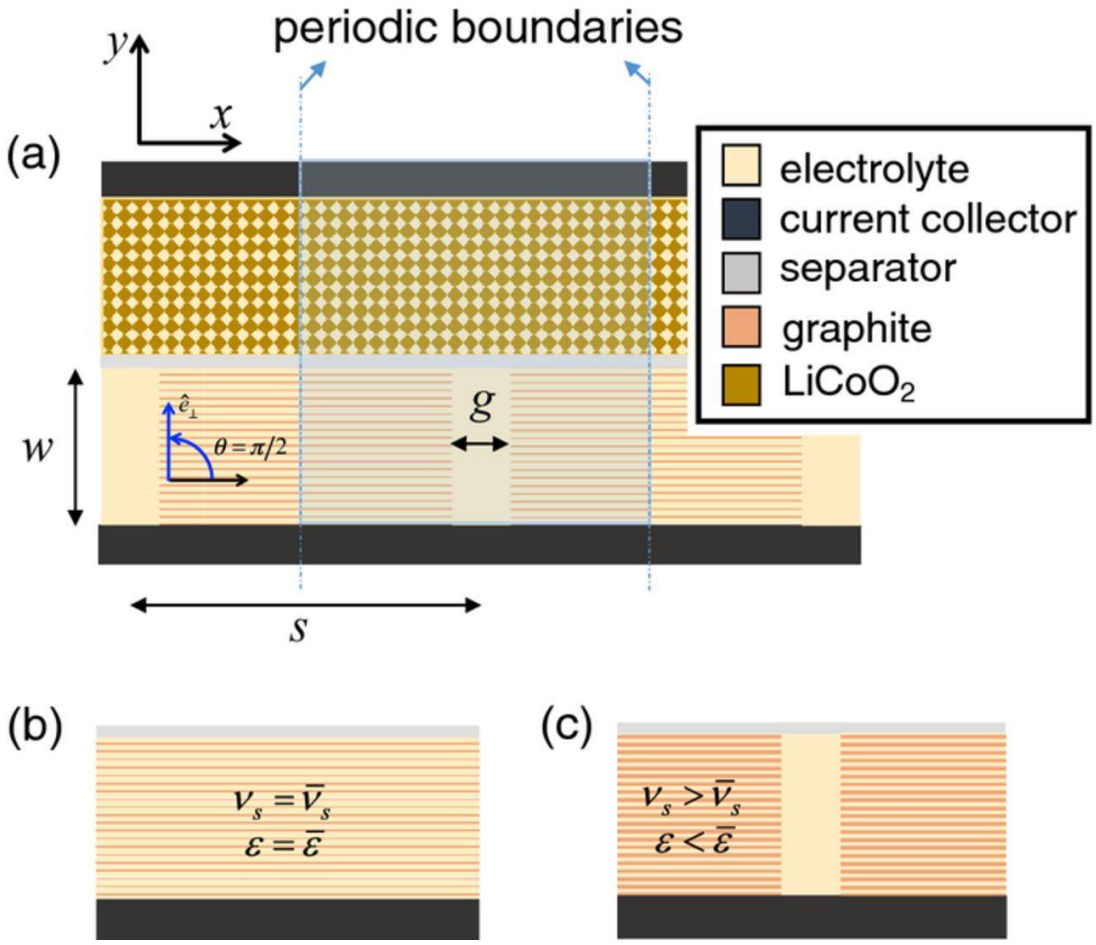

Figure 2.1: Schematic of material distribution in the two-dimensional full-cell simulated here. (a) Periodic boundaries (marked in blue) are used to simulate an infinite cell. The structured anode contains electrolyte-rich macro-pores with width g and spacing s. Comparison of active-material volume-fraction and porosity for (b) a homogeneous graphite-anode and (c) bi-tortuous graphite anode

Here, we focus on particular designs for the anode that incorporate rectangular “macro-pores” (i.e., grooves when projected in the third dimension) that contain 100% electrolyte.

These electrode structures are bi-tortuous in the sense that macro-pores possess a unit tortuosity, while the region containing electroactive material (i.e., where $\nu_s > 0$) exhibits a different[2], direction-dependent[1] tortuosity. Figures 2.1(b) and 2.1(c) contrast the structures simulated for a homogeneous graphite anode with a bi-tortuous one. These macro-pores are assigned width g and are separated by regular spacing s. The regular spacing between macro-pores enables the simulation of an infinite electrode by a single "unit cell" of a periodic structure.

Figure 2.2

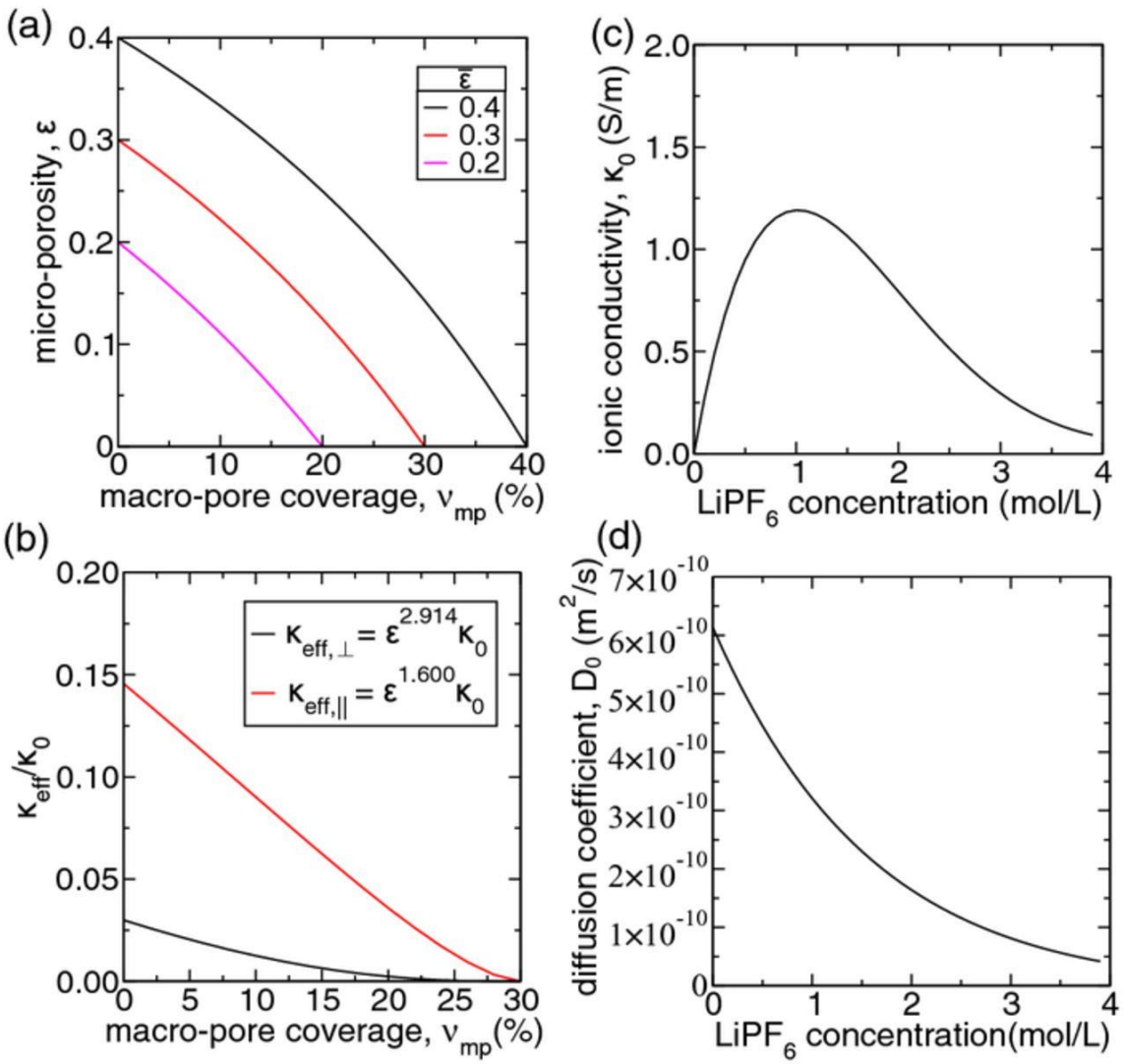

Figure 2.2 (cont.)

Figure 2.2: (a) Variation of micro-porosity ϵ with increasing macro-pore coverage ν_{mp} for various average porosity levels $\bar{\epsilon}$. (b) Variation of ionic-conductivity-tensor components with macro-pore coverage in the graphite anode (30% average porosity) along the directions perpendicular and parallel to the current collector. (c) Variation of bulk ionic-conductivity κ_0 and (d) bulk chemical-diffusion coefficient D_0 as a function of $LiPF_6$ concentration

We introduce constraints on the distribution of electroactive-material loading and porosity, such that the area-specific capacity is the same when comparing between bi-tortuous and homogeneous electrodes. In other words, local micro-porosity ϵ (inside regions of the electrode containing electroactive material) is lower than the average porosity $\bar{\epsilon}$. The extent of variation between these local and average values depends on the macro-pore coverage ν_{mp}, which is defined as the volume fraction of the electrode covered by the macro-pore. For the two-dimensional electrode here macro-pore coverage is affected by the width of and spacing between macro-pores, $\nu_{mp} = g/s$ (a different expression can be derived for arbitrarily shaped and spaced macro-pores). Assuming negligible volume occupied by the conductive carbon-binder domains, the local micro-porosity depends on average porosity and macro-pore coverage in the following way:

$$\epsilon = \frac{\bar{\epsilon} - \nu_{mp}}{1 - \nu_{mp}}. \quad (1)$$

The variation of local micro-porosity with macro-pore coverage is shown in Fig. 2.2(a). These curves reveal that the maximum possible macro-pore coverage that can be achieved (i.e., where porosity vanishes) depends on the magnitude of average porosity (and implicitly on the average volume-fraction of electroactive material because $\bar{\nu_s} = 1 - \bar{\epsilon}$). The local volume fraction of electroactive material ν_s (also called "loading") depends on the average value $\bar{\nu_s}$ and macro-pore coverage, as well:

$$\nu_s = \frac{\bar{\nu_s}}{1-\nu_{mp}}. \tag{2}$$

2.2 Anisotropic Ion-transport Parameters

Preferential orientation of pores in the microstructure of calendered graphite electrodes has been shown to produce anisotropic tortuosity that is high in the direction perpendicular to the current collector and low parallel to the current collector.[1] For the multi-dimensional system being modeled presently, this tortuosity anisotropy manifests in the effective diffusivity $\underline{\underline{D_{eff}}}$ and ionic-conductivity $\underline{\underline{\kappa_{eff}}}$ tensors, which relate salt-diffusion rates and ionic current to their driving forces (i.e., salt-concentration and solution-potential gradients, respectively). When normalized by the bulk chemical-diffusivity of salt D_0 and bulk ionic-conductivity κ_0 (i.e., of the pure electrolyte), these tensors exhibit a particular functional form $\underline{\underline{f}}$ (assuming an orthotropic microstructure):

$$\underline{\underline{\kappa_{eff}}}/\kappa_0 = \underline{\underline{D_{eff}}}/D_0 = \underline{\underline{f}} = \epsilon \begin{bmatrix} \tau_{\perp}^{-1} & 0 \\ 0 & \tau_{\parallel}^{-1} \end{bmatrix} \tag{3}$$

Here, the tensor $\underline{\underline{f}}$ depends on local porosity ϵ and the local components of tortuosity normal to ($\tau_{\perp}$) and parallel with ($\tau_{\parallel}$) the dominant planar orientation. These tortuosity components increase with local microporosity $\boldsymbol{\varepsilon}$ as $\tau_j = \epsilon^{-\alpha_j}$,[1] where α_j is the tortuosity scaling-exponent for transport in direction j. We model the scaling exponents theorized previously[1] for graphite and $LiCoO_2$ electrodes that are listed in Table 2.1. In general the microstructure's orientation can vary in space, and the transport tensor $\underline{\underline{f}}$ would rotate in the fixed Cartesian-frame:

$$\underline{\underline{f_{cart}}} = \underline{\underline{R^T}} \left(\underline{\underline{f}} \right) \underline{\underline{R}}, \tag{4}$$

where $\underline{\underline{f_{cart}}}$ is the transport tensor in the fixed Cartesian-frame and $\underline{\underline{R}}$ is a space-dependent rotation-matrix describing the microstructure's local orientation. For the two-dimensional system here $\underline{\underline{R}}$ is given in terms of the polar angle θ between the *x*-axis and the direction perpendicular to the plane of microstructural orientation [see Fig. 2.1(a)]:

$$\underline{\underline{R}} = \begin{bmatrix} cos\theta & -sin\theta \\ sin\theta & cos\theta \end{bmatrix}, \tag{5}$$

Here, we assume uniform orientation along the plane of the current collector [i.e., $\theta(x, y) = \pi/2$].

The normal $\underline{\underline{\kappa_{eff,\perp}}}$ and parallel $\underline{\underline{\kappa_{eff,\parallel}}}$ components of the effective ionic-conductivity tensor are shown as a function of macro-pore coverage in Fig. 2.2(b) for a pressed-graphite anode with 30% average porosity. Each macro-pore coverage level ν_{mp} has a corresponding microporosity ϵ given by Eq. 1. The normal and parallel components of

tortuosity decrease with increasing microporosity. Consequently, both components of effective conductivity (normal and parallel) decrease with increasing macro-pore coverage because microporosity decreases with increasing macro-pore coverage. The anisotropy of effective ion conductivity[1] is also evident from Fig. 2.2(b), where conductivity perpendicular to the current collector $\underline{\underline{\kappa}}_{eff,\perp}$ is more than three times lower than the conductivity parallel to the current collector $\underline{\underline{\kappa}}_{eff,\parallel}$.

Table 2.1: Pore-space tortuosity scaling-exponents[1] used in the present simulations

Exponent	graphite	$LiCoO_2$
perpendicular (thru-plane), $\alpha_\perp$	1.914	0.830
parallel (in-plane), $\alpha_\parallel$	0.600	0.640

2.3 Governing Equations

Porous-electrode theory[3,4] is used presently to model the coupling between ion conduction, electron conduction, Li intercalation, and electrochemical reactions in heterogeneous, composite electrodes. Ion conduction occurs in the pores of the heterogeneous electrode. The particular electrolyte considered here contains $1\,mol/L$ $LiPF_6$ salt in mixed-carbonate solvent that exhibits a bulk ionic-conductivity κ_0 and bulk chemical-diffusivity of salt D_0 that varies with the local concentration of salt c_e [see Ref. [5,6] and Figs. 2.2(c,d)]. Ion conduction in the present monovalent, binary electrolyte (with constant transference number) is governed by charge conservation and salt conservation for a concentrated solution:[3,4,7,8]

$$\nabla.\left[-\underline{\underline{\kappa}}_{eff}\left(\nabla\phi_e - \frac{2R_gT}{F}\gamma_{\pm}(1-t_+)\nabla ln\, c_e\right)\right] - av_s i_n = 0, \qquad (5)$$

$$\frac{\partial(\epsilon c_e)}{\partial t} + \nabla.\left(-\underline{\underline{D}}_{eff}\nabla c_e\right) a v_s \frac{i_n}{F}(1 - t_+) = 0, \quad (6)$$

where ϕ_e is the solution-phase potential and c_e is the salt concentration in the electrolyte. These conservation equations incorporate the effects of ion-transport anisotropy through the effective-transport tensors $\underline{\underline{\kappa}}_{eff}$ and $\underline{\underline{D}}_{eff}$ that were described previously. Here, R_g, F, and T are the universal gas-constant, Faraday's constant, and temperature, respectively. For the Li-ion transference number t_+ we assume a constant value of 0.38,[5] and we assume a constant value of unity for the thermodynamic factor[7] $\gamma_\pm$, which is defined in terms of the mean-molar activity-coefficient $f_\pm$as $\gamma_\pm = (1 + \partial \ln f_\pm / \partial \ln c_e)$. The source terms in these equations are proportional to both the reaction current-density i_n at the electroactive-particle/electrolyte interface and the surface-area per unit-electrode-volume *a* of electroactive particles (see Table 2.2). Electron conduction occurs through conductive material driven by the solid-phase potential ϕ_s and is governed by:

$$\nabla.(-\sigma_s \nabla \phi_s) + a v_s i_n = 0, \quad (7)$$

where σ_s is the effective electronic conductivity whose value (see Table 2.2) is taken from the literature.[9]

Electrochemical reactions between the electrolyte and solid-state electroactive particles produce gradients of intercalated-Li concentration in electroactive particles. Here, the concentration of intercalated Li c_s is given in terms of the intercalated-Li fraction x_{Li} and the terminal concentration of intercalated Li $c_{s,max}$ as $c_s = x_{Li} c_{s,max}$. For the present electroactive particles ($2\mu m$ diameter for both graphite and $LiCoO_2$) at the C-rates of interest (0.5C to 3C), intercalated-Li gradients have been neglected in electroactive

particles because the difference is less than 0.25% for the cathode and 0.1% for the anode between the intercalated-Li fraction at the surface of and on average in electroactive particles cycled at 3C.[10] Under these conditions Li conservation in the solid phase is given by:

$$\nu_s c_{s,max} \frac{\partial x_{Li}}{\partial t} + a \frac{i_n}{F} = 0 \,, \tag{8}$$

where ν_s is the volume fraction of the electroactive material.

The driving force for electrochemical reactions is the surface overpotential at the solid/electrolyte interface, $\eta = \phi_s - \phi_e - \phi_{eq}$, where ϕ_{eq} is the equilibrium potential of the electroactive material that depends on the fraction of intercalated Li. Functions from the previous literature (Ref. [9] for graphite and Ref. [11] for $LiCoO_2$) were used to model the variation of equilibrium potential ϕ_{eq} versus the fraction of intercalated Li x_{Li} in each electrode. Electrochemical reaction-kinetics are modeled with the Butler-Volmer equation for reaction current-density i_n:[8]

$$i_n = i_0 \left[exp\left(\frac{0.5F\eta}{RT}\right) - exp\left(-\frac{0.5F\eta}{RT}\right)\right]. \tag{9}$$

The exchange current-density i_0 depends on the concentration of salt in the electrolyte c_e, the fraction of intercalated Li x_{Li}, and the kinetic rate-constant k for the particular reaction (see Table 2.2):[12]

$$i_0 = Fkc_{s,max}(c_e)^{0.5}(1 - x_{Li})^{0.5}(x_{Li})^{0.5}. \tag{10}$$

Table 2.2: Electrochemical-transport material-parameters used in the present simulations

parameter	graphite	$LiCoO_2$
electronic conductivity, $\sigma_s\ (S/m)$	$10^{\dagger}$	$10^{\dagger}$
volumetric surface-area, $a/v_s\ (1/m)$	3×10^6	3×10^6
terminal lithium concentration, $c_{s,max}(mol/m^3)$	$30{,}555^{\dagger}$	$51{,}554^{\dagger}$
rate constant, $k(mol/m^2 - s\times m^{4.5}/mol^{1.5})$	$5.03\times10^{-11\dagger}$	$2.34\times10^{-11\dagger}$

†Ref [9]

2.4 Boundary Conditions

The average current-density i applied to the cathode's current collector is held constant to simulate galvanostatic charge and discharge process. During galvanostatic cycling the anode current-collector is grounded with solid-phase potential $\phi_{s,-}$ set to 0 V, and the solid-phase potential of the cathode current-collector $\phi_{s,+}$ floats, such that the cell voltage ($\phi_{s,+} - \phi_{s,-}$) varies with time. The flux of Li ions is zero in the outward normal direction at the current collectors. At the separator a null electronic-current boundary-condition is imposed to replicate the electronically insulating property of the separator. Periodic boundary conditions are used to relate the solid-phase potentials, solution-phase potentials, and salt concentration on the opposing sides of the two-dimensional domain. The ionic resistance due to the separator is presently neglected because its thickness (~$10\ \mu m$) is small relative to that of the cell sandwich ($100 - 400\ \mu m$).

2.5 Numerical Discretization, Model Implementation, and Validation

The governing equations are discretized using the finite-volume method with implicit differencing and central differencing in time and space, respectively.[13] The fully coupled set of equations is solved iteratively to resolve non-linearities in the governing equations.[11] The solution algorithm is composed of two nested iteration-loops. In the inner loop, non-linearities in the kinetics of intercalation are resolved with respect to lithium concentration in the electroactive material and in the electrolyte using Newton-Raphson iteration and the algebraic-multigrid method.[14–16] If the change in kinetic overpotential between successive iterations exceeds a threshold value ($200mV$ presently), an under-relaxation factor for the kinetic overpotential (10% presently) is used to stabilize convergence of the iterative sequence until changes in kinetic overpotential decrease below the specified threshold value. In the outer loop, non-linearities in ionic conductivity are resolved with respect to salt concentration in the electrolyte using deferred correction, and no relaxation parameters are used to stabilize these iterations. Convergence of the iterative scheme is achieved when potentials differ by less than $10^{-9}V$ and salt concentrations differ by less than $10^{-9}\ mol/L$ between values during successive iterations.

For two-dimensional implementations of porous-electrode theory, the interpolation schemes for ion transport parameters and the choices for the maximum time-step can dramatically affect the stability of the numerical scheme and its convergence. We note that the issues described subsequently are not apparent in the one-dimensional implementation of porous-electrode theory that is ubiquitous in the literature. We use harmonic-mean formulas to interpolate effective salt-diffusivity values at the faces of

finite-volume cells. In contrast, the bulk ionic-conductivity on a given face of a finite-volume cell is approximated by that of the upwind cell-centroid, where the upwind direction is determined by the direction of the product of (1) the migration velocity $\overrightarrow{v_m}$ for Li ions in the electrolyte ($\overrightarrow{v_m} = \underline{\underline{\kappa}}_{eff}\nabla\phi_e/\epsilon F c_e$) and (2) the slope $\delta_k(c_e)$ of the bulk ionic-conductivity with respect to salt concentration ($\delta_k(c_e) = \partial\kappa_0/\partial c_e$). Similar schemes have been used previously to discretize the Poisson-Nernst-Planck equations for dilute solutions with the finite-volume method[17]. The latter factor accounts for the non-monotonic variation of bulk ionic conductivity at moderate salt concentrations [see $ce > 0.5\ mol/L$ in Fig. 2.2(c)].

Furthermore, solution of the discrete equations for ion transport can converge slowly and be altogether unstable when the velocity of Li-ion migration ($\overrightarrow{v_m} = \underline{\underline{\kappa}}_{eff}\nabla\phi_e/\epsilon F c_e$) exceeds a critical value of $\Delta u/\Delta t$, where Δu is the discrete spacing between cell centroids. When cells are cycled at high enough rates the electric field magnitude $|\nabla\phi_e|$ becomes large and salt concentration depletes ($c_e \to 0$), causing migration velocity to diverge and exacerbate this stability issue. Similar instabilities have been observed in the numerical solution of the drift/diffusion equations for electron/hole transport in semi-conductors, where Scharfetter and Gummel[18] developed an exponential interpolation scheme to stabilize numerical solutions to these equations. In lieu of using a similar exponential scheme, we stabilize the solution by adaptively reducing the time step such that $\Delta t \leq CFL_{m,tol}\Delta u/|\overrightarrow{v_m}.\hat{n}|$, where $CFL_{m,tol}$ is a Courant-Friedrichs-Lewy-number tolerance for migration (which we often take as 0.5) and $\hat{n}$ is the unit-normal on the cell-face spaced at Δu.

The present model was validated with Dualfoil 5.0 (Ref. [3]) for a $LiCoO2$ (50 vol.%)/graphite (60vol.%) cell with 100-micron-thick homogeneous electrodes, $1\,mol/L\ LiPF6$ salt in EC:DMC solvent, and tortuosity-scaling exponents of 0.5. Equilibrium potentials and bulk electrolyte properties were taken as those provided in Dualfoil 5.0 for the materials of interest. The simulated parameters that were compared with the present model were (1) the cell voltage over the discharge process, (2) the salt concentration profile at 30 and 60 minutes, and (3) the solution-phase potential at 30 and 60 minutes. Among all the data compared with the results of Dualfoil 5.0, the difference was less than the numerical precision with which data is output by Dualfoil 5.0.

2.6 References

1. Ebner, M., Chung, D.-W., García, R. E. & Wood, V. Tortuosity Anisotropy in Lithium-Ion Battery Electrodes. *Advanced Energy Materials* **4**, 1301278 (2014).
2. Bae, C.-J., Erdonmez, C. K., Halloran, J. W. & Chiang, Y.-M. Design of Battery Electrodes with Dual-Scale Porosity to Minimize Tortuosity and Maximize Performance. *Advanced Materials* **25**, 1254–1258 (2013).
3. Doyle, M., Fuller, T. F. & Newman, J. Modeling of Galvanostatic Charge and Discharge of the Lithium/Polymer/Insertion Cell. *J. Electrochem. Soc.* **140**, 1526–1533 (1993).
4. John Newman, W. T. Porous-electrode theory with battery applications. *AIChE Journal* **21**, 25–41 (2004).
5. Valøen, L. O. & Reimers, J. N. Transport Properties of LiPF6-Based Li-Ion Battery Electrolytes. *J. Electrochem. Soc.* **152**, A882–A891 (2005).
6. Forster, J. D., Harris, S. J. & Urban, J. J. Mapping Li+ Concentration and Transport via In Situ Confocal Raman Microscopy. *J. Phys. Chem. Lett.* **5**, 2007–2011 (2014).

7. Lai, W. & Ciucci, F. Mathematical modeling of porous battery electrodes—Revisit of Newman's model. *Electrochimica Acta* **56**, 4369–4377 (2011).
8. Newman, J. & Thomas-Alyea, K. E. *Electrochemical Systems*. (John Wiley & Sons, 2012).
9. Dao, T.-S., Vyasarayani, C. P. & McPhee, J. Simplification and order reduction of lithium-ion battery model based on porous-electrode theory. *Journal of Power Sources* **198**, 329–337 (2012).
10. Subramanian, V. R., Diwakar, V. D. & Tapriyal, D. Efficient Macro-Micro Scale Coupled Modeling of Batteries. *J. Electrochem. Soc.* **152**, A2002–A2008 (2005).
11. Smith, K. C., Chiang, Y.-M. & Carter, W. C. Maximizing Energetic Efficiency in Flow Batteries Utilizing Non-Newtonian Fluids. *J. Electrochem. Soc.* **161**, A486–A496 (2014).
12. Thomas, K. E., Newman, J. & Darling, R. M. Mathematical Modeling of Lithium Batteries. in *Advances in Lithium-Ion Batteries* (eds. van Schalkwijk, W. A. & Scrosati, B.) 345–392 (Springer US, 2002). doi:10.1007/0-306-47508-1_13
13. Patankar, S. *Numerical Heat Transfer and Fluid Flow*. (CRC Press, 1980).
14. Notay, Y. AN AGGREGATION-BASED ALGEBRAIC MULTIGRID METHOD. 24
15. Notay, Y. Aggregation-Based Algebraic Multigrid for Convection-Diffusion Equations. *SIAM J. Sci. Comput.* **34**, A2288–A2316 (2012).
16. Napov, A. & Notay, Y. An Algebraic Multigrid Method with Guaranteed Convergence Rate. *SIAM J. Sci. Comput.* **34**, A1079–A1109 (2012).
17. Mathur, S. R. & Murthy, J. Y. A multigrid method for the Poisson–Nernst–Planck equations. *International Journal of Heat and Mass Transfer* **52**, 4031–4039 (2009).
18. Scharfetter, D. L. & Gummel, H. K. Large-signal analysis of a silicon Read diode oscillator. *IEEE Transactions on Electron Devices* **16**, 64–77 (1969).

CHAPTER 3: Design of Bi-tortuous Electrodes

In this chapter, we first present results that elucidate the ion transport mechanisms that occur in bi-tortuous electrodes. Subsequently, we present a systematic study of discharge capacity for a variety of bi-tortuous structures, identifying key design-parameters and their influence on cycling performance. Lastly sensitivity analysis of optimized bi-tortuous electrodes designs is conducted to quantify how the performance of these electrodes is affected by cycling rate, electrode thickness, average loading, and average porosity. The metric used to quantify performance is discharge capacity, defined as the percentage of charge transferred during the discharge process relative to the theoretical maximum under open-circuit conditions.

The results presented in Sec. 3.1 and 3.2 are for full-cells cycled at a C-rate of C/2 having 200μm-thick electrodes with 30% average porosity and 70% average volume-fraction of electroactive material. In Sec. 3.3 these parameters are varied for optimized bi-tortuous anode designs. In all cases we benchmark the performance of bi-tortuous anodes with homogeneous anodes having the same average porosity (and loading) and electrode thickness. In all cases the same values of electrode thickness, average porosity, and electroactive-material volume-fraction are used for both the cathode and anode. We also assume that all space not filled by electrolyte is occupied by electroactive-material (i.e., neglecting the volume of binder and conductive carbon).

3.1 Ion Transport During Galvanostatic Cycling

Figure 3.1 shows the development of voltage with time for the charge/discharge process at C/2 for three different cases: (a) a homogeneous anode containing no macro-pores, (b) a bi-tortuous anode containing macro-pores having 20% coverage and spaced at wide intervals ($s/w = 2.0$), and (c) a bi-tortuous anode containing macro-pores having 20% coverage and spaced at short intervals ($s/w = 0.5$). The thumbnails inside the voltage plots correspond to the anodic structure for each of the cases and the snapshots adjacent to the plot represent the fraction of intercalated Li at five instants in time indicated on the voltage-versus-time curves in Fig. 3.1. At two instants in time (2 and 3) the lines of along which ionic current density flows (i.e., the ionic current-density lines) are shown, where the ionic current-density vector $\overrightarrow{\imath_e}$ at a given point in space is defined as $\overrightarrow{\imath_e} = -\underline{\underline{\kappa}}_{eff}(\nabla\phi_e - 2\gamma_{\pm}(1-t_+)RT/F\nabla \ln c_e)$.

For each voltage-versus-time curve the cell voltage increases from 3V to 4V (cutoff) during the charging process. Immediately afterward the discharge process starts and cell voltage decreases as time proceeds. Charge/discharge curves are shown as loops in order to illustrate the effect of polarization, which is proportional to the difference in voltage between charge and discharge. Comparing each of the voltage curves with the theoretical limit (which is 120 min at C/2) it is evident that the battery with a homogeneous anode has poor performance [Fig. 3.1(a)], while a cell having optimized macro-pores reaches a capacity much closer to the theoretical limit [Fig. 3.1(c)]. Also the bi-tortuous electrode in Fig. 3.1(c) shows smaller polarization than the homogeneous electrode. The mechanisms explaining the improved performance of the design in Fig. 3.1(c) and lower performance of the design in Fig. 3.1(b) are explained below.

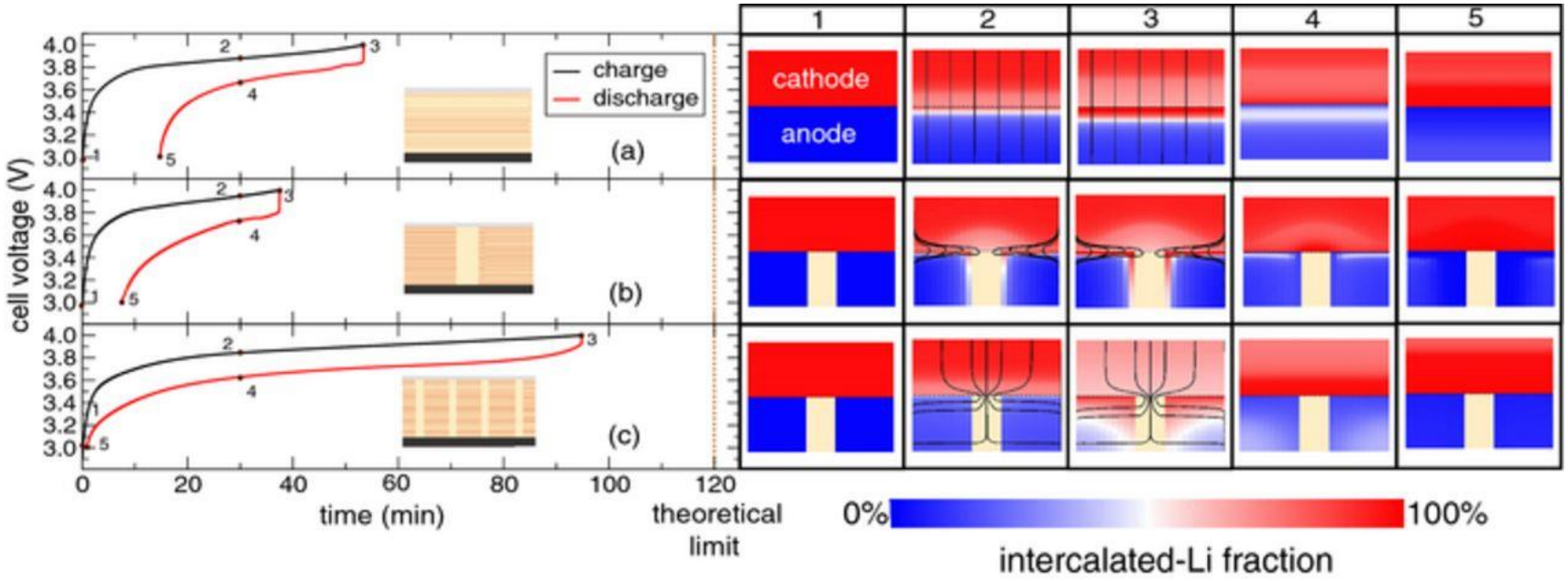

Figure 3.1: Voltage as a function of time for galvanostatic charge and discharge at C/2 rate for the following cases: (a) a homogeneous anode, (b) a bi-tortuous anode with s/w = 2.0 and 20% macro-pore coverage, and (c) a bi-tortuous anode with s/w = 0.5 and 20% macro-pore coverage. Snapshots of intercalated-Li fraction (not drawn to scale) at different instants in time marked on the voltage curves are shown as well. Lines of ionic current-density are shown at two instants in time for the three cases.

As stated previously, the high anisotropy of pressed-graphite electrodes leads to low ion-conductivity (i.e., high tortuosity) in the direction perpendicular to the current collector. As a result, a large potential difference is required to conduct Li ions through the anode's depth. However since the cell's charging voltage is limited to 4V, Li intercalates to a small degree throughout much of the anode's depth (see Fig. 3.1(a), snapshot 3). In contrast, deintercalation of Li in the cathode ($LiCoO2$) proceeds over a larger extent than in the anode, because the $LiCoO2$ cathode is more isotropic and has a higher thru-plane ionic conductivity than the graphite anode.

For cases (2) and (3) that contain macro-pores, Li intercalation initiates along the macro-pore's edge (Figs. 3.1(b,c), snapshot 3). This initial reaction front becomes curved as it propagates into the interior of the anode. However in case (2) the distance between macro pores *s* is large and ion transport parallel to the current collector is impeded by this large distance. Also, incorporation of a macro-pore with 20% coverage reduces the local porosity from 30% (for a homogeneous electrode) to 12.5% for the same average porosity. This produces an additional increase in the transverse ionic resistance inside the anode. As a result of these two effects, the reaction front in the anode becomes pinned near the separator at the end of charging cycle (Fig. 3.1(b), snapshot 3). We note that intercalation proceeds along the edges of the macro-pore but only within a small region near the macro-pore's surface. Similarly, at the end of discharge (Fig. 3.1(b), snapshot 5), capacity is underutilized in the regions between macro-pores in the anode.

Case (3) exhibits much better cycling performance than case (2), because of the shorter distance between macro-pores. The proper balance between the macro-pore coverage

(effecting local micro-porosity) and the spacing between macro-pores enables high utilization of graphite (as much as 80%). This is apparent from the high intercalated-Li fraction throughout the entire anode at the end of charging process (Fig. 3.1c, snapshot 3).

In order to further elucidate this, lines of ion current-density are plotted for the three cases. The homogeneous electrode shows ion current-density lines that are perpendicular to the current collector (Fig. 3.1(a), snapshot 2, 3). When the spacing between macro-pores is large [Fig. 3.1(b)] the intercalation of Li is concentrated close to the separator and at the interface between the macro-pore and graphite. As mentioned above, the large distance between macro-pores impedes transverse ion transport; consequently, ion current-density lines concentrate around the separator (Fig. 3.1(b), snapshot 2, 3). When the spacing-to-thickness ratio is small [Fig. 3.1(c)], ion current-density lines route preferentially through the macro-pore and extend transversely into the micro-porous region of the anode. The intercalation of Li occurs through the depth of anode (as does the delithiation in cathode), and it is evident that the primary direction of ion transport in the porous, graphite anode is parallel to the current collector.

3.2 Optimizing Macro-Pore Design: Coverage, Spacing, Shape, and Placement

The results in the previous section demonstrate that the dimensions and arrangement of macro-pores dictate their effectiveness in enhancing cycling performance. Here, effects of macro-pore coverage, spacing, shape, and placement are explored systematically. Firstly, the effect of macro-pore coverage and shape is studied. Figure 3.2 shows the

discharge capacity obtained for cycling $LiCoO2$/ graphite cells having particular macro-pore designs in the anode of a given cell. Straight macro-pores having certain coverage and spacing levels are considered first, though tapered shapes are considered later.

Figure 3.2

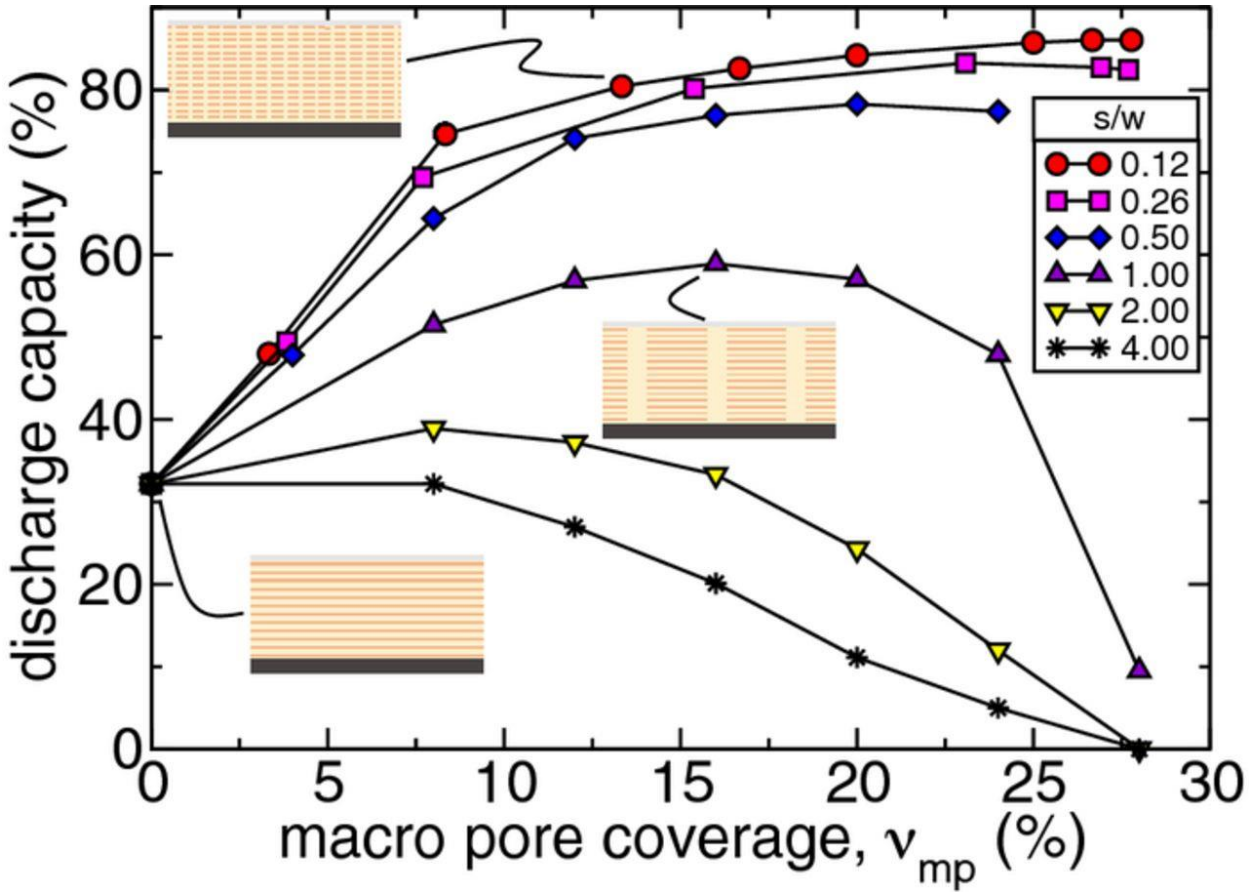

Figure 3.2: Variation of discharge capacity with macro-pore coverage for various spacing-to-thickness ratios in a graphite anode with 30% average porosity, 200 μm thickness, and cycled at C/2 rate.

For a spacing-to-thickness ratio of $s/w = 0.12$ discharge capacity increases monotonically with increasing macro-pore coverage. For larger spacing-to-thickness ratios (e.g., $s/w = 0.50$) discharge capacity is maximized at a particular macro-pore coverage level. This optimum appears as macro-pore coverage increases because of the competition between (1) increasing in-plane transport resistance in the micro-porous region of the anode and (2) decreasing thru-plane resistance of the macro-pore. Initially, increasing macro-pore coverage produces an increase of discharge capacity because of reduced thru-plane resistance to ion transport. However beyond the optimal coverage level, local porosity in the micro-porous region of the anode approaches zero [see Fig. 2.2(a)] leading to high resistance in both the in-plane and thru-plane directions. As a consequence of the polarization induced by ion-transport resistance, charge/discharge capacity reduces below the theoretical limit.

Incorporating a macro-pore into a graphite anode will not always result in a cell with enhanced performance relative to a homogeneous electrode. For instance, increasing the spacing between macro-pores beyond a certain limit at a fixed coverage level (e.g., $s/w \geq 2$ for 15% coverage) can result in poorer performance than a homogeneous electrode of the same average porosity (see Fig. 3.2, yellow triangles). Also, as the spacing-to-thickness ratio increases, the maximum discharge-capacity decreases. The optimal macro-pore coverage at which the maximum discharge-capacity is obtained shifts to low macro-pore coverage levels as the spacing-to-thickness ratio increases. This result reveals that, in general, the effectiveness of macro-pores decreases as spacing-to-thickness ratio increases. In other words, macro-pore dimensions must be sufficiently small if they are going to produce a measurable enhancement in cycling performance.

Figure 3.3

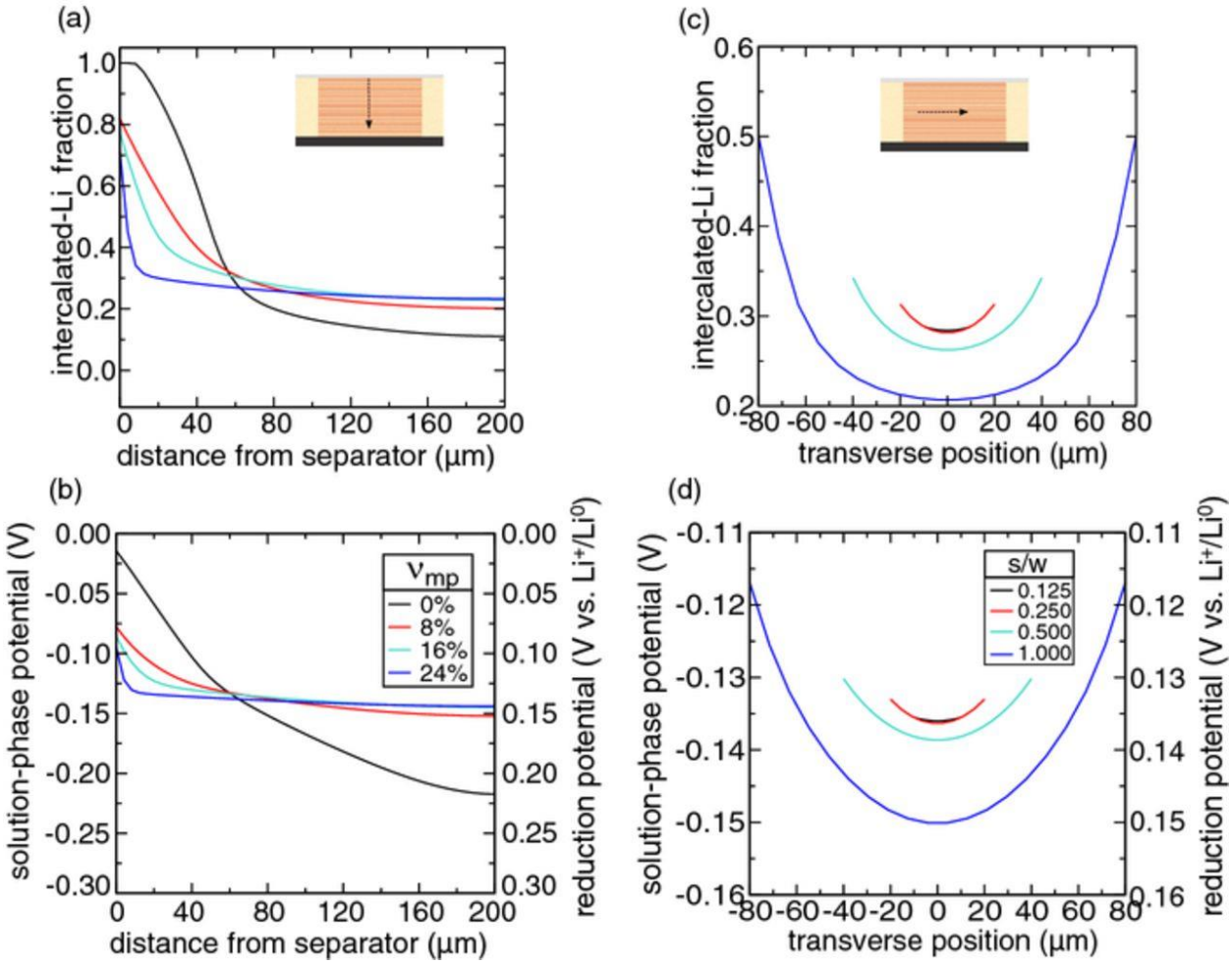

Figure 3.3: Profiles of (a) intercalated-Li fraction and (b) solution-phase potential through the thickness of graphite anodes (as shown in the thumbnail). These profiles are shown for increasing macro-pore coverage with a particular spacing-to-thickness ratio of 0.5. Profiles of (c) intercalated-Li fraction and (d) solution-phase potential across the transverse direction and through the center of graphite anodes. These profiles are shown for increasing spacing-to-thickness ratio and having fixed macro-pore coverage of 25%. All profiles are shown after 50 min from the start of the charging process at C/2.

To understand the particular mechanisms that produce the behavior displayed in Fig. 3.2, solution-phase potential and intercalated-Li profiles are plotted in Fig. 3.3. In Figs. 3.3(a,b) these profiles are shown through the thickness of the graphite anode, and the curves shown correspond to various macro-pore coverage levels, all after 50 minutes of charging each cell and with the same spacing-to-thickness ratio ($s/w = 0.5$). The magnitude of the potential drop across the graphite anode decreases as macro-pore coverage increases [Fig. 3.3(b)]. This trend occurs because more current flows through macro-pores as coverage increases. Consequently, less current flows through the thickness of the micro-porous region and potential drop is less across it as a result. We also note that the large potential drop in the homogeneous anode is coincident with the termination of charging and that complete intercalation of graphite near the separator occurs as well [Fig. 3.3(a)]. In contrast, cells with bi-tortuous anodes show less extreme variation of intercalated-Li fraction. The plateau of intercalated-Li fraction far from the separator is a result of uniform reactions that occur inside the bi-tortuous anode. In reality, cells cycled to extreme states-of-charge would be accompanied by the deposition of Li metal that would induce rapid capacity fade. This tendency is also reflected by the reduction potential (defined locally inside the electrode as $\phi s - \phi e$) approaching 0 V vs. Li^+/Li^0 near the separator [Fig. 8(b)]. Thus, macro-pores could improve capacity retention in $LiCoO2$/graphite cells, in addition to enhancing their discharge capacity, since extreme states-of-charge can be avoided. Previous work[1] has predicted that Li-metal deposition is exacerbated at electrode edges, but extension of anode surfaces beyond the cathode helped to prevent such deposition. The results shown in Fig. 3.3d reveal that variations in reduction potential are most extreme for macro-pores with large spacing.

These trends suggest that Li-metal deposition could be a problem for macro-pores spaced at large intervals, but Li-metal deposition is unlikely for designs with sufficiently small spacing (e.g., the $100\ mm$ spacing case shown in Fig. 3.3b). The effect of macro-pore spacing is apparent on the solution-phase potential-drop (which produces a variation in reduction potential) is smallest for Solution-phase potential and intercalated-Li fraction profiles are also plotted in the in-plane direction through the center of the graphite anode [Fig. 3.3(c, d)]. The curves shown correspond to various spacing-to-thickness ratios, all after 50 minutes of charging each cell and with 15% macro-pore coverage. More frequently spaced macro-pores (given by small *s*/*w* values) produce more uniform Li intercalation in the transverse direction. Li intercalation becomes more uniform across the anode when spacing between macro-pores decreases, because in-plane resistance of the micro-porous region of the electrode reduces. This effect is reflected by the reduction in solution-phase potential-drop across the anode when spacing is decreased [Fig. 3.3(d)].

A straight macro-pore shape is not necessarily optimal electrochemically and may be difficult to manufacture, since a line-of-sight process would be required to produce it. To quantify the effect of pore shape on electrochemical performance, we have also considered an angled taper on the pore's sidewall. A single macro-pore of this type was simulated in Ref. [2]. Fig. 3.4 shows the charge capacity of such a cell as a function of taper angle for a fixed macro-pore coverage of 24% and spacing-to-thickness ratio of $s/w = 0.5$ (for an electrode thickness of $200\ \mu m$). For this particular coverage and spacing, the maximum taper-angle was 6.84° for a macro-pore extending completely through the anode's thickness. Positive taper-angles enhance cycling capacity by ~5%

over that of the straight macro-pore, while negative taper-angles produce a dramatic drop in capacity (>50%). This dependence on taper angle is a result of the fact that the amount of thru-plane ionic-current flowing from the cathode to the anode is largest near the separator. Negative taper angles constrict ionic current near the separator to a small cross-sectional area. This constriction results in high current-density and large potential drop through the macro-pore. In the opposite sense, positive taper angles reduce the thru-plane current-density flowing through the macro-pore, reducing solution-phase potential-drop through the macro-pore.

Figure 3.4

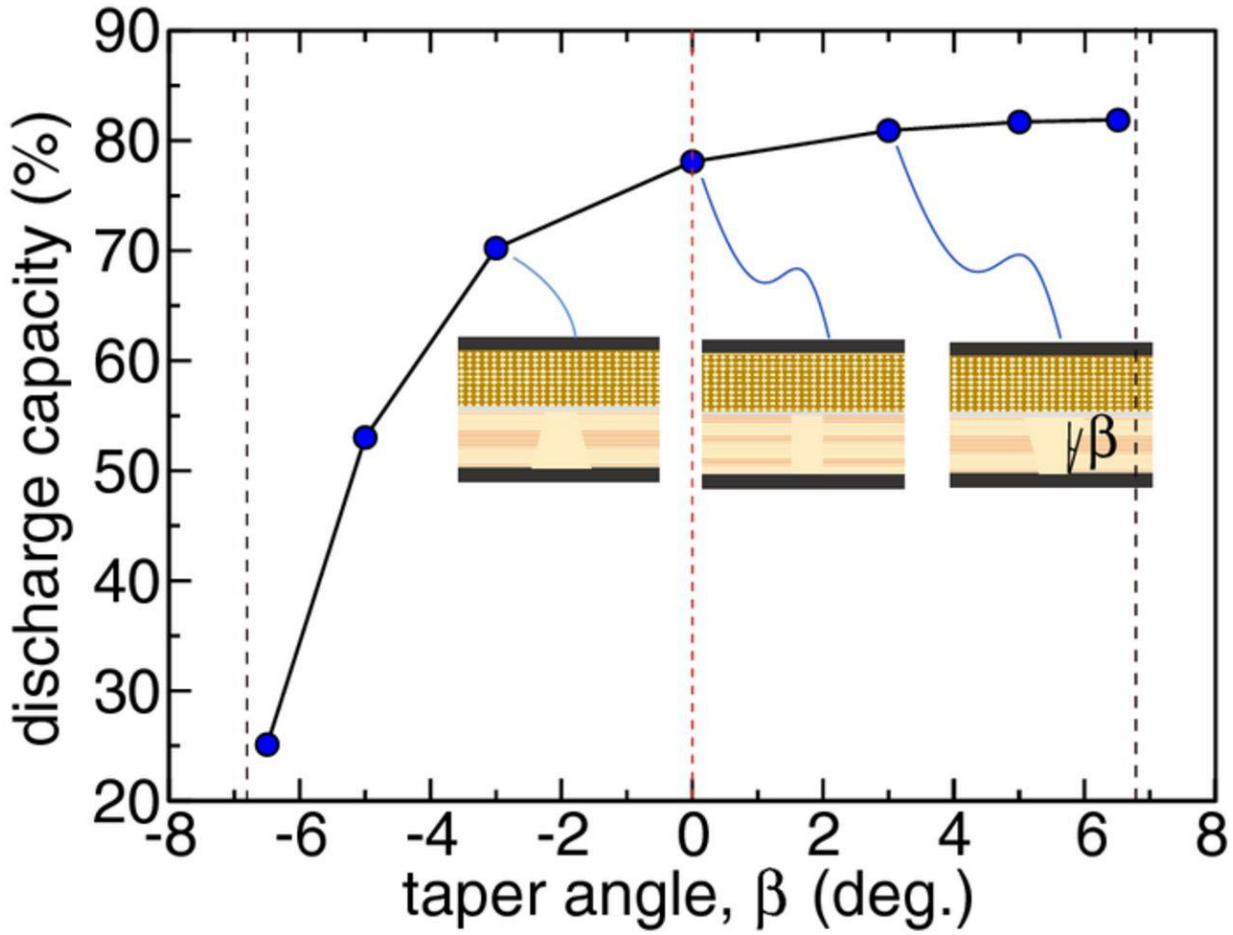

Figure 3.4 (cont.)

Figure 3.4: Discharge capacity as a function of macro-pore taper-angle. Macro-pore coverage in the graphite anode is fixed to 24% in all cases with 30% average porosity, spacing-to-thickness ratio of 0.5, and cycled at C/2.

The previous results demonstrate that macro-pores in anisotropic graphite anodes can enhance full-cell cycling performance, but we find here that performance can be further improved by structuring the $LiCoO2$ cathode together with the graphite anode. This improvement is shown in Fig. 3.5, where discharge capacity is shown as a function of macro-pore coverage in the cathode with 15% macro-pore coverage in the anode and $s/w = 0.5$ for macro-pores in both electrodes (red squares). Here, the discharge capacity increases with increasing macro-pore coverage to a maximum discharge capacity at 25% cathode macro-pore coverage, after which discharge capacity decreases. As a reference, discharge capacity is shown for various macro-pore coverage-levels in the anode alone (i.e., without macro-pores in the cathode). A clear trend of improved performance is observed: (1) the homogeneous electrode achieves 35% discharge capacity, (2) the anode with optimized macro-pore coverage and spacing achieves 80% discharge capacity, and (3) the cell with both electrodes having optimized macro-pores achieves 90% discharge capacity. Using macro-pores in the cathode cuts the amount of capacity lost in half relative to the case with macro-pores in the anode alone. Further, the present analysis assumes that the cathode macro-pores align with anode macro-pores, which provides an upper bound on the enhancement in capacity that could be expected if macro-pores were not aligned in the respective electrodes. In practice, lateral alignment

between the two electrodes during cell assembly will be difficult because of the fine features that the electrodes possess (~10 μm).

Figure 3.5

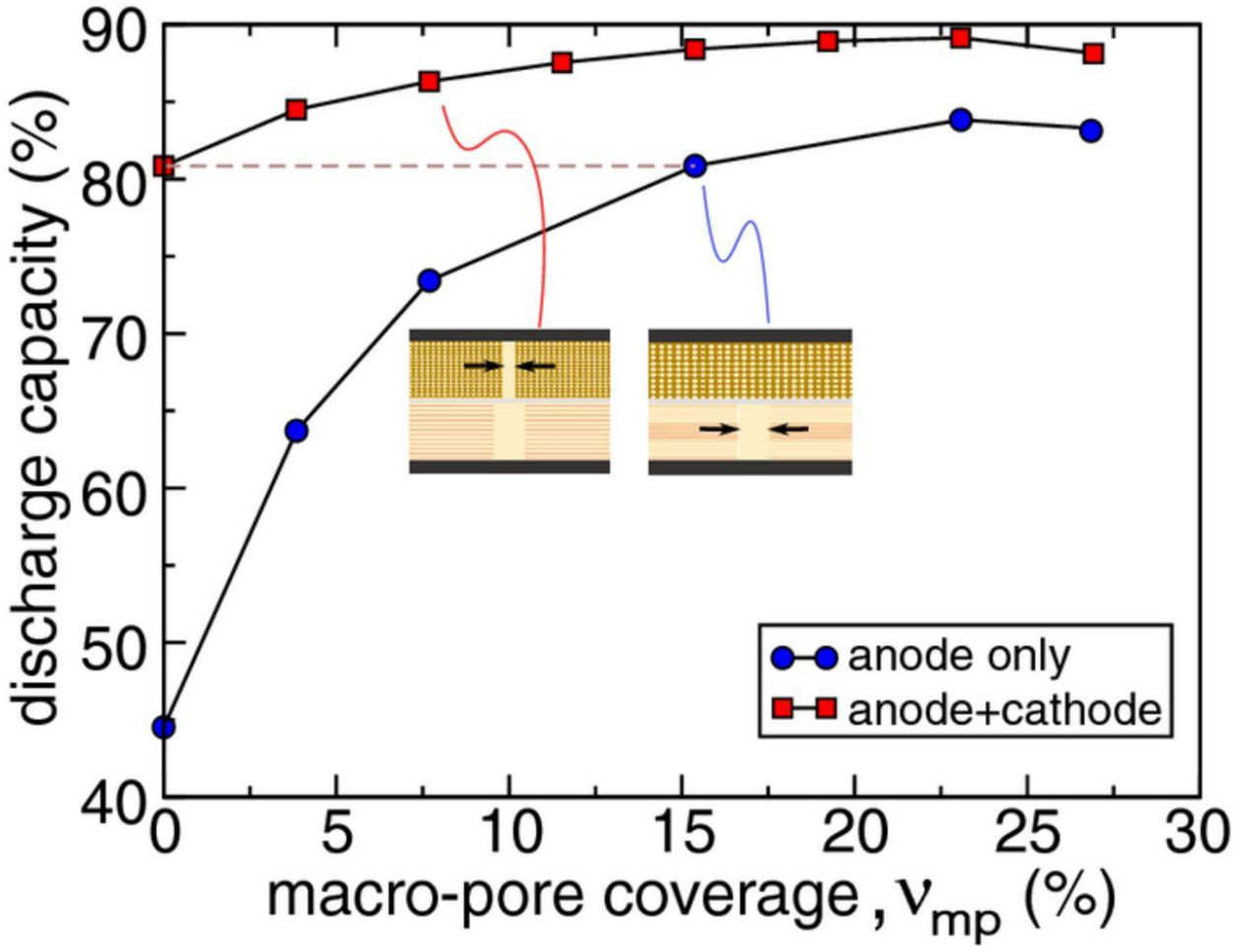

Figure 3.5: Discharge capacity as a function of cathode macro-pore coverage with fixed anode macro-pore coverage of 15%. As a benchmark, discharge capacity is plotted as a function of anode macro-pore coverage for a cell having no macro-pore in the cathode. Both electrodes have an average porosity of 30% and spacing-to-thickness ratio of 0.5. Discharge capacity was obtained by cycling at C/2 rate.

3.3 Sensitivity of Performance: Cycling Rate, Electrode Thickness, Average Porosity, and Electroactive-material Loading

The results presented thus far are for full-cells cycled at a C-rate of C/2 and having 200μm-thick electrodes with 30% average porosity and 70% average volume-fraction of electroactive material. Optimized cells may have different electrode thicknesses, average porosities, and electroactive-material loading depending on their particular material, manufacturing, and cost constraints. Further, the rate at which a given cell is cycled will vary during its use and will depend on the particular application in which the cell is used. Thus, it is important to understand how the performance of optimized bi-tortuous electrode structures is affected by cell-manufacturing and operating parameters. Subsequently, we predict the sensitivities of performance of optimized bi-tortuous anodes with respect to these parameters.

Firstly, we consider the sensitivities of performance with respect to cycling rate and electrode thickness. Figure 3.6 shows discharge capacity as a function of C-rate for cells having three different electrode thicknesses ($200\ \mu m$, $100\ \mu m$, and $50\ \mu m$). Figure 3.6(a) shows that thicker electrodes have lower capacity than thinner ones at a given C-rate. Also, for a given electrode thickness the bi-tortuous electrode produces higher capacity than the homogeneous electrode at all C-rates. Figure 3.6(c) shows the difference in capacity between bi-tortuous and homogeneous electrodes. The maximum enhancement in capacity for the bi-tortuous electrode is obtained at a particular C-rate that increases as electrode thickness decreases.

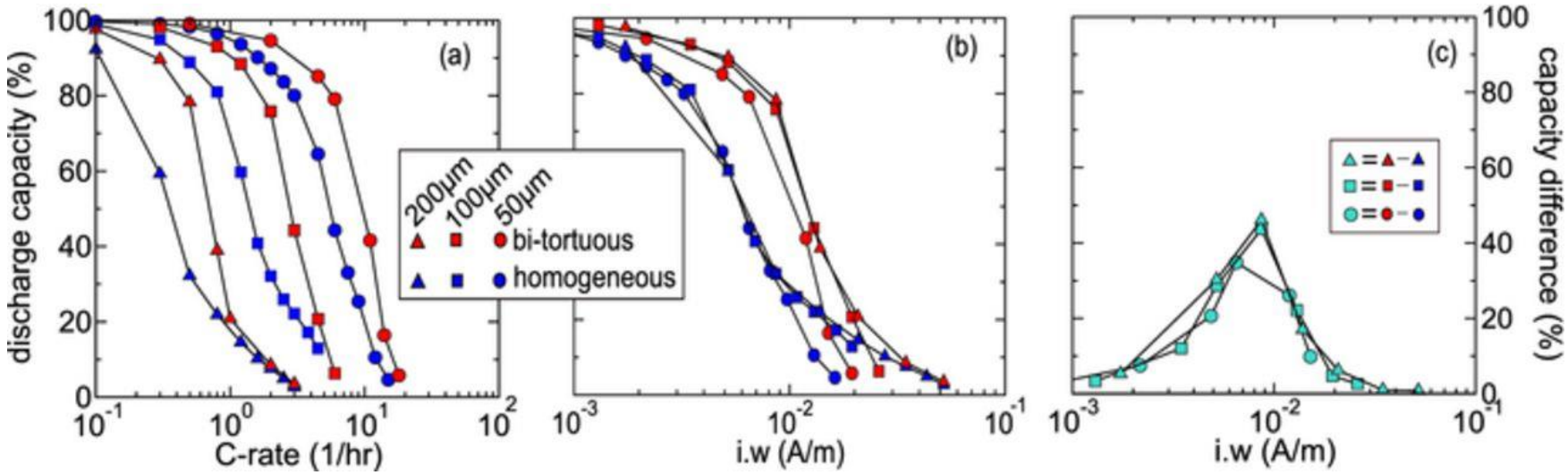

Figure 3.6: (a) Discharge capacity as a function of C-rate. Six cases are shown: three different electrode thicknesses, each with a bi-tortuous (20% macro-pore coverage and spacing-to-thickness ratio of 0.5) or homogenous anode. In (b) discharge capacity is plotted against the product of average applied current-density i and the electrode thickness w. (c) The difference in capacity between the bi-tortuous and homogeneous electrodes is shown as a function of iw.

The sensitivity with respect to electrode thickness and rate can be simplified by considering the theoretical scaling of polarization among these cases. A simple equivalent-circuit model of ohmic, ionic conduction within these electrodes suggests that cell polarization scales proportionally with average applied current-density i and electrode thickness w. Figure 3.6(b) shows the capacity of these cells as a function of iw (the product of the average current-density and electrode thickness). For sufficiently large electrode thicknesses ($w \geq 100\mu m$) these curves collapse on each other, because ohmic, ionic conduction dominates polarization for large enough electrodes. For thinner electrodes (e.g., $50\ \mu m$) capacities of both bi-tortuous and homogeneous anodes are less than those of thicker electrodes at a given value of iw, because other mechanisms than ionic conduction (e.g., electrochemical reaction-kinetics and solid-state mass-transfer) contribute more cell polarization for thin electrodes.

The average porosity and loading of electroactive material are important to study from the standpoint of manufacturing constraints and cost: (1) porosities will be limited by the packing density of electroactive-material (see Ref. [3]) and the amount inactive additives used (e.g., binder and conductive carbon) and (2) the average porosity will affect the total amount of electrolyte used for a given cell and will affect the cost-contribution from it (relative to the total cell-cost). Accordingly, capacity is shown in Fig. 3.7 as a function of average porosity (and average loading of electroactive material) for anodes with various macro-pore coverage-levels. In all cases we fix $s/w = 0.5$ and $w = 200\mu m$. Here, the particular C-rate (or average current density) used to cycle a cell of certain average porosity was varied proportionally with the average volume-fraction of active material $\overline{v_s}$ and the thru-plane effective ionic conductivity of the benchmark homogeneous-electrode

$\kappa_{eff,\perp} \propto \bar{\epsilon}^{2.914}$ at the average porosity $\bar{\epsilon}$ [see Fig. 3.7(b)]. For these C-rates, bi-tortuous structures having 20% and 40% macro-pore coverage achieve discharge capacities of 80-90% for average porosities ranging between 20-80% [Fig. 3.7(a)]. In all cases, the bi-tortuous structures show higher discharge capacity than their homogeneous counterparts having the same average porosity and loading [Fig. 3.7(a)]. We note that the enhancement gained by the bi-tortuous structures (relative to their homogeneous counterparts) decreases as porosity increases. Therefore, the present bi-tortuous structures will be particularly effective when minimal amounts of electrolyte are used inside the battery.

Figure 3.7

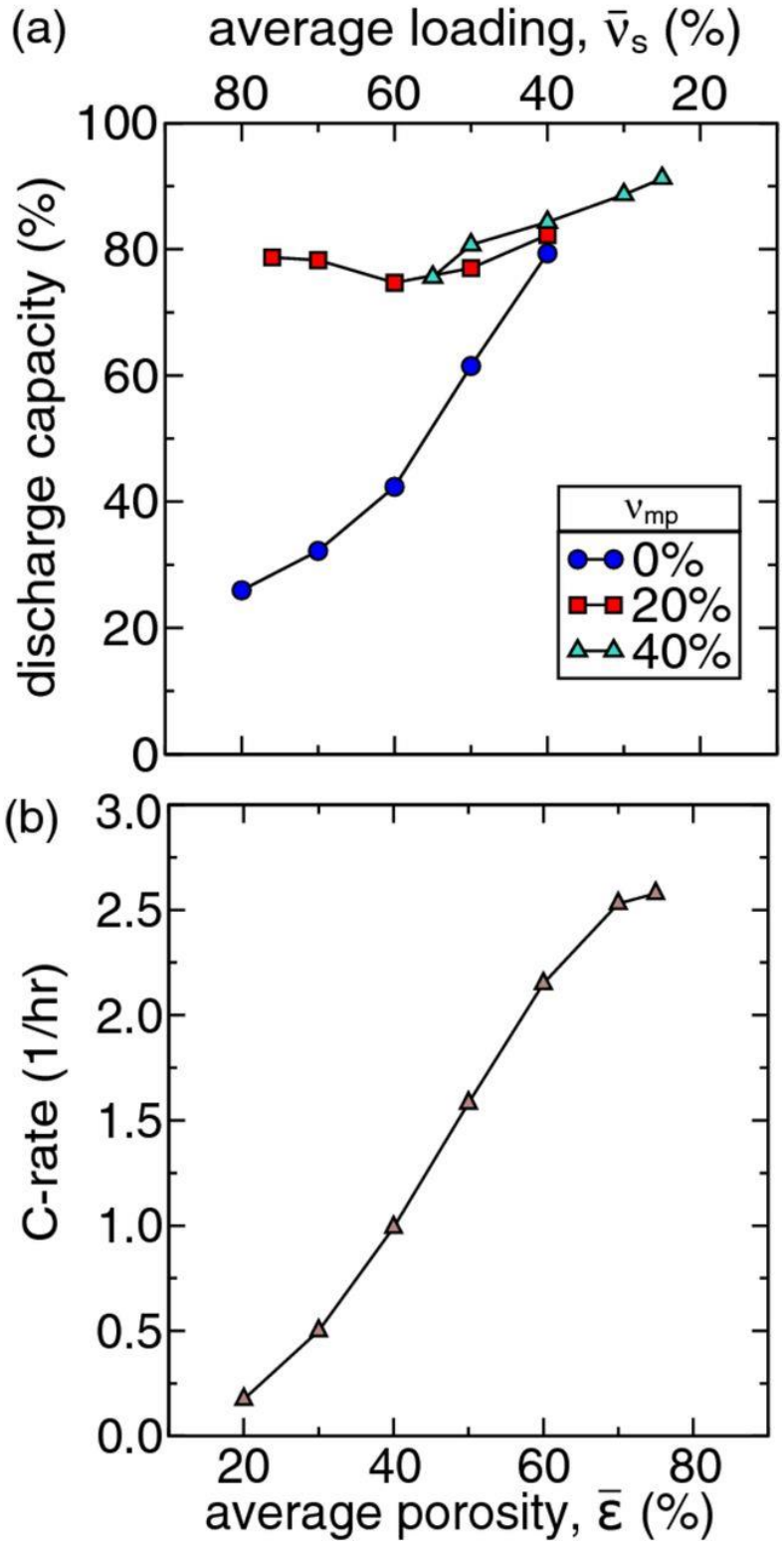
(a)
average loading, $\bar{\nu}_s$ (%)
80
60
40
20
100
80
60
40
20
0
discharge capacity (%)
ν_{mp}
0%
20%
40%
(b)
3.0
2.5
2.0
1.5
1.0
0.5
0.0
C-rate (1/hr)
20
40
60
80
average porosity, $\bar{\varepsilon}$ (%)

Figure 3.7 (cont.)

Figure 3.7: (a) Discharge capacity as a function of average porosity (and average electroactive-material volume-fraction/loading) for various macro-pore coverage levels in a graphite anode. Spacing-to-thickness ratio was fixed to 0.5 in all cases. For each porosity the C-rate was chosen as shown in (b).

3.4 References

1. Tang, M., Albertus, P. & Newman, J. Two-Dimensional Modeling of Lithium Deposition during Cell Charging. *J. Electrochem. Soc.* **156**, A390–A399 (2009).
2. Cobb, C. L. & Blanco, M. Modeling mass and density distribution effects on the performance of co-extruded electrodes for high energy density lithium-ion batteries. *Journal of Power Sources* **249**, 357–366 (2014).
3. Smith, K. C., Mukherjee, P. P. & Fisher, T. S. Columnar order in jammed LiFePO4 cathodes: ion transport catastrophe and its mitigation. *Phys. Chem. Chem. Phys.* **14**, 7040–7050 (2012).

CHAPTER 4: Porous Electrode Modeling of Redox Flow Batteries

The multiphysics nature of RFBs challenges both the design and operation of RFBs. Mathematical modeling of the physical processes in an RFB aids in narrowing the design space in a cost-, resource-, and time-effective manner. Atomistic simulations through density functional theory predict the thermodynamic equilibrium properties of redox-active molecules and their interactions with electrolyte[1]. Macro-scale simulations capture spatial and temporal variation of redox concentration, overpotential and current density, thus predicting the performance of RFBs. The first 2D transient model of vanadium RFB was developed by Shah et al[2] following which other models[3–8] for VRFBs have been presented. In addition, models for polysulfide redox flow battery[9,10], hydrogen bromine flow battery[11,12] and metal free organic-inorganic flow batteries[13] have been developed. In addition to the specific chemistries, it is important model transport through the non-selective separator or selective ion-exchange membrane. Non-selective separators (NSSs) are treated as a porous medium with certain pore size, porosity, and tortuosity[14,15]. Ion exchange membranes (IEMs), on the other hand, require special treatment because of the presence of fixed charges which doesn't satisfy the electroneutrality condition near the membrane-electrode interface[16]. Researchers, in the field of RFBs and other similar electrochemical systems, often use the concept of Donnan potential[16] to force a discontinuous jump in the solution potential across the membrane/ electrode interface assuming quasi-equilibrium conditions[17,18]. A more rigorous approach

---

Sections of this chapter are reprinted from

1) Nemani V. P., Smith K. C., Uncovering the role of flow rate in redox-active polymer flow batteries: simulation of reaction distributions with simultaneous mixing in tanks, Electrochim. Acta, 247, Copyright (2017), with permission from Elsevier

2) Nemani, V. P.; Smith, K. C. Analysis of Crossover-Induced Capacity Fade in Redox Flow Batteries with Non-Selective Separators. J. Electrochem. Soc.. 2018, 165(13), A3144–A3155, Copyright (2018), with permission from The Electrochemical Society

is to incorporate the Poisson equation along with the Nernst-Planck equation for species fluxes to realize the electric double layer effects near the membrane-electrode interface[19–21] in a continuous manner. However, most of these models were developed for specific redox chemistries and focused on the processes within the reactor alone.

We develop a transient two-dimensional continuum model based on porous electrode theory which encompasses the effects of species reactions and transport through the electrode and the membrane. The porous electrode theory is implemented by homogenizing the micro-scale processes (such as reaction kinetics) and the macro-scale processes (such as diffusion) by locally volume-averaging the concentration and the potential fields throughout the reactor domain. The electrolyte storing tanks are assumed to be well mixed with uniform species concentration throughout the volume of the tank.

4.1 Reactor Design and Electrochemistry

The RFB simulated here consists of a reactor and two well-mixed tanks connected through a network of pipes. The reactor contains two carbon paper electrodes separated by an IEM. We model the reactors to have either a parallel flow field (PFF) or an interdigitated flow field (IDFF). The electrochemical performance of PFF is better than IDFF due to effective wetting of electrodes. However, PFF requires a larger pressure head to ensure flow through the electrodes[22]. IDFF can be established by designing alternate inlet and outlet channel creating a 2D flow within the electrodes (Figure 4.1). Monitoring pressure drops is important in the context of Non-aqueous redox flow batteries (NAqRFBs) as the electrolyte viscosity increases rapidly with redox concentration[23,24].

Moreover, operating RFBs at higher magnitudes of pressure would force bulk movement of electrolytes through the separator leading to electrolyte loss (and thus capacity loss) and possibly affecting the life of the membrane. Also, pumping costs increase, reducing the net effective energy stored/delivered by the battery system.

A simple schematic showing a representative unit cell of a PFF and an IDFF reactor is shown in Fig. 4.2 (a) and (b) respectively (the schematic shows just one electrode-tank for illustration). The representative unit cell of length L_e along the direction of the current collector has two electrodes with a thickness H_e, and porosity ϵ_e each. The membrane is treated as an electron-insulating porous medium with a fixed charge concentration $c_{f,membrane}$, thickness H_m, porosity ϵ_m and tortuosity τ_m. The membrane properties are dependent on several parameters such a relative humidity, the functional groups attached and electrolyte composition. For this study, representative values for the membrane properties are chosen.

The properties of the reactor and membrane are listed in Table 4.1.

Figure 4.1

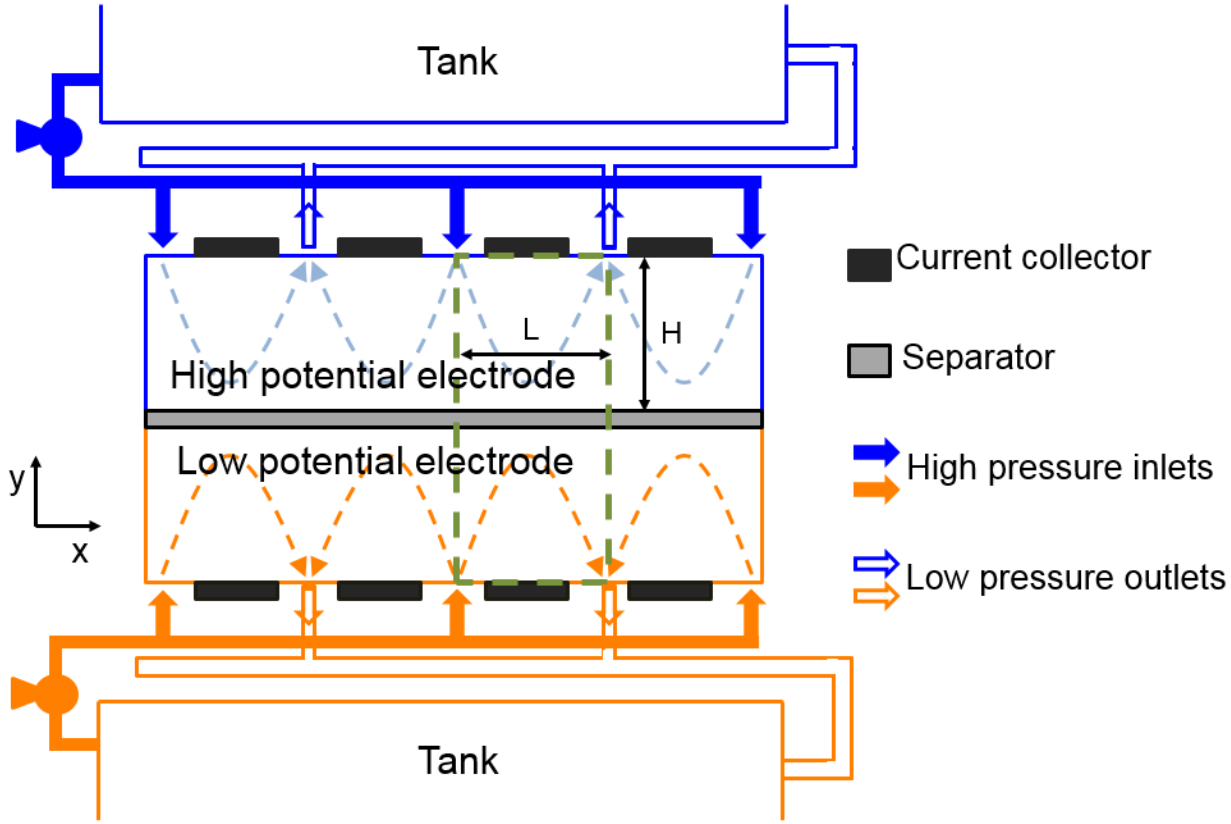

Figure 4.1: Schematic of the simulated flow battery using a 2D interdigitated flow field (IDFF) in its reactor. H is the electrode thickness and L is the length of representative basic repeat unit (green box) modeled here.

Figure 4.2

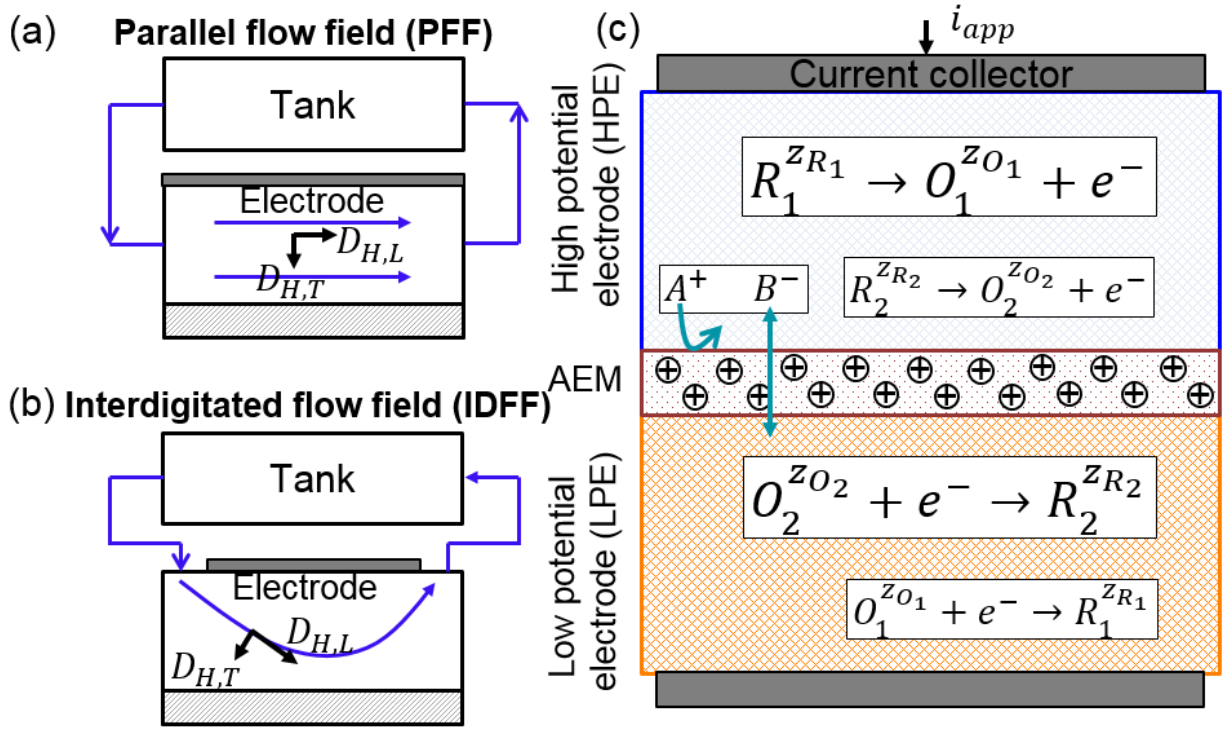

Figure 4.2: (a) Parallel flow field (PFF), (b) A single unit cell of an interdigitated flow field (IDFF) and (c) electrochemistry within the reactor. The reactions with larger text size are primary to the electrode and the other reaction is a result of crossover of species from the counter electrode.

In this study, we model the transport of two redox couples, one redox couple primary to the high potential electrode (HPE) $R_1^{z_{R_1}}, O_1^{z_{O_1}}$ and other primary to the low potential electrode (LPE) $R_2^{z_{R_2}}, O_2^{z_{O_2}}$. The non-reactive species A^+ and B^-, which come from the supporting electrolyte, ensure charge balance in the bulk of the electrolyte during the charge/ discharge cycles by transferring across the membrane. Our model also accounts for crossover effects[15] where species primary to one electrode transports across the membrane into the counter electrode. The species that crossed over now experience

reaction environments of the counter electrode and are forced to react leading to a second set of reactions (shown in smaller font in Fig 4.2.(c)) which reduces the coulombic efficiency and causes permanent loss of capacity. Such crossover arises due to diffusion and migration[28] of redox species from one electrode to another.

Table 4.1: Reactor geometry, carbon felt electrode and separator properties

Parameter	Value
length of current collector, $L_e\ (mm)$	2
electrode flow entry length,$L_{ent}\ (mm)$	0.5
electrode thickness, $H_e\ (\mu m)$	200
porosity of carbon felt electrode, ϵ_e	0.9
solid volume fraction of carbon felt, ν_e	0.1
tortuosity of electrode, τ_e	1.05*
Permeability of electrolyte in carbon felt, $K_e(m^2)$	6×10^{-11}**
Membrane thickness, $H_m\ (\mu m)$	60
porosity of separator, ϵ_m	0.37[#]
Tortuosity of separator, τ_m	6[ł]

*Bruggeman relationship[26] [#]Ref. [27] [ł]Ref. [25]

The primary redox reactions in the high potential and low potential electrode at 50% state-of-charge (SOC) can be represented as

$$R_1^{z_{R1}} \leftrightharpoons O_1^{z_{O1}} + e^- \quad E_{HPE,eq}$$

$$O_2^{z_{O2}} + e^- \leftrightharpoons R_2^{z_{R2}} \quad E_{LPE,eq}$$

The above set of reactions can be classified as a rocking-chair mechanism where the redox species have similarly signed, non-zero oxidation states[31]. Based on our previous study with non-selective separators[15], we choose to operate the RFB in a sufficient supporting electrolyte regime where the amount of salt (A^+B^-) is significantly larger than the redox active concentration.

4.2 Reaction Kinetics

The pore-scale reaction current density i_n is modeled using Marcus-Hush-Chidsey (MHC) kinetics. The MHC model is based on the microscopic theory of electron transfer while accounting for the interaction between electrode surface, redox species and the solvent[45–47]. The energy required to reorganize the atomic configurations during charge transfer are accounted as the reorganization energy λ. The most commonly used Butler-Volmer (BV) kinetics assumes the chemical potential to vary linearly with reaction co-ordinates (through charge transfer coefficient α). BV model follows Tafel relationship where the current density is exponentially related with the over-potential at 50% state-of-charge η^0, and the oxidation and reduction reaction rate constants for BV are given as

$$k_{ox}^{BV} = k_0 e^{(1-\alpha)F\eta^0/RT}$$

$$k_{red}^{BV} = k_0 e^{-\alpha F\eta^0/RT}$$

MHC kinetic model, on the other hand, considers several energy levels around Fermi level to participate in the redox reaction and has a harmonic oscillatory type variation of

chemical potential with reaction progress[45,48]. The rate constant is expressed as an integral of electron energy level x with respect to Fermi level with a pre-exponent factor A as:

$$k_{ox/red}^{MHC} = A\int_{-\infty}^{\infty} exp\left(-\frac{(x-\lambda\pm e\eta^0)^2}{4\lambda k_B T}\right)\frac{dx}{1+exp(x/k_B T)}$$

A simplified analytical expression[49] for the integral expression of $k_{ox/red}^{MHC}$ is reported in terms of dimensionless overpotential $\eta^{0,*} = \eta^0 e/k_B T$ and re-organization energy $\lambda^* = \lambda/k_B T$

$$k_{ox/red}^{MHC} = A\frac{\sqrt{\pi\lambda^*}}{1+\exp(\mp\eta^{0,*})}erfc\left(\frac{\lambda^* - \sqrt{1+\sqrt{\lambda^*}+{\eta^{0,*}}^2}}{2\sqrt{\lambda^*}}\right)$$

Figure 4.3 compares the reaction rate constants for both BV and MHC kinetics against overpotential η^0. Due to its exponential nature, k_{ox}^{BV} increases with η^0 whereas, k_{ox}^{MHC} saturates with η^0 limiting the maximum reaction rate constant achievable.

The net reaction current i_n for the redox reaction $R \rightleftharpoons O + e^-$ can be written as

$$i_n = F(k_{ox}c_R^S - k_{red}c_O^S)$$

Where c_O and c_R are the concentrations of the oxidized and reduced species respectively. The reaction overpotential η^0 which drives the redox reaction can be expressed as solid phase/ electrode potential ϕ_s, solution potential ϕ_e and the equilibrium potential $\phi_{eq,50\%}$ at 50% state-of-charge of the redox active species: $\eta^0 = \phi_s - \phi_e - \phi_{eq,50\%}$. The

equilibrium potential at every instant in time during the charge/ discharge cycle is determined using the Nernst equation:

$$\phi_{eq} = (E^{eq}_{HPE} - E^{eq}_{LPE}) - \frac{RT}{n_e F} ln \frac{c^s_R}{c^s_O}$$

where n_e is the number of electrons transferred in the redox reaction ($n_e = 1$ in our present study).

Figure 4.3

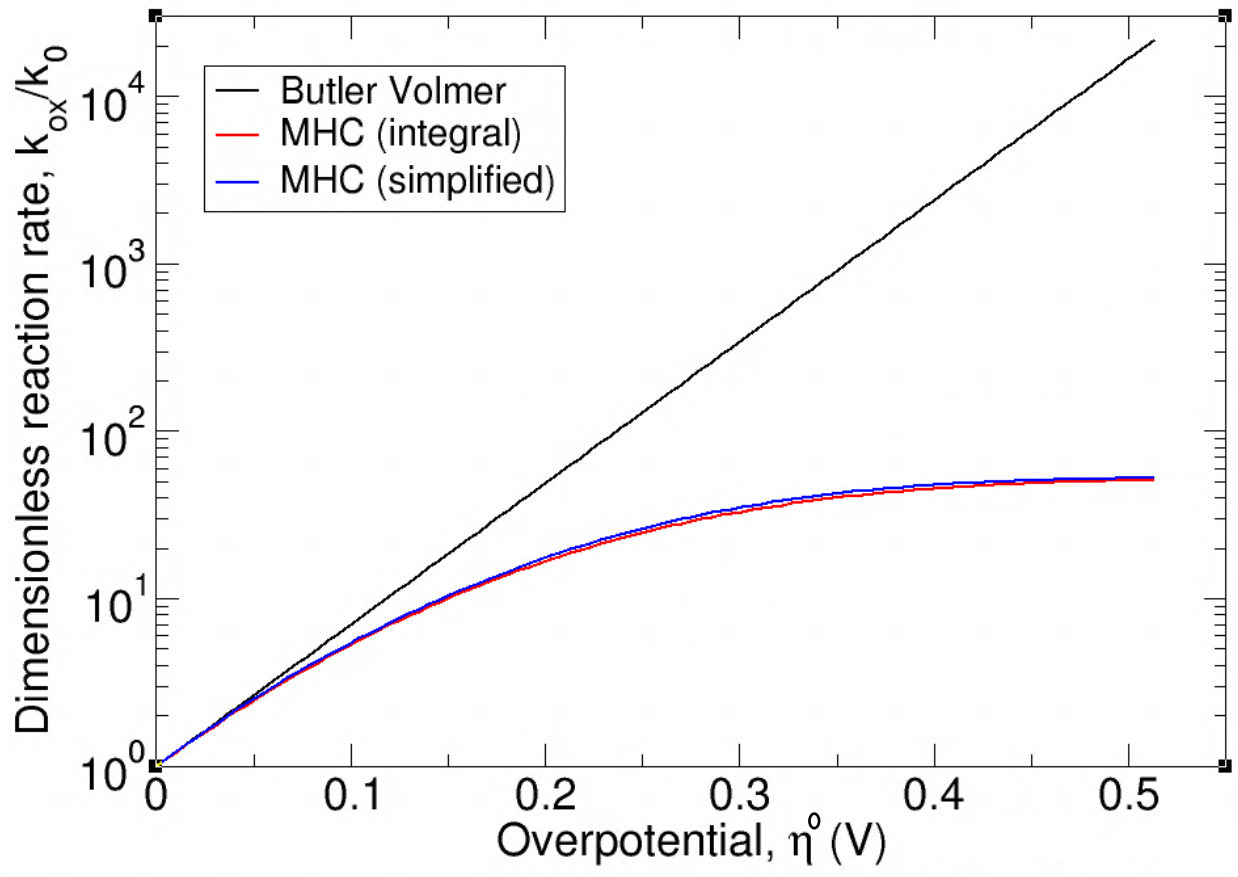

Figure 4.3: Variation of the dimensionless reaction rate constant with overpotential for oxidation, as predicted by BV and MHC (λ =257meV).

4.3 Species Transport Modeling

The RFB model we developed determines the spatial distribution of concentration of six different species: four redox species ($R_1^{z_{R_1}}, O_1^{z_{O_1}}, R_2^{z_{R_2}}, O_2^{z_{O_2}}$) and two salt ions ($A^+, B^-$), at each instant in time during the charge/ discharge cycles. The local bulk concentrations of each of these six species is affected by the transport processes and pore-scale redox reactions. The species conservation equations for each of the six species can be stated as:

$$\epsilon \frac{\partial c_i^b}{\partial t} + \nabla . \overrightarrow{N_i} + S_i = 0$$

Here, the rate of change of local volume averaged bulk concentration of each species c_i^b within the electrolyte filling the pores of the electrode of porosity ϵ depends on the superficial flux $\overrightarrow{N_i}$ entering/ leaving the control volume and the rate of generation given by the source term S_i. The source term $S_i = \pm a i_{n,i}/F$ is related with the volume-averaged pore-scale reaction current density $i_{n,i}$ and the surface area available for conducting the reactions per unit volume of the electrode a. In preparing the electrolytes with these redox active materials, typically a salt containing the redox active species is dissolved in a solvent. In this model, we assume the non-reactive counter-anion of each of the redox active species in the salt to have similar properties as that of the supporting electrolyte anion. The superficial flux $\overrightarrow{N_i}$ is most commonly modeled to include the effects of gradients in pressure (advection), concentration (diffusion) and solution potential (migration) through the Nernst-Planck formulation for dilute solutions[15]. To the best of our knowledge, hydrodynamic dispersion phenomenon is not accounted in the RFB models

till date. Mechanical dispersion in the porous medium is caused by velocity variations within microscopic pathways in the pore region and diversion of flow paths within the porous structure[32–34]. Hydrodynamic dispersion effects are often studied in porous media flow[35–38] such as chromatography, solute transport in ground water flow, catalysis and aquifers. Hydrodynamic dispersion fluxes can be described using Fick's first law which includes the effects of molecular diffusion and mechanical dispersion.

The dispersion coefficients along the flow direction (longitudinal: D_L) and perpendicular to the flow direction (transverse: D_T) scale with the pore-scale Peclet number[36,39] ($Pe = ud_f/D_b$ where u is the magnitude of superficial velocity, d_f is the characteristic length and D_b is the bulk diffusion coefficient of the species). The modified Nernst-Planck flux equation for dilute solutions which includes the effects of advection, migration and dispersion can be stated as[40]:

$$\overrightarrow{N_i} = \vec{N}_{advection,i} + \vec{N}_{migration,i} + \vec{N}_{dispersion,i}$$

$$\overrightarrow{N_i} = c_i^b \vec{u} - z_i c_i^b D_i^{eff} F \nabla \phi_e / RT - \underline{\underline{D_{H,i}}} \nabla c^b$$

The superficial velocity $\vec{u}$ of the electrolyte with viscosity (μ), flowing through the porous medium of permeability K under the influence of a varying pressure field p can be obtained from the Darcy's law in porous medium $\vec{u} = -(K/\mu)\nabla P$ and continuity $\nabla . \vec{u} = 0$ (assuming incompressible electrolyte). The effective diffusion coefficient D_i^{eff} of each species i in the porous medium with porosity ϵ and tortuosity τ is given as $D_i^{eff} = D_{b,i}\epsilon/\tau$. The hydrodynamic dispersion flux $\vec{j}_{dispersion,i}$ is obtained by the product of the dispersion coefficient tensor $\underline{\underline{D_{H,i}}}$ and the divergence of concentration. The tensor $\underline{\underline{D_{H,i}}}$ contains the

longitudinal $D_{L,i}$ and transverse $D_{T,i}$ dispersion coefficients as the diagonal components along and perpendicular to the direction of the velocity field. The superficial velocity direction varies spatially within the porous electrodes for an IDFF and doesn't align with the Cartesian co-ordinates. The Dispersion coefficient tensor $\underline{\underline{D_{H,i}}}$ in Cartesian co-ordinates can be stated as:

$$\underline{\underline{D_{H,i}}} = D_i^{eff} I + \underline{\underline{R^T}} \begin{bmatrix} D_{L,i} & 0 \\ 0 & D_{T,i} \end{bmatrix} \underline{\underline{R}}$$

The rotation matrix $\underline{\underline{R}}$ transforms the dispersion coefficients from the velocity vector direction to the Cartesian co-ordinates. In a 2D system, $\underline{\underline{R}}$ can be defined in terms of the angle θ between the velocity vector and the area vector on which the dispersion flux is calculated.

$$\underline{\underline{R}} = \begin{bmatrix} \cos(\theta) & \sin(\theta) \\ -\sin(\theta) & \cos(\theta) \end{bmatrix}$$

The coefficients, $D_{L,i}$ and $D_{T,i}$, depend on the electrode morphology. For a regular cylindrically packed microstructure, $D_{L,i}$ has a power law relationship with Pe, whereas $D_{T,i}$ is found to saturate with Pe[36] and are given as[36,39]:

$$\frac{D_{L,i}}{D_i^{eff}} = 0.05\ Pe^{1.2}$$

$$\frac{D_{T,i}}{D_i^{eff}} = \frac{0.08\ Pe}{1 + 0.085\ Pe}$$

Apart from bulk movement of species in the porous structure, the local pore-scale mass transfer, given in terms of Sherwood number $Sh = h_m d_f / D^0$, scales with the local Reynold's number/ flow velocity[41,42]. Zhou et al[43] report an effective mass transfer coefficient which is a result of a macroscopic and pore-scale mass transfer coefficient. Instead, we use a pore-scale Sherwood number correlation from the heat-mass transfer analogy for a single cylindrical fiber[42,44].

$$Sh = 0.9Re^{0.385}Sc^{0.31} \quad 0.1 < Re < 50$$

Where the Schmidt number is defined as $Sc = \mu/\rho D^0$. The pore-scale mass transport equation describes the flux of species i between the local bulk of the electrolyte c_i^b and the surface of the carbon fiber c_i^s is given as:

$$h_m\left(c_i^b - c_i^s\right) = \pm\frac{i_n}{F}$$

4.4 Membrane Modeling

The NSS is treated as a porous medium with thickness H_m, porosity ϵ_m and tortuosity τ_m. Absence of fixed charges ensures electroneutrality is satisfied throughout the reactor domain. The electroneutrality can be defined as:

$$\sum z_i c_i^b = 0$$

The use of a selective IEM encourages the formation of electric double layer near the electrode-IEM interface and electroneutrality condition is not valid. We use the Poisson equation to relate the gradient of the electric field within the electrolyte and total charge distribution[20].

$$-\nabla.(p\nabla\phi_e) = F\epsilon\left(z_f c_f + \sum_i z_i c_i^b\right)$$

Where p is the permittivity of the electrolyte and c_f is the fixed charge density with charge number z_f. An anion exchange membrane (AEM) has a positive c_f.

$$c_f = \begin{cases} c_{f,membrane} & within\ membrane \\ 0 & everywhere\ else \end{cases}$$

Note that this model also captures the crossover of species between the electrodes, however, such crossover is significantly small due to the high c_f of IEM. Lastly, we implement electronic current conservation within the electrode and current collector to relate the gradient of solid phase potential ϕ_s and the net reaction current density

$$\nabla.(-\sigma_s\nabla\phi_s) + \sum ai_n = 0$$

4.5 Boundary Conditions

The total number of variables solved temporally and spatially are the two potentials ϕ_s, ϕ_e, six bulk concentrations $c_{R1}^b, c_{O1}^b, c_{R2}^b, c_{O2}^b, c_{A^+}^b, c_{B^-}^b$ and four surface concentrations of the redox species $c_{R1}^s, c_{O1}^s, c_{R2}^s, c_{O2}^s$. We use the following boundary conditions to solve the above-mentioned system of equations.

- The AEM is assumed to be electronically insulating.
- Constant current density at the HPE current collector (galvanostatic cycling).

- LPE current collector is grounded $\phi_s = 0$.
- For an IDFF: symmetric boundary conditions on the left and right sides of the unit cell (Fig. 4.2(b)).
- Neumann boundary condition at the inlet for a set flow rate.
- Zero pressure outlet.

The electrolyte storing tanks are assumed to be perfectly mixed. Operating the RFB at higher flow rate is crucial to reduce the polarization due to mixing.

4.6 References

1. Zhang, C. *et al.* Progress and Prospects of Next-Generation Redox Flow Batteries. *Energy Storage Materials* doi:10.1016/j.ensm.2018.06.008
2. Shah, A. A., Watt-Smith, M. J. & Walsh, F. C. A dynamic performance model for redox-flow batteries involving soluble species. *Electrochimica Acta* **53**, 8087–8100 (2008).
3. Tang, A., Bao, J. & Skyllas-Kazacos, M. Dynamic modelling of the effects of ion diffusion and side reactions on the capacity loss for vanadium redox flow battery. *Journal of Power Sources* **196**, 10737–10747 (2011).
4. Gandomi, Y. A., Aaron, D. S., Zawodzinski, T. A. & Mench, M. M. In Situ Potential Distribution Measurement and Validated Model for All-Vanadium Redox Flow Battery. *J. Electrochem. Soc.* **163**, A5188–A5201 (2016).
5. Wei, Z. *et al.* An adaptive model for vanadium redox flow battery and its application for online peak power estimation. *Journal of Power Sources* **344**, 195–207 (2017).
6. Qiu, G. *et al.* 3-D pore-scale resolved model for coupled species/charge/fluid transport in a vanadium redox flow battery. *Electrochimica Acta* **64**, 46–64 (2012).
7. Ke, X., Alexander, J. I. D., Prahl, J. M. & Savinell, R. F. A simple analytical model of coupled single flow channel over porous electrode in vanadium redox flow battery with serpentine flow channel. *Journal of Power Sources* **288**, 308–313 (2015).

8. Ke, X., Prahl, J. M., Alexander, J. I. D. & Savinell, R. F. Mathematical Modeling of Electrolyte Flow in a Segment of Flow Channel over Porous Electrode Layered System in Vanadium Flow Battery with Flow Field Design. *Electrochimica Acta* **223**, 124–134 (2017).
9. Fan, F. Y. *et al.* Polysulfide Flow Batteries Enabled by Percolating Nanoscale Conductor Networks. *Nano Lett.* **14**, 2210–2218 (2014).
10. Scamman, D. P., Reade, G. W. & Roberts, E. P. L. Numerical modelling of a bromide–polysulphide redox flow battery: Part 1: Modelling approach and validation for a pilot-scale system. *Journal of Power Sources* **189**, 1220–1230 (2009).
11. Cho, K. T. *et al.* High Performance Hydrogen/Bromine Redox Flow Battery for Grid-Scale Energy Storage. *J. Electrochem. Soc.* **159**, A1806–A1815 (2012).
12. Braff, W. A., Buie, C. R. & Bazant, M. Z. Numerical and Analytic Modeling of a Membraneless Hydrogen Bromine Laminar Flow Batter. *ECS Trans.* **53**, 51–62 (2013).
13. Li, X. Modeling and simulation study of a metal free organic–inorganic aqueous flow battery with flow through electrode. *Electrochimica Acta* **170**, 98–109 (2015).
14. Zhou, X. L., Zhao, T. S., An, L., Zeng, Y. K. & Wei, L. Modeling of ion transport through a porous separator in vanadium redox flow batteries. *Journal of Power Sources* **327**, 67–76 (2016).
15. Nemani, V. P. & Smith, K. C. Analysis of Crossover-Induced Capacity Fade in Redox Flow Batteries with Non-Selective Separators. *J. Electrochem. Soc.* **165**, A3144–A3155 (2018).
16. Ohshima, H. & Ohki, S. Donnan potential and surface potential of a charged membrane. *Biophysical Journal* **47**, 673–678 (1985).
17. Ashraf Gandomi, Y., Aaron, D. S. & Mench, M. M. Coupled Membrane Transport Parameters for Ionic Species in All-Vanadium Redox Flow Batteries. *Electrochimica Acta* **218**, 174–190 (2016).
18. Smith, K. C. & Dmello, R. Na-Ion Desalination (NID) Enabled by Na-Blocking Membranes and Symmetric Na-Intercalation: Porous-Electrode Modeling. *J. Electrochem. Soc.* **163**, A530–A539 (2016).

19. Mafé, S., Pellicer, J. & Aguilella, V. M. A numerical approach to ionic transport through charged membranes. *Journal of Computational Physics* **75**, 1–14 (1988).
20. Lei, Y., Zhang, B. W., Bai, B. F. & Zhao, T. S. A transient electrochemical model incorporating the Donnan effect for all-vanadium redox flow batteries. *Journal of Power Sources* **299**, 202–211 (2015).
21. Harnisch, F., Warmbier, R., Schneider, R. & Schröder, U. Modeling the ion transfer and polarization of ion exchange membranes in bioelectrochemical systems. *Bioelectrochemistry* **75**, 136–141 (2009).
22. Dennison, C. R., Agar, E., Akuzum, B. & Kumbur, E. C. Enhancing Mass Transport in Redox Flow Batteries by Tailoring Flow Field and Electrode Design. *J. Electrochem. Soc.* **163**, A5163–A5169 (2016).
23. Nagarjuna, G. *et al.* Impact of Redox-Active Polymer Molecular Weight on the Electrochemical Properties and Transport Across Porous Separators in Nonaqueous Solvents. *J. Am. Chem. Soc.* **136**, 16309–16316 (2014).
24. Iyer, V. A. *et al.* Assessing the impact of electrolyte conductivity and viscosity on the reactor cost and pressure drop of redox-active polymer flow batteries. *Journal of Power Sources* **361**, 334–344 (2017).
25. Thorat, I. V. *et al.* Quantifying tortuosity in porous Li-ion battery materials. *Journal of Power Sources* **188**, 592–600 (2009).
26. Bruggeman, D. A. G. Berechnung verschiedener physikalischer Konstanten von heterogenen Substanzen. I. Dielektrizitätskonstanten und Leitfähigkeiten der Mischkörper aus isotropen Substanzen. *Annalen der Physik* **416**, 636–664 (1935).
27. Grew, K. N. & Chiu, W. K. S. A Dusty Fluid Model for Predicting Hydroxyl Anion Conductivity in Alkaline Anion Exchange Membranes. *J. Electrochem. Soc.* **157**, B327–B337 (2010).
28. Darling, R. M., Weber, A. Z., Tucker, M. C. & Perry, M. L. The influence of electric field on crossover in redox-flow batteries. *Journal of the Electrochemical Society* **163**, A5014–A5022 (2016).
29. Wang, W. *et al.* Recent Progress in Redox Flow Battery Research and Development. *Adv. Funct. Mater.* **23**, 970–986 (2013).

30. Wang, W. *et al.* A new redox flow battery using Fe/V redox couples in chloride supporting electrolyte. *Energy Environ. Sci.* **4**, 4068–4073 (2011).
31. Dmello, R., Milshtein, J. D., Brushett, F. R. & Smith, K. C. Cost-driven materials selection criteria for redox flow battery electrolytes. *Journal of Power Sources* **330**, 261–272 (2016).
32. Taylor, G. Dispersion of Soluble Matter in Solvent Flowing Slowly through a Tube. *Proceedings of the Royal Society of London Series A* **219**, 186–203 (1953).
33. *Groundwater Contamination*. (National Academies, 1984).
34. Bear, J. *Dynamics of Fluids in Porous Media*. (Courier Corporation, 2013).
35. Whitaker, S. Diffusion and dispersion in porous media. *AIChE Journal* **13**, 420–427 (1967).
36. Daneyko, A., Hlushkou, D., Khirevich, S. & Tallarek, U. From random sphere packings to regular pillar arrays: Analysis of transverse dispersion. *Journal of Chromatography A* **1257**, 98–115 (2012).
37. Bear, J. & Verruijt, A. *Modeling Groundwater Flow and Pollution*. (Springer Netherlands, 1987).
38. Carbonell, R. G. & Whitaker, S. Heat and Mass Transfer in Porous Media. in *Fundamentals of Transport Phenomena in Porous Media* (eds. Bear, J. & Corapcioglu, M. Y.) 121–198 (Springer Netherlands, 1984). doi:10.1007/978-94-009-6175-3_3
39. Delgado, J. M. P. Q. Longitudinal and Transverse Dispersion in Porous Media. *Chemical Engineering Research and Design* **85**, 1245–1252 (2007).
40. Rolle, M., Sprocati, R., Masi, M., Jin, B. & Muniruzzaman, M. Nernst-Planck-based Description of Transport, Coulombic Interactions, and Geochemical Reactions in Porous Media: Modeling Approach and Benchmark Experiments. *Water Resources Research* **54**, 3176–3195 (2018).
41. Milshtein, J. D. *et al.* Quantifying Mass Transfer Rates in Redox Flow Batteries. *J. Electrochem. Soc.* **164**, E3265–E3275 (2017).
42. Schmal, D., Van Erkel, J. & Van Duin, P. J. Mass transfer at carbon fibre electrodes. *J Appl Electrochem* **16**, 422–430 (1986).

43. Zhou, X. L., Zhao, T. S., An, L., Zeng, Y. K. & Wei, L. Critical transport issues for improving the performance of aqueous redox flow batteries. *Journal of Power Sources* **339**, 1–12 (2017).
44. Jakob, M. *Heat Transfer*. (John Wiley & Sons Inc, 1949).
45. Marcus, R. A. On the Theory of Oxidation-Reduction Reactions Involving Electron Transfer. I. *The Journal of Chemical Physics* **24**, 966–978 (1956).
46. Marcus, R. A. Electron transfer reactions in chemistry. Theory and experiment. *Rev. Mod. Phys.* **65**, 599–610 (1993).
47. Henstridge, M. C., Laborda, E., Rees, N. V. & Compton, R. G. Marcus–Hush–Chidsey theory of electron transfer applied to voltammetry: A review. *Electrochimica Acta* **84**, 12–20 (2012).
48. Bazant, M. Z. Theory of Chemical Kinetics and Charge Transfer based on Nonequilibrium Thermodynamics. *Acc. Chem. Res.* **46**, 1144–1160 (2013).
49. Zeng, Y., Smith, R. B., Bai, P. & Bazant, M. Z. Simple formula for Marcus–Hush–Chidsey kinetics. *Journal of Electroanalytical Chemistry* **735**, 77–83 (2014).

CHAPTER 5: Numerical Method

The governing equations presented are non-linear and tightly coupled. Therefore, we use numerical methods to discretize the governing equations and to iteratively solve them to obtain solutions. In this study, we use the finite-volume technique and first order accurate Taylor series expansions to discretize the equations on a 2D domain. The discretized equations are solved in MATLAB using UMFPACK[1] for solving sparse, square and unsymmetrical matrices. In sec 5.1, we present the discrete form of the governing equations using finite volume method followed by several numerical methods in sec 5.2. A detailed algorithm to arrive at converged solutions is described in sec 5.3. We establish mesh independence in sec 5.4 and verify the implementation of the discrete equations by comparing with analytical results under certain simplifying conditions in sec 5.5.

5.1 Discretization of the Governing Equations

We develop the discrete equations for the RFB model using a rectangular finite volume stencil shown in Fig. 5.1. Let the number of discrete elements along the thickness direction be N_t and along the current collector be N_c. In this particular representation, there are 12×8 finite volume elements within the reactor and the two tanks, assumed to be fully mixed, are considered as one unit cell each. The variables solved at the cell centers are pressure p, potentials ϕ_s, ϕ_e and six bulk species concentrations $c_{R1}^b, c_{O1}^b, c_{R2}^b, c_{O2}^b, c_{A^+}^b, c_{B^-}^b$. The transport fluxes are calculated at the cell faces. The model allows for having spatially varying transport properties. For example, the diffusion coefficient of species is different in the electrode and the IEM. Effective transport

properties at the cell faces between two finite volume stencils is estimated based on a resistance model. Figure 5.2 depicts a typical finite volume stencil where each cell is surrounded with 8 neighboring cells (except at boundaries). The cell centers are represented by capital alphabets (in black) whereas the cell faces are denoted by small letter alphabets (in orange).

Figure 5.1

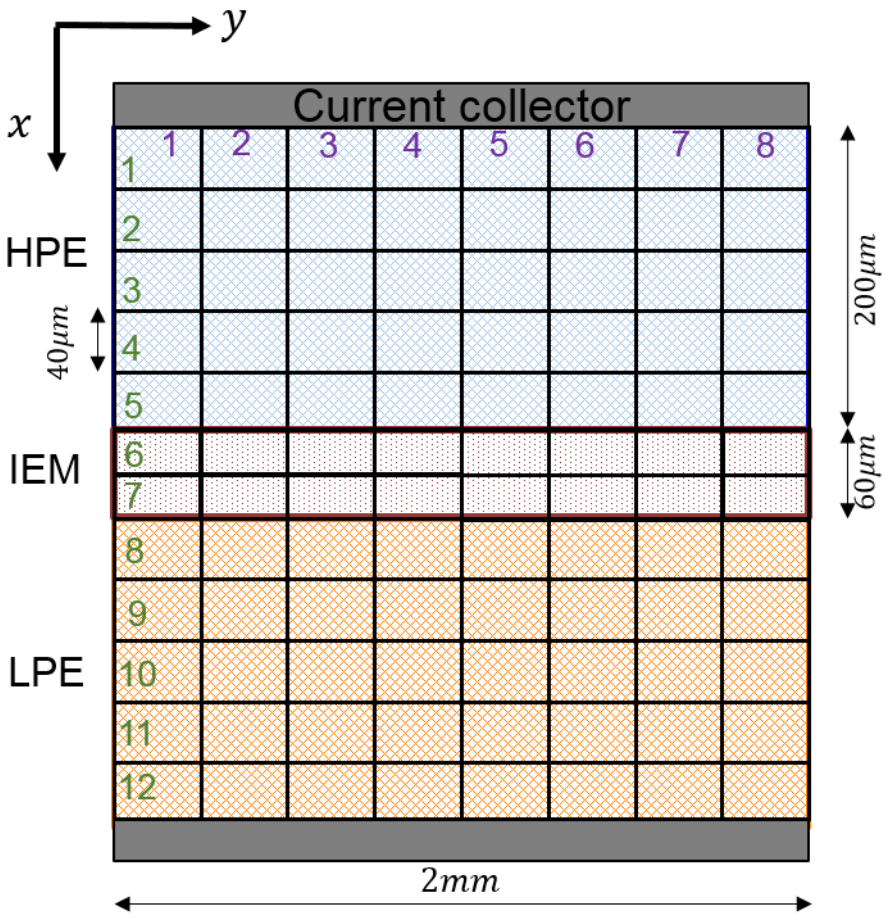

Figure 5.1: Representative rectangular mesh for implementing finite volume method. In this illustration, there are a total of $12\times8+2$ (tanks) finite volume stencils. The x direction is chosen along the thickness of the electrode and y is chosen along the current collector direction.

Figure 5.2

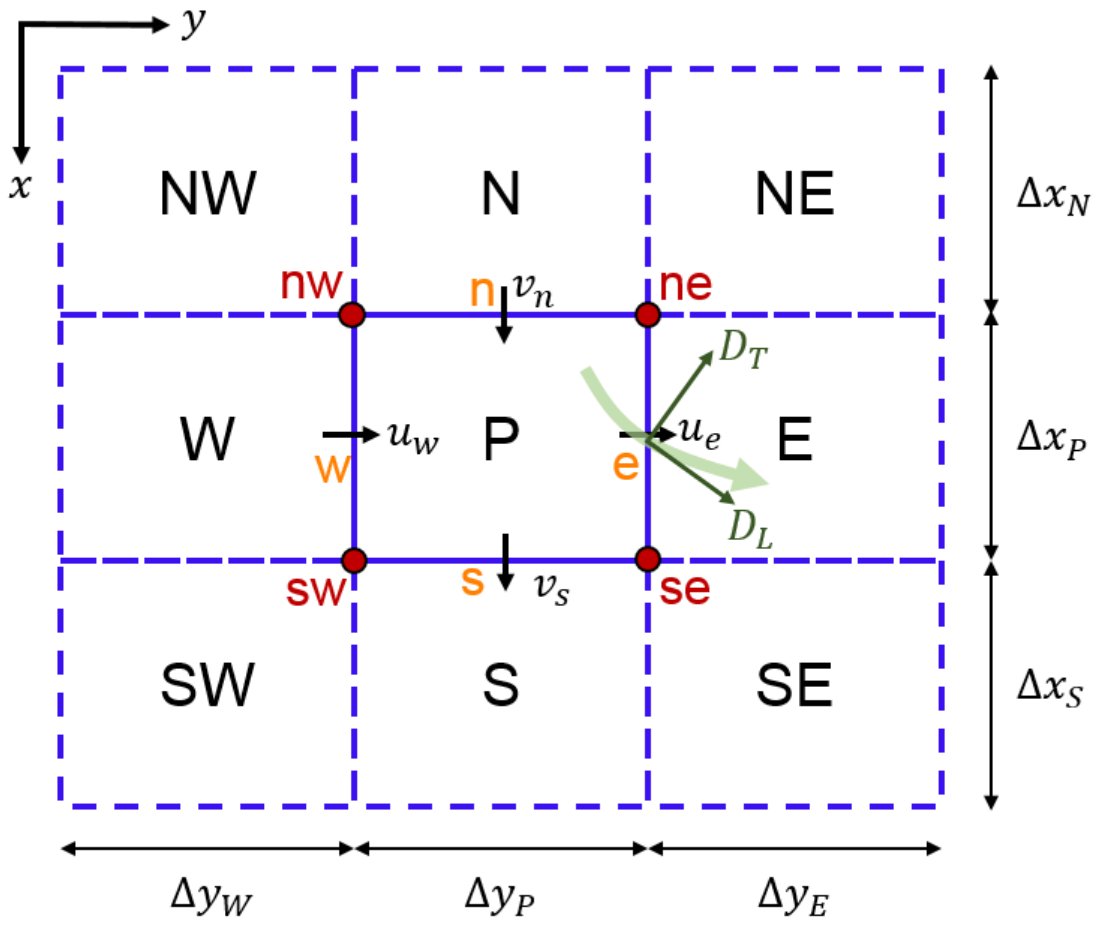

Figure 5.2: Discrete finite volume neighbors to P. The cell centers are marked in black, faces are marked in orange with velocity components. For a representative flow velocity on the east face (curved green arrow) the solid green arrows mark the longitudinal D_L and transverse D_T dispersion coefficients.

5.1.1 Establishing Flow Field

In this section, we calculate the pressure field and flow velocities in the reactor for both PFF and IDFF (see Fig. 5.3). The pressure field $p(x, y)$ is established using the Darcy's law for porous media flow along with continuity.

$$\vec{u} = -\left(\frac{K}{\mu}\right)\nabla p \tag{5.1}$$

$$\nabla.\vec{u} = 0 \tag{5.2}$$

Boundary conditions: We use a Neumann type boundary condition at the inlet by setting an input flow rate and a Dirichlet boundary condition of a zero-pressure outlet. The boundary conditions for PFF and IDFF are shown in Fig. 5.2.

Integrating equation 5.2 over the volume

$$\iiint_V \nabla.\vec{u}\, dV = \iiint_V 0\, dV$$

By applying divergence theorem

$$\oiint_A \vec{u}.\overrightarrow{dA} = 0$$

$$\oiint_A -\left(\frac{K}{\mu}\right)\left(\frac{\partial p}{\partial x}\hat{x} + \frac{\partial p}{\partial y}\hat{y}\right).\overrightarrow{dA} = 0$$

For each finite volume with at most eight neighbors as shown in Figure 5.2, the discrete pressure equations can be written as a sum of flow rates across the east, north, west and south faces:

$$\Phi_e + \Phi_n + \Phi_w + \Phi_s = 0 \tag{5.3}$$

$$\frac{K_e}{\mu_e}\frac{\Delta x_P}{\Delta \mathrm{y_{PE}}}(p_P - p_E) + \frac{K_n}{\mu_n}\frac{\Delta y_P}{\Delta \mathrm{x_{PN}}}(p_P - p_N) + \frac{K_w}{\mu_w}\frac{\Delta x_P}{\Delta \mathrm{y_{PW}}}(p_P - p_W) + \frac{K_s}{\mu_s}\frac{\Delta y_P}{\Delta \mathrm{x_{PS}}}(p_P - p_S) = 0 \tag{5.4}$$

Here K_e and μ_e are the effective permeability and viscosity at the east face of P and Δy_{PE} is the distance between the cell centers $\Delta y_{PE} = \Delta y_P/2 + \Delta y_E/2$. These effective

parameters are important when considering tailored electrodes and at electrode-membrane interface. The viscosity is dependent on the concentration of the redox active species[2] which varies with the state of charge and transport. However, in this study we assume viscosity to be a constant and the resultant velocity field is independent of time. The effective properties at the faces can be determined using a resistance model.

$$\dot{V} = -\frac{K\mathrm{A}}{\mu}\frac{\Delta P}{\mathrm{L}} = -\frac{\Delta P}{(\mu \mathrm{L}/K\mathrm{A})}$$

The 'resistance' can be defined as $R = \mu \mathrm{L}/K\mathrm{A}$. To determine $\frac{K_e}{\mu_e}\frac{\Delta x_P}{\Delta \mathrm{y_{PE}}}$ from eqn. 5.4 we can write a net resistance between cell P and E.

$$\Omega_{\mathrm{e}} = \Omega_P/2 + \Omega_E/2$$

$$\frac{\mu_e \Delta \mathrm{y_{PE}}}{K_e \Delta \mathrm{x_P}} = \frac{\mu_P \Delta \mathrm{y_P}}{2K_P \Delta \mathrm{x_P}} + \frac{\mu_E \Delta \mathrm{y_E}}{2K_E \Delta \mathrm{x_E}}$$

Similar approach can be used for the north, west and south faces. The inlet boundary condition is Neumann type where the volumetric flow rate is fixed. For the Dirichlet boundary condition of zero-pressure outlet, we assign the pressure at the face to be 0. These boundary conditions must be taken care when writing discrete equations of the form 5.3.

For the PFF:

$$\Phi_w = \dot{V}_{inlet}, \qquad for\ j = 1, \forall i$$

$$\Phi_n = 0, \qquad for\ i = 1, \forall j$$

$$\Phi_s = 0, \qquad for\ i = N_t, \forall j$$

$$\Phi_e = 2\frac{K\Delta x_P}{\mu\Delta y_P}p_P, \qquad for\ j = N_c, \forall i$$

Similar boundary conditions can be established for IDFF based on Fig. 5.3. The equations can be assembled in the form

$$a_P p_P = a_E p_E + a_N p_N + a_W p_W + a_S p_S + b \qquad 5.5$$

These linear equations can be assembled in the form of $AX = B$ and solved for X to obtain the pressure field. The velocities at the faces can be determined by eqn. 5.1.

Figure 5.3

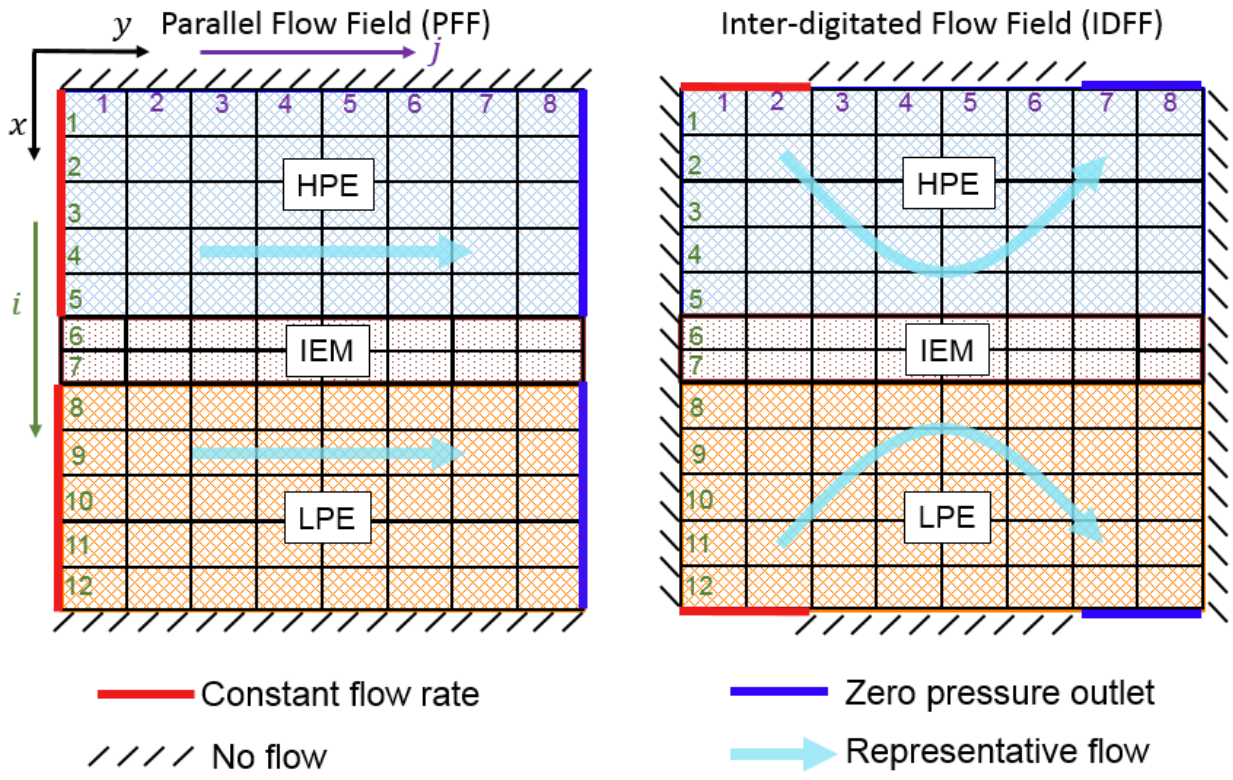

Figure 5.3: Boundary conditions for establishing the PFF and IDFF within the reactor.

5.1.2 Discretizing Reaction kinetics

In this section we present the discretized version of the source term (or the pore-scale reaction current density) for two redox reactions. We establish the discrete form for both Butler Volmer and Marcus Hush Chidsey kinetic models.

The two sets of reversible redox reactions in the reactor are

$$Reaction\ 1\text{: } R_1^{z_{R_1}} \rightleftharpoons O_1^{z_{O_1}} + e^- \text{ with current density } i_{n,1}$$

$$Reaction\ 2\text{: } R_2^{z_{R_2}} \rightleftharpoons O_2^{z_{O_2}} + e^- \text{ with current density } i_{n,2}$$

As the RFB is cycled, crossover of all the four different redox species from their primary electrode to the counter electrode forces a second set of redox reactions in the counter electrode (see Fig. 4.2(c)). The net pore-scale reaction current density for either reaction is

$$i_{n,i} = F\left(k_{ox} c_{R_i}^s - k_{red} c_{O_i}^s\right) \tag{5.6}$$

The volume averaged source term is

$$S_i = \pm \frac{a i_{n,i}}{F} \tag{5.7}$$

Since $i_n = f(\eta, c_R^s, c_O^s)$ and $\eta^0 = \phi_s - \phi_e - \phi_{eq,50\%}$ where $\phi_{eq} = E_0 - \frac{RT}{F} \ln\left(\frac{c_R^s}{c_O^s}\right)$, we use the Taylor series expansion to express our discrete source term S in terms of the local state variables expanded about the previous guess (indicated by $*$)

$$S_i \cong S_i^* + \left.\frac{\partial S_i}{\partial \phi_s}\right|_* (\phi_s - \phi_s^*) + \left.\frac{\partial S_i}{\partial \phi_e}\right|_* (\phi_s - \phi_e^*) + \left.\frac{\partial S_i}{\partial c_{R_i}^s}\right|_* \left(c_{R_i}^s - {c_{R_i}^s}^*\right) + \left.\frac{\partial S_i}{\partial c_{O_i}^s}\right|_* \left(c_{O_i}^s - {c_{O_i}^s}^*\right) \tag{5.8}$$

$$\frac{\partial S}{\partial \eta} = a\left(c_R \frac{\partial k_{ox}}{\partial \eta^0} - c_O \frac{\partial k_{red}}{\partial \eta^0}\right) \tag{5.9}$$

$$\frac{\partial S}{\partial \phi_s} = \frac{\partial S}{\partial \eta^0}\frac{\partial \eta^0}{\partial \phi_s} = \frac{\partial S}{\partial \eta^0} \tag{5.10}$$

$$\frac{\partial S}{\partial \phi_e} = \frac{\partial S}{\partial \eta^0}\frac{\partial \eta^0}{\partial \phi_e} = -\frac{\partial S}{\partial \eta^0} \tag{5.11}$$

$$\frac{\partial S}{\partial c_R^s} = a\left(c_R^s \frac{\partial k_{ox}}{\partial \eta^0}\frac{\partial \eta^0}{\partial c_R^s} + k_{ox} - c_O^s \frac{\partial k_{red}}{\partial \eta^0}\frac{\partial \eta^0}{\partial c_R^s}\right) \tag{5.12}$$

$$\frac{\partial S}{\partial c_O^s} = a\left(c_R^s \frac{\partial k_{ox}}{\partial \eta^0}\frac{\partial \eta^0}{\partial c_O^s} - k_{red} - c_O^s \frac{\partial k_{red}}{\partial \eta^0}\frac{\partial \eta^0}{\partial c_O^s}\right) \tag{5.13}$$

For Butler Volmer kinetics ($\alpha = 0.5$):

$$k_{ox} = k_0 e^{0.5F\eta^0/RT} \text{ and } k_{red} = k_0 e^{-0.5F\eta^0/RT}$$

$$S_i^* = a k_0 c_{R_i}^{0.5} c_{O_i}^{0.5}\left[exp\left(\frac{0.5F\eta^0}{RT}\right) - exp\left(-\frac{0.5F\eta^0}{RT}\right)\right] \tag{5.14}$$

$$\frac{\partial S}{\partial \eta^0} = \frac{0.5F}{RT} a k_0 c_{R_i}^{0.5} c_{O_i}^{0.5}\left[exp\left(\frac{0.5F\eta^0}{RT}\right) + exp\left(-\frac{0.5F\eta^0}{RT}\right)\right] \tag{5.15}$$

$$\frac{\partial S}{\partial c_R} = a k_0 e^{0.5F\eta^0/RT} \tag{5.16}$$

$$\frac{\partial S}{\partial c_O} = -a k_0 e^{-0.5F\eta^0/RT} \tag{5.17}$$

Marcus Hush Chidsey kinetics, the kinetic rate constants can be stated as

$$k_{ox/red}^{MHC} = A\frac{\sqrt{\pi\lambda^*}}{1+\exp(\mp\eta^{0,*})}erfc\left(\frac{\lambda^* - \sqrt{1+\sqrt{\lambda^*}+\eta^{0,*^2}}}{2\sqrt{\lambda^*}}\right) \quad 5.18$$

$$A = \frac{2k_0}{\left(\sqrt{\pi\lambda^*}erfc\left(\frac{\lambda^* - \sqrt{1+\sqrt{\lambda^*}}}{2\sqrt{\lambda^*}}\right)\right)} \quad 5.19$$

Let γ be defined as

$$\gamma = \frac{\lambda^* - \sqrt{1+\sqrt{\lambda^*}}}{2\sqrt{\lambda^*}}$$

The Taylor series coefficients (from equations 5.9 – 5.13) take the form:

$$\frac{\partial k_{ox}}{\partial\eta} = A\frac{\sqrt{\pi\lambda^*}}{1+exp\left(-\frac{\eta^0 F}{RT}\right)}\left(\frac{F}{RT}\frac{exp\left(-\frac{\eta^0 F}{RT}\right)}{1+exp\left(-\frac{\eta^0 F}{RT}\right)}erfc(\gamma) - \frac{\partial\gamma}{\partial\eta}\frac{2e^{-\gamma^2}}{\sqrt{\pi}}\right) \quad 5.20$$

$$\frac{\partial k_{red}}{\partial\eta} = A\frac{\sqrt{\pi\lambda^*}}{1+exp\left(\frac{\eta^0 F}{RT}\right)}\left(-\frac{F}{RT}\frac{exp\left(\frac{\eta^0 F}{RT}\right)}{1+exp\left(\frac{\eta^0 F}{RT}\right)}erfc(\gamma) - \frac{\partial\gamma}{\partial\eta}\frac{2e^{-\gamma^2}}{\sqrt{\pi}}\right) \quad 5.21$$

$$\frac{\partial\gamma}{\partial\eta} = \left(\frac{F}{RT}\right)^2\frac{\eta}{2\sqrt{\lambda^*}\sqrt{1+\sqrt{\lambda^*}+\left(\frac{\eta F}{RT}\right)^2}} \quad 5.22$$

$$\frac{\partial\eta^0}{\partial c_R} = 0 \quad 5.23$$

$$\frac{\partial\eta^0}{\partial c_O} = 0 \quad 5.24$$

Equations $5.20 - 24$ can be substituted back into Taylor series equations 5.8 to get the linearized dependence of S_i on the potentials ϕ_s, ϕ_e and the redox concentrations.

5.1.3 Discretizing the Electronic Current Conservation

$$\nabla.(-\sigma_s \nabla \phi_s) + \sum_{i=1,2} S_i = 0 \tag{5.25}$$

Integrate over volume and time

$$\int_t \iiint_V \nabla.(-\sigma_s \nabla \phi_s) dV dt + \sum_i \int_t \iiint_V S_i = 0 \tag{5.26}$$

Using the divergence theorem and assuming constant electronic conductivity σ_s, we get

$$-\sigma_s \Delta t \oiint_A \nabla \phi_s . \overrightarrow{dA} + (S_1 + S_2)\Delta x \Delta y \Delta t = 0$$

Expanding the integral on the four sides of the stencil gives (using $\phi \equiv \phi_s$ to avoid confusion with south face notation)

$$\Phi_e + \Phi_n + \Phi_w + \Phi_s + (S_1 + S_2)\Delta x \Delta y \Delta t = 0$$

$$\sigma_s \Delta t \left[\frac{\Delta x_P}{\Delta y_{PE}}(\phi_P - \phi_E) + \frac{\Delta y_P}{\Delta x_{PN}}(\phi_P - \phi_N) + \frac{\Delta x_P}{\Delta y_{PW}}(\phi_P - \phi_W) + \frac{\Delta y_P}{\Delta x_{PS}}(\phi_P - \phi_S)\right]$$
$$+ (S_1 + S_2)\Delta x \Delta y \Delta t = 0$$

Note that the discrete S_1 and S_2 are expressed as functions of ϕ_s, ϕ_e and concentration fields in eqn. 5.8. The potential across the length of the two current collectors is uniform. The LPE current collector is grounded and a constant current input is provided to HPE

current collector. For an applied current density i_{cc} at HPE, we can write the discrete equation for current collectors as (refer Figs. 5.1 and 5.3)

$$\sigma_s \Delta t \sum_{j=1}^{N_c} \frac{\Delta y_P}{\Delta x_P/2}\left(\phi_{HPE,cc} - \phi_S\right) - i_{cc} L_{cc} = 0 \; for \; HPE$$

$$\phi_{LPE,cc} = 0 \; for \; LPE$$

5.1.4 Discretizing the Species Conservation Equation

In this section, we develop the discrete equations governing the transport of each species using the finite volume stencil shown in Fig. 5.2.

$$\epsilon \frac{\partial c_i^b}{\partial t} + \nabla . \overrightarrow{N_\iota} + S_i = 0 \tag{5.27}$$

$$\overrightarrow{N_\iota} = \vec{N}_{advection,i} + \vec{N}_{migration,i} + \vec{N}_{dispersion,i}$$

$$\overrightarrow{N_\iota} = c_i^b \vec{u} - \frac{z_i c_i^b D_i^{eff} F \nabla \phi_e}{RT} - \underline{\underline{D_{H,i}}} \nabla c_i^b \tag{5.28}$$

$$\underline{\underline{D_{H,i}}} = D_i^{eff} I + \underline{\underline{R^T}} \begin{bmatrix} D_{L,i} & 0 \\ 0 & D_{T,i} \end{bmatrix} \underline{\underline{R}} \tag{5.29}$$

By integrating the species conservation eqn. 5.27 over the discrete volume and time

$$\int_t \iiint_V (\epsilon \frac{\partial c_i^b}{\partial t} + \nabla . \overrightarrow{N_\iota} + S_i) dV dt = 0 \tag{5.30}$$

The transport fluxes are expressed in terms of bulk concentration. For now, we drop the superscript b to avoid confusion. The transient term can be discretized as

$$\int_t \iiint_V \frac{\epsilon \partial c_i^b}{\partial t} dV dt = \epsilon (c_i^{n+1} - c_i^n) \Delta x_P \Delta y_P \tag{5.31}$$

Integrating the flux term and applying divergence theorem, we obtain

$$\int_t \iiint_V \nabla . \overrightarrow{N_l} dV dt = \int_t \oiint_A \overrightarrow{N_l} . \overrightarrow{dA} dt \tag{5.32}$$

The flux term $\overrightarrow{N_l}$ has three components: advection, migration and hydrodynamic dispersion. We discretize the advection term by using third order accurate QUICK (Quadratic Upstream Interpolation for Convective Kinematics) scheme. The discrete equation for the stencil shown in Fig. 5.2 looks like

$$\int_t \oiint_A c\vec{u} . \overrightarrow{dA} dt = c_e \mathrm{u_e} \Delta x_P + c_n v_n \Delta y_p - c_w \mathrm{u_w} \Delta x_P - c_s v_s \Delta y_p \tag{5.33}$$

The velocities at the cell faces u_e, v_n, u_w, v_s are obtained from section 5.1.1. QUICK scheme allows us to predict the species concentration at the cell faces and is dependent on the velocity direction at the cell faces. The approximation for c_e:

$$\overrightarrow{u_e} . \hat{y} > 0, c_e = \frac{3}{8} c_E + \frac{6}{8} c_P - \frac{1}{8} c_W \tag{5.34}$$

$$\overrightarrow{u_e} . \hat{y} < 0, c_e = \frac{3}{8} c_P + \frac{6}{8} c_E - \frac{1}{8} c_{EE} \tag{5.35}$$

In other words, the face concentration is weighed by a factor of $3/8$ for the upstream finite volume, $6/8$ for the first downstream finite volume and $-1/8$ for the second downstream finite volume. The face concentration values for the other three faces can be written similar to $5.34 - 35$. Upwind scheme (first order accurate) is used to calculate the species fluxes at the boundaries. This can be stated as

If $\overrightarrow{u_e}.\hat{y} > 0$ then $c_e = c_P$

If $\overrightarrow{u_e}.\hat{y} < 0$ then $c_e = c_E$

The migration flux term is non-linear as the concentration is multiplied with the gradient in potential $c \times \nabla\phi_e$. To linearize this, we use the concentration values from the previous guess (c^*) and iteratively solved to obtain converged solution. The discrete form of migration fluxes for the finite volume stencil for each species looks like

$$\int_t \oiint_A -\frac{z_i c_i D_i^{eff} F}{RT} \nabla\phi_e . \overrightarrow{dA} dt$$

$$= -\frac{z_i F}{RT}\left[c_{e,i}^* D_{e,i}^{eff} \frac{\Delta x_P}{\Delta y_{PE}}(\phi_E - \phi_P) + c_{n,i}^* D_{n,i}^{eff} \frac{\Delta y_P}{\Delta x_{PN}}(\phi_N - \phi_P)\right.$$

$$\left. + c_{w,i}^* D_{w,i}^{eff} \frac{\Delta x_P}{\Delta y_{PW}}(\phi_W - \phi_P) + c_{s,i}^* D_{s,i}^{eff} \frac{\Delta y_P}{\Delta x_{PS}}(\phi_S - \phi_P)\right] \quad 5.36$$

The coefficients appearing in eqn. 5.36 such as $\frac{c_e D_e^{eff}}{\Delta y_{PE}}$ can be determined through a resistance model. The 'resistance' $\Omega_{migration}$ for transporting a flux $\Phi_{migration}$ against a gradient $\Delta\phi_e$ is given as $\Phi_{migration} = \Delta\phi_e / \Omega_{migration}$. Rearranging the migration fluxes over a length L across a cross sectional area A given by eqn. 5.28, we get

$$\Phi_{migration} = \frac{zFcDA}{RT}\frac{\Delta\phi_e}{L} = \frac{\Delta\phi_e}{RTL/zFcDA}$$

$$\Omega_{migration} = \frac{RTL}{zFcDA}$$

To evaluate $\frac{c_e D_e^{eff}}{\Delta y_{PE}}$ for the east face, the net resistance on the east face Ω_e between the cell centers E and P is given as

$$\Omega_e = \frac{\Omega_P}{2} + \frac{\Omega_E}{2}$$

$$\frac{1}{c^*_{e,i} D^{eff}_{e,i}} \frac{\Delta y_{PE}}{\Delta x_P} = \frac{1}{c^*_{P,i} D^{eff}_{P,i}} \frac{\Delta y_P/2}{\Delta x_P} + \frac{1}{c^*_{E,i} D^{eff}_{E,i}} \frac{\Delta y_E/2}{\Delta x_P} \qquad 5.37$$

The coefficients for the north $c^*_{n,i} D^{eff}_{n,i} \frac{\Delta y_P}{\Delta x_{PN}}$, west $c^*_{w,i} D^{eff}_{w,i} \frac{\Delta x_P}{\Delta y_{PW}}$ and south $c^*_{s,i} D^{eff}_{s,i} \frac{\Delta y_P}{\Delta x_{PS}} c^*_{s,i} D^{eff}_{s,i} \frac{\Delta y_P}{\Delta x_{PS}}$ fluxes in eqn. 5.36 can be developed similar to 5.37.

The hydrodynamic dispersion fluxes include species fluxes arising due to diffusion and dispersion. Integrating the dispersion term in eqn. 5.28 we get:

$$\int_t \iiint_V \nabla . \left(-\underline{\underline{D_{H,i}}} \nabla c_i \right) dV dt = \int_t \oiint_A -\underline{\underline{D_{H,i}}} \nabla c_i . \overrightarrow{dA} dt \qquad 5.38$$

The Dispersion coefficient tensor $\underline{\underline{D_{H,i}}}$ varies with the velocity direction. The tensor $\underline{\underline{D_{H,i}}}$ contains the longitudinal $D_{L,i}$ and transverse $D_{T,i}$ dispersion coefficients as the diagonal components along and perpendicular to the direction of the velocity field. In Cartesian co-ordinates $\underline{\underline{D_{H,i}}}$ can be stated as:

$$\underline{\underline{D_{H,i}}} = D^{eff}_i I + \underline{\underline{R^T}} \begin{bmatrix} D_{L,i} & 0 \\ 0 & D_{T,i} \end{bmatrix} \underline{\underline{R}} \qquad 5.39$$

The rotation matrix $\underline{\underline{R}}$ transforms the dispersion coefficients from the velocity vector direction to the Cartesian co-ordinates. In a 2D system, $\underline{\underline{R}}$ can be defined in terms of the angle θ between the velocity vector and the area vector on which the dispersion flux is calculated.

$$\underline{\underline{R}} = \begin{bmatrix} \cos(\theta) & \sin(\theta) \\ -\sin(\theta) & \cos(\theta) \end{bmatrix} \tag{5.40}$$

Combining eqns. 5.40 and 5.39, we get

$$\underline{\underline{D_{H,i}}} = \begin{bmatrix} D_{xx} & D_{xy} \\ D_{xy} & D_{yy} \end{bmatrix}$$

$$\int_t \oiint_A -\underline{\underline{D_{H,i}}} \nabla c_i . \overrightarrow{dA} dt = \Phi_{disperion,e} + \Phi_{disperion,n} + \Phi_{disperion,w} + \Phi_{disperion,s} \tag{5.41}$$

The dispersion flux for the east face (see Fig. 5.2) can be written in discrete form as

$$\Phi_{dispersion,e} = -\begin{bmatrix} D_{xx} & D_{xy} \\ D_{xy} & D_{yy} \end{bmatrix}_e \begin{bmatrix} \frac{\partial c_i}{\partial x} \\ \frac{\partial c_i}{\partial y} \end{bmatrix}_e . \begin{bmatrix} A_x \hat{x} \\ A_y \hat{y} \end{bmatrix}_e = -\begin{bmatrix} D_{xx} \frac{\partial c_i}{\partial x} + D_{xy} \frac{\partial c_i}{\partial y} \\ D_{xy} \frac{\partial c_i}{\partial x} + D_{yy} \frac{\partial c_i}{\partial y} \end{bmatrix} . \begin{bmatrix} 0 \\ \Delta x_P \hat{y} \end{bmatrix} \tag{5.42}$$

$$\Phi_{dispersion,e} = -\left(D_{xy} \frac{\partial c_i}{\partial x} + D_{yy} \frac{\partial c_i}{\partial y} \right) \Delta x_P \tag{5.43}$$

$$\frac{\partial c_i}{\partial y} = \frac{c_{E,i} - c_{P,i}}{\Delta y_{PE}} \tag{5.44}$$

$$\frac{\partial c_i}{\partial x} = \frac{c_{se,i} - c_{ne,i}}{\Delta x_P} \tag{5.45}$$

Here, c_{ne} is concentration at the node intersected by P, E, NE, N (Fig. 5.2). c_{ne} can be approximated by inversely weighing the distance of node c_{ne} from the surrounding cell centers.

$$c_{ne} = \frac{\frac{c_P}{\Delta x_P \Delta y_P} + \frac{c_E}{\Delta x_P \Delta y_E} + \frac{c_N}{\Delta x_N \Delta y_P} + \frac{c_{NE}}{\Delta x_N \Delta y_E}}{\left(\frac{1}{\Delta x_P} + \frac{1}{\Delta x_N} \right) \left(\frac{1}{\Delta y_P} + \frac{1}{\Delta y_E} \right)} \tag{5.46}$$

Similarly, c_{se} can be interpolated from the cell values at P, S, SE and E.

$$c_{se} = \frac{\frac{c_P}{\Delta x_P \Delta y_P} + \frac{c_E}{\Delta x_P \Delta y_E} + \frac{c_S}{\Delta x_S \Delta y_P} + \frac{c_{SE}}{\Delta x_S \Delta y_E}}{\left(\frac{1}{\Delta x_P} + \frac{1}{\Delta x_S}\right)\left(\frac{1}{\Delta y_P} + \frac{1}{\Delta y_E}\right)} \tag{5.47}$$

Equations 5.45 and 5.46 can be used to calculate $\frac{\partial c}{\partial x}$ from eqn. 5.44 and finally evaluate dispersion flux through the east face $\Phi_{dispersion,e}$. Similarly hydrodynamic fluxes through north, west and south can be calculated and substituted back into eqn 5.41 to get:

$$\int_t \oiint_A -\underline{\underline{D_{H,i}}} \nabla c_i . \overrightarrow{dA} dt = a_P c_{P,i} + \sum_{nb} a_{nb} c_{nb,i} \tag{5.48}$$

Conservation of species in tank: The tanks are assumed to be well-mixed. Figure 5.4 shows a single tank-reactor connection for a PFF. The species conservation in the tank can be written as

$$\frac{d(c_i V_{tank})}{dt} = \sum c_{in}^{n+1} \dot{V}_{in} - \sum c_{out} \dot{V}_{out} \tag{5.49}$$

$$V_{tank} \frac{c_{tank,i}^{n+1} - c_{tank,i}^{n}}{\Delta t} = \sum_{i=1}^{5} c_i^{n+1}(i,8) u_e(i,8) \Delta x_i - \dot{V}_{out} c_{tank,i}^{n+1} \tag{5.50}$$

$$c_{tank,i}^{n+1}\left(V_{tank} + \dot{V}_{\text{out}} \Delta t\right) - \sum_{i=1}^{5} c_i^{n+1}(i,8) u_e(i,8) \Delta x_i = V_{tank} c_{tank,i}^{n} \tag{5.51}$$

Figure 5.4

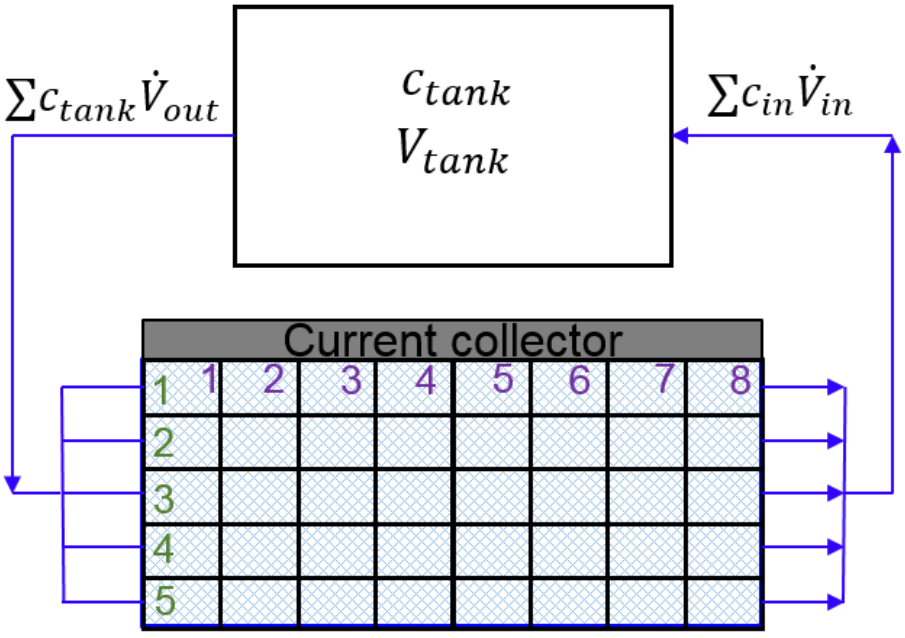

Figure 5.4: Flow structure connecting the reactor and the well mixed tank.

5.1.5 Discretizing Pore-scale Mass Transport

The transport of species from the bulk c_i^b to the reaction surface c_i^s is given through a convective correlation.

$$h_m\left(c_i^b - c_i^s\right) = \pm\frac{i_n}{F} = \pm\frac{S_i}{a} \qquad 5.52$$

Equation 5.52 combined with the discrete version of S_i (eqn. 5.8) gives the discretized pore-scale mass transfer equation for each finite volume stencil.

5.1.6 Discretizing Electroneutrality Condition

When using a NSS, electroneutrality is ensured. The discrete version of electroneutrality relating the bulk concentration of the six species is given as

$$\sum z_i c_i^b = 0 \tag{5.53}$$

5.1.7 Discretizing Poisson Equation

The electroneutrality condition is not valid when IEM is used. The presence of local fixed charges forms electric double layer. We use the Poisson equation to relate the gradient of the electric field within the electrolyte and total charge distribution.

$$-\nabla.(p\nabla\phi_e) = F\epsilon\left(z_f c_f + \sum_i z_i c_i^b\right) \tag{5.54}$$

Apply divergence theorem after integrating over volume and time step, we get:

$$\int_t \iiint_V -\nabla.(p\nabla\phi_e)\, dVdt = \int_t \iiint_V F\epsilon\left(z_f c_f + \sum_i z_i c_i^b\right) dVdt \tag{5.55}$$

$$\int_t \oiint_A -p\nabla\phi_e.\overrightarrow{dA}dt = F\epsilon\left(z_f c_f + \sum_i z_i c_i^b\right)\Delta x_P \Delta y_P \Delta t$$

$$\Delta t\left[\frac{\mathrm{p_e}\Delta x_P}{\Delta y_{PE}}\left(\phi_{e,P} - \phi_{e,E}\right) + \frac{\mathrm{p_n}\Delta y_P}{\Delta x_{PN}}\left(\phi_{e,P} - \phi_{e,N}\right) + \frac{\mathrm{p_w}\Delta x_P}{\Delta y_{PW}}\left(\phi_{e,P} - \phi_{e,W}\right)\right.$$

$$\left. + \frac{\mathrm{p_s}\Delta y_P}{\Delta x_{PS}}\left(\phi_{e,P} - \phi_{e,S}\right)\right] = F\epsilon\left(z_f c_f + \sum_i z_i c_i^b\right)\Delta x_P \Delta y_P \Delta t \tag{5.56}$$

The effective permeability at the interface p_e, p_n, p_w, p_s can be determined by using a resistance model for electric flux. For example, at the east face, the coefficient p_e can be written as:

$$\frac{1}{p_e}\frac{\Delta y_{PE}}{\Delta x_P} = \frac{1}{p_P}\frac{\Delta y_P/2}{\Delta x_P} + \frac{1}{p_E}\frac{\Delta y_E/2}{\Delta x_P} \tag{5.57}$$

5.2 Numerical Methods

The system of linear equations presented above, are arranged in form of $AX = B$. The structure of matrices A and X will be as shown in Figure 5.5. This system of equations is solved iteratively to achieve convergence before proceeding to the next time step.

Figure 5.5

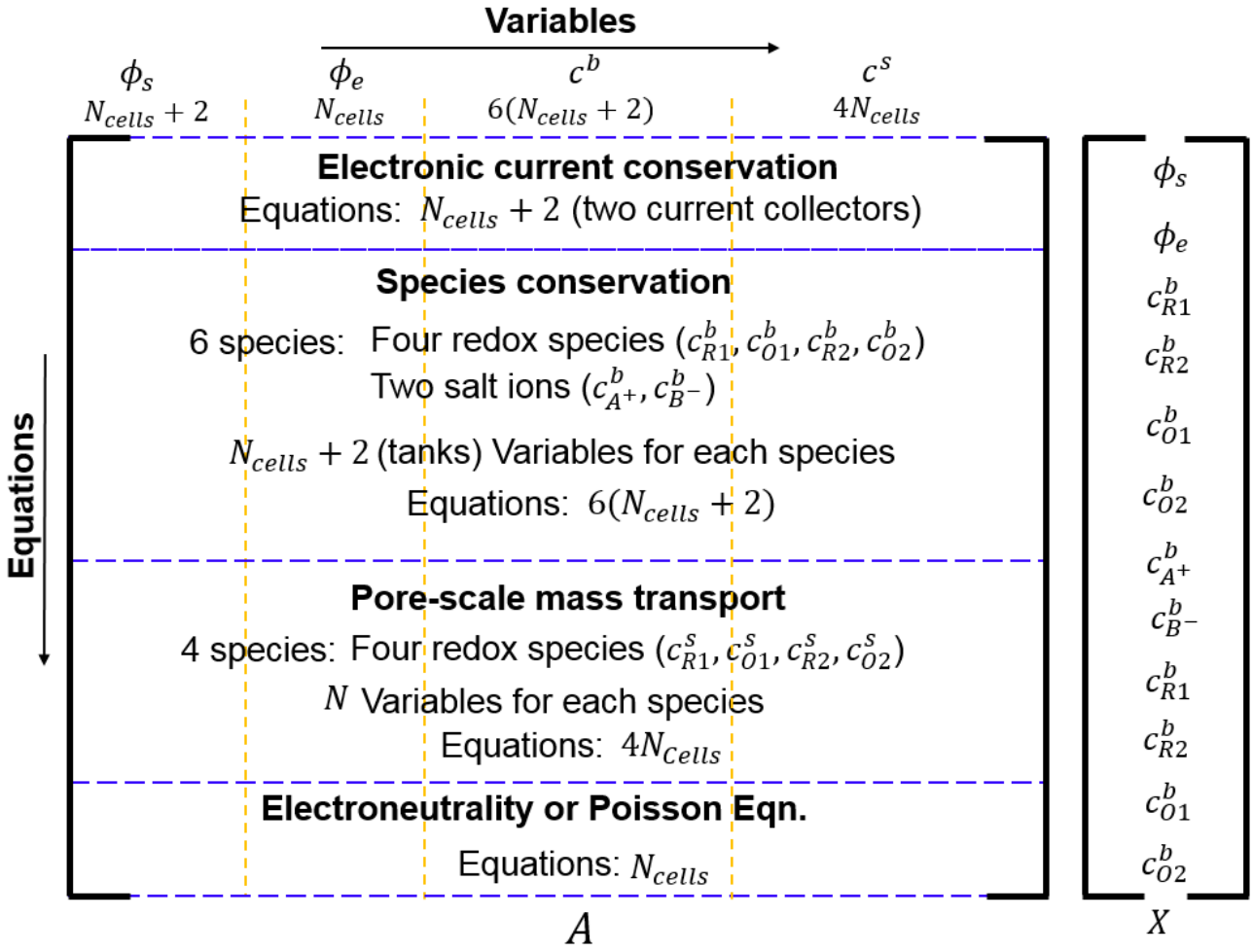

Figure 5.5: Structure of matrices A and X after assembling the system of linear equations.

5.2.1 Choosing Time Step: CFL and Fixed Point Iteration Convergence

One challenge in all numerical methods is to choose an appropriate time stepping to ensure converged solutions. A large time step Δt could lead to unstable solutions and also affect the measurements related to transport of species and reaction kinetics. The use of iteration schemes to arrive at a converged solution requires establishing existence and uniqueness of the solution. When using fixed point iteration schemes, the system of equations is posed as

$$x = g(x)\ \forall x \tag{5.58}$$

During iteration, this takes the form

$$x_{n+1} = g(x_n) \tag{5.59}$$

And the solution is converged when

$$|x_{n+1} - x_n| < \epsilon \tag{5.60}$$

The function $g(x)$ is Lipschitz continuous. A unique converged solution for eqn. 5.59 is guaranteed when

$$|g'(x)| < 1\ \forall x \tag{5.61}$$

Equation 5.62 restricts the max time step that can be used in the simulations. We use a simplified model for reaction kinetics to estimate the maximum time step Δt_{max} that can be used to achieve convergence.

For a redox reaction, with initial concentration of reduced species R as c_R and oxidized species O at concentration c_O, let x be the change in redox concentration over the time step Δt. The concentrations at $t = 0$ and $t = \Delta t$ can be written as:

	R	$\rightleftharpoons$	O	$+ \ e^-$
$t = 0$	c_R		c_O	
$t = \Delta t$	$c_R - x$		$c_O + x$	

We will first perform the time stepping scaling analysis for Butler-Volmer reaction kinetics and then we present the analysis for any kinetic model. For a reversible redox reaction $R \rightleftharpoons O + e^-$ with rate constant for oxidation and reduction as k_{ox} and k_{red} respectively, the rate of change of concentration of R can be given as

$$S = a(k_{ox}c_R - k_{red}c_O)$$

$$S = \frac{dc}{dt} = \frac{x}{\Delta t} = 2ak_0\sqrt{c_R - x}\sqrt{c_O + x}sinh\left(\frac{F\eta}{2RT}\right) \quad 5.62$$

Where $\eta = \phi_s - E_0 + \frac{RT}{F}log\left(\frac{c_R - x}{c_O + x}\right)$. Following from the definition of fixed point iteration convergence scheme, we can express 5.62 as eqn. 5.58 such that $x = g(x)$. The function $g(x)$ takes the form:

$$g(x) = 2\Delta tak_0\sqrt{c_R - x}\sqrt{c_O + x}sinh\left(\frac{F\eta}{2RT}\right) \quad 5.63$$

To ensure convergence, the fixed-point iteration requires $|g'(x)| < 1$ from eqn 5.61.

$$\Delta tak_0\left[\sqrt{\frac{c_R - x}{c_O + x}}e^{-\frac{F\eta}{2RT}} + \sqrt{\frac{c_O + x}{c_R - x}}e^{\frac{F\eta}{2RT}}\right] < 1$$

Simplifying further using the definition of η, we get

$$\Delta t < \left[2ak_0 cosh\left(\frac{F\eta}{2RT}\right)\right]^{-1} \tag{5.64}$$

Equation 5.65 indicates that the max time step decreases exponentially with overpotential. This is significant when considering the use of non-aqueous electrolytes where the RFB is operated at larger potentials. Also, the crossed over species are subjected extreme overpotentials in the counter electrodes limiting the time step.

We now extend the fixed-point iteration scheme to other kinetic models. For the simplified reaction presented above,

$$S = \frac{dc}{dt} = a(k_{ox}c_R - k_{red}c_O)$$

We use the Taylor series approximation to relate the change in concentration with the state variables.

$$S \cong S^* + \frac{\partial S}{\partial \phi_s}\Big|_* (\phi_s - \phi_s^*) + \frac{\partial S}{\partial \phi_e}\Big|_* (\phi_s - \phi_e^*) + \frac{\partial S}{\partial c_R}\Big|_* (c_R - c_R^*) + \frac{\partial S}{\partial c_O}\Big|_* (c_O - c_O^*) \tag{5.65}$$

Assuming negligible change in ϕ_s and ϕ_e during the change x, we get

$$S = \frac{x}{\Delta t} = S^* + \frac{\partial S}{\partial c_R}\Big|_* (c_R - c_R^*) + \frac{\partial S}{\partial c_O}\Big|_* (c_O - c_O^*) \tag{5.66}$$

$$S = \frac{x}{\Delta t} = S^* + \frac{\partial S}{\partial c_R}\Big|_* (-x) + \frac{\partial S}{\partial c_O}\Big|_* (x) \tag{5.67}$$

From eqn. 5.59

$$g(x) = \Delta t\left[S^* + \frac{\partial S}{\partial c_R}\Big|_* (-x) + \frac{\partial S}{\partial c_O}\Big|_* (x)\right] \tag{5.68}$$

For convergence, $|g'(x)| < 1$

$$|g'(x)| = \Delta t \left| \left(\frac{\partial S}{\partial c_O}\Big|_* \right) - \left(\frac{\partial S}{\partial c_R}\Big|_* \right) \right| < 1 \qquad 5.69$$

Equation 5.69 can be used set limits on the time step. For Butler-Volmer kinetics, $S = 2ak_0\sqrt{c_R}\sqrt{c_O}sinh\left(\frac{F\eta}{2RT}\right)$ and equation 5.64 can be reproduced using 5.69. Figure 5.6 shows the variation of maximum time step Δt_{max} with overpotential η for Butler-Volmer (BV) and Marcus-Hush-Chidsey (MHC) kinetic models using 5.69. The exponential nature of BV kinetic model requires orders of magnitude lower Δt_{max}. On the other hand, MHC predicts saturating reaction rate constants with η. Therefore, Δt_{max} saturates with η making it more suitable to simulate the redox kinetics.

Figure 5.6

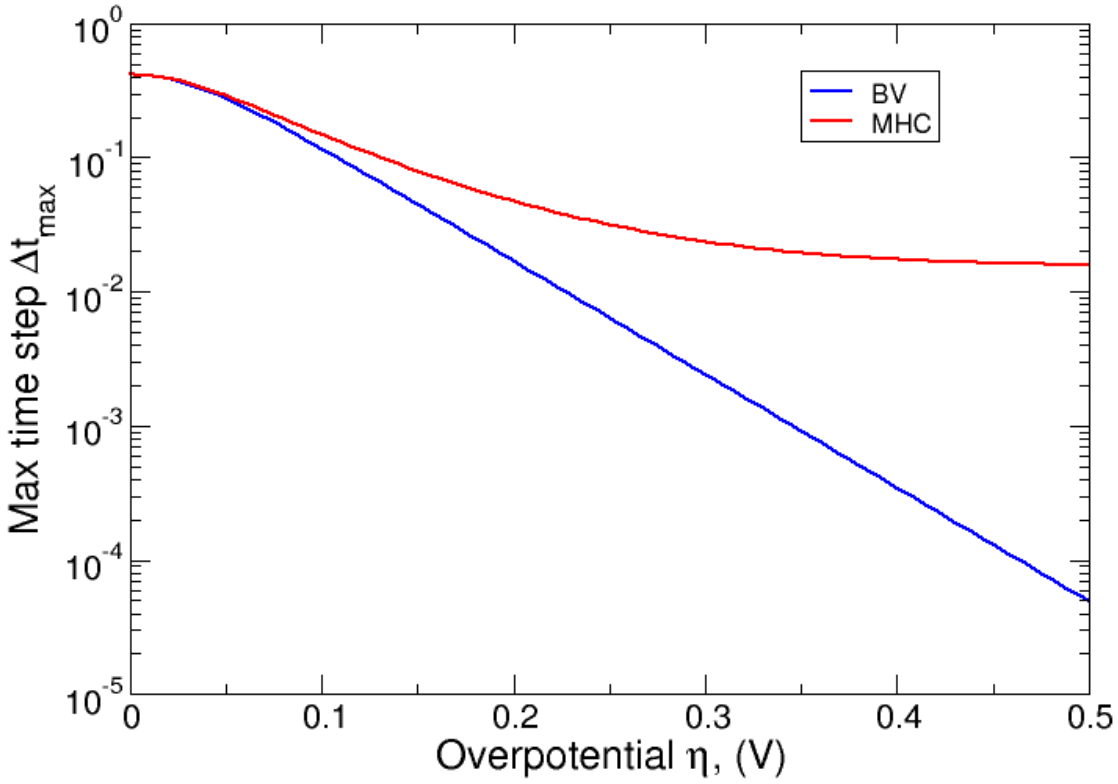

Figure 5.6 (cont.)

Figure 5.6: Max time step that can be used to ensure convergence using fixed-point iteration scheme for both Butler-Volmer (BV) and Marcus-Hush-Chidsey (MHC) kinetic models.

To address the transport based limitation on choosing the time step, we use the Courant-Friedrichs-Lewy condition[3]. The transport of species within the time step must be smaller the length scales of discretization over the time step. The CFL_{num} number can be defined as $CFL_{num} = \frac{max|\vec{u}|\Delta t}{\Delta x}$. The CFL number should be less than 1 to ensure convergence. We set the maximum CFL number to be 0.5

$$\Delta t \leq \frac{CFL_{max}\Delta x}{max|\vec{u}|}$$

$$\Delta t \leq \frac{0.5\Delta x}{max|\vec{u}|} \qquad 5.70$$

5.2.2 Damping Reactions at Low Concentrations

In this section, we propose reaction limiters at low redox concentrations. Consider an RFB electrode with two sets of redox reactions at equilibrium $\eta = 0$, the primary reaction equilibrium due to redox species $R1, O1$ (with standard potential E_1) and the secondary reaction arising due to crossed over species $R2, O2$ (with standard potential E_2). Let the electrode surface and the electrolyte be at potentials ϕ_s and ϕ_e respectively. The ratio of redox species concentrations depends on the potentials E_1 and E_2. Writing the over

potential as $\eta = \phi_s - \phi_e - \phi_{eq}$ for the primary reaction and using the Nernst equation $\phi_{eq} = E_1 - \frac{RT}{F} log\left(\frac{c_{R1}}{c_{O1}}\right)$, we get

$$R1 \rightleftharpoons O1 + e^-$$

$$\eta_1 = 0 = \phi_s - \phi_e - E_1 + \frac{RT}{F} log\left(\frac{c_{R1}}{c_{O1}}\right) \quad 5.71$$

Writing the overpotential equation for the secondary reaction with $\phi_{eq} = E_2 - \frac{RT}{F} log\left(\frac{c_{R2}}{c_{O2}}\right)$

$$R2 \rightleftharpoons O2 + e^-$$

$$\eta_2 = 0 = \phi_s - \phi_e - E_2 + \frac{RT}{F} log\left(\frac{c_{R2}}{c_{O2}}\right) \quad 5.72$$

Equations 5.71 and 5.72 relate the dependence of the concentration $c_{R1}, c_{O1}, c_{R2}, c_{O2}$ on ϕ_s, ϕ_e, E_1, E_2. Simplifying equations 5.71 and 5.72, we get

$$\frac{c_{R2}}{c_{O2}} = \frac{c_{R1}}{c_{O1}} e^{-\frac{F}{RT}(E_1 - E_2)} \quad 5.73$$

For an RFB working voltage of $E_1 - E_2 = 1V$ and assuming $c_{R1} \sim c_{O1}$, we get $c_{R2} = c_{O2} \times 10^{-17}$. In other words, the crossed over redox couple experience high overpotential where almost all of $R2$ is oxidized to $O2$ leaving only trace concentrations of $R2$. The trace amounts of $R2$ become even smaller with increasing the working voltage of RFBs. The machine precision limits the capability of numerically capturing concentration changes at such orders of magnitude. A double machine precision is about 10^{-16}. Moreover, physically speaking, such low redox concentrations (on order of 10^{-16}) contribute insignificantly to the reaction current density and only introduces unnecessary numerical complexity. We therefore proposed a reaction rate damper at low concentrations which

essentially acts as a reaction switch. A sigmoid function $\Psi(c)$, pinned about a certain cut-off concentration c_{cutoff}, is used to damp out the reaction currents. Species concentrations below c_{cutoff} do not participate in redox reactions. If $c > c_{cutoff}$, $\Psi = 1$ and if $c < c_{cutoff}$, $\Psi = 0$. The function Ψ should be continuous, consistent with the rest of continuous equations used in our RFB model.

$$\Psi(c) = 1 - \frac{1}{e^{\frac{c - c_{cutoff}}{\sigma}} + 1} \qquad 5.74$$

The σ governs the spread of the function about c_{cutoff}. In our simulations, we choose $c_{cutoff} = 10^{-5}M$ and $\sigma = 5{\times}10^{-7}M$. Figure 5.7 shows the variation of Ψ around c_{cutoff}.

Figure 5.7

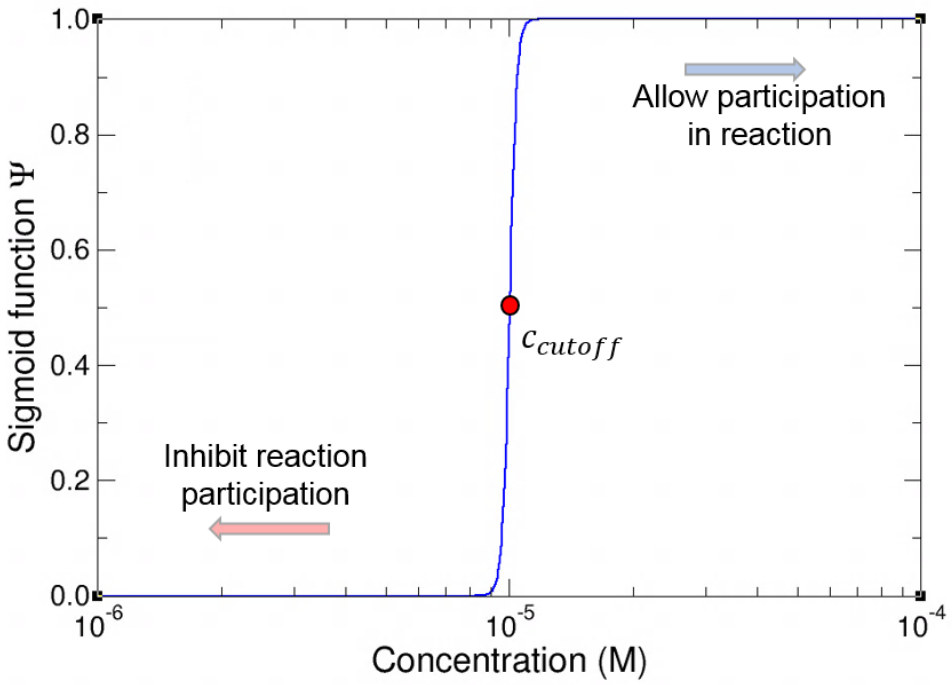

Figure 5.7: Variation of the reaction damping function around c_{cutoff}.

For a reaction $R \rightleftharpoons O + e^{-}$, the forward reaction rate is $k_{ox}c_R$ and the reverse reaction rate is $k_{red}c_O$. The net rate of reaction is given as

$$S = a(k_{ox}c_R - k_{red}c_O)$$

With the damping function Ψ, the net reaction rate can be given as

$$S = a\big(k_{ox}c_R\Psi(c_R) - k_{red}c_O\Psi(c_O)\big) \tag{5.75}$$

Equation 5.75 will replace eqns. $5.6 - 7$ in discretizing the source term. The discrete form of the source term S is now given as (in terms of the surface concentrations)

$$S_i \cong S_i^* + \left.\frac{\partial S_i}{\partial \phi_s}\right|_* (\phi_s - \phi_s^*) + \left.\frac{\partial S_i}{\partial \phi_e}\right|_* (\phi_s - \phi_e^*) + \left.\frac{\partial S_i}{\partial c_{R_i}^s}\right|_* \left(c_{R_i}^s - c_{R_i}^{s\ *}\right) + \left.\frac{\partial S_i}{\partial c_{O_i}^s}\right|_* \left(c_{O_i}^s - c_{O\,i}^{s\ *}\right) \tag{5.76}$$

$$\frac{\partial S}{\partial \eta^0} = a\left(c_R\frac{\partial k_{ox}}{\partial \eta^0}\Psi(c_R^s) - c_O\frac{\partial k_{red}}{\partial \eta^0}\Psi(c_O^s)\right) \tag{5.77}$$

$$\frac{\partial S}{\partial \phi_s} = \frac{\partial S}{\partial \eta^0}\frac{\partial \eta^0}{\partial \phi_s} = \frac{\partial S}{\partial \eta^0} \tag{5.78}$$

$$\frac{\partial S}{\partial \phi_e} = \frac{\partial S}{\partial \eta^0}\frac{\partial \eta^0}{\partial \phi_e} = -\frac{\partial S}{\partial \eta^0} \tag{5.79}$$

$$\frac{\partial S}{\partial c_R^s} = a\left(c_R^s\frac{\partial k_{ox}}{\partial \eta^0}\frac{\partial \eta^0}{\partial c_R^s}\Psi(c_R^s) + k_{ox}\Psi(c_R^s) + c_R^s k_{ox}\frac{\partial \Psi(c_R^s)}{\partial c_R^s} - c_O^s\frac{\partial k_{red}}{\partial \eta^0}\frac{\partial \eta^0}{\partial c_R^s}\Psi(c_O^s)\right) \tag{5.80}$$

$$\frac{\partial S}{\partial c_O^s} = a\left(c_R^s\frac{\partial k_{ox}}{\partial \eta^0}\frac{\partial \eta^0}{\partial c_O^s}\Psi(c_R^s) - k_{red}\Psi(c_O^s) - c_O^s\frac{\partial k_{red}}{\partial \eta^0}\frac{\partial \eta^0}{\partial c_O^s}\Psi(c_O^s) - c_O^s k_{red}\frac{\partial \Psi(c_O^s)}{\partial c_O^s}\right) \tag{5.81}$$

5.2.3 Logarithmic Transformation of Concentration Field

We observed in the previous section 5.2.2 that the crossed species concentration is orders of magnitude different. In section 5.2.2 we damp the reactions to avoid concentrations decreasing below a cutoff. In this section, we modify the system of linear equations to solve for $log(c_R, c_O)$ instead of direct c_R, c_O to embrace the orders of magnitude variation in the species concentrations and check for convergence.

The coefficient matrix A multiplies the variable vector X to give residual vector B $Ax = B$ (section 5.2). The concentration variables in X are expressed directly. We transform the coefficient matrix A and the residual vector B to enable solving for $log(c)$ instead of c directly. Let $g_i = log(c_i)$ or $c_i = e^{g_i}$. By using Taylor series expansion about the best guess of c_i which is the concentration at the previous iteration c_i^*, we get

$$c_i \cong c_i^* + \left.\frac{\partial c_i}{\partial g_i}\right|_{g_i = g_i^*} (g_i - g_i^*) \qquad 5.82$$

In vector form, eqn. 5.82 can be re-written as

$$\vec{c} = \overrightarrow{c^*} + \underline{\underline{D}}\left(\vec{g} - \overrightarrow{g^*}\right) \qquad 5.83$$

where $\underline{\underline{D}}$ contains $\frac{\partial c_i}{\partial g_i}$ terms along the diagonal. We substitute eqn. 5.83 into our linear system of equations to get

$$\underline{\underline{A}}\vec{c} = \vec{b}$$

$$\underline{\underline{A}}\left(\overrightarrow{c^*} + \underline{\underline{D}}\left(\vec{g} - \overrightarrow{g^*}\right)\right) = \vec{b}$$

$$\underline{\underline{A}}\,\underline{\underline{D}}\vec{g} = \vec{b} + \underline{\underline{A}}\,\underline{\underline{D}}\overrightarrow{g^*} - \underline{\underline{A}}\overrightarrow{c^*} \qquad 5.84$$

Solving the linear system of equations presented as eqn. 5.84, we can obtain the concentration fields by

$$c_i = exp(g_i)$$

5.2.4 Chemical Potential Formulation of Species Fluxes

We present the discrete equation of the transport equation in section 5.1.4. The species flux is given as eqn. 5.28.

$$\overrightarrow{N_\iota} = c_i^b\vec{u} - \frac{z_i c_i^b D_i^{eff} F\nabla\phi_e}{RT} - \underline{\underline{D_{H,i}}}\nabla c^b$$

However, when using an IEM, the large concentration and potential gradients at the electrode-membrane interface could affect the stability of the system of linear equations. However, the electrochemical potential is continuous at the interface. The Nernst-Planck flux equation can be rearranged to incorporate the electrochemical potential $\tilde{\mu}$.

$$\overrightarrow{N_\iota} = c_i^b\vec{u} - \frac{z_i c_i^b D_i^{eff} F\nabla\phi_e}{RT} - \underline{\underline{D_{H,i}}}\nabla c_i^b$$

$$\overrightarrow{N_\iota} = c_i^b\vec{u} - \frac{z_i c_i^b D_i^{eff} F\nabla\phi_e}{RT} - \left(D_i^{eff} + \underline{\underline{D_{disp,i}}}\right)\nabla c_i^b$$

$$\overrightarrow{N_\iota} = c_i^b\vec{u} - \frac{z_i c_i^b D_i^{eff} F\nabla\phi_e}{RT} - D_i^{eff}\nabla c_i^b - \underline{\underline{D_{disp,i}}}\nabla c_i^b$$

Rearranging the terms,

$$\overrightarrow{N_\iota} = c_i^b \vec{u} - \underline{\underline{D_{disp,i}}} \nabla c^b - \frac{z_i c_i^b D_i^{eff} F \nabla \phi_e}{RT} - D_i^{eff} \nabla c_i^b$$

$$\overrightarrow{N_\iota} = c_i^b \vec{u} - \underline{\underline{D_{disp,i}}} \nabla c^b - \frac{D_i^{eff} c_i^b}{RT} z_i F \nabla \Phi_e - D_i^{eff} \mathrm{c_i^b} \nabla \ln\left(c_i^b\right)$$

$$\overrightarrow{N_\iota} = c_i^b \vec{u} - \underline{\underline{D_{disp,i}}} \nabla c^b - \frac{D_i^{eff} c_i^b}{RT} \left(\mathrm{RT} \nabla \ln\left(c_i^b\right) + z_i F \nabla \phi_e\right) \quad 5.85$$

$$\overrightarrow{N_\iota} = c_i^b \vec{u} - \underline{\underline{D_{disp,i}}} \nabla c^b - \frac{D_i^{eff} c_i^b}{RT} \nabla \tilde{\mu}_i \quad 5.86$$

Where, the electrochemical potential $\tilde{\mu}$ is defined as $\tilde{\mu} = \mathrm{RT} \ln\left(c_i^b\right) + z_i F \phi_e$. Note that $\underline{\underline{D_{disp,i}}}$ in eqn. 5.86 accounts for dispersion alone without diffusion. The chemical potential gradient in eqn. 5.86 can be discretized similar to those mentioned in section 5.1.4. Integrating and applying divergence to the fluxes leads to

$$\int_t \oiint_A \overrightarrow{N_\iota} . \overrightarrow{dA} = \Phi_e + \Phi_n + \Phi_w + \Phi_s$$

The chemical potential based discrete equation for the east face in the finite volume stencil (Fig. 5.2) can be written as

$$\Phi_e = -\frac{D_i^{eff} c_i}{RT} \tilde{\mu}_i . \Delta x_P \hat{x}$$

$$\Phi_e = -\frac{D_{e,i}^{eff} c_{e,i} \Delta x_P}{RT} \frac{(\widetilde{\mu_E} - \widetilde{\mu_P})}{\Delta y_{PE}}$$

$$\Phi_e = -\frac{D_{e,i}^{eff} c_{e,i} \Delta x_P}{RT} \frac{\left(\mathrm{RT} \ln\left(c_{E,i}^b\right) + z_i F \phi_E - \mathrm{RT} \ln\left(c_{P,i}^b\right) - z_i F \phi_P\right)}{\Delta y_{PE}} \quad 5.87$$

Using Taylor series expansion for $\ln\left(c_{E,i}^{b}\right)$ around the previous iteration $c_{E,i}^{b*}$

$$\ln\left(c_{E,i}^{b}\right) \cong \ln\left(c_{E,i}^{b*}\right) + \frac{\left(c_{E,i}^{b} - c_{E,i}^{b*}\right)}{c_{E,i}^{b*}} \tag{5.88}$$

Substituting eqn. 5.88 into 5.87, we get

$$\Phi_e = -\frac{D_{e,i}^{eff} c_{e,i} \Delta x_P}{RT} \frac{\left(\mathrm{RT}\ln\left(c_{E,i}^{b*}\right) + RT\frac{\left(c_{E,i}^{b} - c_{E,i}^{b*}\right)}{c_{E,i}^{b*}} + z_i F\phi_E - \mathrm{RT}\ln\left(c_{P,i}^{b*}\right) - RT\frac{\left(c_{P,i}^{b} - c_{P,i}^{b*}\right)}{c_{P,i}^{b*}} - z_i F\phi_P\right)}{\Delta y_{PE}} \tag{5.89}$$

The effective face values $\frac{D_{e,i}^{eff} c_{e,i}}{\Delta y_{PE}}$ can be determined by

$$\frac{\Delta y_{PE}}{D_{e,i}^{eff} c_{e,i}} = \frac{\Delta y_E/2}{D_{E,i}^{eff} c_{E,i}} + \frac{\Delta y_P/2}{D_{P,i}^{eff} c_{P,i}} \tag{5.90}$$

5.2.5 Smearing Negative Concentration Predictions

During the course of iterations with a possible low concentration solution, the iteration scheme could predict negative concentration values and cause undefined logarithms. To avoid this, we smear the concentrations to always have very low (close to zero) but positive values. Negative predictions of concentrations are smeared to have value of $c_{smear} = 10^{-8} mol/m^3$. The smearing function is given as

$$\Theta(\mathrm{c}) = 0.5c\left(1 + \mathrm{erf}\left(\frac{c}{c_{smear}}\right)\right) + \frac{c_{smear} e^{-\frac{c^2}{c_{smear}^2}}}{2\sqrt{\pi}} \tag{5.91}$$

Figure 5.8 shows the concentration values after using the smearing function $\Theta(c)$. We use $c_{smear} = 0.5$ for illustration whereas in actual simulations we use $c_{smear} = 10^{-8} mol/m^3$.

Figure 5.8

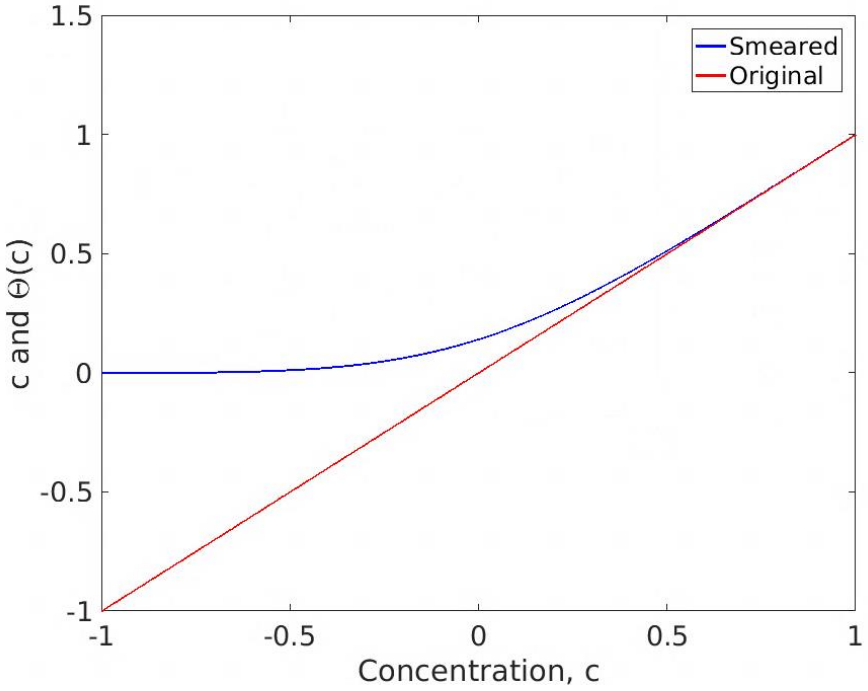

Figure 5.8: Concentration values with and without smearing. $c_{smear} = 0.5$ in this plot.

5.3 Numerical Solution Algorithm

The system of equations is solved iteratively to achieve convergence within each time step. If convergence is not achieved within certain iterations, the time step is reduced. This iteration procedure is repeated for every time step until the RFB is cycled with set number of charge/ discharge cycles. The solution procedure is depicted as a flow chart in Figure 5.9.

Figure 5.9

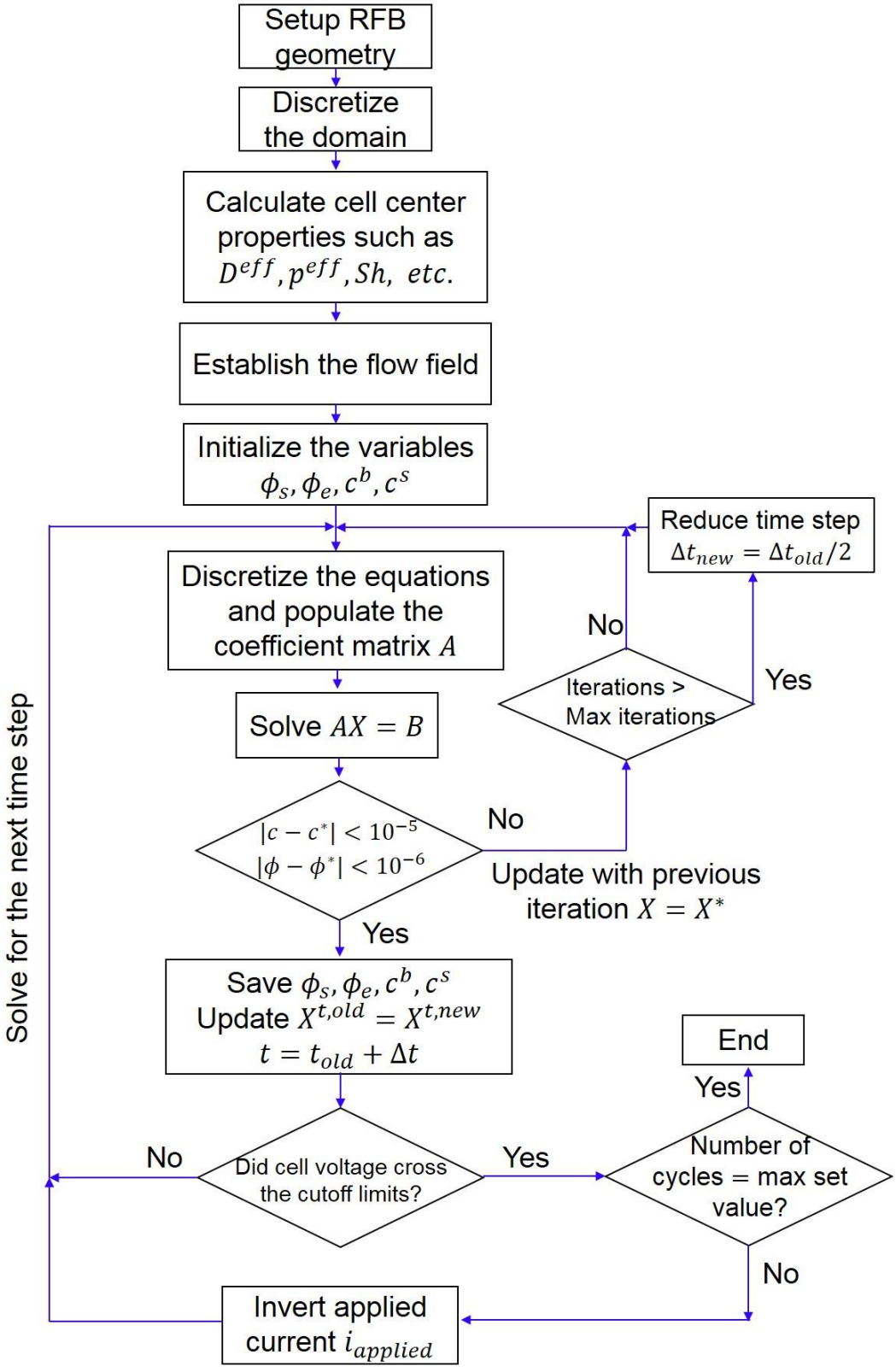
Setup RFB geometry
Discretize the domain
Calculate cell center properties such as $D^{eff}, p^{eff}, Sh,\ etc.$
Establish the flow field
Initialize the variables ϕ_s, ϕ_e, c^b, c^s
Discretize the equations and populate the coefficient matrix A
Solve $AX = B$
$|c - c^*| < 10^{-5}$
$|\phi - \phi^*| < 10^{-6}$
No
Update with previous iteration $X = X^*$
Yes
Iterations > Max iterations
No
Yes
Reduce time step $\Delta t_{new} = \Delta t_{old}/2$
Save ϕ_s, ϕ_e, c^b, c^s
Update $X^{t,old} = X^{t,new}$
$t = t_{old} + \Delta t$
Did cell voltage cross the cutoff limits?
No
Yes
Number of cycles = max set value?
Yes
No
End
Invert applied current $i_{applied}$
Solve for the next time step

Figure 5.9 (cont.)

Figure 5.9: Flow chart depicting the solution algorithm.

5.4 Mesh Independence Study

In numerical solution procedures, establishing mesh independence is necessary to remove the subjectivity of solution data on the particular mesh size/ number used. In this section, we vary the number of finite volume stencil both along the thickness N_t and in the current collector direction N_c, and observe the variation of performance metrics such as discharge capacity utilization and cell polarization. The results of the mesh independence study are shown in Fig. 5.10. Simulation of coarsely discretized RFB predicts very low discharge capacity with high polarization, with converged solution. For mesh sizes 16×8 and beyond, the change in the performance metrics (discharge utilization and cell polarization) is insignificant. Although a finer mesh predicts more accurate solution, it is computationally expensive. We adopt the mesh 16×8 for further studies on RFBs.

Figure 5.10

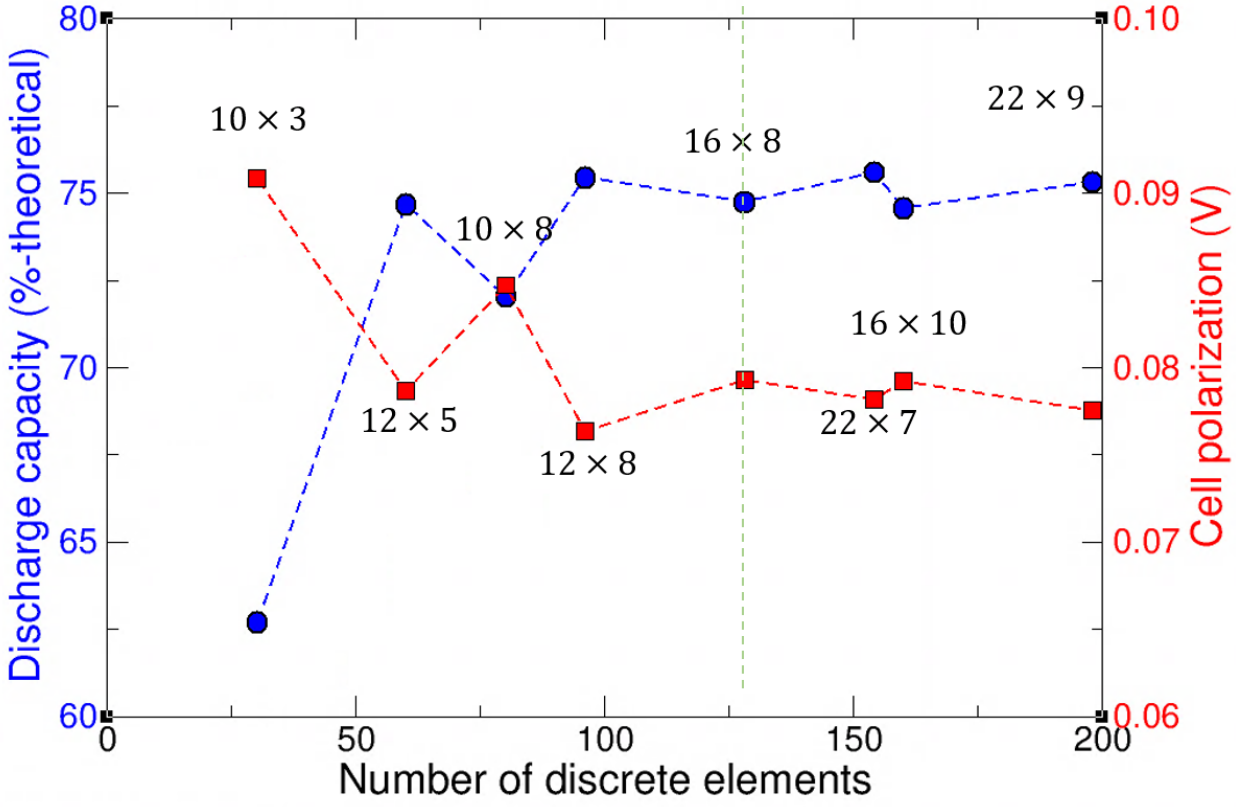

Figure 5.10: Variation of the discharge utilization and polarization with number of discrete cells. The indices for each point indicate the number of cells along the thickness N_t and along the current collector N_c written as $N_t \times N_c$. The dashed-vertical green line corresponds to the mesh adopted for further studies.

5.5 Verification

Verification is an important step in numerical modeling to check the correctness of implementation as computer programming language. We verify the present model by

choosing appropriate conditions under which analytical solutions exist and by comparing the predictions of the 2D simulation with those analytical solutions.

To verify species conservation equations a test was performed with certain flow rate with zero applied current, in which case the total amount of each species in the RFB was conserved to within machine precision. The advection of active species was verified by testing a 20-cm reactor, so as to approach a one-dimensional superficial velocity field. To this reactor, a discontinuity in concentration was introduced at the inlet, and the discontinuity was found to propagate at a velocity within 0.1% of the value expected based on the applied flow rate that is attributable to numerical diffusion. We also take inspiration from Wolfrum and co-workers[4] who studied the redox active shuttling of catechol-quinone redox couple in a nano gap electrode. The shuttling between the two electrodes is limited by diffusion processes and, under no flow conditions, the diffusion limited current density in a channel of height h with $< n >$ redox active molecules is given as $i_{diff} =< n > \frac{Dze}{h^2}$.[4] Under similar conditions of operation, the diffusion limited current density predicted by our simulation is in 98% agreement with the analytical expressions over three orders of magnitude variation in redox species concentrations (Fig. 5.11). This comparison verifies our implementation of the species transport equation.

Figure 5.11

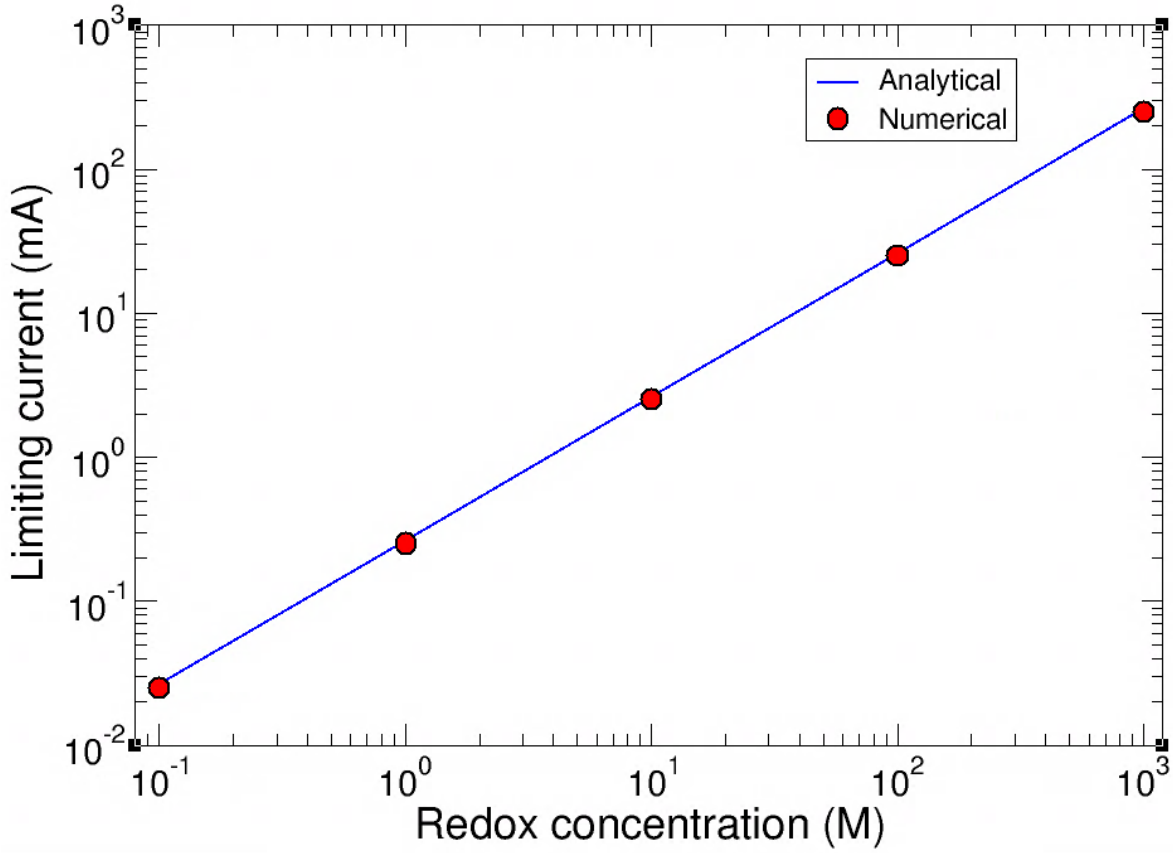

Figure 5.11: Verification of diffusion-limited current density for nano gap electrodes[4].

To verify implementation of reaction kinetics, the RFB with no flow was operated at large Wagner number (representing the scale of kinetic overpotential relative to ohmic polarization and defined as $Wa = \frac{\kappa_{eff} RT}{k_0 a c^0 H^2 F^2}$), such that kinetic polarization dominates and active species concentration is uniform. In practice, ionic conductivity was increased two-fold and the reaction rate constant was decreased by two orders of magnitude. We find that for a constant applied current density of 1.0 mA/cm^2, the concentrations of active species are uniform to within 1% of c^0. Also, the value of the reaction current density, as

determined by current balance over the current collector and carbon felt, agrees with simulated values within 1%, confirming the implementation of the kinetic model.

Lastly, we verify our implementation of Poisson equation by constructing a simplified model with binary electrolyte under steady-state conditions and compare with analytical expressions for the Donnan effect[5]. Our model prediction of the Donnan potential jump is within 5% of the analytical value.

5.6 References

1. Davis, T. A. Algorithm 832: UMFPACK V4.3—an Unsymmetric-pattern Multifrontal Method. *ACM Trans. Math. Softw.* **30**, 196–199 (2004).
2. Iyer, V. *et al.* Assessing the impact of electrolyte conductivity and viscosity on the reactor cost and pressure drop of redox active polymer flow batteries. *Journal of Power Sources*
3. Patankar, S. *Numerical Heat Transfer and Fluid Flow*. (CRC Press, 1980).
4. Wolfrum, B., Zevenbergen, M. & Lemay, S. Nanofluidic Redox Cycling Amplification for the Selective Detection of Catechol. *Anal. Chem.* **80**, 972–977 (2008).
5. Ohshima, H. & Ohki, S. Donnan potential and surface potential of a charged membrane. *Biophysical Journal* **47**, 673–678 (1985).

CHAPTER 6: Effects of Electrolyte Mixing in Tanks

In this chapter, we elucidate the role of flow rate in determining the energy-storage performance of RAP-based RFBs. To do this we first explore the galvanostatic cycling characteristics of an RFB for low and high flow rates. In all simulations for this chapter, we choose a target charge/discharge time of 5 hours, which is typical for grid-scale energy storage applications. With such a constraint on cycling, the current density applied to each cell that is simulated will depend on the size of the RFB's tanks relative to the electrolyte volume within the reactor. We start by considering small systems for which the current density is also small ($1\ mA/cm^2$). Later, we confirm that the findings obtained under such conditions are similar to those obtained for large systems with higher current densities.

Though polarization decreases with increasing flow rate (as a result of the increased uniformity of current density across the separator), we find that the polarization due to transport processes within the electrodes is not the dominant factor responsible for capacity loss when cycling at low flow rates. Subsequently, we examine the temporal dynamics of active species concentration within the tanks, and find, instead, that capacity loss under such conditions is primarily a result of mixing between solution entering the RFB's tanks and solution stored in the tanks themselves. Subsequently, we present a simplified model for charge utilization and use it to develop maps of charge utilization and polarization as a function of non-dimensional flow rate and tank size.

Sections of this chapter are reprinted from Nemani V. P., Smith K. C., Uncovering the role of flow rate in redox-active polymer flow batteries: simulation of reaction distributions with simultaneous mixing in tanks, Electrochim. Acta, 247, Copyright (2017), with permission from Elsevier

We define several non-dimensional parameters that we use to correlate results. The utilization χ is defined as the fraction of theoretical capacity utilized during either charge or discharge of a given cycle, where theoretical capacity Q_{theory} is expressed as $Q_{theory} = (V_{tank} + V_{elec})c^0F$. We also use non-dimensional parameters to quantify the size of and the flow rate within an RFB: the tank-to-electrode volume ratio, defined as $\alpha = V_{tank}/V_{elec}$, and the non-dimensional flow rate, $\beta = \dot{V}/\dot{V}_{stoich}$, respectively. Here, the stoichiometric flow rate $\dot{V}_{stoich}$ is set by the total solution volume within a given half of the RFB divided by the theoretical charge time τ_c, $\dot{V}_{stoich} = (V_{tank} + V_{elec})/\tau_c$, where $\tau_c = Q_{theory}/I_{applied}$ for a total current $I_{applied}$ at the current collectors. The polarization $\Delta\phi$ is calculated based on simulated results as half the difference of average voltages during charge and discharge.

We use galvanostatic conditions to charge and discharge for each case that follows, so as to produce a theoretical charge/discharge time of 5 hours in each case. In most cases considered the corresponding current density is $1\ mA/cm^2$, and we show that consistent behavior is observed at current densities as high as $10\ mA/cm^2$. Also, charge and discharge processes are terminated at cell voltages of $3.35V$ and $2.65V$, respectively. Figure 6.1 shows the variation of cell voltage with time for the first five charge/discharge cycles with a particular actives concentration of $c^0 = 0.5M$, tank-to-electrode volume ratio $\alpha = 20$, and non-dimensional flow rate $\beta = 20$. Because the catholyte is oxidized and the anolyte is reduced during charging, cell voltage increases until it reaches the upper voltage limit. This particular case shows near-theoretical utilization during the first charge step, but charge and discharge capacity decrease and approach an asymptote after a certain number of cycles. We refer to a cycle exhibiting this asymptotic behavior as a

"limit cycle." Subsequently, we present performance metrics for limit cycles to avoid anomalous capacity variations due to short-time behavior. In practice, we obtain metrics for limit cycles by simulating a finite number of cycles and classify a limit cycle as a cycle with coulombic efficiency in excess of 99.8%.

Figure 6.1

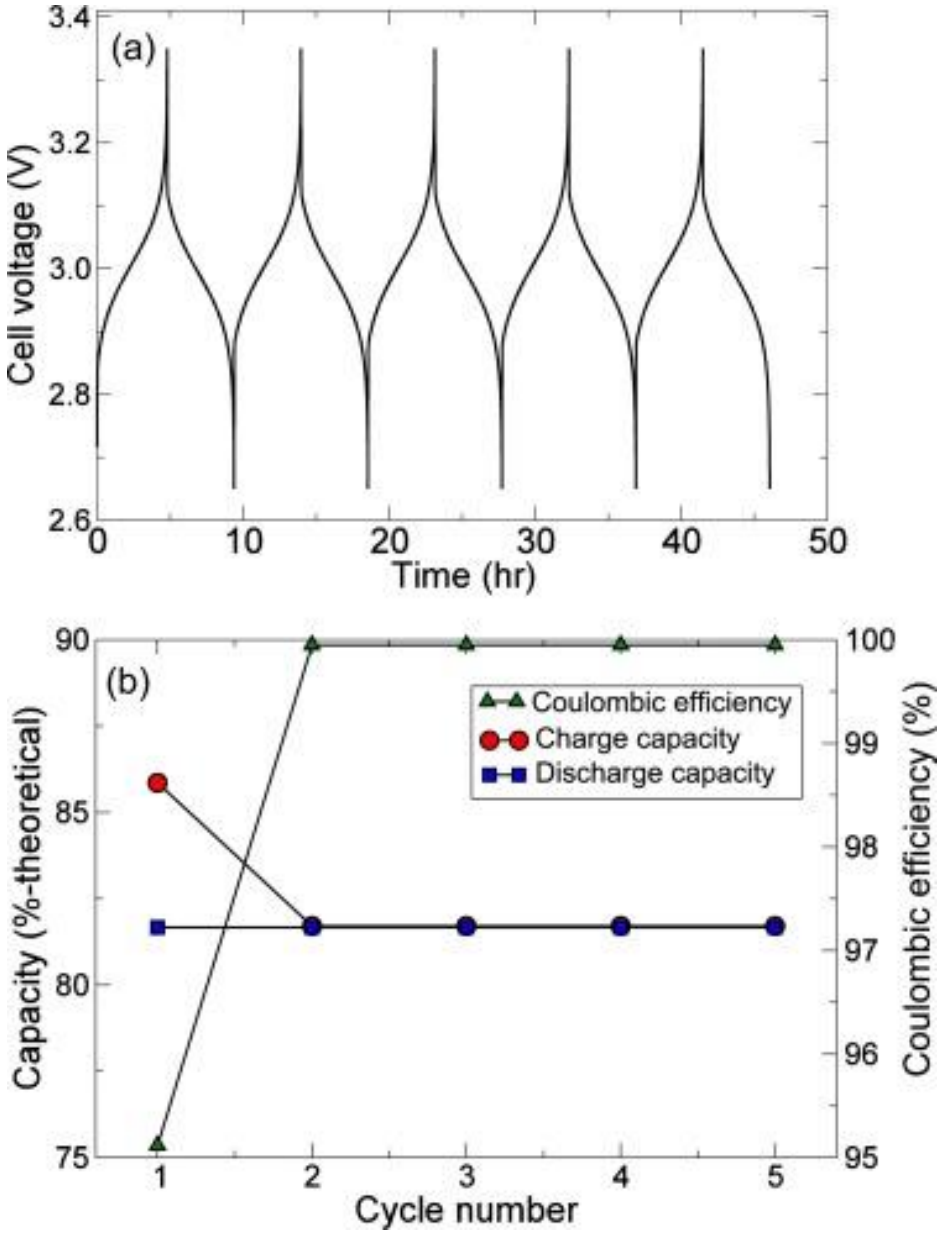

Figure 6.1 (cont.)

Figure 6.1: (a) Variation of cell voltage with time and (b) variation of charge/discharge capacities and coulombic efficiency with cycle number for an RFB configuration having an initial active-species concentration $c^0 = 0.5M$ having a tank-to-electrode volume ratio $\alpha = 20$ operated at $\beta = 20$.

6.1 Cycling Behavior at Flow Rate Extremes

We first explore the effect of flow rate on cycling performance by considering two extreme values of flow rate. Here, we consider multiples of the stoichiometric flow rate, because, in theory, the stoichiometric flow rate is the smallest flow rate that can be maintained without consuming an electrolyte's charge capacity prior to exiting the electrode. Specifically, we compare the performance of cases with $\beta = 2$ and with $\beta = 20$, using twice and twenty times the stoichiometric flow rate, respectively. The limit-cycle cell-voltage curves for these two cases are shown in Fig. 6.2, as a function of the cell's average state-of-charge. On these plots the terminal state-of-charge determines utilization and polarization is the difference between the charge and discharge voltage curves. At low flow rates, only 20% utilization is achieved, whereas at high flow rates, utilization is approximately 90%. The RFB using low flow rate experiences higher polarization ($110mV$) than at high flow rate ($11mV$). Experimentally, similar results have been observed[1] with respect to the voltage curves (better capacity) and energy capabilities (high peak power density and limiting current). They hypothesized that high flow rates would enable greater utilization of the electrode volume, thus leading to better performance. Also previous vanadium RFB models have predicted improved coulombic efficiency with increased flow rate[2].

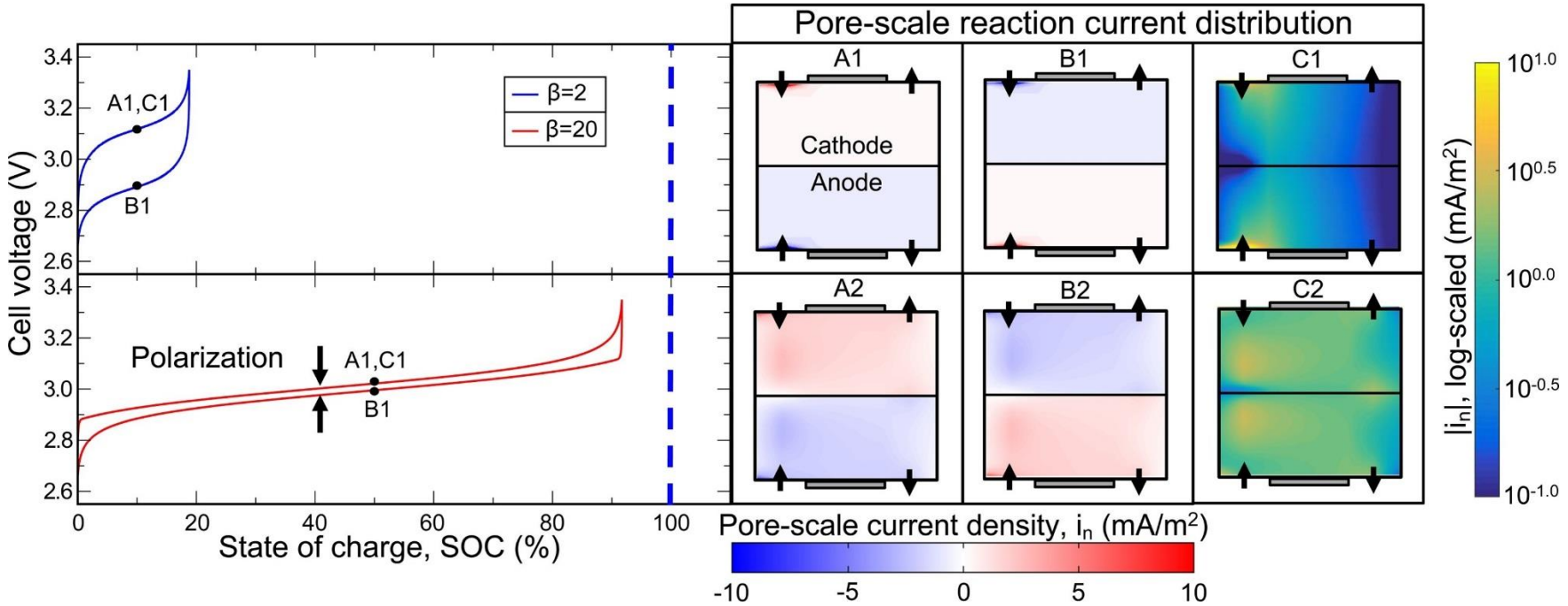

Figure 6.2: Cell voltage variation with state of charge (SOC) during charge and discharge process at low ($\beta = 2$) and high ($\beta = 20$) flow rates for a RFB configuration having an active species concentration $c^0 = 0.5M$ and tank-to-electrode volume ratio $\alpha = 20$. Snapshots of the pore scale reaction current density with linear and logarithmic contour mapping (geometry not drawn to scale) halfway through the charge and discharge process are shown along with flow directions.

To link the macroscopic trends of polarization with flow rate the spatial variation of the pore-scale reaction current density $i_n(x, y, t)$ are shown in Fig. 6.2 for times half-way through state-of-charge range accessed during a limit cycle. This current density is generated at the microscopic interface between carbon-felt fibers and electrolyte, and, consequently, it is substantially smaller than the average electronic current density applied to the reactor, due to the carbon felt's high specific surface area. We note that the distributions at the specific instants in time chosen are similar to those observed over the entire charge/discharge process. These distributions reveal that reaction current density is concentrated at the entry region for both anode and cathode at low flow rate, while the remainder of the electrode is practically inactive (A1 and B1). Regions of high reaction rates (also called "hot spots") and low reaction rates (also called "dead zones") are made even more apparent by examining reaction current distribution on a logarithmic scale (C1 and C2). When flow rate is slow enough hot spots form at the electrode entry, while at high flow rates, the hot spot migrates closer to the separator in both electrodes. In general, reaction rates are more uniformly distributed along the separator at high flow rate than at low flow rate. Thus, at high flow rates, the electrode volume is efficiently utilized, eliminating dead zones across the electrode's length. These observations also help to explain the reduced polarization observed at high flow rates; the path length through which ions must transport decreases when reactions shift closer to the separator at high flow rate. In contrast, the hotspots at low flow rates are farther away than at high flow rates, leading to high polarization. This reaction localization effect can also be observed in the solution-phase current density across the separator, as shown in Fig. 6.3. At low flow rates, the solution-phase current density is maximized near inlets. As flow

rate increases this current distribution becomes more uniform, enabling more efficient transport of ions between electrodes.

Figure 6.3

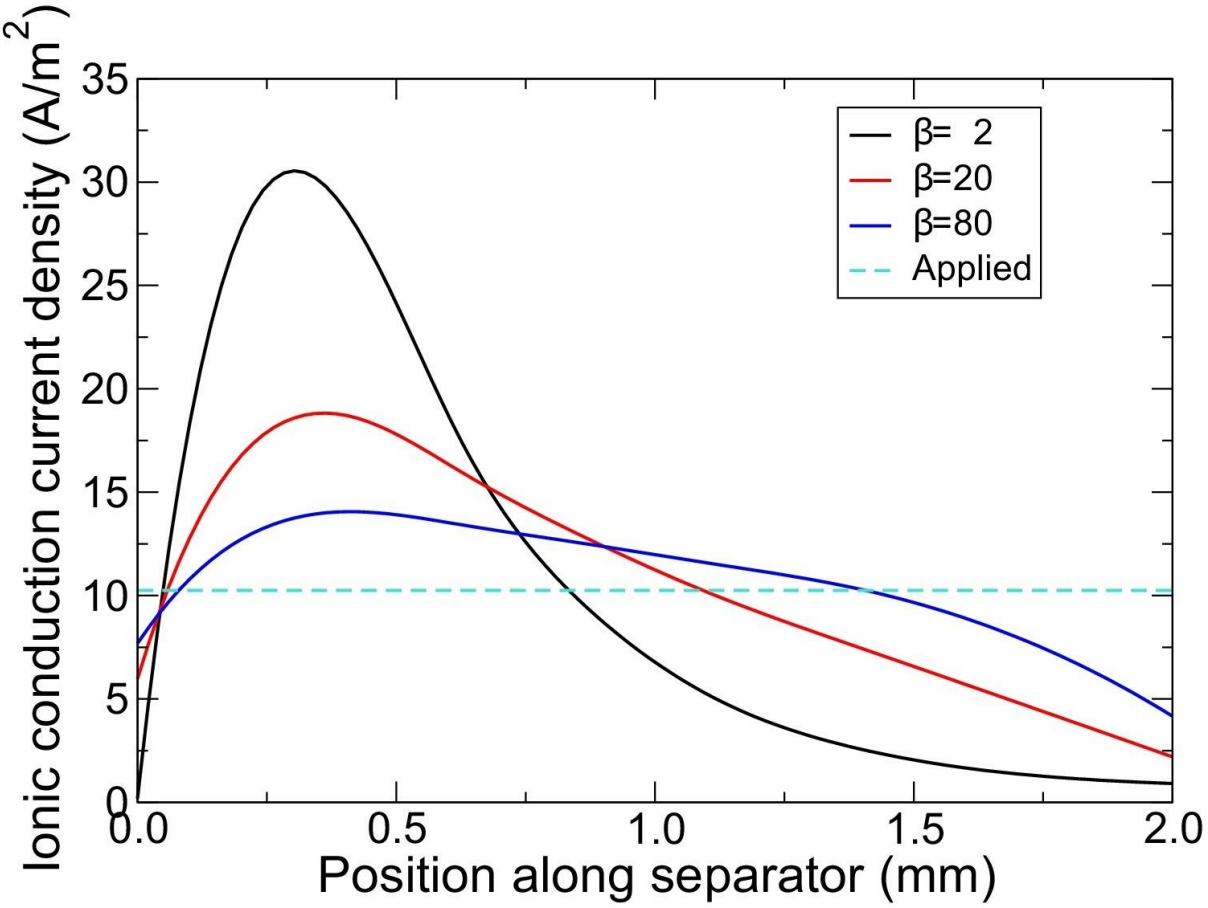

Figure 6.3: Variation of thru-plane (x-direction) ionic current density along the separator for different flow rates in a RFB with initial ion concentration c^0 = 0.5M and tank-to-electrode volume ratio α = 20. The dashed line shows the electronic current density applied to the current collectors.

The variations of reaction-rate distributions observed with flow rates can explain the trends of polarization, but polarization alone is not the root cause of the low capacity

obtained at low flow rates. In general, when electrochemical cells (including flow batteries and Li-ion batteries) are cycled at high enough rate, polarization can reduce utilization as a result of the finite size of the voltage window over which cycling occurs. For the lowest flow rate investigated thus far ($\beta = 2$) polarization is approximately $110\,mV$, which is substantially smaller than the $700\,mV$ range through which the RFB was cycled ($2.65V$ to $3.35V$). Furthermore, the sharp rise and fall in potential at the termination charge and discharge, respectively, suggests that active-species capacity has been locally exhausted, rather than due to the effect of polarization.

6.2 Effect of Tank Mixing on Capacity Loss

Investigation of mechanisms other than reactor polarization is required to identify the dominant sources of capacity loss at low flow rates and to identify operating conditions to achieve satisfactory utilization during RFB operation. Though we are unaware of prior studies focused on the effects of tanks in conventional RFBs, previous work on suspension-based flow batteries showed that dispersive mixing of charge[3,4] and extension of electrochemical reactions outside of the reaction zone defined by metal current collectors[5] can result in the loss of capacity and energy efficiency during a complete charge/discharge cycle. Consequently, we explore the effect of mixing processes within the RFB's tank on the capacity loss observed when operating near stoichiometric conditions.

Here, we find that capacity loss near stoichiometric conditions arises primarily due to mixing within tanks, and we first illustrate this phenomenon with the aid of an idealized

batch-mode operating scheme for an RFB. With this operating scheme solution is pumped into the electrode in discrete batches and the residence time of each batch in the reactor sets the time-averaged flow rate through the reactor. We note that similar schemes, referred to as the "intermittent flow mode," have been employed with suspension-based RFBs to enable efficient operation[3,4,6]. Figure 6.4 shows half of two batch-mode RFBs: one is operated at low time-averaged flow rate ($\beta = 1$) and the other at high flow rate ($\beta = 10$). For this example, tanks are chosen to be twice as large as the electrode ($\alpha = 2$) and to contain electrolyte with 100% state-of-discharge at the beginning of the first charging cycle.

Figure 6.4

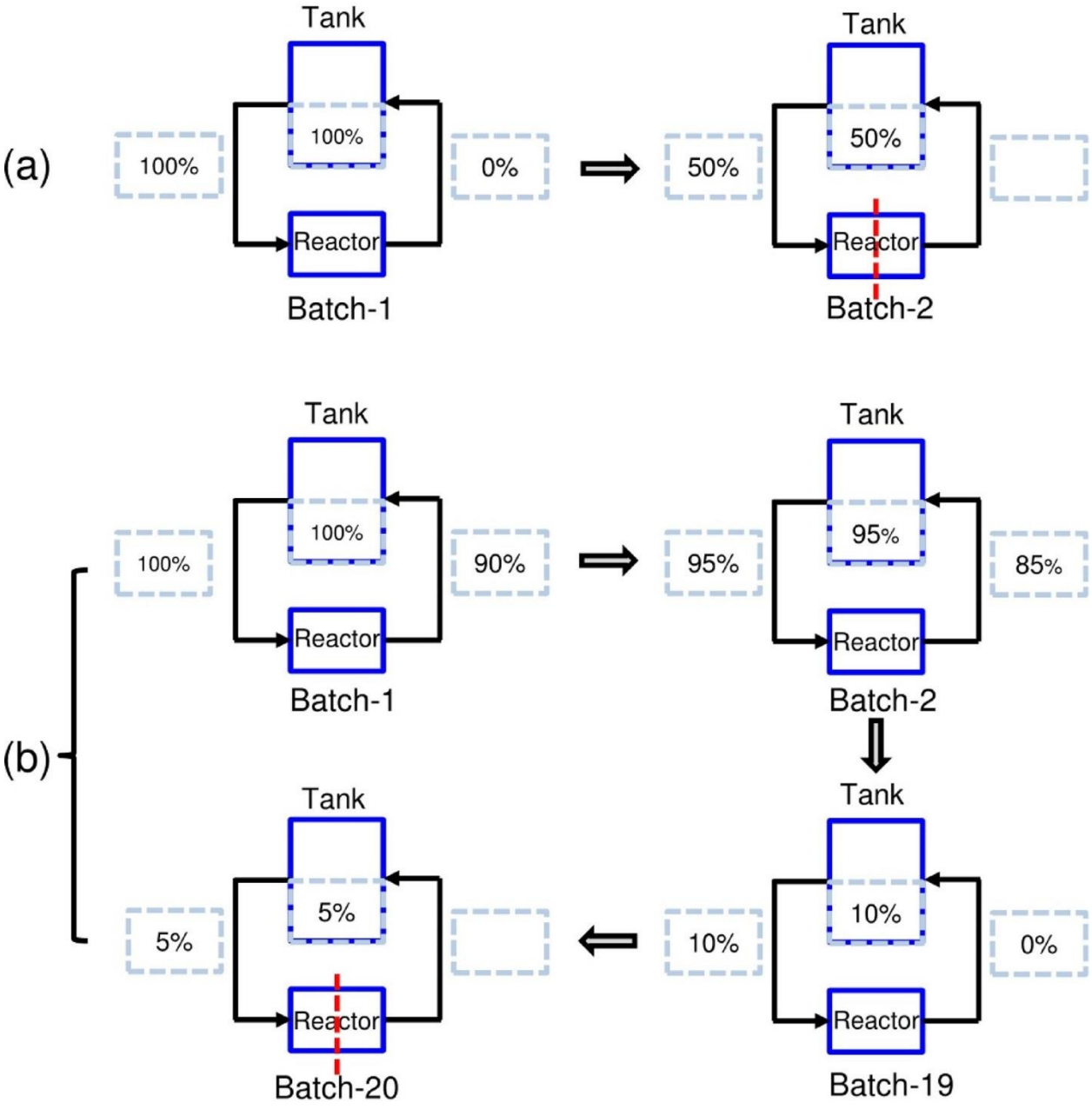

Figure 6.4: Schematics depicting variation of state-of-discharge in a batch mode operated RFB with $\alpha = 2$ operated at (a) stoichiometric flow rate and at (b) ten times the stoichiometric flow rate.

Figure 6.4a shows the corresponding state-of-discharge variation for a stoichiometric flow rate ($\beta = 1$) within the tank and within the inlet and outlet of the electrode. The residence time for stoichiometric conditions we denote as τ_{stoich}. By definition, under stoichiometric conditions, the electrolyte's capacity is consumed after a single pass through the electrode by cycling for a time period of τ_{stoich}. In this particular representation, one batch of solution (equal to the reactor volume) enters the reactor at 100% state-of-discharge and exits the electrode at 0% state-of-discharge. Subsequently this electrolyte, which is fully charged, is now combined with solution in the tank, where it is mixed to form solution with 50% state-of-discharge. The next batch of solution entering the electrode is at 50% state-of-discharge, which contains substantially less charge capacity than the first batch. As a result, this solution's capacity will be exhausted in a time period 50% shorter than that of the first batch. As a result, the total charge time for two batches is approximately $1.5\tau_{stoich}$ with stoichiometric flow, while the cell should have charged for $3.0\tau_{stoich}$ if mixing had not occurred within its tanks. Thus, this cell produces a utilization of approximately 50%. The corresponding capacity loss is further evidenced by the remaining solution within the RFB's tank, which is filled with solution having 50% state-of-discharge. With larger, more practical tank-to-electrode volume ratios, capacity losses due to mixing are even more significant.

Operating the RFB at high flow rates can improve charge utilization by minimizing the difference in state-of-discharge between the tank and electrode. Figure 6.4b shows an RFB operated in batches with ten times the stoichiometric flow rate ($\beta = 10$) for the same tank size as in the previous example. At this flow rate, residence time reduces tenfold to $0.1\tau_{stoich}$. Therefore, the state-of-discharge consumed during a single pass of each batch

is 10%, and the state-of-discharge for the first batch reduces from 100% to 90% (Fig. 6.4b,i) when the batch is finished. When combined with solution in the tank its state-of-discharge decreases to 95% (Fig. 6.4b,ii). The next batch enters with 95% state-of-discharge. After 19 such batches the tank concentration reduces to 5% (Fig. 6.4b,iv). As a result, the batch's capacity is exhausted during the 20th batch, resulting in 95% utilization.

Similar dynamics of actives concentration within tanks and electrodes are observed when using continuous flow coupled to electrode reactions. Figure 6.5 shows the average concentration of reduced species in the cathode tank and electrode, in addition to the corresponding cell voltage profiles for a RFB with an initial tank concentration $c^0 = 0.5M$ and $\alpha = 20$ at two different flow rates. At low flow rate during the first charging step (Fig. 6.5a), the average concentration in the electrode rapidly drops to around $c^0/2 = 0.25M$. Thereafter, concentrations in the tank and electrode evolve at similar rates until concentration within the electrode reduces to zero. At the same instant in time, cell voltage diverges due to the exhaustion of capacity within the electrode, while the tank concentration is approximately $0.24M$. When a subsequent discharge step begins immediately following the end of the charge step, active species in the electrode are initially in a fully reduced state, producing a rise in reduced species concentration with time when solution from the tank is pumped to it with a concentration of $0.24M$. After sufficient time discharging, reduced species concentration in the electrode increases to $0.5M$ and no oxidized species exist. Consequently, capacity is exhausted at this instant in time. As a result of the short duration of the discharge process, concentration within the tank increases by a small degree during the discharge process (from $0.24M$ to about

$0.26M$). The next charge cycle starts with the tank now at approximately 0.26M. This process repeats as a limit cycle for the remainder of charge/discharge cycles, where tank concentration fluctuates between $0.24M$ and $0.26M$, and produces a miniscule charge utilization of approximately 4%.

In contrast, when flow rate is high (Fig. 6.5b, $\beta = 20$), the difference in concentration between the tank and the electrode (on average) is very small (approximately $0.5M$ divided by 20). The reduction in this concentration difference allows the tank and electrode to approach zero state-of-discharge at the end of the first charging cycle (Fig. 6.5b, zoomed inset plot). Charge utilization is therefore complete in the sense that almost all of the active species are oxidized/reduced in the catholyte/anolyte during the charge cycle. As a result, each charge/discharge cycle starts with tanks having nearly pure state-of-discharge tank at high flow rates, and this effect produces high energy-storage capacity.

Figure 6.5

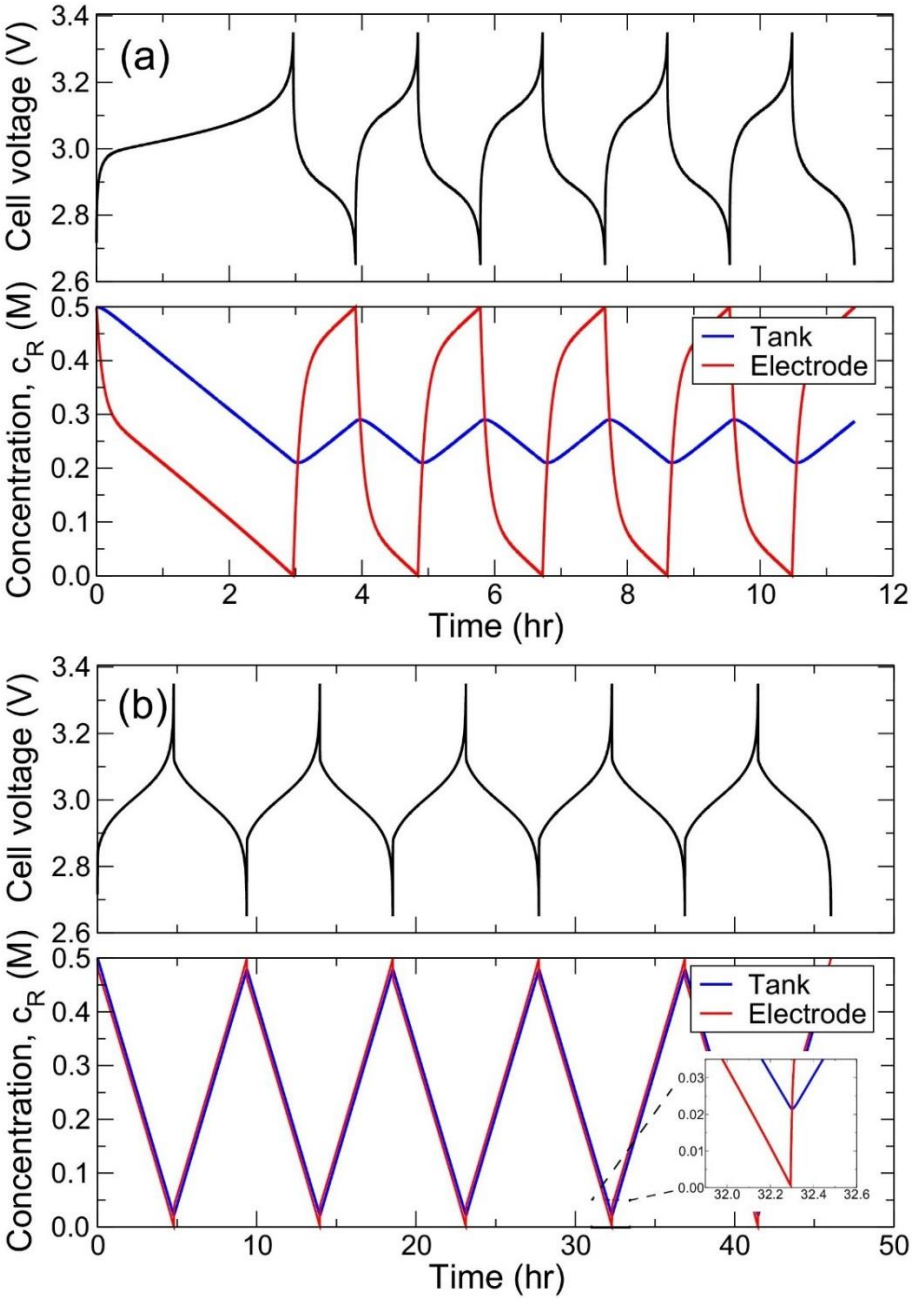

Figure 6.5: Variation of reduced active species concentration in tank and electrode (space averaged) for (a) low ($\beta = 2$) and (b) high ($\beta = 20$) flow rates in an RFB with initial active-species concentration c^0 = 0.5M and tank-to-electrode volume ratio α = 20.

Based on our findings of cycling behavior at extreme flow rates we simulated cycling for a range of flow rates to assess its effect on utilization. Two different initial active species concentrations and tank-to-electrode volume ratios with the same amount of active species were simulated (Fig. 6.6a). For flow rates with $\beta < 2$ the simulations predict near zero utilization. As the flow rate is increased, utilization increases monotonically and about 90% utilization is obtained at $\beta = 20$. At higher flow rates, the porous electrode model predicts the capacities to asymptote close to 100% of theoretical value. Also, our simulations show that polarization ($\Delta\phi$) decreases as flow rate increases for $\beta > 2$ (Fig. 6.6b), and, therefore, energy efficiency losses due to electrochemical processes will be small when operating with high flow rates. For flow rates close to stoichiometric value ($\beta < 2$) the RFB operates like a stationary battery where only the electrolyte in the reactor is utilized towards energy storage. This can be observed in Fig. 6.6a where utilization approaches a value of $\chi = \frac{1}{\alpha+1}$. Therefore, the polarization value decreases as the flow rate approaches zero.

Thus, to facilitate high utilization and efficiency RFBs must be operated at high flow rates, but high flow rate operation necessitates increased pumping pressure that could result in increased pressure-driven crossover of actives and that could require bulky and costly reactor designs to support mechanical loads. Furthermore, the energy required to pump electrolyte could reduce the net energy efficiency of an RFB, including balance-of-plant energy losses. In practice, the choice of operating conditions must be balanced among these factors.

Figure 6.6

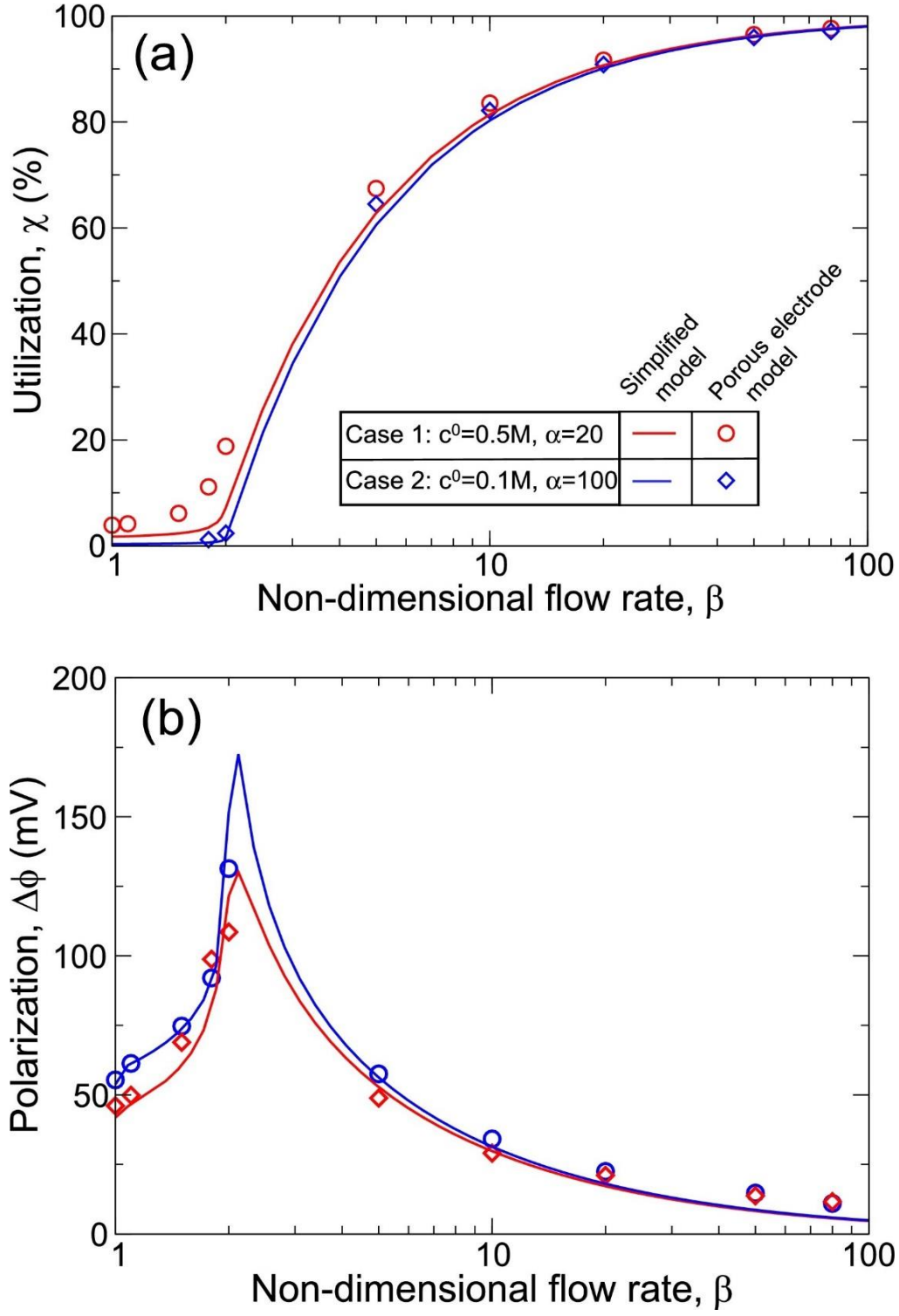
(a)
Utilization, χ (%)
Non-dimensional flow rate, β
Simplified model
Porous electrode model
Case 1: c⁰=0.5M, α=20
Case 2: c⁰=0.1M, α=100
(b)
Polarization, Δϕ (mV)
Non-dimensional flow rate, β

Figure 6.6 (cont.)

Figure 6.6: Simplified model and porous electrode model predictions of (a) utilization χ (%) and (b) polarization (mV), with the non-dimensional flow rate for two different cases which have the same theoretical capacity.

6.3 Utilization and Polarization Maps from a Simplified Model

A simple model is developed to predict the aforementioned behavior of the tank concentration with flow rate and tank size, and from this we estimate the actual capacity that can be obtained after the mixing losses in the tanks during a complete charge/discharge cycle. This model assumes negligible loss in capacity due to kinetic and ohmic polarization, and, therefore, it provides an upper bound on the obtainable capacities that an RFB can achieve with losses due polarization.

Figure 6.7

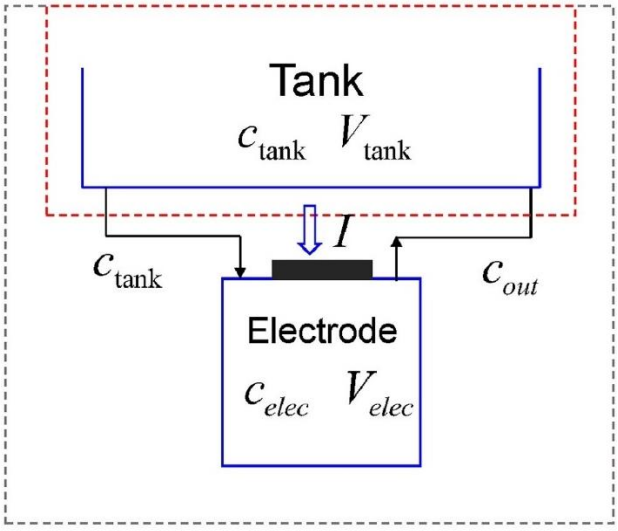

Figure 6.7: Diagram of one half of the RFB unit cell with two control volumes.

Figure 6.7 shows the appropriate control volumes of the cathode half of an RFB during the charging process. By applying species conservation to control volumes around the tank and the entire system the governing equations are:

$$\frac{d(c_{tank}V_{tank})}{dt} = (c_{out} - c_{tank})\dot{V}$$

$$\frac{d(c_{elec}V_{elec} + c_{tank}V_{tank})}{dt} + \frac{I}{F} = 0$$

where c_{elec}, c_{tank}, and c_{out} are average actives concentration within a given electrode, within its corresponding tank, and exiting the electrode, respectively. To close this set of linear ordinary differential equations (ODEs) we assume that the average electrode concentration is an average of concentrations entering and exiting the reactor (i.e., $c_{elec} = (c_{tank} + c_{out})/2$). We solve these ODEs subject to the initial condition that $c_{tank}(t = 0) = c^0$. From this solution the utilization χ can be determined based by the ratio of actual capacity obtained Q_{actual} relative to Q_{theory}, which is equal to a ratio of the actual charge/discharge time t_{actual} to the theoretical charge time τ_c when galvanostatic conditions are used. After expressing these equations in non-dimensional form, utilization χ can be determined by a universal function dependent on (1) tank-to-electrode volume ratio α and (2) non-dimensional flow rate β: $\chi = f(\alpha, \beta)$.

Polarization can also be predicted based on this model, even though it does not include ohmic processes explicitly. This polarization results from irreversible processes within both the tanks and electrodes that are inherent to the chose RFB architecture. Heat generation occurs due to mixing between solution entering the tank and solution stored in the tank, each having different concentrations of active species. Although the local

distribution of current within electrodes does not affect the outlet concentration of active species (considering all distributions having the same total current), in the present flow configuration current is biased toward the inlet of the cell because a common cell potential is imposed across the entire electrode, while the state-of-charge of solution varies along its length. Hence, solution will be charged near the inlet with a potential that exceeds its thermodynamically reversible value, and, thus, this effect contributes to polarization. In contrast to ohmic polarization (which scales linearly with current density), this polarization will occur even as applied current approaches zero, and, hence, it represents the minimum energy loss attainable with an RFB configuration of certain tank size α and flow rate β. We calculate this polarization with the simplified model by assuming that overpotential is negligible at the outlet of both electrodes, in which case cell voltage may be determined as the difference of equilibrium potentials at the outlet of these two electrodes (i.e., $V_{cell} = \phi_{eq}^{+} - \phi_{eq}^{-}$). Such analysis shows that, similar to the utilization, polarization $\Delta\phi$ normalized by the "thermal voltage" RT/F is a function only of α and β (i.e.,$\frac{\Delta\phi F}{RT} = g(\alpha, \beta)$). Hereafter, we refer to polarization produced by the simplified model as the polarization due to inherent irreversibility.

The results of the capacity and polarization predictions of this simplified model were compared to those of the porous electrode model in Fig. 6.6 and were found to have excellent agreement of over 95%. We also confirm that the effect of tank mixing on utilization that is predicted by the simplified model is consistent with porous electrode simulations even at higher current densities. Specifically, Table 6.1 compares the charge capacities predicted by the porous electrode model to that of the simplified model for three different current densities of increasing magnitude at low ($\beta = 3$) and high ($\beta = 20$) flow

rates respectively. Here, the tank size was increased with current density to achieve a theoretical 5 hour charge/discharge time using the following relationship: $\alpha = i_{app}\tau_c/(c^0 FH\epsilon) - 1$. Utilization predictions of the simplified model are about 95% in agreement with the predictions of the porous electrode model, indicating that the dependence of utilization on the two dimensionless numbers (α and β) is true even at higher current densities.

Table 6.1: Comparison of utilization predictions from the porous electrode model and the simplified model at different current densities in low ($\beta = 3$) and high ($\beta = 20$) non-dimensional flow regimes.

α	$i_{applied}$ (mA/cm^2)	β	$\chi_{simulation}$ (%)	$\chi_{simplified}$ (%)	$\Delta\phi$ (mV)
128.55	1	3	36.45	34.10	80.96
		20	91.96	90.11	20.21
646.77	5	3	31.89	33.48	107.14
		20	91.23	90.02	46.06
1294.5	10	3	31.34	33.41	136.2
		20	90.56	90.01	77.27

Now, we examine the variation of polarization with system size, and we show that the polarization due to inherent irreversibility dominates at small system sizes. Figure 6.8 shows the variation of polarization with the relative total volume of electrolyte with respect to the electrolyte volume in the electrode, $\alpha + 1$, obtained from the porous electrode

simulations of RFBs. Polarization predictions of the simplified model and a propagating reaction front (PRF) model[7,8] are also shown for comparison with porous electrode model predictions. The PRF model accounts for ohmic resistance from reactions that propagate as a planar front through each electrode, in which case the area-specific resistance R_{asr} is:[7,8]

$$R_{asr} = \left(\frac{H}{2\kappa_{eff}} + \frac{H_{sep}}{\kappa_0 \epsilon_{sep}/\tau_{sep}} + \frac{H}{2\kappa_{eff}} \right)$$

Here, ionic conductivity values used with this model were chosen consistent with porous electrode simulations. Polarization due to the PRF can be determined as the product of R_{asr} and the applied current density i_{app}. The results are shown for two different concentrations in a high flow rate regime of operation $\beta = 20$, and current density is adjusted to obtain the same theoretical charge/discharge time of 5 hours among all different cases, such that current density increases linearly with α. The polarization due to inherent irreversibilty asymptotes to a particular value of 10mV, while for sufficiently large tanks (e.g., $\alpha = 1000$) the polarization due to area-specific resistance is 100mV, exceeding that due to inherent irreversibility by an order of magnitude because of high current densities needed for large tanks. Thus it can be concluded that for smaller tank sizes the polarization due to the inherent irreversibilities is the dominant source of polarization, whereas for larger tank sizes the polarization due to the area-specific resistance dominates.

Figure 6.8

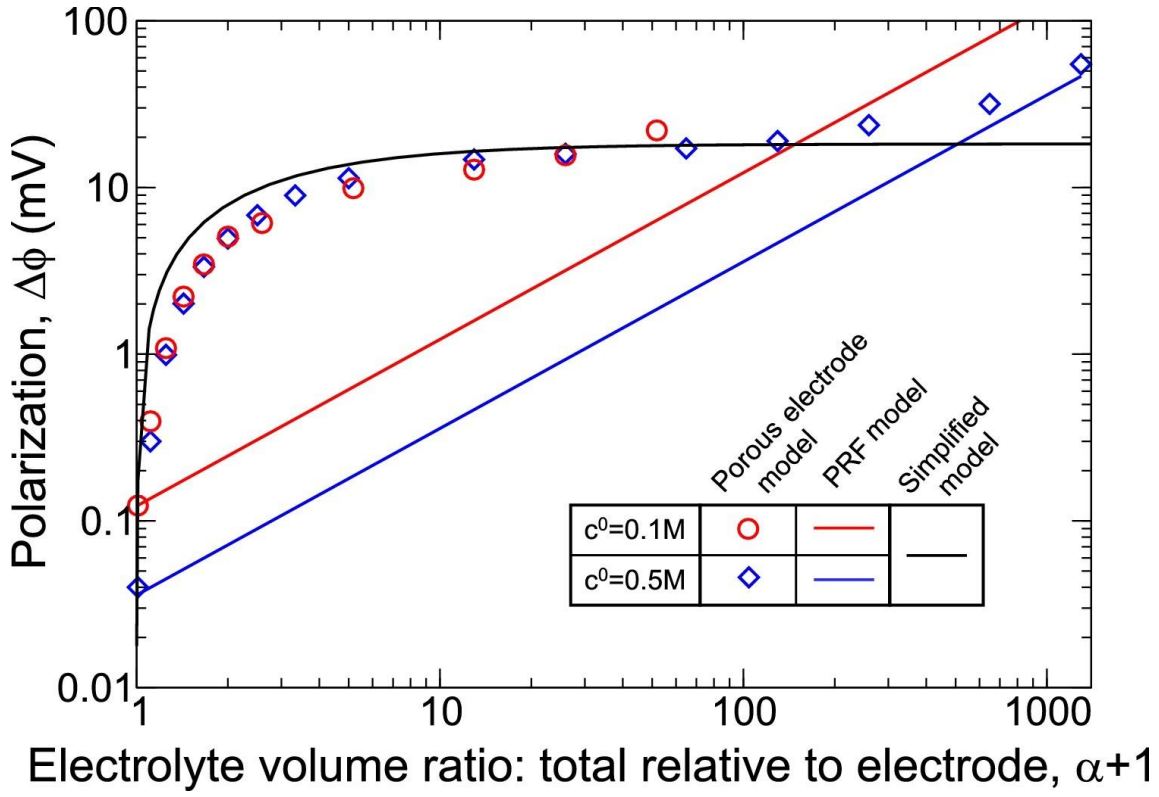

Figure 6.8: Variation of polarization with the ratio of total volume of electrolyte in the RFB to the volume of electrolyte in the electrode. The RFB is operated at a high non-dimensional flow rate $\beta = 20$ for two different active-species concentrations. Polarization predictions from the propagating reaction front model and the simplified model are also shown for comparison.

Since the simplified model predicts utilization and polarization levels similar to the porous electrode model at low current densities, it can be used as an upper-bound estimate of utilization and a lower-bound estimate of polarization for RFBs having various tank sizes and using various flow rates. Figure 6.9 shows the variation of (a) utilization and (b) non-dimensional polarization with flow rate for various tank-to-electrode volume

ratios, as predicted by the simplified model. The charge capacity increases and polarization due to inherent irreversibilities decreases with increasing flow rate. Although the percentage capacity is higher for smaller tank sizes, the base theoretical capacity for such systems is small. For larger tanks, $\alpha > 20$, the degree of change in utilization and polarization with tank size is small indicating that the utilization and polarization are governed by flow rate alone $\chi = \mathrm{f}(\alpha, \beta) \approx f^*(\beta)$ and $\Delta\phi = g(\alpha, \beta) \approx g^*(\beta)$ when $\alpha > 20$. For flow rates near stoichiometric flow velocity ($\beta = 1$), the capacity that can be obtained is very low. The charge utilization increases with increasing flow rate and asymptotes to near 100% capacity for very high flow rates ($\beta = 100$).

Figure 6.9

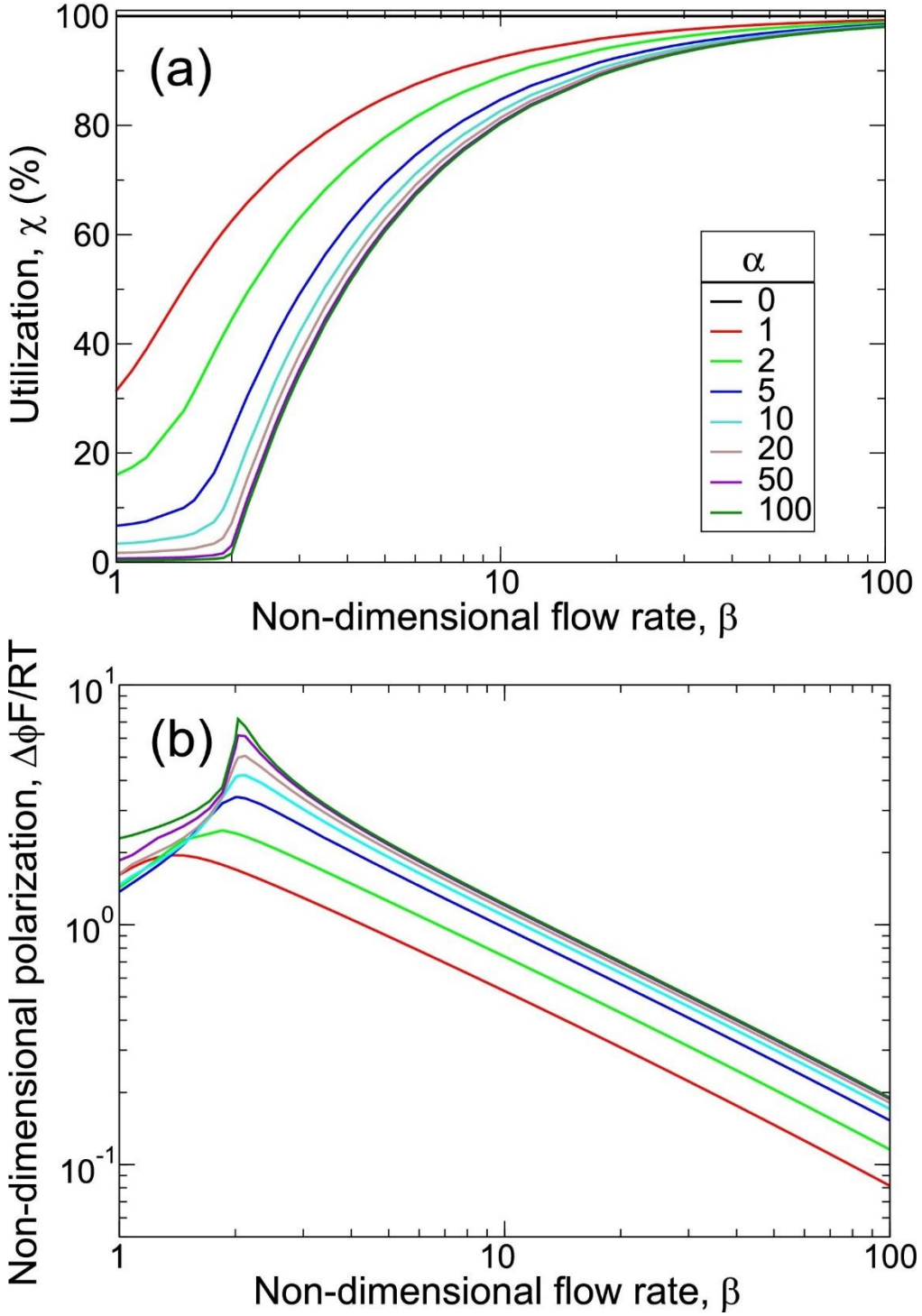
(a)
Utilization, χ (%)
Non-dimensional flow rate, β
α
0
1
2
5
10
20
50
100
(b)
Non-dimensional polarization, ΔϕF/RT
Non-dimensional flow rate, β

Figure 6.9 (cont.)

Figure 6.9: Simplified model predictions of (a) utilization capacity and (b) non-dimensional polarization as a function of the dimensionless flow rate β for various tank-to-electrode volume ratios α.

6.4 References

1. Dennison, C. R., Agar, E., Akuzum, B. & Kumbur, E. C. Enhancing Mass Transport in Redox Flow Batteries by Tailoring Flow Field and Electrode Design. *J. Electrochem. Soc.* **163**, A5163–A5169 (2016).
2. Shah, A. A., Watt-Smith, M. J. & Walsh, F. C. A dynamic performance model for redox-flow batteries involving soluble species. *Electrochimica Acta* **53**, 8087–8100 (2008).
3. Smith, K. C., Chiang, Y.-M. & Carter, W. C. Maximizing Energetic Efficiency in Flow Batteries Utilizing Non-Newtonian Fluids. *J. Electrochem. Soc.* **161**, A486–A496 (2014).
4. Li, Z. *et al.* Aqueous semi-solid flow cell: demonstration and analysis. *Physical Chemistry Chemical Physics* **15**, 15833–15839 (2013).
5. Smith, K. C., Brunini, V. E., Dong, Y., Chiang, Y.-M. & Carter, W. C. Electroactive-Zone Extension in Flow-Battery Stacks. *Electrochimica Acta* **147**, 460–469 (2014).
6. Fan, F. Y. *et al.* Polysulfide Flow Batteries Enabled by Percolating Nanoscale Conductor Networks. *Nano Lett.* **14**, 2210–2218 (2014).
7. Hopkins, B. J., Smith, K. C., Slocum, A. H. & Chiang, Y.-M. Component-cost and performance based comparison of flow and static batteries. *Journal of Power Sources* **293**, 1032–1038 (2015).
8. Wei, T.-S. *et al.* Biphasic Electrode Suspensions for Li-Ion Semi-solid Flow Cells with High Energy Density, Fast Charge Transport, and Low-Dissipation Flow. *Adv. Energy Mater.* **5**, n/a-n/a (2015).

CHAPTER 7: Analysis of Crossover Induced Capacity Fade with Non-Selective Separators

The primary aim of this study is to explain the mechanisms governing the crossover rate of redox active species and its effect on capacity fade. To ensure charge neutrality during the cycling process, redox active species can participate alongside with supporting electrolyte ions by crossing the separator, leading to material loss. The crossover rate is affected by the concentration, diffusion coefficient, and charge number of redox species relative to the supporting electrolyte. Such processes can lead to interesting phenomenon such as redox active shuttling between the two electrodes. Although lumped analytical models have been proposed to understand capacity fade due to crossover[1], an in depth understanding of the local processes that produce capacity fade effects is missing. Here, a 2D model which tracks all dissolved species at all instants in time allows us to quantify the degree of crossover and the spatially resolved reaction currents.

Depending on the oxidation states of the redox species, the reactions can be classified either as salt-splitting (SS) or rocking-chair (RC) configuration. In SS configuration one species in each redox couple is neutral requiring the presence of supporting electrolyte for ion transfer across the separator. In RC configuration all redox species have similarly signed non-zero oxidation state,[2] and these ions, along with their associated counter ions, can transfer across the separator to maintain electroneutrality. Theoretically RC requires lesser salt concentration than SS and could therefore be a

---

Sections of this chapter are reprinted from Nemani, V. P.; Smith, K. C. Analysis of Crossover-Induced Capacity Fade in Redox Flow Batteries with Non-Selective Separators. J. Electrochem. Soc.. 2018, 165(13), A3144–A3155, Copyright (2018), with permission from The Electrochemical Society

potential solution towards economical low-salt RFBs[2]. In this study, we compare the capacity utilization and capacity fade of RC and SS configurations as a function of salt concentration and the diffusion coefficient of redox species. Such analysis can be used to engineer redox active molecules and separator materials.

As there are multiple species and reactions involved, we refer to the redox reactions which are intended for either the high potential electrode (HPE) or the low potential electrode (LPE) as primary reactions. The redox reactions the species experience upon crossing over the separator are referred to as “crossed” reactions (see Figure 4.2).

Primary reactions: $R1^{z_{R1}} \rightleftharpoons O1^{z_{O1}} + e^-$ in HPE and $R2^{z_{R2}} \rightleftharpoons O2^{z_{O2}} + e^-$ in LPE

Crossed reactions: $R2^{z_{R2}} \rightleftharpoons O2^{z_{O2}} + e^-$ in HPE and $R1^{z_{R1}} \rightleftharpoons O1^{z_{O1}} + e^-$ in LPE

We introduce two dimensionless numbers of practical importance to elucidate our results. Molar salt ratio γ is defined as the ratio of the concentration of salt to the concentration of the redox species in the electrolyte $\gamma = c_{salt}/c_{redox}$. Throughout our analysis, the concentration of redox active species is fixed at 0.5M and the concentration of salt is varied from 0M to 1M ($\gamma: 0 \rightarrow 2$). The salt-diffusion ratio ζ is the ratio of the diffusion coefficient of salt ions to that of redox active ions $\zeta = D_{salt}/D_{redox}$. The value of the diffusion coefficient of salt ions (A^+, B^-) is set to that of the PF_6^- anion in EC/PC/DMC[3] and D_{redox} is varied systematically by three orders of magnitude ($\zeta: 10 \rightarrow 10^3$). Practically $\zeta \sim 10$ corresponds to DBBB[4] and $\zeta \sim 100$ represents a 318kDa viologen RAP[5]. A high value of $D_{redox} > 5\times10^{-11} m^2/s$ (low ζ) implies that the diffusion coefficient of the redox active molecules is on par with salt ions. Although increasing D_{redox} increases the ionic

conductivity of electrolyte, the redox active molecules actively compete with salt ions for transport across the separator, leading to large capacity fade. Capacity utilization χ is defined as the percentage of theoretical capacity being utilized during a certain charge/discharge cycle. The RFBs here are cycled galvanostatically between 2.5V to 3.5V.

7.1 Cycling Behavior and Reaction Current Distribution

We first study the cycling performance of an RFB in terms of capacity utilization and coulombic efficiency for ten charge/discharge cycles. For this analysis, a representative RFB with 0.5M salt concentration ($\gamma = 1$) and redox species diffusion coefficient $7.9\times10^{-12}m^2/s$ ($\zeta = 63$ times lower diffusion coefficient than salt ions) is chosen. The cell voltage curve for this case is shown in Figure 7.1 along with the variation of the capacity utilization during discharge at every cycle. Here, the coulombic efficiency, which is correlated to the degree of crossover[1], is 97% indicating that with every cycle there is certain loss of active species due to crossover. Because of this effect the discharge capacity utilization fades by 20% within the first ten cycles.

We first study the cycling performance of an RFB in terms of capacity utilization and coulombic efficiency for ten charge/discharge cycles. For this analysis, a representative RFB with 0.5 M salt concentration ($\gamma = 1$) and with redox species diffusion coefficient $\zeta = 63$ times smaller than that of salt ions, a ratio that is similar magnitude to the "rejection ratio" measured previously[5] for RAPs relative to inert salt ions. For the chosen values of D_{salt}, current density, and salt concentration this simulation produces a salt

Damköhler Da_{salt} equal to 8, which we show later is small enough to facilitate “sufficient supporting electrolyte” behavior where capacity losses are dominated by the diffusive crossover of redox species (rather than by ohmic polarization). Here, we focus on this particular case to illustrate the influence of crossover on reaction current distribution and charge capacity. The cell voltage curve for this case is shown in Figure 7.1 along with the variation of the capacity utilization during discharge at every cycle. Here, the coulombic efficiency, which was previously correlated to the degree of crossover,[1] is 97% indicating that with every cycle there is certain loss of active species due to crossover. Because of this effect the discharge capacity utilization fades by 20% within the first ten cycles.

Figure 7.1

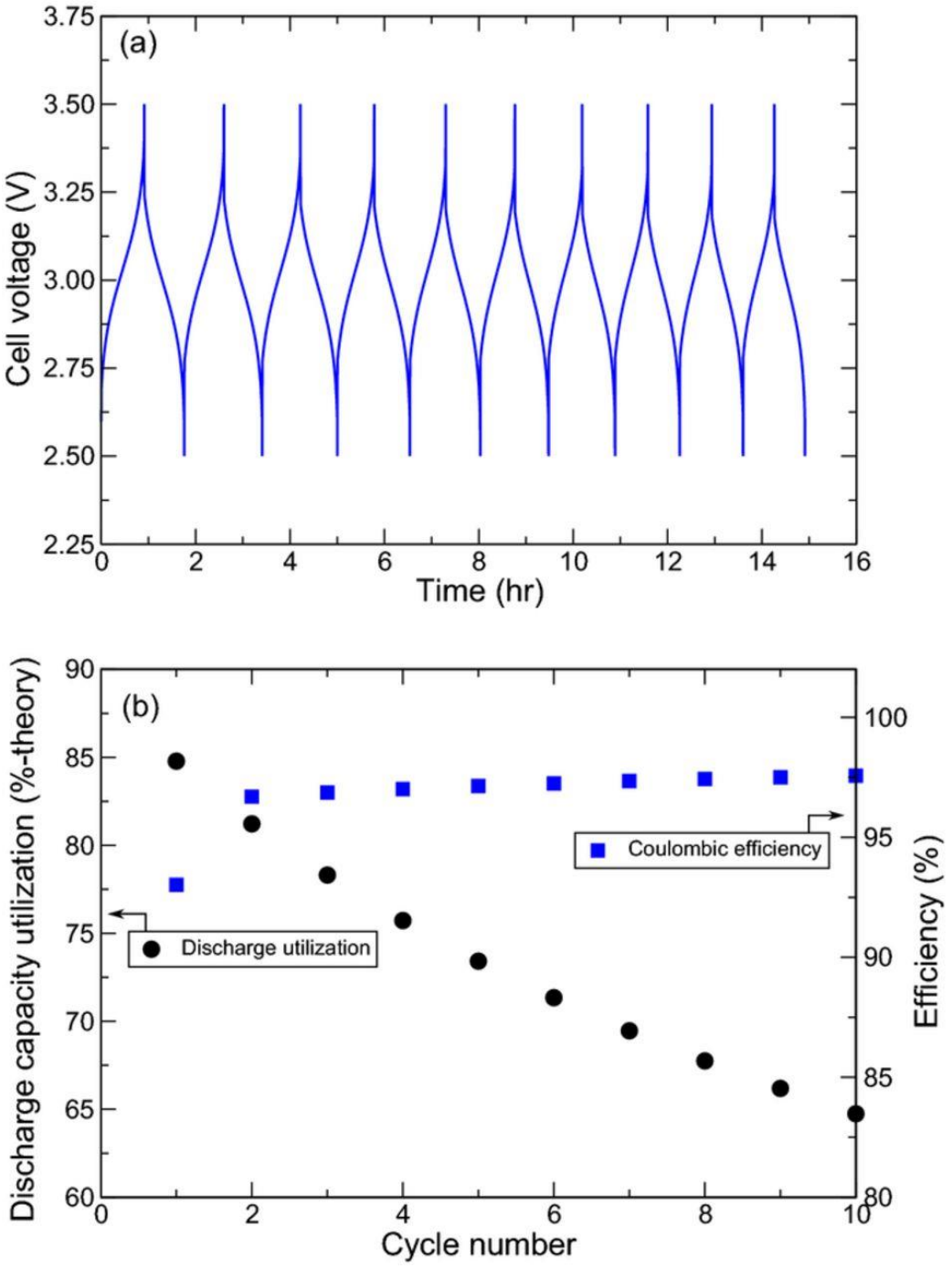

Figure 7.1: (a) Variation of cell voltage with time and (b) variation of discharge-utilization and coulombic efficiency with cycle number for a representative RFB with 0.5 M redox-active species concentration.

7.2 Reaction Current Distribution and Crossover Fluxes

The dynamics of crossover and redox active species shuttling processes vary significantly within a single charge/discharge cycle step. With the variation in state-of-charge, the processes of diffusion and migration can either favor or oppose each other in transferring the redox active species across the separator depending on the direction of current. When the primary redox couple of the HPE ($R1^{z_{R1}}/O1^{z_{O1}}$) crosses over into the LPE, the large negative overpotential environment in the LPE drives the reduction reaction where almost all $O1^{z_{O1}}$ reduces to $R1^{z_{R1}}$. This overpotential is negative throughout the charge/discharge cycle. Similarly, when the primary redox couple of the LPE ($R2^{z_{R2}}/O2^{z_{O2}}$) crosses over to the HPE, the large positive overpotential environment drives the oxidation reaction converting all $R2^{z_{R2}}$to $O2^{z_{O2}}$.

The total pore-scale reaction current density $i_n(x, y, t)$ is a result of electrode-electrolyte interfacial redox reactions and is different from the galvanostatic applied current density at the current collectors. This reaction current density is calculated from the MHC kinetic model. Figure 7.2 shows the development of cell voltage with state-of-charge during the second charge/discharge cycle. Snapshots of the primary and crossed reaction current densities are also shown at two points: near the end of the charge step (A) and early in the discharge step (B). The corresponding cell-voltage is shown as a loop varying with state-of-charge to delineate the capacity utilization during both charge and discharge steps (80% in this case) and the polarization measured by the averaged difference of the voltages during charge and discharge. The cell voltage plot in Fig. 7.2 also shows that the state-of-charge consumed during the discharge process falls short to complete the loop, indicating coulombic inefficiency due to crossover.

The pore-scale reaction current density is positive during the oxidation process and negative during reduction. While charging the RFB, the redox couple in the HPE undergo oxidation generating $O1^{z_{O1}}$ while the redox couple in the LPE undergo reduction generating $R2^{z_{R2}}$. The Oxidation reaction in the HPE is reflected by positive values of $i_{n,primary}(x,y,t)$ in the HPE and reduction reaction in the LPE are associated with negative values of $i_{n,primary}(x,y,t)$ in the LPE as shown in panel A1 of Fig. 7.2. Since a large flow rate is chosen, the reaction currents are well distributed within the electrode volume, effectively using the available surface area for conducting the reactions. This observation of uniform reaction distribution within the electrodes at high flow rates is consistent with the our previous findings[6] and operating the RFB at lower flow rates will bias the reactions near the inlets increasing polarization losses. Similarly, during the discharge process (Fig. 7.2, B1), the primary reaction currents are negative (reduction) in the HPE and positive (oxidation) in the LPE. The primary reaction current distribution $i_{n,primary}(x,y,t)$ shown at points A and B is representative of entire charge/discharge step.

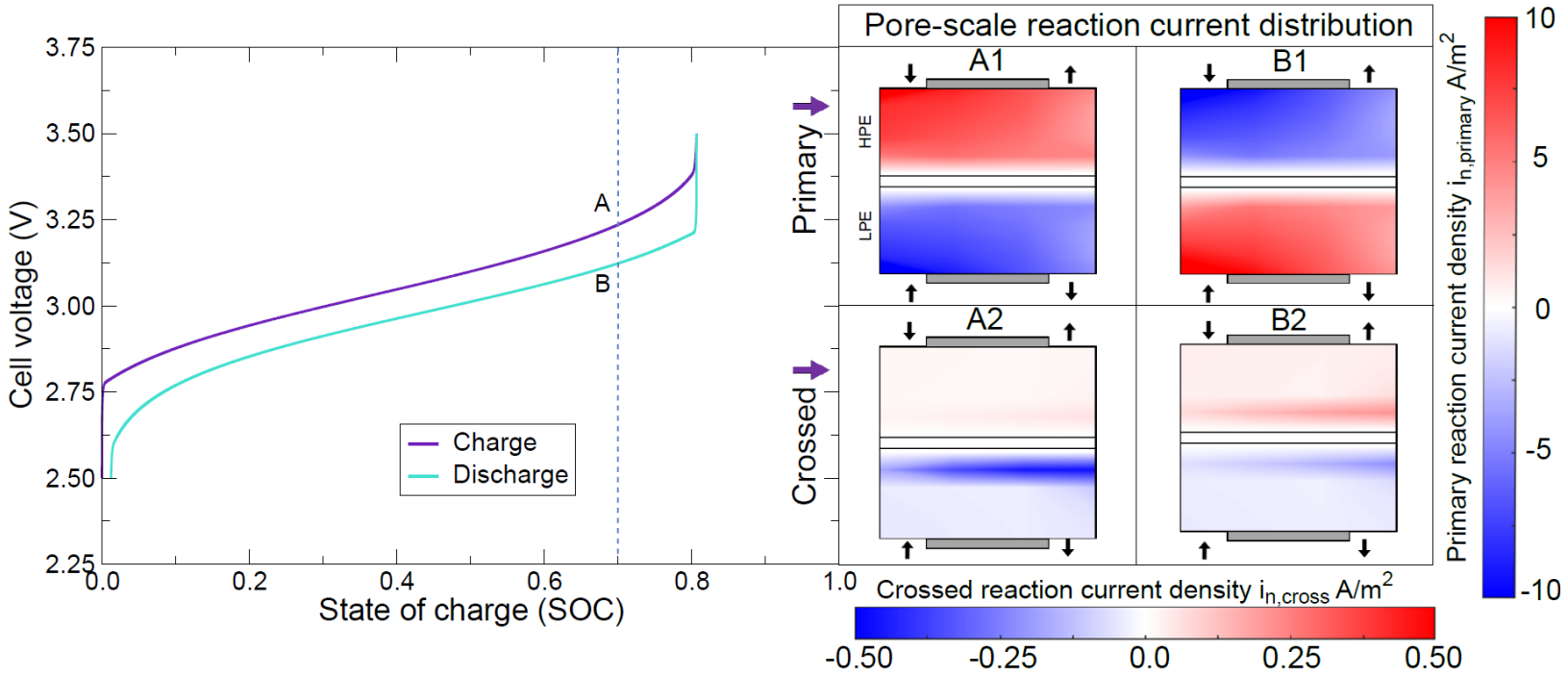

Figure 7.2: Cell voltage variation with state-of-charge during the galvanostatic charge and discharge process of a representative RFB with salt concentration of 0.5 M ($\gamma = 1$) and redox-active species diffusion coefficient $of\ 7.9 \times 10^{-12} m^2/s$ ($\zeta = 63$). Snapshots of primary and crossed reaction current density are shown at points A and B along with flow direction indicated by the black arrows (geometry not drawn to scale).

The crossed reaction current density $i_{n,cross}(x,y,t)$ is affected by local overpotential and the availability of redox active species in the counter electrode (degree of crossover). As explained above, the redox couple $R1^{z_{R1}}/O1^{z_{O1}}$, which is primary to the HPE, undergoes reduction upon crossing over to the LPE. Therefore when $R1^{z_{R1}}$ crosses over, it accumulates in the LPE without undergoing any redox reaction. On the contrary when $O1^{z_{O1}}$ crosses over into the LPE, it undergoes fast reduction to $R1^{z_{R1}}$ due to large negative overpotentials irrespective of the RFB's state-of-charge. The degree of crossover of each species, characterized by its diffusion and migration rates, varies significantly with state-of-charge. The HPE is rich in the oxidized species $O1^{z_{O1}}$ during the end of charging or early in the discharge process, favoring diffusion of $O1^{z_{O1}}$ from the HPE to the LPE which immediately is reduced to $R1^{z_{R1}}$ in the LPE. Therefore, as shown in Fig. 7.2 panels A2 and B2, $i_{n,cross}(x,y,t)$ of the crossed couple $R1^{z_{R1}}/O1^{z_{O1}}$ in the LPE becomes negative (reduction) and dominant near the separator region. At the same instant in the charge/discharge cycle, the LPE electrode is plentiful in $R2^{z_{R2}}$ concentration, which, upon crossing over to the HPE, undergoes oxidation to $O2^{z_{O2}}$. Thus, $i_{n,cross}(x,y,t)$ in both electrodes is significant in magnitude only during the second half of the charging process and during the first half of discharging process. Crossover magnitudes are relatively small otherwise, a mechanistic explanation of which is given later by comparing diffusion and migration contributions. Also, note that the values of $i_{n,cross}(x,y,t)$ are at least an order of magnitude lower than $i_{n,primary}(x,y,t)$ and the sign of $i_{n,cross}(x,y,t)$ is maintained consistently in the HPE and in the LPE (i.e., oxidation and reduction respectively) regardless of the charge/discharge cycling phase of the RFB.

To qualitatively estimate the distribution of the crossed reaction current density $i_{n,cross}(x,y,t)$, the kinetically limited current $I_{kinetic}^{\lim}$in the electrode is compared to the species ionic crossover current passing through the separator $I_{crossover}$. At high overpotentials ($|\eta| \gg k_B T/e$) MHC theory predicts a limiting kinetic rate constant:

$$k_{ox/red}^{lim} = 4k_0/erfc\left(\frac{\lambda^* - \sqrt{1+\sqrt{\lambda^*}}}{2\sqrt{\lambda^*}}\right)$$

For the present simulations we estimate $I_{kinetic}^{\lim}/I_{crossover} \sim 10^4$, implying that active species should react instaneously once they have crossed through the separtor. This expectation is confirmed by our simulations where reaction hotspots are observed adjacent to the separator, as shown in panels A2 and B2 of Fig. 7.2.

Diffusion and migration mechanisms govern the crossover process. The relative contribution of these two processes towards crossover varies significantly with the charge number, the diffusion coefficient, and the transient concentration fields of all the redox active and salt species involved. Although zero-dimensional, time-independent heuristic models haven been proposed to quantify the degree and effects of crossover[1,7], a more comprehensive picture is needed to design RFBs and to engineer their electrolytes. Using the 2D transient model presented here, we track the time varying diffusion and migration rates of selected redox species, and we further elucidate the findings about crossed reaction current density in Fig. 7.2. The variation of the concentration of $O1^{z_{O1}}$ in the HPE electrode is shown for a single charge/discharge cycle in Fig. 7.3(a) along with cell voltage. The diffusion and migration crossover fluxes are shown in Fig. 7.3(b) in terms of

crossover current fraction along with thumbnails indicating the direction of crossover during charge/discharge. The crossover current fraction is defined as the ratio of the ionic current due to a particular species passing through the separator and the total applied galvanostatic current at the current collector. The crossover current fraction is positive when species crossover from HPE to LPE and is negative otherwise. The ionic current of $O1^{z_{O1}}$ is calculated by multiplying each component of the molar flux (Eq. 7) through the porous separator with the oxidation state of $O1^{z_{O1}}$ (here $z_{O1} = +3$). During the charging process the concentration of $O1^{z_{O1}}$increases in the HPE along with the solution potential and cell voltage. Therefore, during the charging process, the gradient of $O1^{z_{O1}}$concentration and solution potential across the separator continuously increases, leading to increased diffusion and migration fluxes with time. The migration fluxes have a squared dependence on the oxidation state of the species involved. As can be seen from Fig. 7.3(b), migration dominates diffusive crossover fluxes for a high oxidation state redox molecule ($z_{O1} = +3$) during the charging process. During the discharge process, the polarity of electrolyte potential difference across the separator reverses, and the electric field induced migration is thereafter directed from the LPE to the HPE, opposing the direction of diffusive fluxes. Therefore, the net crossover of $O1^{z_{O1}}$ is insignificant and is reflected by the decreasing magnitude of the crossed reaction current density during discharge in the LPE (compare LPE in panels A2 and B2 Fig. 7.2). On the contrary, the crossover of the redox molecule $R2^{z_{R2}}$ ($z_{R2} = +1$) from the LPE to the HPE is sizable during the discharge process. Figure 7.3(c) shows the variation of $R2^{z_{R2}}$ concentration in the LPE, and Fig. 7.3(d) shows the transient variation of the crossover flux components. During the charge process, the diffusive and migration fluxes oppose each other, resulting

in net crossover that is practically insignificant. With the change in polarization of electrolyte potential during discharge, the diffusion and migration mechanisms ensure a net crossover of $R2^{z_{R2}}$ from the LPE to the HPE. Therefore, we observe small crossed reaction current density in the HPE during charge (Fig. 7.2, panel A2), and it is more significant during discharge (Fig. 7.2, panel B2). In summary, the redox species with the largest charge number in the high potential electrode experiences the maximum degree of crossover, and this process is dominated by migration. Therefore, it is crucial to engineer such high oxidation state redox active molecules to have low diffusion coefficients.

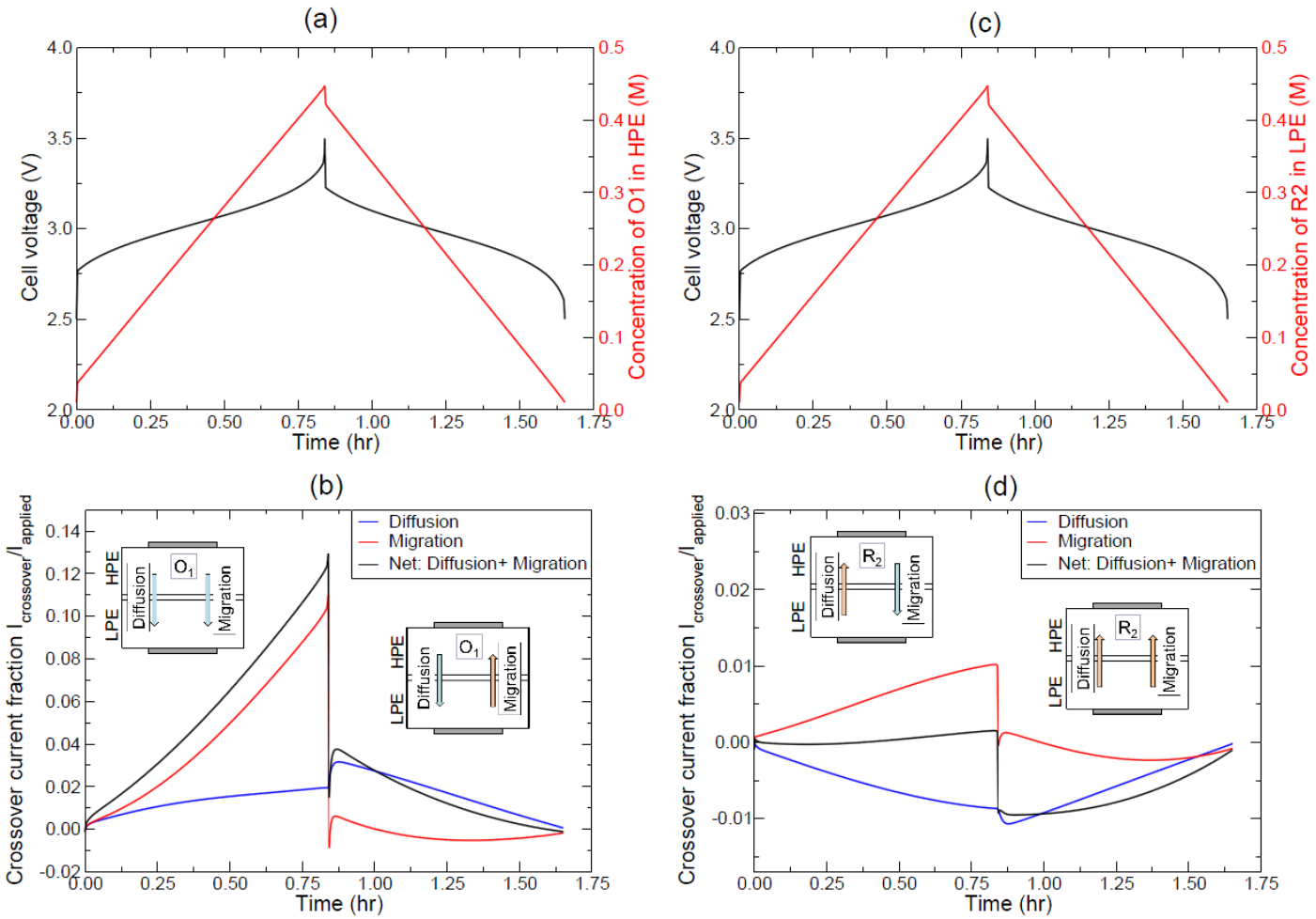

Figure 7.3: (a) Variation of the concentration of $O1^{z_{O1}}$ in the HPE with time, overlapped with cell voltage during galvanostatic cycling. (b) Diffusive and migration components of the crossover fluxes of $O1^{z_{O1}}$ expressed as fractions of current contributions crossing the separator with respect to the applied current. (c) Variation of concentration of $R2^{z_{R2}}$ in the LPE during cycling, along with cell voltage. (d) Diffusive and migration components of crossover flux for $R2^{z_{R2}}$.

7.3 Effects of Supporting Electrolyte and Diffusion Coefficient

In this section we analyze the effects of salt concentration and redox active species diffusion coefficient on rocking-chair (RC) and salt-splitting (SS) RFB configurations. Discharge capacity utilization and capacity fade for ten charge/discharge cycles are the metrics used here to characterize the performance and cycle life of RFBs. The SS configuration requires a threshold salt concentration for conduction through the separator to maintain charge neutrality in either electrode. In SS configuration, every mole of active species undergoing redox reactions requires at least half mole of salt (which splits into two ions) to maintain charge neutrality. The RC configuration has no such restrictions and therefore could be a potential solution in designing salt free RFBs[2]. Here we show that although the RC configuration allows operating RFBs at low salt concentration levels, the capacity utilization at such extremes is very low and is impractical. Both RC and SS configurations require a certain minimum amount of salt to minimize electric field and thereby obtain sufficient discharge utilization. In both these configurations the performance of RFBs is mapped using two non-dimensional variables: (1) the molar-salt ratio defined as the ratio of salt concentration to redox-active species concentration in electrolyte ($\gamma = c_{salt}/c_{redox}$) and (2) the salt-diffusion ratio which is the ratio of the diffusion coefficient of salt ions to redox active species ($\zeta = D_{salt}/D_{redox}$). The concentration of redox active molecules is fixed to $c_{redox} = 0.5M$. Larger values of γ means that more salt is dissolved in the electrolyte. In addition, the diffusion coefficient of salt ions is set to be representative of fluoride salt derivatives $D_{salt} = 5{\times}10^{-10} m^2/s$ and D_{redox} is varied to parameterize redox active molecule design. A fast diffusing redox active molecule (small value of ζ) has diffusion coefficient comparable to that of salt ions

and therefore has more crossover. The variation of ionic conductivity in the 2D design space of concentration (γ) and diffusion coefficient (ζ) is given by the Nernst-Einstein equation $\kappa^0 = \sum z_i^2 c_i D_i F^2/RT$ with contributions coming from the four redox-active species and the two salt ions. Electrolytes with large γ and low ζ are most conductive and possess lowest ohmic polarization. Despite this advantage such electrolytes necessarily experience high crossover rates. On the other hand designing redox molecules with high ζ can reduce crossover, but ohmic polarization increases due to decreased ionic conductivity.

A total of forty-two and forty-eight cases spanning the 2D design space of $\gamma: 0 \rightarrow 2$ and $\zeta: 1 \rightarrow 1000$ were simulated for both RC and SS configurations, respectively. A contour map of discharge utilization and capacity fade for RC configuration is shown in Fig. 6. The dashed lines correspond to the difference in discharge capacity of the first and tenth cycle expressed as a percentage of theoretical capacity. We observe that although salt free RFBs ($\gamma \rightarrow 0$) are attractive for the development of economical RFBs, their capacity utilization is as low as 20%. This low discharge capacity utilization at small salt concentrations is not due to a lack of redox active supply to the reactor but is a result of the deficiency of positive salt ions in the HPE during charging. The concentration and potential gradient across the separator drives the movement of salt ions from one electrode to another. To maintain the balance of charge at finite applied current density, the transport of both positive and negative salt ions across the separator is needed. When there is deficiency of one of the ions, the solution phase potential difference across separator increases to force the migration transport of the available salt ions to ensure

electroneutrality in both electrodes. In other words, the cell voltage increases to cause enough solution potential gradient across the separator for the negative salt ions to migrate from the LPE to the HPE and subsequently to balance out the applied current in the absence of positive salt ions. Therefore, the cutoff voltage limits are prematurely reached. Note that the limiting mechanism in such low salt operating regimes is the availability of both positive and negative ions for conduction across the separator and is not necessarily a result of the bulk ionic conductivity of either electrolyte. The predictions of discharge utilization capacity for low salt RFBs with the RC configuration is about 20-30% from Fig. 7.4. This is consistent with experimental findings of proof-of-concept salt free RFB by Milhstein et al[8]. Figure 7.4 shows that the salt concentration should be more than 60% of the redox active concentration to obtain at least 80% discharge utilization. Although high diffusion coefficients for redox active molecules may be attractive from the perspective of ionic conductivity, the capacity fade due to crossover will be enormous. The diffusion coefficient must be three orders of magnitude smaller than the salt diffusion coefficient to obtain a capacity retention of 95% for 10 cycles. For values of $\gamma > 1$, capacity fade becomes independent of salt concentration. We identify this region as the excess supporting electrolyte domain commonly used in dilute solution theories[9].

Figure 7.4

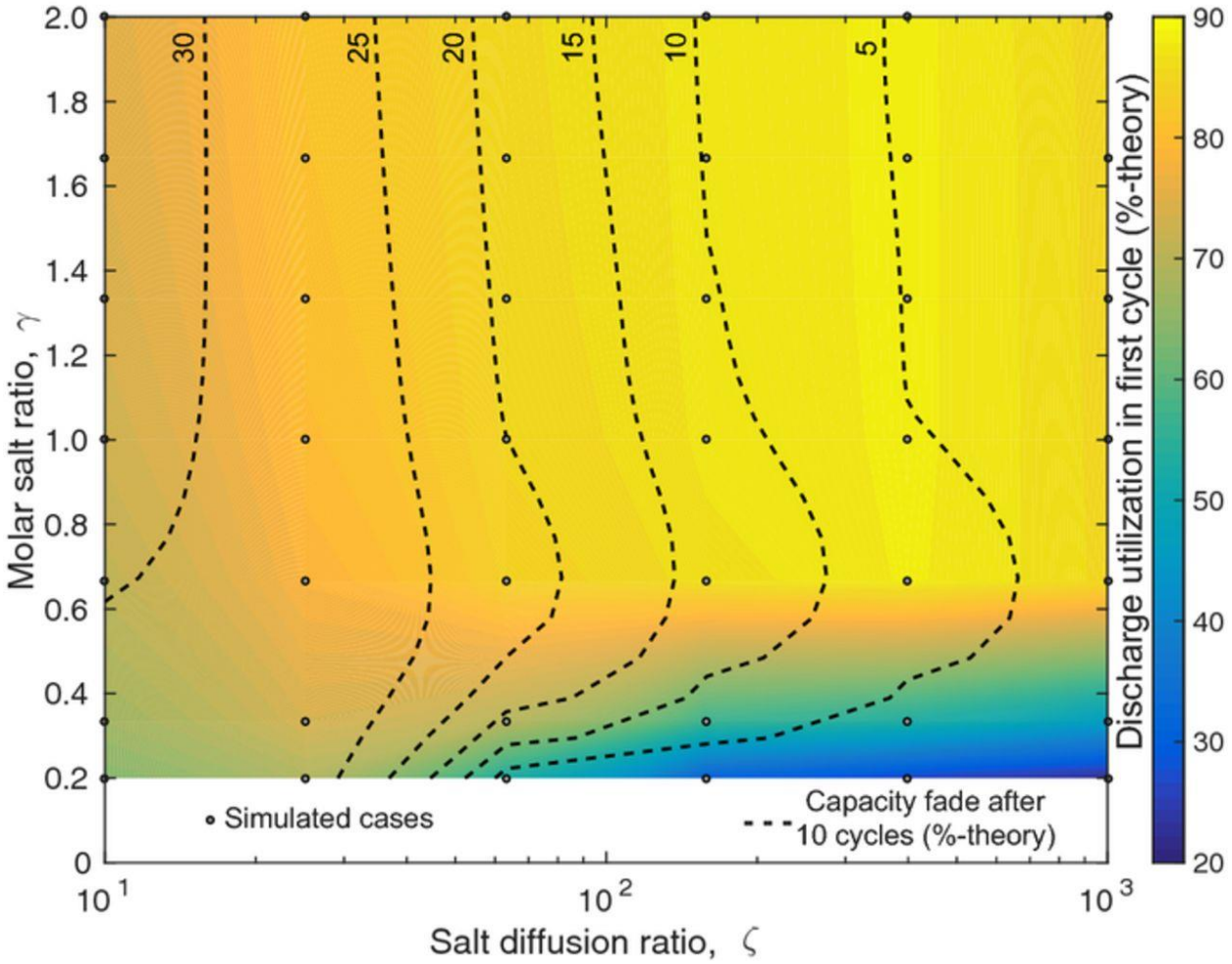

Figure 7.4: Contour map of discharge utilization during the first cycle along with capacity fade after ten cycles (% theoretical) for the rocking-chair (RC) configuration as a function of dimensionless molar salt ratio γ and salt diffusion ratio ζ. The forty-two dots on the plot show the simulation cases interpolated to populate the figure.

The SS configuration theoretically requires the salt concentration to be greater than half of the redox active concentration[2] ($\gamma \geq 0.5$). However, such theoretical analysis assumes that the utilization capacity is 100%, i.e., for every mole of redox actives undergoing reaction, half a mole of salt is needed to preserve charge neutrality by splitting

into two ions. If the capacity utilization is less than 100%, the SS configured RFB can be operated with $\gamma < 0.5$. Also, the presence of salt is essential to ensure sufficient ionic conductivity, as some of the redox species in the SS RFB are neutral. Figure 7.5 shows the performance of SS configured RFBs as a function of molar salt ratio γ and salt diffusion ratio ζ. An appreciable discharge utilization of 80% can be achieved when $\gamma > 0.5$. Also, capacity fade rate becomes independent of concentration for $\gamma > 0.6$, consistent with excess supporting electrolyte behavior. Compared with the RC configuration (Fig. 7.4), the SS configuration (Fig. 7.5) has better capacity retention. The use of smaller charge number redox materials in the SS configuration decreases migration crossover fluxes benefitting capacity retention. Contrary to the hypothesis that RC configuration could be the potential pathway for developing low salt RFBs, Figs. 7.4 and 7.5 show that the SS configuration has similar performance to the RC configuration. Both configurations require minimum salt concentration levels ($\gamma > 0.5$) for profitable capacity utilization and the SS configuration has an advantage over RC in capacity retention by smaller migration crossover fluxes. Also, the SS configuration achieves the excess electrolyte regime sooner than the RC configuration, reducing its sensitivity of performance to the changes in salt concentration. That said, the results and conclusions presented thus far are for RFBs using a porous non-selective membrane/separator. Crossover and transport mechanisms will change with the use of ion selective membranes.

Figure 7.5

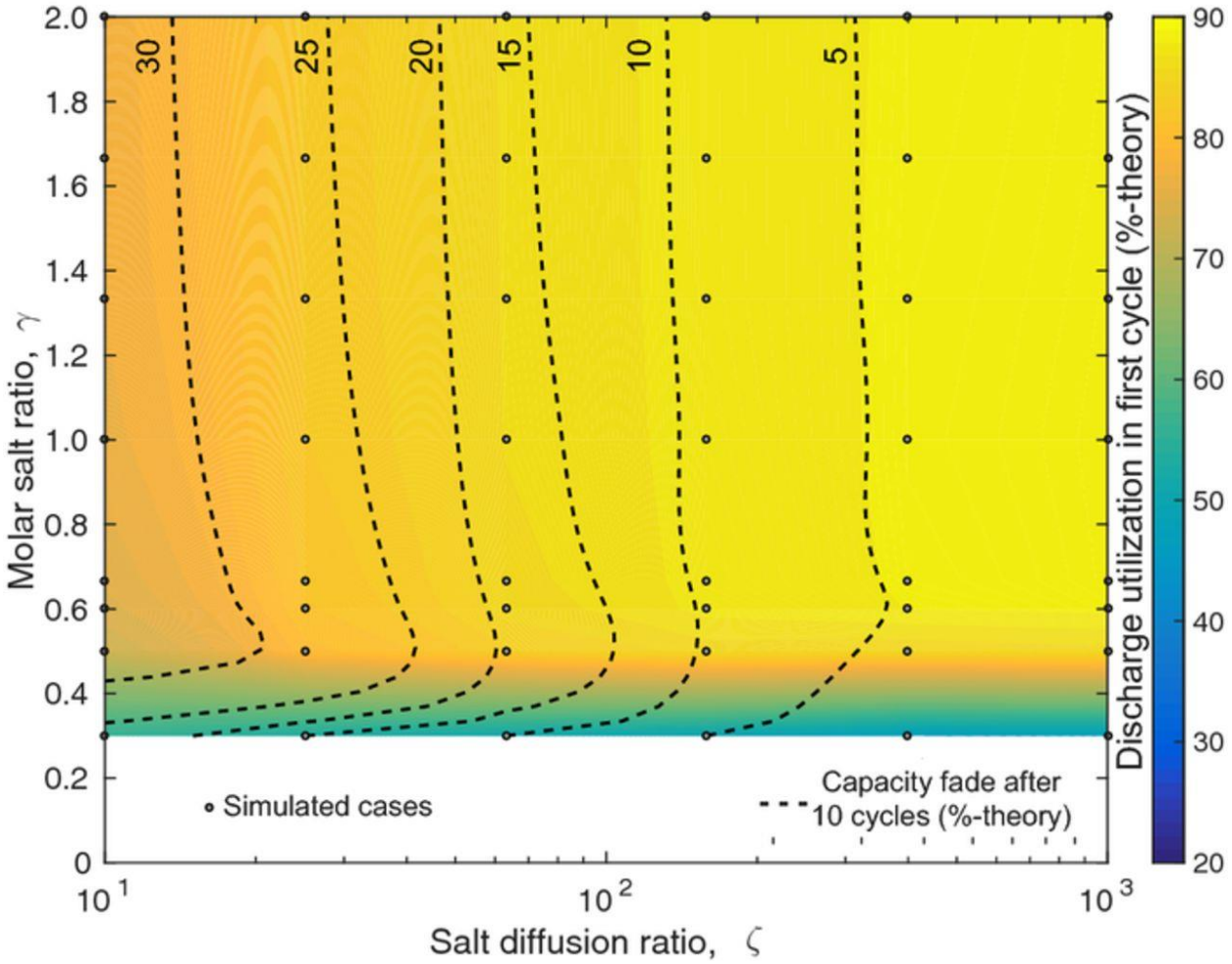

Figure 7.5: Contour map of discharge capacity utilization during the first cycle, along with capacity fade after ten cycles (% theoretical) for salt-splitting (SS) configuration as a function of the dimensionless molar salt ratio γ and the salt diffusion ratio ζ. The forty-eight dots on the plot show the simulation cases interpolated to populate the figure.

7.4 Non-dimensional Analysis using Damköhler Numbers

The results presented thus far are for a single value of applied current density and for a certain redox species concentration. To extend the scope of application of the present simulations to an RFB with generic materials, design, and operating conditions, we now introduce Damköhler numbers for redox species Da_{redox} and salt ions Da_{salt}. Here, the Damköhler number of a particular species quantifies the characteristic magnitude of the net reaction rate relative to the rate of species transport across the separator. For a redox reaction where n_e electrons are transferred for every s_i formula units of redox active species i, the Damköhler number is $Da_i = i_{app}H/\left(FD_{sep,i}^{eff}n_e c_i/s_i\right)$. The rate of capacity fade due to crossover is expected to scale with the transport rate of redox active species across the separator relative to the transport rate of salt ions. This ratio of rates can be estimated by the ratio of salt and redox-active species Damköhler numbers multiplied by the charge number of the particular redox-active species, i.e., $z_i Da_{salt}/Da_{redox,i}$. This non-dimensional quantity can also be expressed in terms of molar salt ratio and salt-to-redox diffusion ratio as $z_i Da_{salt}/Da_{redox,i} = z_i c_{redox} D_{sep,redox}^{eff}/2c_{salt}D_{sep,salt}^{eff} = z_i/2\gamma\zeta$. Thus, the dimensionless number $z_i Da_{salt}/Da_{redox,i}$ is independent of applied current density. Figure 8 (a) maps the variation of discharge capacity utilization in the first cycle and of capacity fade after the first ten cycles using $\bar{z}Da_{salt}/Da_{redox}$ and Da_{redox}. Here, $\bar{z}$ is the arithmetic average charge number among all redox species involved with $\bar{z} = 2$ for the present RC RFB simulations. On this 2D design space of $\bar{z}Da_{salt}/Da_{redox}$and Da_{redox} three regimes are labeled: (1) redox-shuttle limited, (2) ohmic polarization dominated, and (3) sufficient supporting electrolyte. In the redox shuttle limit regime, the transport rate of redox molecules is comparable to that of salt and therefore the redox molecules shuttle between the two electrodes constantly, leading to poor capacity retention. In the ohmic

polarized regime polarization ($Da_{salt} > 5$) limits capacity utilization due to its low concentration of supporting electrolyte. The most favorable regime for the efficient and long-term operation of RFBs with non-selective separators is the sufficient supporting electrolyte region, where discharge capacity utilization exceeds 80%. To achieve such conditions requires that $\bar{z}Da_{salt}/Da_{redox} < 10^{-1}$ and $Da_{salt} < 5$, such that neither redox shuttling nor ohmic polarization limits cycling. From Figure 7.6(a), operating RFBs in the sufficient supporting electrolyte region and at large values of Da_{redox} will yield greatest capacity retention. Da_{redox} can be increased either by increasing applied current density or by engineering redox species to have low diffusion coefficients.

Figure 7.6

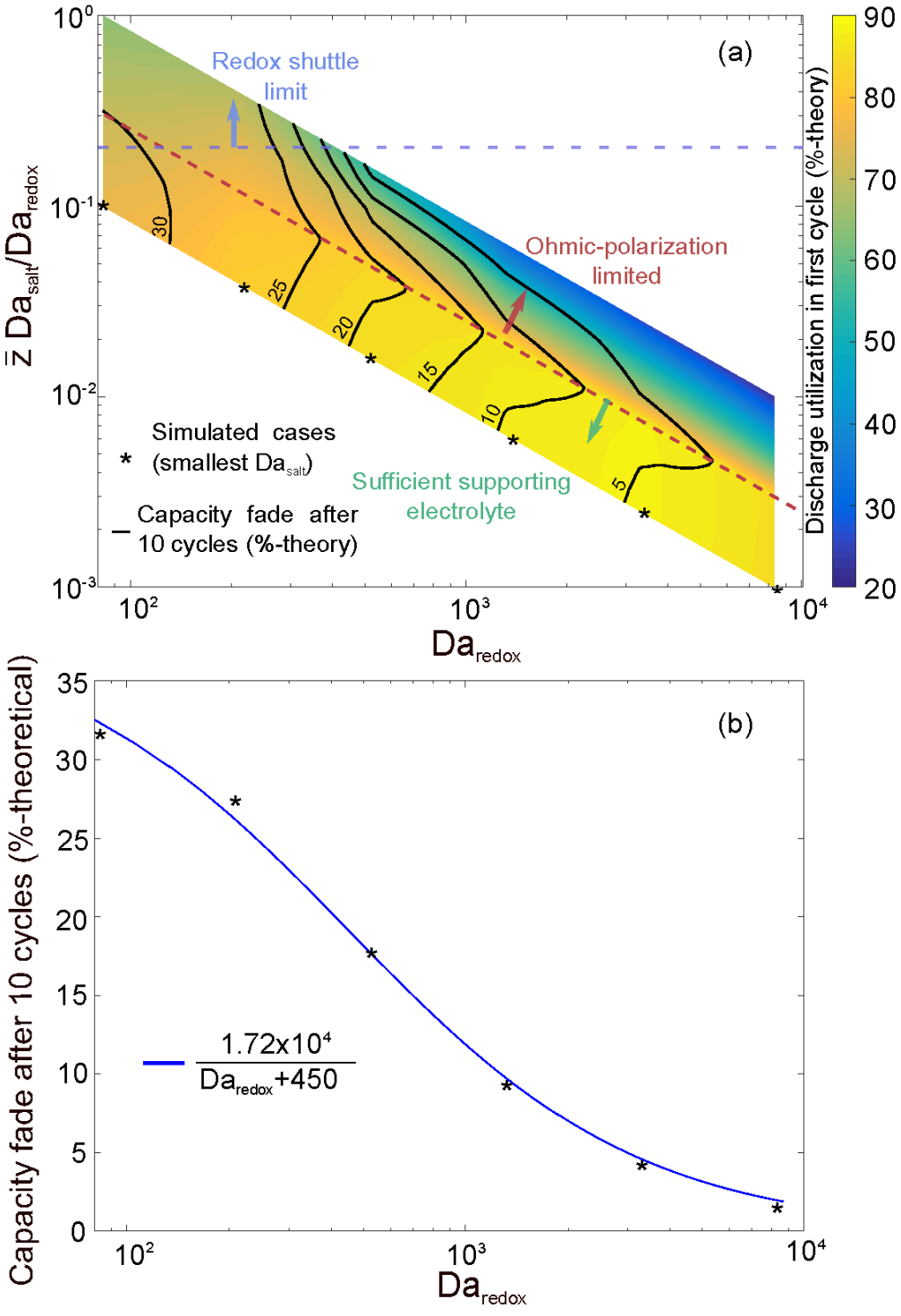
(a)
Redox shuttle limit
Ohmic-polarization limited
Sufficient supporting electrolyte
Simulated cases (smallest Da_salt)
Capacity fade after 10 cycles (%-theory)
30
25
20
15
10
5
Discharge utilization in first cycle (%-theory)
90
80
70
60
50
40
30
20
z̄ Da_salt/Da_redox
Da_redox
(b)
Capacity fade after 10 cycles (%-theoretical)
1.72x10^4 / (Da_redox+450)
Da_redox

Figure 7.6 (cont.)

Figure 7.6: (a) Contour map of discharge capacity utilization at the first cycle, along with capacity fade after ten cycles (%-theoretical) for RC configuration as a function of the dimensionless numbers $\bar{z}Da_{salt}/Da_{redox}$ and Da_{redox}. (b) Variation of capacity fade after ten cycles (%-theoretical) with the Damköhler number of redox active species Da_{redox} in sufficient supporting electrolyte regime. The simulated data points are correlated using a least-squares fit.

In the sufficient supporting electrolyte regime, the ratio $\frac{\bar{z}Da_{salt}}{Da_{redox}}$ translates to a monotonic function of the transference number of redox active species t_i, given as $\frac{\bar{z}Da_{salt}}{Da_{redox}} = \frac{t_i}{1-t_i}$. In the context of the molecular engineering of RFB electrolytes low transference number is cruicial to maintain high capacity utilization over many cycles. In the sufficient supporting electrolyte region capacity fade is weakly dependent on Da_{salt} and thus depends primarily on Da_{redox}. We use the six simulated data points in the sufficient supporting electrolyte regime that have smallest Da_{salt} (marked by '*' in Fig. 7.6(a)) to correlate the variation of capacity fade with the Damköhler number of redox species Da_{redox}, as shown in Fig. 7.6(b). The capacity fade decreases with increasing Da_{redox} as $\Delta\chi_{10}(\%) = 1.72\times10^4/(Da_{redox} + 450)$ with a coefficient of determination value R^2 of 0.9965. For very large values of Da_{redox}, this expression takes the form of a power law dependence where $\Delta\chi \propto Da_{redox}^{-1}$. This expression can be used in the engineering of redox active molecules and to determine operating conditions for a given RFB electrolyte that are necessary to achieve a target capacity retention level. For example, Da_{redox} must be greater than 1.7×10^5 to obtain a capacity retention of 99.9%

after ten cycles. Comparing Figs. 7.4 and 7.5, the capacity utilization and capacity fade for RC and SS configurations are qualitatively and quantitatively similar. Therefore, the non-dimensional analysis presented through Fig. 7.6 holds true for both RC and SS configurations.

7.5 Corrections

We duly note that the results presented eariler in the chapter (and the original publication: *J. Electrochem. Soc. 2018 volume 165, issue 13, A3144-A3155*) have a minor discrepancy in implementing the Marcus-Hush-Chidsey (MHC) model. The rate constants $k_{ox/red}^{MHC}(\eta)$ defined previously are defined based on overpotential $\eta = \phi_s - \phi_e - \phi_{eq}$. However, upon reconsidering the original definitions based on Refs.[10,11], the overpotential that quantifies the $k_{ox/red}^{MHC}$ is defined at 50% state-of-charge. Such definition satisfies the de Donder relation for chemical equilibrium. The corrected definition η^0 which defines $k_{ox/red}^{MHC}(\eta^0)$ is $\eta^0 = \phi_s - \phi_e - \phi_{eq,50\%}$.

The correction in our implementation of MHC kinetics only effects the shape of the voltage curves pinned midway of the charge/discharge cyle without significantly affecting the charge/ discharge time. In the supporting electrolyte regime, the reaction current density distribution within the electrodes is similar qualitatively and quantitatively (see Fig. 7.7 compared against Fig. 7.2). We re-simulated the cases presented in 7.4 and 7.6, and find that the difference in capacity fade between the ‘previous’ model and ‘corrected’ model is less than 0.1%. In Fig. 7.8(a) we compare the discharge utilization for the first cycle

between the two models in the supporting electrolyte regime. The corrected model predicts almost similar discharge utilization (less than 0.5% difference) in the first cycle to the model established previously. The capacity fade for ten cycles between the two models is compared in Fig 7.8(b) in the supporting electrolyte regime (replicating Fig. 7.6(b)). The correlation between capacity fade in ten cycles $\Delta\chi_{10}(\%)$ and Da_{redox} $\Delta\chi_{10}(\%) = 1.72\times10^{4}/(Da_{redox} + 450)$ established in section 7.4 still holds true for the corrected model based on Fig. 7.8(b). The similarity in the first cycle discharge utilization between 'previous' and 'corrected' model also holds true for low salt concentration. We re-simulated RFBs with $\gamma = 0.2$ using the corrected model and compare the discharge utilization in Fig. 7.9 with the previous results ($\gamma = 0.2$ from Fig. 7.4). The difference between the two models is less than 2%. The above tests and the results of the corrected implementation presented in Figs. 7.7-9 gives confidence that the conclusions presented in the previous sections of this chapter are valid after correcting the MHC kinetic model implementation.

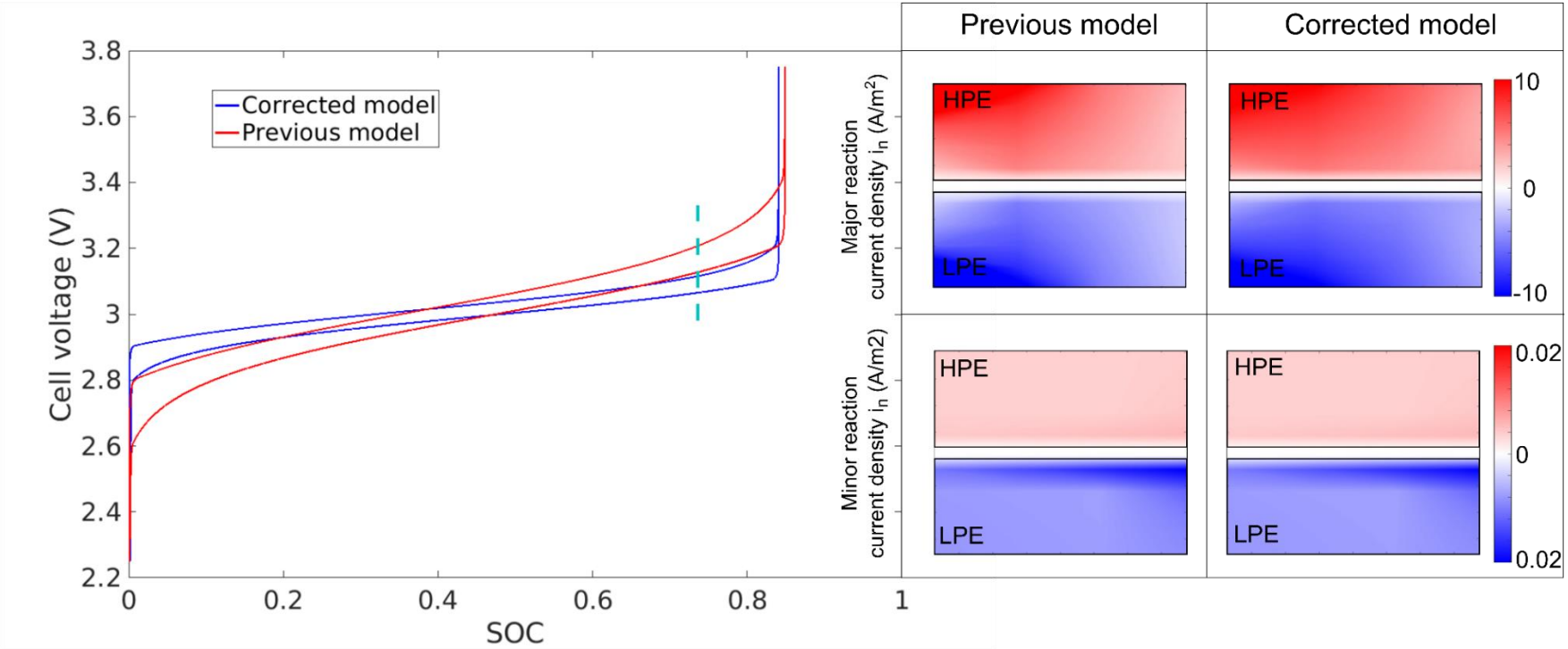

Figure 7.7: Comparing the cell voltage variation with state-of-charge during the galvanostatic charge and discharge process of a representative RFB with salt concentration of 1 M ($\gamma = 2$) and $\zeta = 63$ between the 'previous' and 'corrected' model. Snapshots of primary and crossed reaction current density are shown at the vertical dashed line for both the models (geometry not drawn to scale).

Figure 7.8

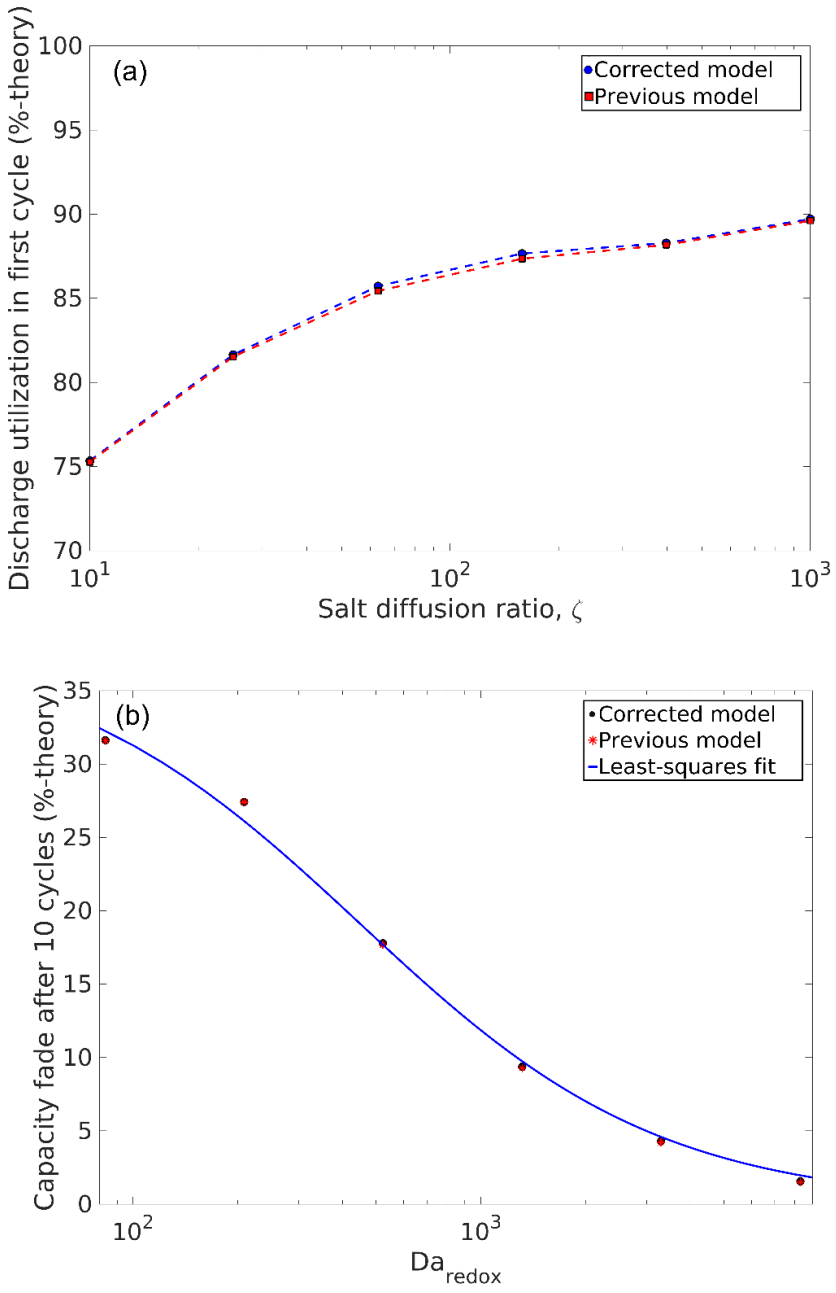

Figure 7.8: Comparing the variation of (a) discharge utilization in the first cycle with ζ and (b) capacity fade after ten cycles with Da_{redox} between the corrected model and the previous model in the supporting electrolyte regime.

Figure 7.9

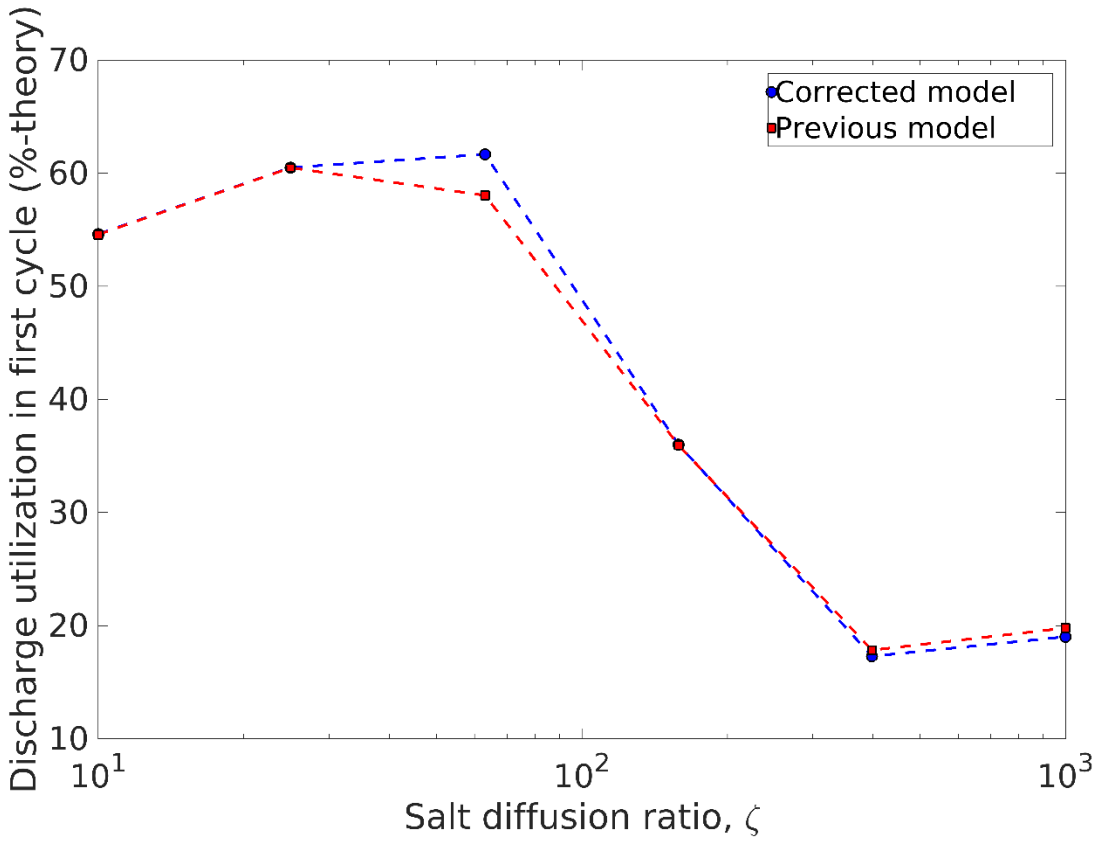

Figure 7.9: Comparing the variation of first cycle discharge utilization with ζ between the 'corrected' model and the 'previous' model in low supporting electrolyte regime $\gamma = 0.2$.

7.5 References

1. Darling, R., Gallagher, K., Xie, W., Su, L. & Brushett, F. Transport Property Requirements for Flow Battery Separators. *J. Electrochem. Soc.* **163**, A5029–A5040 (2016).
2. Dmello, R., Milshtein, J. D., Brushett, F. R. & Smith, K. C. Cost-driven materials selection criteria for redox flow battery electrolytes. *Journal of Power Sources* **330**, 261–272 (2016).

3. Hayamizu, K. Temperature Dependence of Self-Diffusion Coefficients of Ions and Solvents in Ethylene Carbonate, Propylene Carbonate, and Diethyl Carbonate Single Solutions and Ethylene Carbonate + Diethyl Carbonate Binary Solutions of LiPF6 Studied by NMR. *J. Chem. Eng. Data* **57**, 2012–2017 (2012).
4. Brushett, F. R., Vaughey, J. T. & Jansen, A. N. An All-Organic Non-aqueous Lithium-Ion Redox Flow Battery. *Adv. Energy Mater.* **2**, 1390–1396 (2012).
5. Nagarjuna, G. *et al.* Impact of Redox-Active Polymer Molecular Weight on the Electrochemical Properties and Transport Across Porous Separators in Nonaqueous Solvents. *J. Am. Chem. Soc.* **136**, 16309–16316 (2014).
6. Nemani, V. P. & Smith, K. C. Uncovering the role of flow rate in redox-active polymer flow batteries: simulation of reaction distributions with simultaneous mixing in tanks. *Electrochimica Acta* **247**, 475–485 (2017).
7. Darling, R. M., Weber, A. Z., Tucker, M. C. & Perry, M. L. The influence of electric field on crossover in redox-flow batteries. *Journal of the Electrochemical Society* **163**, A5014–A5022 (2016).
8. Milshtein, J. D., Fisher, S. L., Breault, T. M., Thompson, L. T. & Brushett, F. R. Feasibility of a Supporting-Salt-Free Nonaqueous Redox Flow Battery Utilizing Ionic Active Materials. *ChemSusChem* **10**, 2080–2088 (2017).
9. John Newman & Karen E. Thomas-Alyea. *Electrochemical Systems*. (1991).
10. Henstridge, M. C., Laborda, E., Rees, N. V. & Compton, R. G. Marcus–Hush–Chidsey theory of electron transfer applied to voltammetry: A review. *Electrochimica Acta* **84**, 12–20 (2012).
11. Zeng, Y., Smith, R. B., Bai, P. & Bazant, M. Z. Simple formula for Marcus–Hush–Chidsey kinetics. *Journal of Electroanalytical Chemistry* **735**, 77–83 (2014).

CHAPTER 8: Exergy Destruction Quantification and Assignment of Energy Loss to the Various Polarization Mechanisms in Redox Flow Batteries

The design of the reactor along with the redox chemistry employed largely affects the power density of the RFB system whereas the amount of redox active species dissolved in the electrolyte affects the net energy capacity[1–3]. Every component of the RFB contributes to polarization losses affecting the power density of the RFBs[4] and are primarily categorized into three categories based on the cause of polarization[5]: (1) ohmic (2) kinetic and (3) mass transport. The electrical conductivity of the electrode material, the effective transport properties of the species in the electrolyte through the porous electrode and membrane, and the contact resistance between components contribute to ohmic polarization[6]. The effect of ohmic polarization can be reduced by appropriate material selection[7–10], surface modification[8], compressing the electrodes[7,11] and improving cell engineering[6,12]. Kinetic polarization caused by sluggish reaction mechanisms could also significantly add to cell polarization losses. However, the reaction kinetics are specific to redox chemistry and efforts in this regard lead to the development of several new chemistries for both aqueous RFBs[13–16] and non-aqueous RFBs[17–20]. Polarization due to pore-scale mass transport arises when the rate of the reaction exceeds the supply rate of active species from the bulk of the electrolyte to the reaction sites[21]. Additionally, in our previous work, we found polarization losses arising due to the irreversible thermodynamic mixing processes in the tank[22].

The motivation to determine mass transfer coefficients for solutes in fluids dates back to 1950s where flow through porous packed beds are studied for industrial application such as leaching, drying, ion exchange, and chromatography[23–25]. The

experiments typically involved using soluble spherical particles packed in a column with a gas/ solvent flowing through the packed bed. The film theory of mass transport[26] was commonly used to deduce the mass transport coefficient from the experimental results. Later, Peter and Newman employed the limited current method to determine mass transfer coefficients in packed beds at low Reynolds number[27]. Recent studies in RFB literature use the limited current technique along with a simplified model to deduce a correlation of the Sherwood number with Reynolds number[5,21,28,29]. The simplified models were often derived from the porous electrode theory involve several assumptions such as steady-state, constant bulk concentration of the redox species and have identified mass transport as the dominating polarization mechanism at high current densities. The correlations from these methods, therefore, have an implicit sense of being time-averaged and space-averaged, and not strictly local. Also, to the best of our knowledge, no RFB model using homogenized Nernst-Planck formulation for species transport considers the effect of hydrodynamic dispersion. Dispersive transport occurs due to the chaotic nature of pore-level velocity fields arising as a result of the morphology of the porous medium[30,31]. The dispersive coefficients along the flow direction (longitudinal) and transverse to the flow direction scale with local Peclet number and are strongly dependent on the electrode morphology[32]. One other problem is that the bulk concentration in a porous medium is defined as a volume-averaged concentration, unlike in free-stream flows. More recent efforts were aimed at micro-scale simulations using Lattice Boltzmann's methods to determine local Sherwood numbers[33,34]. In addition to the mass transfer, limited polarization at high currents, the use of selective ion-exchange membranes (IEMs) in electrodialysis is shown to have significant polarization arising from

the local concentration gradients especially at high current densities[35–37]. In this chapter, we attempt to quantify concentration polarization losses in an RFB in terms of local chemical exergy destruction caused by species transport through an electrochemical potential gradient within the electrodes and the IEM.

In this chapter, we present a multi-species RFB model which uses IEM. The work we present here is an effort to unify and comprehensively understand the polarization mechanisms and exergy destruction losses in an RFB by mapping the RFB performance on a non-dimensional space. The non-dimensional nature of the results allows the conclusions of this work relevant to various RFB chemistries subjected to different design and operating conditions for RFBs. We incorporate Marcus-Hush-Chidsey kinetics[38–41] instead of the standard Butler-Volmer kinetic model. We use the dilute solution theory to model species transport using the Poisson-Nernst-Planck equation where the flux of each species is governed by advection, diffusion, dispersion, and migration. Using this model, we seek to explain the cell polarization variation through two characteristic non-dimensional numbers: (1) Pore-scale Damköhler number Da_p (a measure of pore-scale mass transfer), and (2) Salt Damköhler number, Da_s (a measure of salt transport affecting concentration polarization). The applied current density and fiber diameter are systematically varied to map capacity utilization and polarization against Da_p and Da_s. We observe that Da_p strongly influences capacity utilization whereas, both, Da_p and Da_s strongly governs cell polarization, indicating that concentration polarization effects that arise by using an IEM cannot be neglected in cell level modeling. We also compare the

results using two different flow field architectures (1) parallel flow field (PFF) and (2) interdigitated flow field (IDFF).

A major contribution of this work is to quantify the causes of irreversibilities[42] (or entropy generation) resulting from various physical processes within RFBs. Using the first and second laws of thermodynamics[42] we derive expressions for exergy destruction associated with (1) pore-scale mass transfer, (2) reaction kinetics, (3) irreversible tank mixing, (4) bulk species transport, and (5) electronic conduction. We show that for the multi-species RFB model presented here, the above five processes completely account for the energy inefficiencies during charge/discharge cycles. Such analysis is not limited to RFBs but also applicable to other systems such as electrodialysis, electrochemical desalination, fuel cells, Li-ion batteries, and chemical mixing reactors. We choose to adopt the electrochemical properties of the $Fe^{2+}_{aq}|Fe^{3+}_{aq}$ || $V^{3+}_{aq}|V^{2+}_{aq}$ RFB in acidic medium (HCl) to obtain an RFB with a working voltage of 1.02 V[3,43]. We note that such adoption is done solely to use properties of real materials used in RFBs, however, the model we developed is not restricted to that particular chemistry. The primary redox reactions in the high potential and low potential electrode at 50% state-of-charge (SOC) can be represented as

$$R_1^{2+} \leftrightharpoons O_1^{3+} + e^- \quad E_{HPE,eq} = 0.77V$$

$$O_2^{3+} + e^- \leftrightharpoons R_2^{2+} \quad E_{LPE,eq} = -0.25V$$

Based on a previous characterization study[44], the carbon felt electrodes are chosen to be 90% porous $\epsilon = 0.9$ with an effective electrical conductivity $\sigma_s^{eff} = 370 S/m$. The specific

surface area for unit electrode volume is dependent on the fiber diameter as $a = \frac{4(1-\epsilon)}{d_f}$.[45]

We use an anion exchange membrane (AEM) to enable Donnan exclusion effect to reduce crossover of the positively charged redox species. The properties of AEM have been derived from previous a experimental study on poly(2,6-dimethyl-1,4-phenylene oxide) (PPO) based AEM[46]. The AEM with a porosity of $\epsilon_m = 0.3$ has a fixed charge concentration in the pores as $\epsilon c_f = 2.5M$. The tortuosity of the AEM is set to 5 $\tau_m = 5$. Tables 8.1 lists the reactor design parameters used in our simulations.

Table 8.1: Reactor geometry, carbon felt electrode and separator properties for RFBs with AEMs

Parameter	Value
length of the current collector, L_e (mm)	2
electrode flow entry length, L_{ent} (mm)	0.5
electrode thickness, H_e (μm)	200
porosity of carbon felt electrode, ϵ_e	0.9
solid volume fraction of carbon felt, ν_e	0.1
tortuosity of the electrode, τ_e	1.05*
permeability of electrolyte in carbon felt, $K_e(m^2)$	6×10^{-11}
membrane thickness, H_m (μm)	100‡
porosity of AEM, ϵ_m	0.3#
tortuosity of the membrane, τ_m	5#

*Bruggeman relationship[48] #Ref.[49] ‡Ref. [46]

The properties of all the redox active species are listed in Table 8.2. Previous numerical models on vanadium RFBs use specific area a times the rate constant k as $a.k = 0.35\ s^{-1}$ [50]. Considering that the reaction rate constant for $V_{aq}^{3+}|V_{aq}^{2+}$ can vary significantly by two orders of magnitude[51] and the surface roughness of the electrodes to increase the available area for reaction a, we choose $a.k = 10s^{-1}$ to ensure low reaction kinetic losses (low Wagner number, defined later). For an electrode with nominal diameter $d_f = 10\mu m$ with $\epsilon = 0.9$, gives $k = 2.5\times10^{-4}m/s$. The redox concentration is fixed at $c_{redox}^{0} = 0.2M$. Based on our previous study with non-selective separators[52], we choose to operate the RFB in a sufficient supporting electrolyte regime where the amount of salt (A^+B^-) is significantly larger than the redox active concentration $c_{salt} = 0.5M$. The viscosity of electrolyte, listed in Table 8.2, affects the local Sherwood numbers for pore-scale mass transport.

Table 8.2: System properties used in the simulating RFBs with AEMs

Parameter	Value
electronic conductivity of the electrode, σ_s	370*
Diameter of carbon fibers, $d_f\ (\mu m)$	$5-40$ (varied)
rate constant for the redox reactions, $k_{\eta=0}\ (m/s)$	2.5 x10^{-4} #
equilibrium potential of the redox species at 50%SOC (V), $E_o(V)$	0.77 (HPE) -0.25 (LPE)
Redox species concentration, $c_{redox}^{0}(M)$	0.2
Oxidation states of redox molecules	+2 $\rightarrow$ +3 (HPE and LPE)

Table 8.2 (cont.)

Bulk diffusion coefficient of redox species, $D^b_{redox}\ (m^2/s)$	2.4×10^{-10}‡
Supporting electrolyte concentration, $c^0_{salt}(M)$	0.5
Fixed charge concentration in membrane, $c_{f,membrane}(M)$	8#
Bulk diffusion coefficient of supporting electrolyte ions, $D^b_{salt}\ (m^2/s)$	$9.3\times10^{-9}(H^+)$ $2\times10^{-9}(Cl^-)$**
Viscosity of electrolyte, $\mu\ (Pa.s)$	$8.9\times10^{-4}(water)$

Derived from *Ref[44] #Obtained by equating $a.k$ from Ref [50,51] to our work. Please refer to text for further details ‡For Vanadium V^{2+} Ref [51] ** Ref [53]

8.1 Defining Non-dimensional Numbers

Dimensionless numbers enable the generalization of results expanding the applicability to different RFB chemistries and designs. We first present non-dimensional numbers with respect to the operation of RFBs: electrolyte volume, flow rate, and amount of salt. Following this, we list non-dimensional numbers which characterize causes of polarization: ohmic losses, kinetic losses, pore-scale mass transfer, and concentration polarization.

The non-dimensional numbers representing the operation of RFB:

1. Tank-to-electrode volume ratio: Ratio of electrolyte stored in tanks to electrolyte volume in electrode $\alpha = V_{tank}/V_{electrode}$. We choose $\alpha = 20$ based on a previous study on the effects of mixing in tank[22].
2. Ratio of flow rate to stoichiometric flow rate: $\beta = \dot{V}/\dot{V}_{stoich}$, where the stoichiometric flow rate $\dot{V}_{stoich}$ is defined as the flow rate which completely reduces an incoming 100% SOC to 0%SOC within a single pass through the reactor. For a theoretical charge time of τ_c, $\dot{V}_{stoich}$ can be defined as $\dot{V}_{stoich} = (V_{tank} + V_{electrode})/\tau_c$. We systematically vary β in our study.
3. Membrane - redox charge concentration ratio: $\delta = c_{f,membrane}/\sum z_{redox}c_{redox}$. This number governs the Donnan effect for the crossover of redox active species. Higher the δ, more the capacity retention.

The non-dimensional numbers representing the polarization losses:

1. Pore-scale Damköhler number Da_p: Da_p characterizes polarization due to pore-scale mass transfer. Ratio of pore-scale reaction current density i_n to the limiting current density i_{lim}. $Da_p = i_n/i_{lim}$. The pore-scale limiting current density is limited by the supply of redox active species from the bulk electrolyte to the carbon fibers of diameter d_f. For a pore-scale mass transfer coefficient of h_m, $i_{lim} = Fh_m c_{redox}$. The pore-scale Damköhler number Da_p can also be expressed in terms of applied current density at the current collector i_{cc} and Sherwood number Sh as

$$Da_p = \frac{i_{cc} d_f}{aFHShc_{redox}D_{redox}}$$

2. Salt Damköhler number Da_s: Da_s characterizes salt transport resistance to the applied current. It can be defined as

$$Da_s = \frac{i_{cc}H}{Fc_{salt}D_{salt}}$$

3. Wagner number Wa: Ratio of kinetic resistance to ohmic resistance. Wa can be defined in terms of ionic conductivity κ as

$$Wa = \frac{RT\kappa d_f}{4H^2F^2k_{rxn}^0 c_{redox}(1-\epsilon)}.$$

In this study, we neglect the effects of kinetic and ohmic polarization by assuming facile reaction kinetics (high k_{rxn}^0) and large diffusion coefficients leading to high ionic conductivity κ through the relation $\kappa = \sum z_i^2 c_i D_i F^2/RT$. Note that Wa is independent of the applied current density. We systematically vary Da_p and Da_s by changing the applied current density and fiber diameter at constant dimensionless flow rate $\beta = 100$ (see section 8.2). The performance of the RFBs is evaluated in terms of discharge capacity utilization $\chi(\%)$ defined as the capacity obtained during discharge as a percentage of theoretical capacity $\chi\ (\%)/100 = Q_{actual}/Q_{theory} = t_{discharge}/t_{theory}$ for constant current density. The coulombic efficiency $CE\ (\%)$ is obtained as the ratio of capacity during discharge to charge $CE\ (\%)/100 = Q_{discharge}/Q_{charge} = t_{discharge}/t_{charge}$. The polarization $\Delta\phi$ is measured as the deviation of the voltage plots from equilibrium curves. We can also express $\Delta\phi$ as half the difference between the average voltage during charge and discharge: $\Delta\phi = \left(\bar{V}_{charge} - \bar{V}_{discharge}\right)/2$. The non-dimensional polarization can be obtained by normalizing against cell redox potentials at 50% SOC at equilibrium: $\phi^* = \Delta\phi/E_{50\%\ SOC}^0$.

8.2 Galvanostatic Cycling and Effects of Flow Rate

All the RFBs modeled in this work are subjected to galvanostatic cycling between 0.8V to 1.25V by applying constant current density at the current collector. For this analysis, a representative RFB with $d_f = 10\mu m$ is cycled at $i_{cc} = 20mA/cm^2$ with a membrane charge $c_{f,membrane} = 8M$ with flow rate $\beta = 100$ (PFF) to obtain a 6-minute charge/ discharge process. The cell voltage curve is shown in Figure 8.1 along with the variation of discharge capacity utilization $\chi(\%)$ and coulombic efficiency $CE(\%)$. The coulombic efficiency which is related to the degree of crossover[54] is about 99.9% indicating negligible crossover due to Donnan exclusion of redox active species resulting in low capacity fade of only 0.02% for 10 cycles.

The relative amount of redox active species in the electrolyte with respect to the fixed charge concentration of the membrane (δ) governs the degree of crossover. δ=0 corresponds to a non-selective separator (NSS). Although NSSs are more economically viable than IEMs, they suffer from high capacity fade. In Figure 8.2, we study the effects of membrane concentration by varying δ and observing the capacity fade ($\Delta\chi_{1-10}\%$) for ten cycles with $i_{cc} = 20mA/cm^2$ and $\beta = 100$. We observe that for NSSs ($\delta \to 0$) the capacity fade is almost 15% for ten cycles. The fixed charge in the IEM has to be at least twenty times higher than the redox concentration in the electrolyte to ensure a capacity fade of less than 0.5% for ten cycles.

Figure 8.1

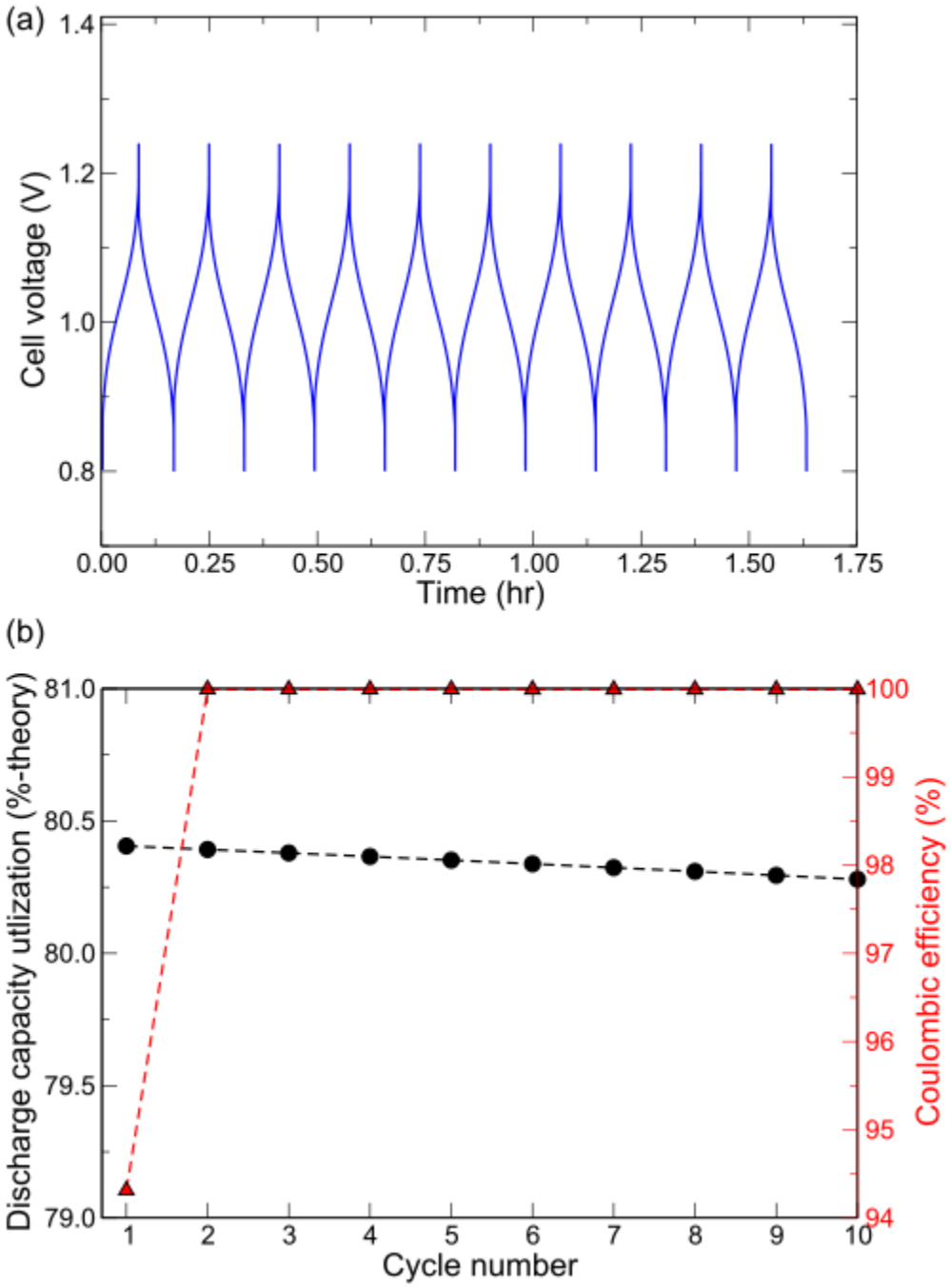

Figure 8.1: (a) Variation of cell voltage with time and (b) variation of discharge capacity utilization and coulombic efficiency with cycle number for a 30-minute charge/discharge cycle.

Figure 8.2

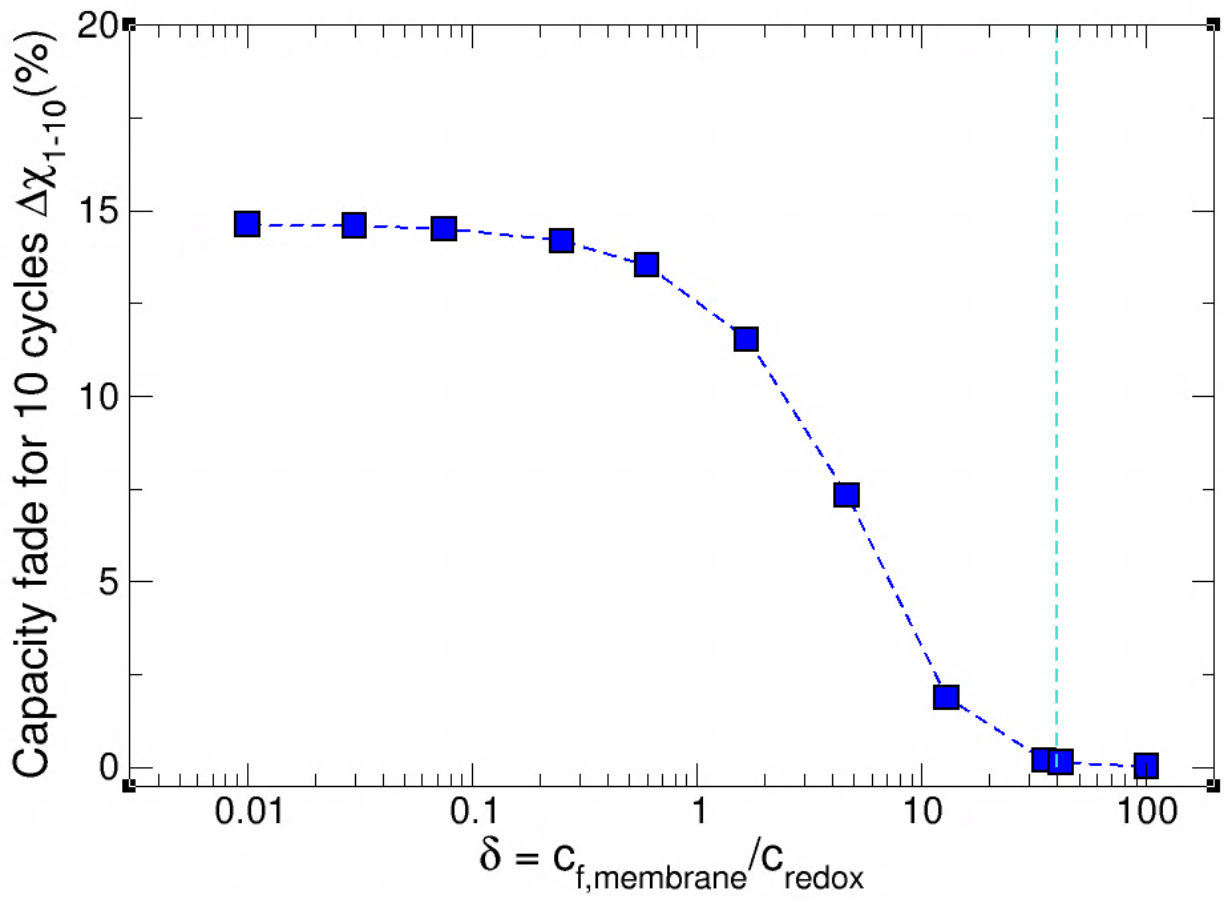

Figure 8.2: Capacity fade in the representative RFB with varying fixed charge concentration in the membrane. $\delta \to 0$ corresponds to a non-selective separator whereas $\delta \to 40$ ensures excellent capacity retention. We subsequently study the polarization mechanisms of RFBs with $\delta = 40$ (represented by the vertical line).

The performance of RFBs are strongly dependent on the flow fields and flow rate[55]. A low flow rate not only affects the mass transfer within the electrode, but it also affects the reactor influent concentration from the tanks[22]. Figure 8.3 shows the variation of the

discharge utilization and polarization of the representative RFB with $\delta = 40$. The capacity utilization at low flow rates ($\beta < 50$) is low with high polarization. Increasing flow rate beyond $\beta = 100$ ensures about 80% capacity utilization towards energy storage. Operating the RFB beyond $\beta = 100$ leads to diminishing returns due to increased pumping costs with only a mild improvement in capacity. To minimize the polarization arising from tank mixing affects, we adopt a flow rate $\beta = 100$ to study concentration polarization mechanism.

Figure 8.3

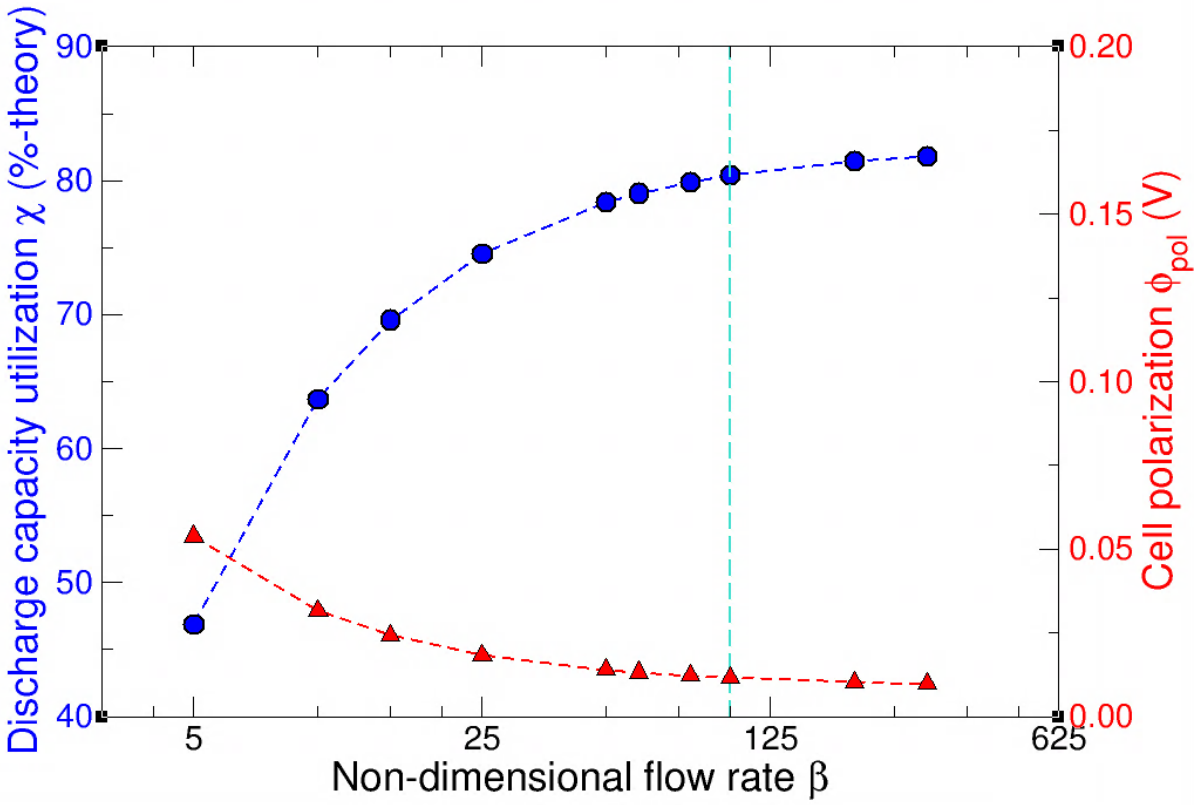

Figure 8.3: Variation of discharge capacity utilization and polarization with non-dimensional flow rate. The vertical line corresponds to the flow rate $\beta = 100$ which is used for further analysis.

8.3 Non-dimensional Mapping of Capacity and Polarization

Based on our study in section 8.2, we use $c_{f,membrane} = 8M$ and $\beta = 100$ (PFF) and map the performance of RFB on a non-dimensional space of Da_p and Da_s. In this analysis, we assume facile kinetics leading to low Wa. Under such assumption, the polarization coming from ohmic dependencies and kinetics are not dominant. We systematically vary Da_s and Da_p by varying the fiber diameter d_f from $5\mu m$ to $40\mu m$. For each fiber diameter d_f, the current density is increased from $i_{cc} = 2.5mA/cm^2$ *to* $400mA/cm^2$. $\dot{V}_{stoich}$ scales with i_{cc} and for a constant $\beta = 100$, volumetric flow rate $\dot{V}$ increases with i_{cc}. Changing d_f affects surface area a, pore-scale mass transfer Sh and dispersion coefficients. From the definition of Da_p, a and Sh, we can see that $Da_p \propto i_{cc} d_f^{1.615}$. On a plot of Da_s vs Da_p, the slope $Da_s/Da_p \propto d_f^{-1.615}$. Figure 8.4 shows the variation of the discharge capacity utilization in the limit cycle. Seventy-three cases were simulated and the results were interpolated to obtain the continuous contours. From Fig. 8.4, we can see that the low diameter carbon fibers have a higher discharge capacity of about 70-80% of theoretical maximum capacity. Larger surface area for conducting the electrochemical reactions ensure good utilization even at high current densities. The presence of larger diameter fibers in the electrodes restrict the utilization of the RFB primarily due to reduced a and Sh. Especially for $d_f > 10\mu m$, we can observe that the capacity utilization is a strong function of Da_p. In other words, for a coarse electrode morphology, $d_f > 10\mu m$, $\chi(\%) = func(Da_p)$ and for a finer electrode morphology, $d_f < 10\mu m$, $\chi = func(Da_s)$.

Figure 8.4

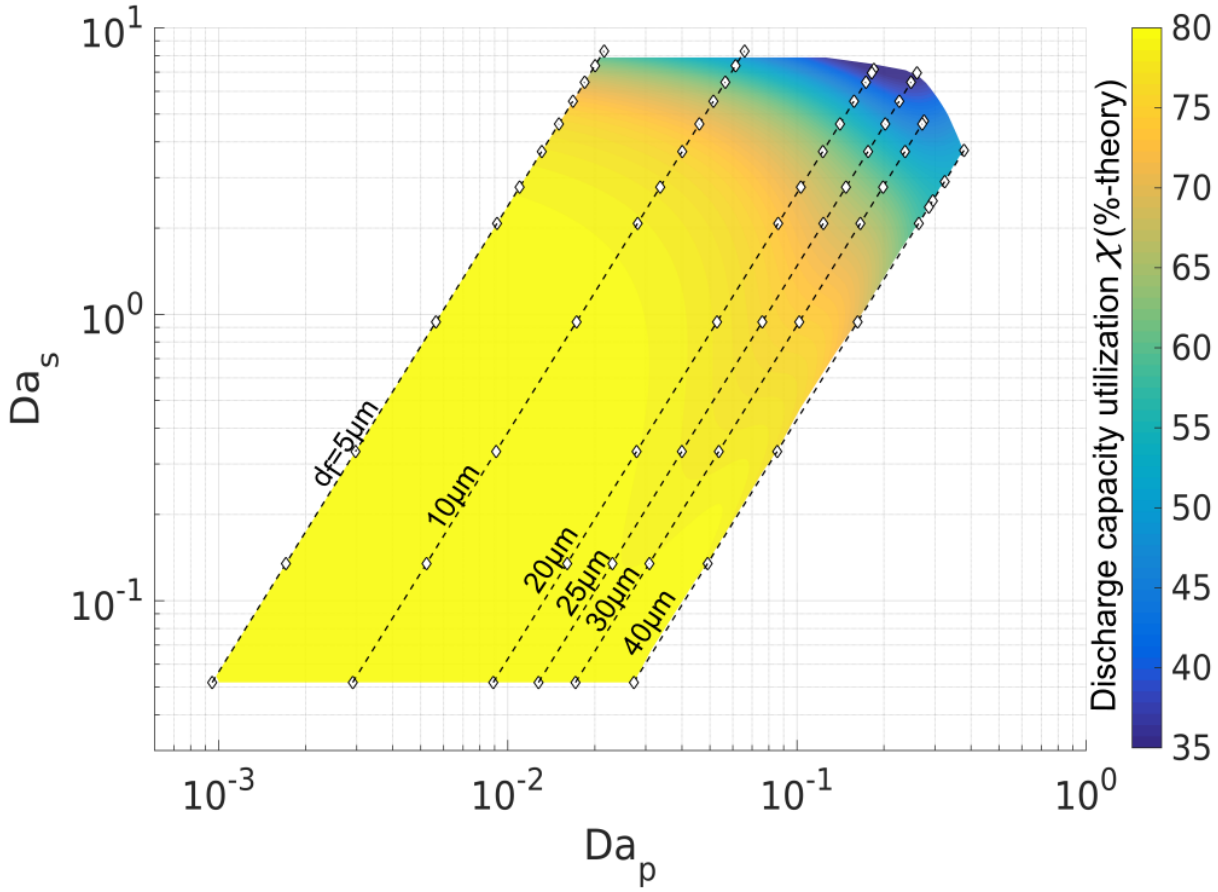

Figure 8.4: Contour map of discharge capacity utilization for PFF as a function of Da_p and Da_s. Each dashed straight line has a fixed fiber diameter d_f. The 65 dots mark the simulated cases used to populate the plot.

Figure 8.5

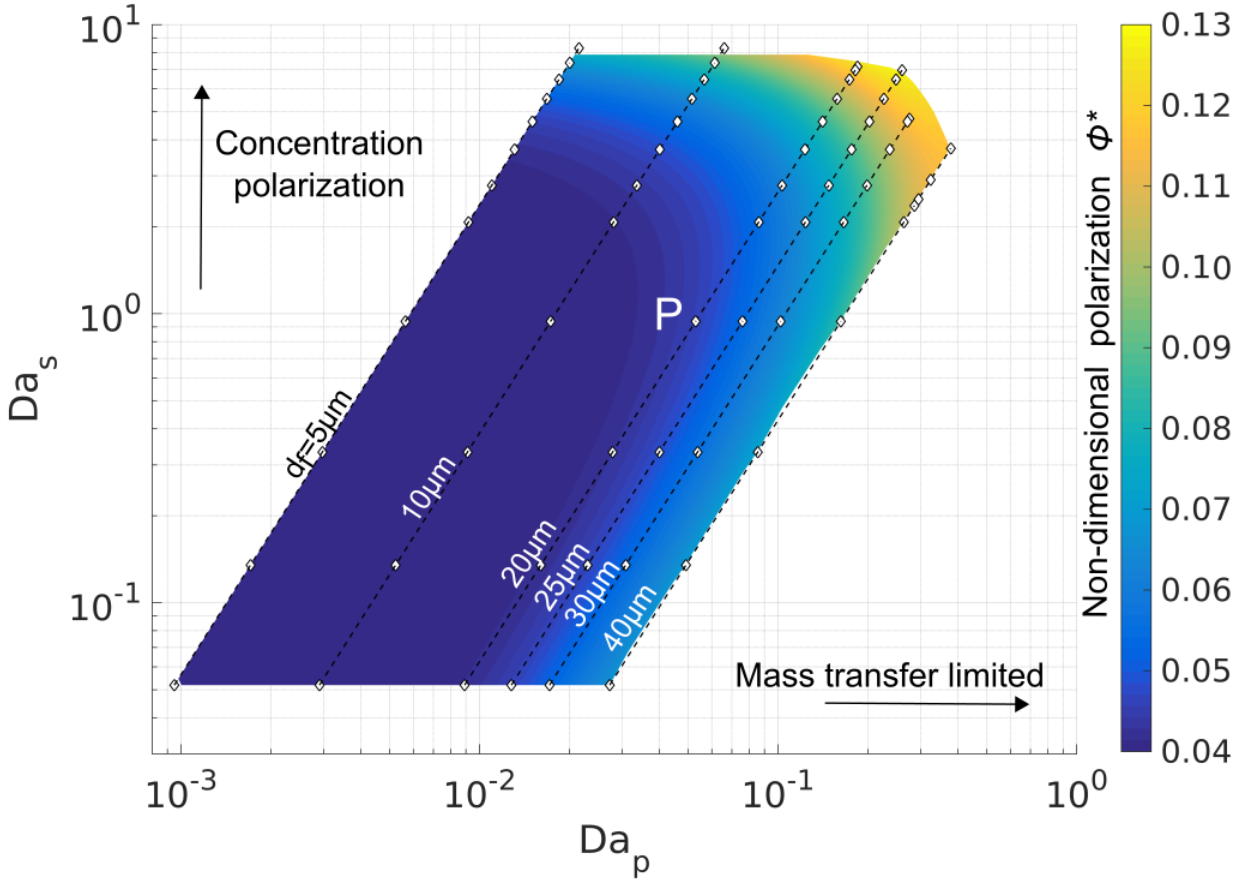

Figure 8.5: Contour map of non-dimensional cell polarization ϕ^* for PFF as a function of Da_p and Da_s. Each dashed straight line has a fixed fiber diameter d_f. The 65 dots mark the simulated cases used to populate the plot. We perform detailed exergy destruction for a representative point P marked in the figure.

The variation of non-dimensional cell polarization against Da_p and Da_s is shown in Figure 8.5. An increase in Da_p corresponds to larger pore-scale reaction current density and is therefore mass transfer limited regime. Whereas, an increase in Da_s indicates polarization

due to salt transport limitations (concentration polarization). For a given current density (constant Da_s), the cell polarization is strongly affected by Da_p particularly at high current densities. Simultaneously, by fixing Da_p, polarization increases substantially with Da_s. This clearly indicates that $\phi^* = func(Da_p, Da_s)$. Therefore, in conducting polarization studies at large current densities, it is important to consider polarization effects due to concentration polarization and not just limit to pore-scale mass transfer. Although the increase in pore-scale Sherwood number Sh with d_f ($Sh \propto d_f^{0.385}$) should help reduce polarization losses, the reduced surface area $a \propto d_f^{-1}$ increases the polarization. The spatial distribution of the local reaction current densities also affect the polarization. The electrochemical performance of PFF is better than IDFF due to better wetting of electrodes and more uniform reaction distribution[55]. The results presented in Figs. 8.4 and 8.5 corresponds to a PFF. Figure 8.6 compares the polarization in a RFB using PFF and IDFF. At all flow rates, the IDFF shows larger polarization. The results shown in Figs. 8.4 and 8.5 qualitatively hold true for an IDFF but quantitatively, IDFF has a slightly higher degree of polarization.

Figure 8.6

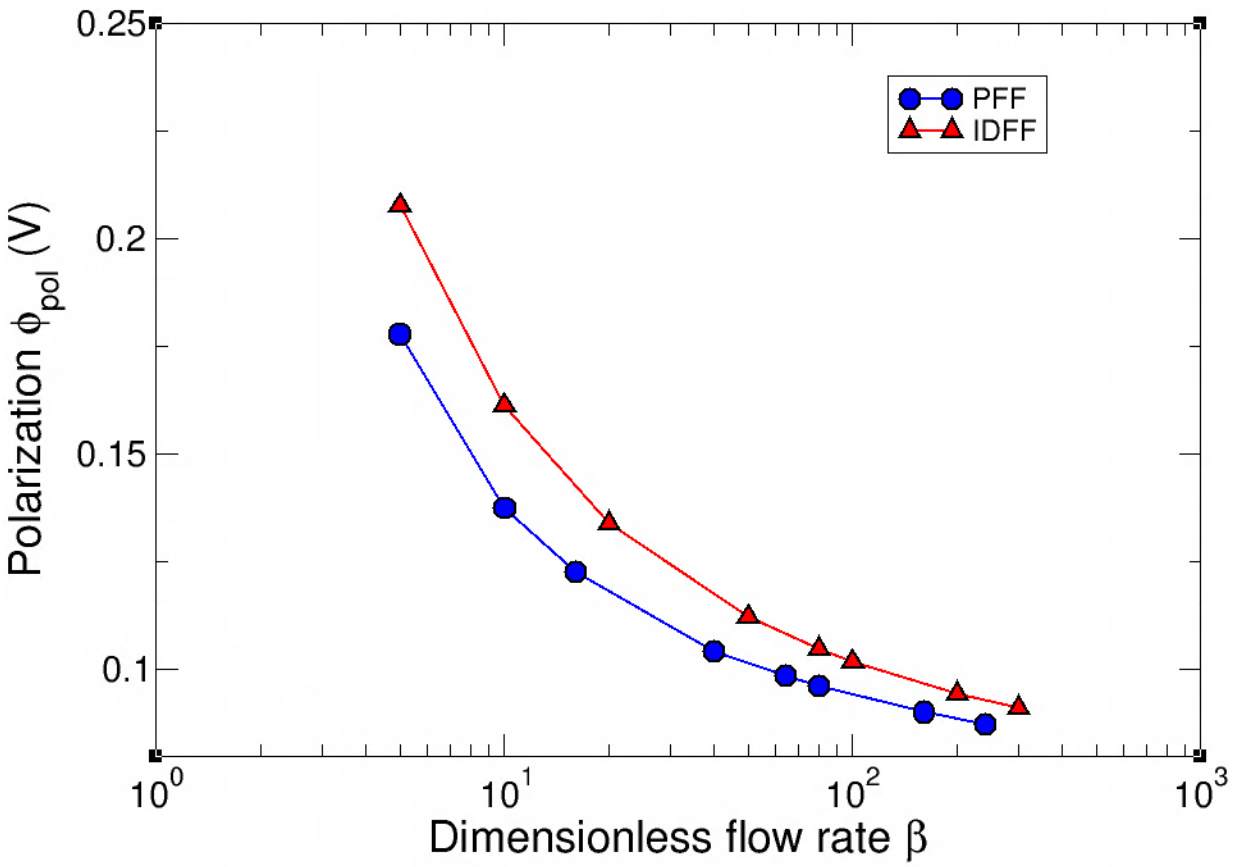

Figure 8.6: Comparing polarization for two different flow fields as a function of non-dimensional flow rate β.

8.4 Instantaneous Exergy Destruction Analysis

In this section, we quantify the exergy destruction associated with every physical process modeled for RFBs. Exergy is destroyed whenever entropy is generated in an irreversible process. For an isothermal process, the volumetric rate of exergy destruction is related to volumetric entropy generation $\dot{s}'''_{gen}$ as

$$\dot{q}'''_{ex} = T\dot{s}'''_{gen}$$

Exergy destruction can also be represented as a product of flux $\vec{N}$ (like species transport flux) against a potential ∇F_k (like electrochemical potential gradient) $\dot{q}'''_{ex} = \vec{N}.\nabla F_k$, where F_k is the driving force. The entropy generation rate for every process can be derived from the first and second laws of thermodynamics. The rate of volumetric exergy destruction for the various processes associated with (1) pore-scale mass transfer, (2) reaction kinetics, (3) irreversible tank mixing, (4) bulk species transport, and (5) electronic conduction can be stated as:

1) Reaction kinetics ($\dot{q}'''_{ex,r}$) : Exergy destruction rate is a result of driving the local pore-scale reaction current density i_n against the local overpotential η.

$$\dot{q}'''_{ex,r}(x,y,t) = i_n\eta$$

2) Pore-scale mass transport ($\dot{q}'''_{ex,p}$): The pore-scale mass transport is driven by the pore-scale concentration gradient between the bulk c^b and the surface c^s of the four redox species. This concentration gradient can be represented as a difference in equilibrium potential at the bulk ϕ^b_{eq} and surface ϕ^s_{eq}, while the pore-scale transport flux can be represented as i_n from eqn (4). The volumetric exergy destruction rate due to pore-scale mass transport can therefore be expressed as

$$\dot{q}'''_{ex,p}(x,y,t) = i_{n,1}\left(\phi^b_{eq} - \phi^s_{eq}\right)|_{R1/O1} + i_{n,2}\left(\phi^b_{eq} - \phi^s_{eq}\right)|_{R2/O2}$$

3) Electron conduction ($q'''_{ex,e}$): The electronic current $\vec{\imath}_e$ within the carbon fibers are driven by the solid phase potential ϕ_s. The volumetric exergy destruction associated with electron conduction can be stated as

$$\dot{q}'''_{ex,e}(x,y,t) = -i_e.\nabla\phi_s = \sigma^{eff}(\nabla\phi_s)^2$$

4) Species transport ($q'''_{ex,s}$): The transport of species i is driven its by the electrochemical potential gradient $\tilde{\mu}_i = \mu_i^0 + RTln(c_i) + z_i F\phi_e$, where μ_i^0 is the standard chemical potential of the species. The species transport flux $\overrightarrow{N_\iota}$ governed by diffusion and migration processes is given as (deduced from eqn (3)).

$$\overrightarrow{N_\iota} = -\frac{D_i^{eff} c_i^b}{RT} \nabla \tilde{\mu}_i$$

The advective component of species transport driven by pressure gradient ∇P is not included in $\vec{N}_i$ as the exergy related to advective transport is compensated by the pumps. The local chemical exergy destruction rate due to species transport can be given as[45,56]

$$\dot{q}'''_{ex,s}(x,y,t) = -\sum_{i=1}^{6} \vec{N}_i . \nabla \tilde{\mu}_i$$

5) Tank mixing ($Q_{ex,t}$): The tanks are assumed to be perfectly mixed. The electrolyte entering the tank with concentration c_{in} and electrochemical potential $\tilde{\mu}_{in}$ mixes with the electrolyte already stored in the tank before exiting the tank at a concentration c_{out} and electrochemical potential $\tilde{\mu}_{out}$. We note that the inlet and outlet of the tanks are the outlet and inlet of the reactor respectively. The net rate of exergy loss due to mixing in a single tank can be given as

$$\dot{Q}_{ex,t}(t) = \sum_{i=1}^{6} \left[-\left(c_i V_{tank} \frac{\partial \tilde{\mu}_\iota}{\partial t} \right)_{tank} + \tilde{\mu}_{i,tank} \left(\dot{V} c_{i,tank} - v \int_{A_{in}} c_{i,in} dA \right) \right.$$
$$\left. + v \left(\int_{A_{in}} c_{i,in} \tilde{\mu}_{i,in} dA - \int_{A_{out}} c_{i,out} \tilde{\mu}_{i,out} dA \right) \right]$$

Substituting $\tilde{\mu}_i = \mu_i^0 + RTln(c_i) + z_i F\phi_e$, using the species conservation and electro-neutrality in the tank, the above equation becomes independent of the solution phase potential ϕ_e and standard chemical potential μ_i^0. Upon simplification, the exergy loss rate because of tank mixing process can be given as:

$$\dot{Q}_{ex,t}(t) = -V_{tank}\left(\sum_{i=1}^{6} RT\frac{dc_i}{dt}\right)_{tank} + \sum_{i=1}^{6} RTv\int_{A_{in}} c_{i,in} ln\left(\frac{c_{i,in}}{c_{i,tank}}\right) dA$$

A detailed derivation of $\dot{q}'''_{ex,s}(x,y,t)$ and $\dot{Q}_{ex,t}(t)$ from the first and second law of thermodynamics is shown in the supplementary information (sec 8.5). Table 8.3 summarizes the various exergy destruction processes.

Table 8.3: List of exergy destruction rates for the various mechanisms in RFBs.

Process	**Flux**	**Potential or gradient of the driving force**	**Volumetric exergy destruction rate $\dot{q}_{ex}'''(W/m^3)$ or Net exergy destruction rate $\dot{Q}_{ex}(W)$**
Reaction kinetics	i_n	η	$\dot{q}_{ex,r}''' = i_n\eta$
Pore-scale mass transport	i_n	$\Delta\phi_{eq} = \phi_{eq}^b - \phi_{eq}^s$	$\dot{q}_{ex,p}''' = i_n(\phi_{eq}^b - \phi_{eq}^s)$ For both redox couples
Electron conduction	$\vec{\imath}_e = -\sigma^{eff}\nabla\phi_s$	$\nabla\phi_s$	$\dot{q}_{ex,e}''' = \sigma^{eff}(\nabla\phi_s)^2$
Species transport	$\overrightarrow{N_i} = -\frac{D_i^{eff}c_i^b}{RT}\nabla\tilde{\mu}_i$	$\nabla\tilde{\mu}_i$	$\dot{q}_{ex,s}''' = -\sum_{i=1}^{6}\vec{N}_i.\nabla\tilde{\mu}_i$
Tank mixing	$\dot{V}c_i$	$\tilde{\mu}, \frac{\partial\tilde{\mu}}{\partial t}, c_i, v$	$\dot{Q}_{ex,t}(t) = -V_{tank}\left(\sum_{i=1}^{6} RT\frac{dc_i}{dt}\right)_{tank} + \sum_{i=1}^{6} RTv\int_{A_{in}} c_{i,in} ln\left(\frac{c_{i,in}}{c_{i,tank}}\right)dA$ In both tanks

The volumetric exergy destruction rate for the reaction kinetics $\dot{q}'''_{ex,r}$, pore-scale mass transport $\dot{q}'''_{ex,p}$, electron conduction $\dot{q}'''_{ex,e}$ and species transport $\dot{q}'''_{ex,s}$ vary spatially within the reactor (x, y) and change with time t. Integrating the rate of volumetric exergy destruction terms $\dot{q}'''_{ex}$ over the reactor volume gives the net exergy $\dot{Q}_{ex,net}(t)$ as a function of time.

$$\dot{Q}_{ex,net}(t) = \int_{V_{total}} \left(\dot{q}'''_{ex,r} + \dot{q}'''_{ex,p} + \dot{q}'''_{ex,e} + \dot{q}'''_{ex,s}\right) dV + \dot{Q}_{ex,t}(t)$$

$$\dot{Q}_{ex,net}(t) = \dot{Q}_{ex,r}(t) + \dot{Q}_{ex,p}(t) + \dot{Q}_{ex,e}(t) + \dot{Q}_{ex,s}(t) + \dot{Q}_{ex,t}(t)$$

During galvanostatic charge-discharge cycles with constant current I_{app}, the net loss of energy for every cycle E_{cycle} can be stated as the difference between energy input during charging and energy output during discharge.

$$E_{cycle} = \int_{charge} V_{cell} I_{app} dt - \int_{discharge} V_{cell} I_{app} dt$$

The average rate of energy loss over the entire cycle can be defined as

$$\dot{\bar{E}}_{cycle} = \frac{E_{cycle}}{t_{cycle}}$$

If $\dot{Q}_{ex,net}(t)$ represents all the exergy destruction rate mechanisms of RFBs, then $\int_{t_{cycle}} \dot{Q}_{ex,net}(t)\, dt$ over the entire cycle should be equal to E_{cycle}. Through all the various cases simulated over the non-dimensional space (shown in Figs. 8.4 and 8.5), we find that $\frac{\int_{t_{cycle}} \dot{Q}_{ex,net}(t) dt}{E_{cycle}} > 0.98$ which gives confidence in the complete exergy analysis of RFBs presented here. The net exergy destruction rates $\dot{Q}_{ex}$ for all the five processes can

be non-dimensionalized against $\dot{\bar{E}}_{cycle}$ to give exergy destruction rate fraction defined as $\dot{Q}^*_{ex,r}(t) = \frac{\dot{Q}_{ex,r}}{\dot{\bar{E}}_{cycle}}$, $\dot{Q}^*_{ex,p}(t) = \frac{\dot{Q}_{ex,p}}{\dot{\bar{E}}_{cycle}}$, $\dot{Q}^*_{ex,e}(t) = \frac{\dot{Q}_{ex,e}}{\dot{\bar{E}}_{cycle}}$, $\dot{Q}^*_{ex,s}(t) = \frac{\dot{Q}_{ex,s}}{\dot{\bar{E}}_{cycle}}$, and $\dot{Q}^*_{ex,t}(t) = \frac{\dot{Q}_{ex,t}}{\dot{\bar{E}}_{cycle}}$. With such non-dimensionalization, we obtain:

$$\frac{\int_{t_{cycle}} \left(\dot{Q}^*_{ex,r}(t) + \dot{Q}^*_{ex,p}(t) + \dot{Q}^*_{ex,e}(t) + \dot{Q}^*_{ex,s}(t) + \dot{Q}^*_{ex,t}(t)\right) dt}{t_{cycle}} = 1$$

The 2D multi-species transport model for RFBs presented in this thesis enables determination of non-dimensional exergy destruction rate $\dot{Q}^*_{ex}$ at every instant in time. Figure 8.7(a) shows the development of cell voltage and Fig. 8.7(b) shows the simultaneous variation of $\dot{Q}^*_{ex}$ for the five different processes for an RFB operated at $i_{cc} = 100 mA/cm^2$ and $d_f = 20\mu m$ (Point P marked in Fig. 8.5). Under these operating conditions, about 55% of total energy lost is attributed to species transport/ concentration polarization followed by pore-scale mass transport process (28%) and reaction kinetics (12%). A large $\beta = 100$ ensures the exergy destruction due to tank mixing is low[22] (4%) and high electronic conductivity σ^{eff} of the carbon felt contributes the least to the total energy lost (1%). The exergy destruction due to species transport is dominated by the membrane counter-ion B^- (Fig. 8.7(c)). At high current densities, the electrochemical potential gradient $\nabla\tilde{\mu}$ is particularly high across the IEM and that combined with the favored transport of the B^- species through the positively charged membrane leads to high exergy destruction in the membrane. On the contrary, the exergy lost by the positively charged species is focused within the electrodes as their transport through the IEM is restricted. We map the exergy destruction fraction due to species transport $Q^*_{ex,s}$ and (b) pore-scale mass transport $Q^*_{ex,p}$ in Fig. 8.8. Energy losses associated with

concentration polarization dominate at high Da_s and low Da_p whereas the energy losses associated with pore-scale mass transport are relatively high for large Da_p almost independent of Da_s. The mapping presented in Fig. 8.8 is important to consider when designing experiments to determine specific properties like the pore-scale mass transfer coefficient. This analysis also shows the importance to consider concentration based polarization in addition to ohmic, kinetic and pore-scale transport effects which are mostly studied in RFB literature. The exergy destruction formulation presented above can help identify major sources of losses/ irreversibilities when designing RFBs to improve the energy efficiency.

Figure 8.7

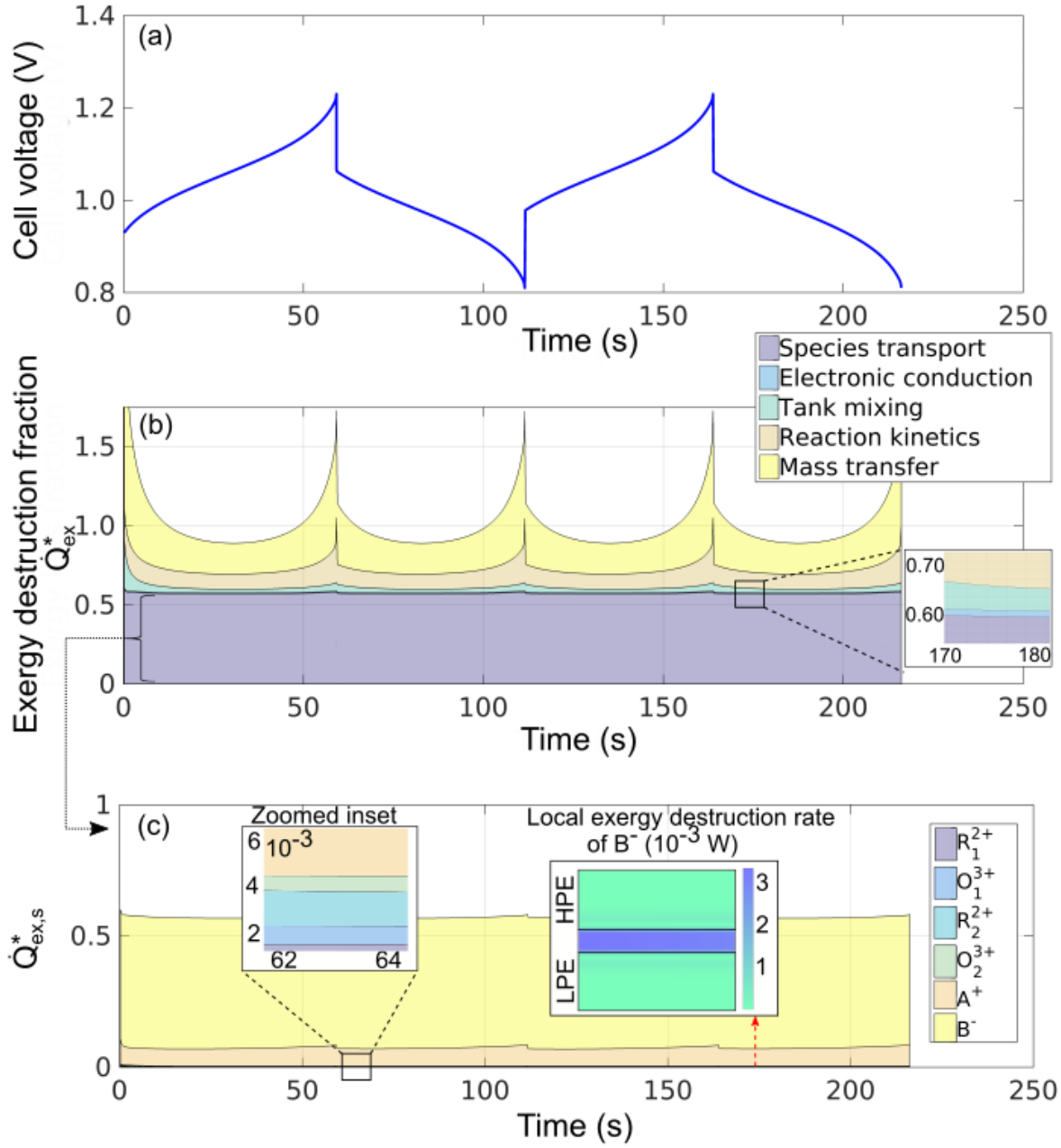

Figure 8.7: (a) Development of cell voltage with time for $i_{cc} = 100mA/cm^2$ and $d_f = 20\mu m$ (b) Area plot showing the variation of exergy destruction fraction $\dot{Q}^*_{ex}$ for the five different processes with zoomed inset plot (c) Variation of exergy destruction fraction for the six different species $\dot{Q}^*_{ex,s}$ with spatial variation of $\dot{Q}_{ex,B^-}$ at $t = 170s$ within the reactor.

Figure 8.8

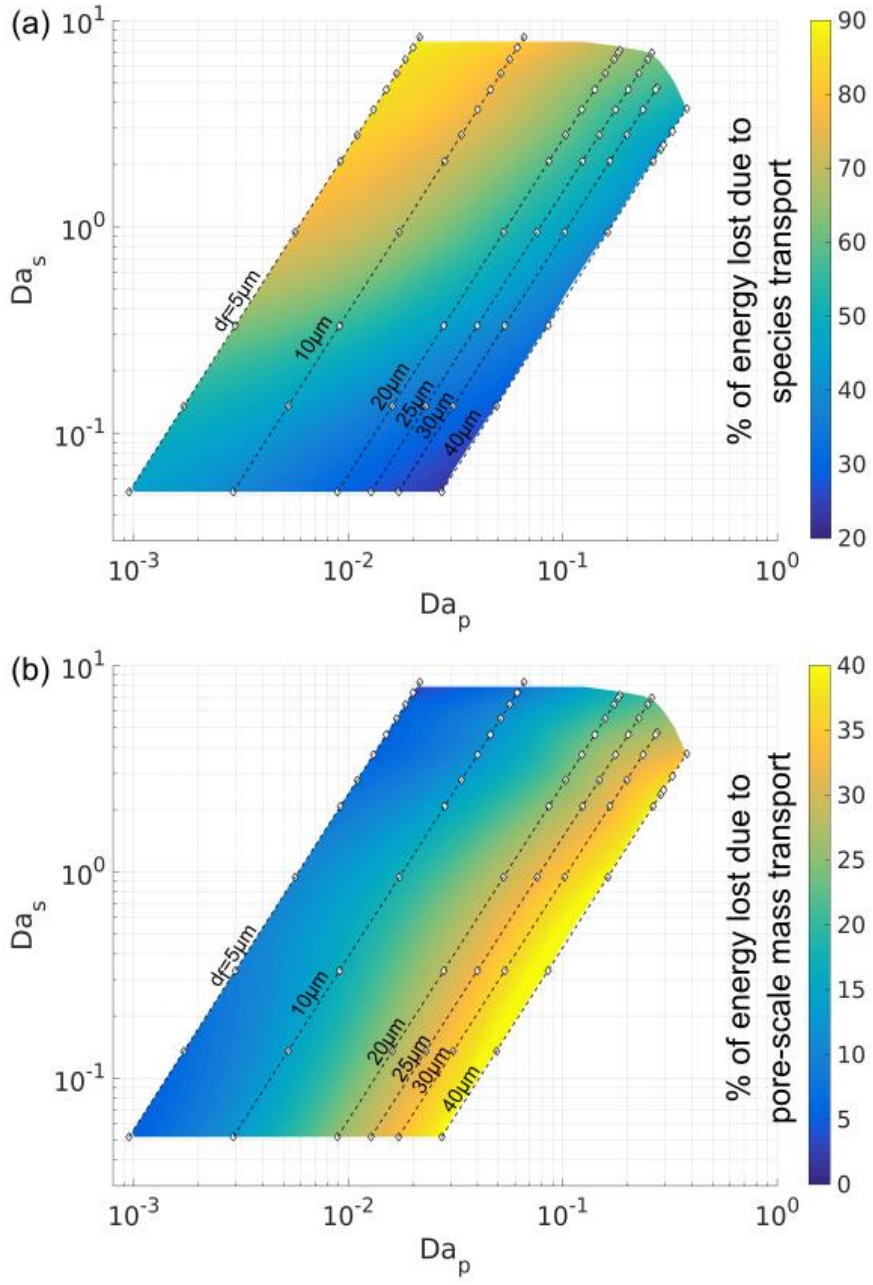

Figure 8.8: Contour map of (a) exergy destruction fraction for species transport $Q^*_{ex,s}\times 100\ (\%)$ and (b) exergy destruction fraction for pore-scale mass transport $Q^*_{ex,p}\times 100\ (\%)$ as a function of Da_p and Da_s. Each dashed straight line has a fixed fiber diameter d_f. The 65 dots mark the simulated cases used to populate the plot.

8.5 Supplementary Information

8.5.1: Derivation of Exergy Destruction for Species Transport

Supplementary Figure 8.1

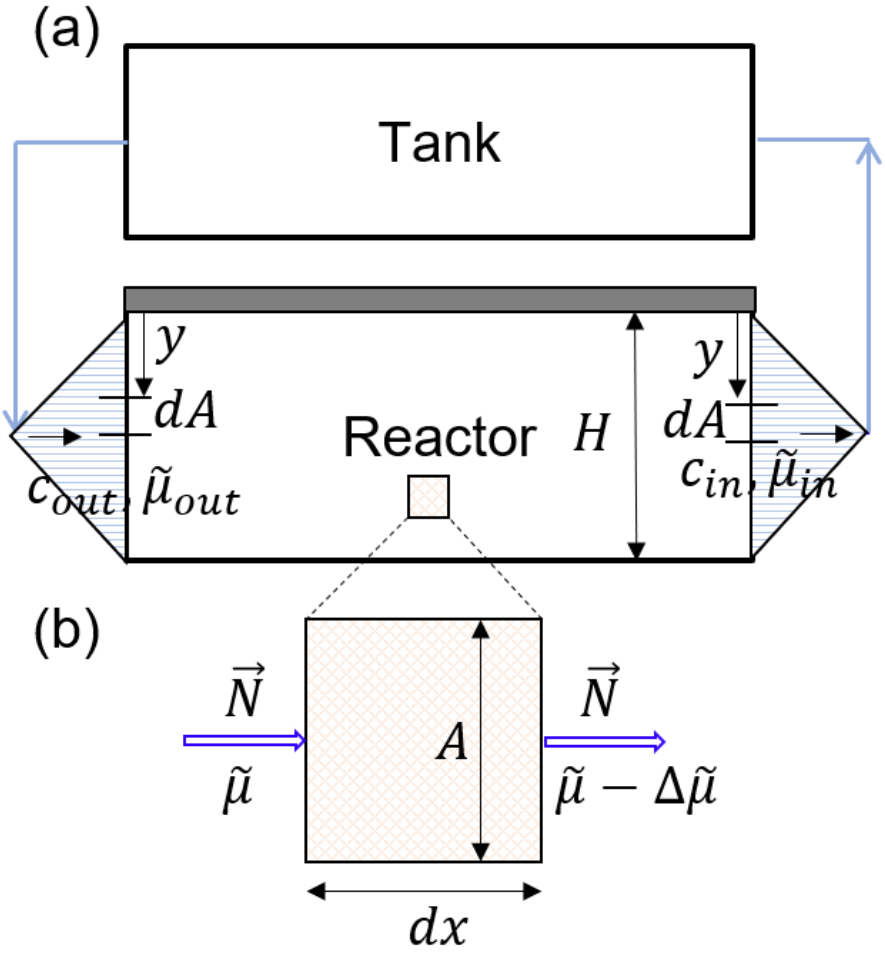

Supplementary Figure 8.1: (a) Reactor-tank connection. (b) Small elemental control volume of length dx within the reactor.

Consider the small elemental volume within the reactor with species flux $\vec{N}$ entering the control volume at chemical potential $\tilde{\mu}$ and leaving the control the volume at $\tilde{\mu} - \Delta\tilde{\mu}$ (Supplementary Figure 8.1(b)).

The first law of thermodynamics states[42]:

$$\frac{dE}{dt} = \dot{Q} - \dot{W} + \left(h\dot{N}\right)_{in} - \left(h\dot{N}\right)_{out} \tag{8.1}$$

Where E: internal energy, $\dot{Q}$: heat transfer, $\dot{W}$: work transfer, h: molar enthalpy, $\dot{N}$: molar flow rate. Since there is no external work transfer, we get

$$\dot{Q} = \frac{dE}{dt} - \left(h\dot{N}\right)_{in} + \left(h\dot{N}\right)_{out} \tag{8.2}$$

The second law of thermodynamics relates the entropy generation rate $\dot{S}_{gen}$ to the rate of entropy stored within the control volume $\frac{dS}{dt}$, entropy through heat transfer and entropy flow rate. Under isothermal conditions, the second law can be stated as:

$$\dot{S}_{gen} = \frac{dS}{dt} - \frac{\dot{Q}}{T} + \left(s\dot{N}\right)_{out} - \left(s\dot{N}\right)_{in} \tag{8.3}$$

$$T\dot{S}_{gen} = \frac{TdS}{dt} - \dot{Q} + \left(Ts\dot{N}\right)_{out} - \left(Ts\dot{N}\right)_{in} \tag{8.4}$$

Eliminating $\dot{Q}$ from eqns 8.2 and 8.4, we get exergy lost due to transport $\dot{Q}_{ex}$ as a function of total Gibbs free energy G and molar Gibbs free energy g.

$$\dot{Q}_{ex} = T\dot{S}_{gen} = -\frac{dG}{dt} + \left(gA\vec{N}\right)_{in} - \left(gA\vec{N}\right)_{out} \tag{8.5}$$

Assuming local quasi-equilibrium condition[45], $\frac{dG}{dt} = 0$. By definition, $\tilde{\mu}$ is the rate of change of the net Gibb's free energy with respect to the number of moles of the species n_i.

$$\frac{dG}{dn_i}|_{P,T,i\neq j} = g_i = \tilde{\mu}_i$$

Equation 8.5 can be re-written as volumetric exergy destruction rate $\dot{q}_{ex}$

$$\dot{q}_{ex} = \frac{\dot{Q}_{ex}}{Adx} = \frac{\vec{N}\Delta\tilde{\mu}}{\Delta x} = \vec{N}.\frac{d\tilde{\mu}}{dx} \qquad 8.6$$

Equation 8.6 is derived for one dimensional flow within the reactor. This can be extended to 2D and 3D flows and eqn. 8.6 can be generalized as[45,56]

$$\dot{q}_{ex} = \vec{N}.\nabla\tilde{\mu} \qquad 8.7$$

8.5.2: Derivation of Exergy Destruction Due to Tank Mixing

Chemical exergy destruction is associated with the mixing processes in the tank. Consider a reactor with parallel flow connected to a well-mixed tank as shown in Supplementary Figure 8.1(a). Since the reactor is modeled as a 2D continuum, the concentrations and electrochemical potential with which the electrolyte exits the reactor varies along the electrode thickness. Let $c_{i,in}(y), \tilde{\mu}_{i,in}(y)$ be the concentration and electrochemical potential of a species i entering the tank (exiting the reactor) from a small element of length dy as shown in Supplementary Figure 8.1(a). Similarly, let $c_{i,out}(y), \tilde{\mu}_{i,out}(y)$ be the concentration and electrochemical potential of species i entering the reactor (exiting the tank). The "in" and "out" are defined with respect to the tank. This

analysis intrinsically accounts for mixing within pipes connecting the reactor-tank although the flow through pipes is not explicitly modeled.

The first law of thermodynamics[42]:

$$\frac{dE_i}{dt} = \dot{Q}_i - \dot{W}_i + \left(h\dot{N}\right)_{i,in} - \left(h\dot{N}\right)_{i,out}$$

Since there is no external transfer of work,

$$\dot{Q}_\imath = \frac{dE_i}{dt} + \left(h\dot{N}\right)_{i,out} - \left(h\dot{N}\right)_{i,in}$$

Expressing $h\dot{N}$ in terms of electrolyte entering or exiting the infinitesimal control volume dy at velocity v, we get

$$\dot{Q}_i = \frac{dE_i}{dt} + \int_{A_{out}} c_{i,out} h_{i,out} v dA - \int_{A_{in}} c_{i,in} h_{i,in} v dA \qquad 8.8$$

The second law of thermodynamics[42] (assuming isothermal conditions):

$$\dot{S}_{i,gen} = \frac{dS_i}{dt} - \frac{\dot{Q}_\imath}{T} + \left(s\dot{N}\right)_{i,out} - \left(s\dot{N}\right)_{i,in}$$

$$T\dot{S}_{i,gen} = \frac{TdS_i}{dt} - \dot{Q}_\imath + \left(Ts\dot{N}\right)_{i,out} - \left(Ts\dot{N}\right)_{i,in}$$

$$T\dot{S}_{i,gen} = \frac{TdS_i}{dt} - \dot{Q}_i + T\int_{A_{out}} c_{i,out} s_{i,out} v dA - T\int_{A_{in}} c_{i,in} s_{i,in} v dA \qquad 8.9$$

Eliminating $\dot{Q}$ from eqns (8.8) and (8.9), using $G = H - TS = E + PV - TS$, $\frac{dG}{dt} = \frac{d(E-TS)}{dt}$ at constant volume and pressure, and molar Gibb's free energy $g = h - Ts$, we get

$$Q_{i,ex} = -\frac{dG_i}{dt} + T\int_{A_{in}} c_{i,in} g_{i,in} v dA - T\int_{A_{out}} c_{i,out} g_{i,out} v dA \tag{8.10}$$

By definition of $\tilde{\mu}$

$$\frac{dG}{dn_i}|_{P,T,i\neq j} = g_i = \tilde{\mu}_i$$

The Gibb's free energy within the tank (assumed to be uniform throughout the tank)

$$G_i = \int_{Vtank} g_{i,tank} c_{i,tank} dV = V_{tank}(\tilde{\mu} c)_{i,tank}$$

$$\frac{dG}{dt} = V_{tank}\left(c_i \frac{\partial \tilde{\mu}_i}{\partial t} + \tilde{\mu}_i \frac{\partial c_i}{\partial t}\right)_{tank} \tag{8.11}$$

Equation (8.10) is derived using the first and second laws of thermodynamics applied to tanks. Apart from the thermodynamic laws, the species conservation must also be satisfied.

$$\frac{d}{dt}\left(c_{i,tank} V_{tank}\right) = \int_{A_{in}} c_{i,in} v dA - \int_{A_{out}} c_{i,out} v dA$$

The concentration of species exiting the tank has the same concentration as that of the tank (upwind scheme).

$$\frac{d}{dt}\left(c_{i,tank} V_{tank}\right) = \int_{A_{in}} c_{i,in} v dA - c_{i,tank}\dot{V} \tag{8.12}$$

Where $\dot{V}$ is the volumetric flow rate. Substitute eqn. 8.12 into 8.11 and simplifying eqn. 8.10, we get the exergy destruction for each species i.

$$\dot{Q}_{i,ex} = -\left(c_i V_{tank} \frac{\partial \tilde{\mu_i}}{\partial t}\right)_{tank} + \tilde{\mu}_{i,tank}\left(\dot{V} c_{i,tank} - v\int_{A_{in}} c_{i,in} dA\right)$$

$$+v\left(\int_{A_{in}} c_{i,in}\tilde{\mu}_{i,in}dA - \int_{A_{out}} c_{i,out}\tilde{\mu}_{i,out}dA\right) \qquad 8.13$$

Expressing the electrochemical potential $\tilde{\mu}_i$ in terms of chemical potential μ_i and solution phase potential ϕ_e for each species with charge number z_i, we get: $\tilde{\mu}_i = \mu_i + z_i F c_i \phi_e$. By adding the $\dot{Q}_{i,ex}$ for all the six different species and using the electroneutrality condition $\sum z_i c_i = 0$, eqn. 8.13 becomes independent of ϕ_e and the net exergy lost due to tank mixing for all the six species can be written as

$$\dot{Q}_{ex} = V_{tank}\left(\sum_{i=1}^{6} c_i \frac{\partial \mu_i}{\partial t}\right)_{tank} + \sum_{i=1}^{6}\int_{A_{in}} c_{i,in}\mu_i v dA - \sum_{i=1}^{6}\mu_{i,tank}\int_{A_{in}} c_{i,in} v dy \qquad 8.14$$

The chemical potential can be expressed in terms of standard chemical potential μ_i^0 and concentration c_i as $\mu_i = \mu_i^0 + RTln(c_i)$. Substituting this into eqn. 8.14 and taking the summation inside the integrals, we obtain a final expression which is dependent only on the species concentration c_i and independent of μ_i^0 as

$$\dot{Q}_{ex} = -V_{tank}\left(\sum_{i=1}^{6} RT\frac{dc_i}{dt}\right) + \sum_{i=1}^{6} RTv\int_{A_{in}} c_{i,in} ln\left(\frac{c_{i,in}}{c_{i,tank}}\right) dy \qquad 8.15$$

8.6 References

1. Weber, A. Z. *et al.* Redox flow batteries: a review. *J Appl Electrochem* **41**, 1137 (2011).
2. Leung, P. *et al.* Progress in redox flow batteries, remaining challenges and their applications in energy storage. *RSC Adv.* **2**, 10125–10156 (2012).
3. Wang, W. *et al.* Recent Progress in Redox Flow Battery Research and Development. *Adv. Funct. Mater.* **23**, 970–986 (2013).
4. Lu, W., Li, X. & Zhang, H. The next generation vanadium flow batteries with high power density – a perspective. *Phys. Chem. Chem. Phys.* **20**, 23–35 (2017).

5. Milshtein, J. D. *et al.* Quantifying Mass Transfer Rates in Redox Flow Batteries. *J. Electrochem. Soc.* **164**, E3265–E3275 (2017).
6. Aaron, D., Tang, Z., Papandrew, A. B. & Zawodzinski, T. A. Polarization curve analysis of all-vanadium redox flow batteries. *J Appl Electrochem* **41**, 1175 (2011).
7. Bromberger, K., Kaunert, J. & Smolinka, T. A Model for All-Vanadium Redox Flow Batteries: Introducing Electrode-Compression Effects on Voltage Losses and Hydraulics. *Energy Technology* **2**, 64–76 (2014).
8. Wei, L., Zhao, T. S., Zhao, G., An, L. & Zeng, L. A high-performance carbon nanoparticle-decorated graphite felt electrode for vanadium redox flow batteries. *Applied Energy* **176**, 74–79 (2016).
9. Bhattarai, A. *et al.* Advanced porous electrodes with flow channels for vanadium redox flow battery. *Journal of Power Sources* **341**, 83–90 (2017).
10. Liu, Q. H. *et al.* High Performance Vanadium Redox Flow Batteries with Optimized Electrode Configuration and Membrane Selection. *J. Electrochem. Soc.* **159**, A1246–A1252 (2012).
11. Chang, T.-C., Zhang, J.-P. & Fuh, Y.-K. Electrical, mechanical and morphological properties of compressed carbon felt electrodes in vanadium redox flow battery. *Journal of Power Sources* **245**, 66–75 (2014).
12. Aaron, D. S. *et al.* Dramatic performance gains in vanadium redox flow batteries through modified cell architecture. *Journal of Power Sources* **206**, 450–453 (2012).
13. Lin, K. *et al.* Alkaline quinone flow battery. *Science* **349**, 1529–1532 (2015).
14. Burgess, M. *et al.* Scanning Electrochemical Microscopy and Hydrodynamic Voltammetry Investigation of Charge Transfer Mechanisms on Redox Active Polymers. *J. Electrochem. Soc.* **163**, H3006–H3013 (2016).
15. Huskinson, B. *et al.* A metal-free organic-inorganic aqueous flow battery. *Nature* **505**, 195–198 (2014).
16. Janoschka, T. *et al.* An aqueous, polymer-based redox-flow battery using non-corrosive, safe, and low-cost materials. *Nature* **527**, 78–81 (2015).
17. Montoto, E. C., Nagarjuna, G., Moore, J. S. & Rodríguez-López, J. Redox Active Polymers for Non-Aqueous Redox Flow Batteries: Validation of the Size-Exclusion Approach. *J. Electrochem. Soc.* **164**, A1688–A1694 (2017).
18. Wei, X. *et al.* TEMPO-Based Catholyte for High-Energy Density Nonaqueous Redox Flow Batteries. *Adv. Mater.* **26**, 7649–7653 (2014).
19. Brushett, F. R., Vaughey, J. T. & Jansen, A. N. An All-Organic Non-aqueous Lithium-Ion Redox Flow Battery. *Adv. Energy Mater.* **2**, 1390–1396 (2012).

20. Gong, K., Fang, Q., Gu, S., Yau Li, S. F. & Yan, Y. Nonaqueous redox-flow batteries: organic solvents, supporting electrolytes, and redox pairs. *Energy & Environmental Science* **8**, 3515–3530 (2015).
21. Zhou, X. L., Zhao, T. S., An, L., Zeng, Y. K. & Wei, L. Critical transport issues for improving the performance of aqueous redox flow batteries. *Journal of Power Sources* **339**, 1–12 (2017).
22. Nemani, V. P. & Smith, K. C. Uncovering the role of flow rate in redox-active polymer flow batteries: simulation of reaction distributions with simultaneous mixing in tanks. *Electrochimica Acta* **247**, 475–485 (2017).
23. Gaffney, B. J. & Drew, T. B. Mass Transfer from Packing to Organic Solvents in Single Phase Flow through a Column. *Ind. Eng. Chem.* **42**, 1120–1127 (1950).
24. Williamson, J. E., Bazaire, K. E. & Geankoplis, C. J. Liquid-Phase Mass Transfer at Low Reynolds Numbers. *Ind. Eng. Chem. Fund.* **2**, 126–129 (1963).
25. Wilson, E. J. & Geankoplis, C. J. Liquid Mass Transfer at Very Low Reynolds Numbers in Packed Beds. *Ind. Eng. Chem. Fund.* **5**, 9–14 (1966).
26. Lewis, W. K. & Whitman, W. G. Principles of Gas Absorption. *Ind. Eng. Chem.* **16**, 1215–1220 (1924).
27. Appel, P. W. & Newman, J. Application of the limiting current method to mass transfer in packed beds at very low reynolds numbers. *AIChE Journal* **22**, 979–984 (1976).
28. You, X., Ye, Q. & Cheng, P. The Dependence of Mass Transfer Coefficient on the Electrolyte Velocity in Carbon Felt Electrodes: Determination and Validation. *J. Electrochem. Soc.* **164**, E3386–E3394 (2017).
29. Schmal, D., Van Erkel, J. & Van Duin, P. J. Mass transfer at carbon fibre electrodes. *J Appl Electrochem* **16**, 422–430 (1986).
30. Whitaker, S. Diffusion and dispersion in porous media. *AIChE Journal* **13**, 420–427 (1967).
31. Sahimi, M., Hughes, B. D., Scriven, L. E. & Ted Davis, H. Dispersion in flow through porous media—I. One-phase flow. *Chemical Engineering Science* **41**, 2103–2122 (1986).
32. Daneyko, A., Hlushkou, D., Khirevich, S. & Tallarek, U. From random sphere packings to regular pillar arrays: Analysis of transverse dispersion. *Journal of Chromatography A* **1257**, 98–115 (2012).
33. Xu, A., Zhao, T. S., Shi, L. & Xu, J. B. Lattice Boltzmann Simulation of Mass Transfer Coefficients for Chemically Reactive Flows in Porous Media. *J. Heat Transfer* **140**, 052601-052601–8 (2018).

34. Kok, M. D. R. *et al.* Mass transfer in fibrous media with varying anisotropy for flow battery electrodes: Direct numerical simulations with 3D X-ray computed tomography. *Chemical Engineering Science* **196**, 104–115 (2019).
35. Spiegler, K. S. Polarization at ion exchange membrane-solution interfaces. *Desalination* **9**, 367–385 (1971).
36. Krol, J. J., Wessling, M. & Strathmann, H. Concentration polarization with monopolar ion exchange membranes: current–voltage curves and water dissociation. *Journal of Membrane Science* **162**, 145–154 (1999).
37. Tanaka, Y. Concentration polarization in ion-exchange membrane electrodialysis: The events arising in an unforced flowing solution in a desalting cell. *Journal of Membrane Science* **244**, 1–16 (2004).
38. Marcus, R. A. On the Theory of Oxidation-Reduction Reactions Involving Electron Transfer. I. *The Journal of Chemical Physics* **24**, 966–978 (1956).
39. Marcus, R. A. Electron transfer reactions in chemistry. Theory and experiment. *Rev. Mod. Phys.* **65**, 599–610 (1993).
40. Henstridge, M. C., Laborda, E., Rees, N. V. & Compton, R. G. Marcus–Hush–Chidsey theory of electron transfer applied to voltammetry: A review. *Electrochimica Acta* **84**, 12–20 (2012).
41. Zeng, Y., Smith, R. B., Bai, P. & Bazant, M. Z. Simple formula for Marcus–Hush–Chidsey kinetics. *Journal of Electroanalytical Chemistry* **735**, 77–83 (2014).
42. Bejan, A. *Advanced Engineering Thermodynamics*. (Wiley, 2006).
43. Wang, W. *et al.* A new redox flow battery using Fe/V redox couples in chloride supporting electrolyte. *Energy Environ. Sci.* **4**, 4068–4073 (2011).
44. González-García, J. *et al.* Characterization of a carbon felt electrode: structural and physical properties. *J. Mater. Chem.* **9**, 419–426 (1999).
45. Bird, R. B., Stewart, W. E. & Lightfoot, E. N. *Transport Phenomena*. (John Wiley & Sons, 2007).
46. Geise, G. M., Hickner, M. A. & Logan, B. E. Ionic Resistance and Permselectivity Tradeoffs in Anion Exchange Membranes. *ACS Appl. Mater. Interfaces* **5**, 10294–10301 (2013).
47. Thorat, I. V. *et al.* Quantifying tortuosity in porous Li-ion battery materials. *Journal of Power Sources* **188**, 592–600 (2009).
48. Bruggeman, D. A. G. Berechnung verschiedener physikalischer Konstanten von heterogenen Substanzen. I. Dielektrizitätskonstanten und Leitfähigkeiten der Mischkörper aus isotropen Substanzen. *Annalen der Physik* **416**, 636–664 (1935).

49. Thieu, L. M., Zhu, L., Korovich, A. G., Hickner, M. A. & Madsen, L. A. Multiscale Tortuous Diffusion in Anion and Cation Exchange Membranes. *Macromolecules* **52**, 24–35 (2019).
50. Shah, A. A., Watt-Smith, M. J. & Walsh, F. C. A dynamic performance model for redox-flow batteries involving soluble species. *Electrochimica Acta* **53**, 8087–8100 (2008).
51. Yamamura, T., Watanabe, N., Yano, T. & Shiokawa, Y. Electron-Transfer Kinetics of Np3 + ∕ Np4 + , NpO2 + ∕ NpO2 2 + , V2 + ∕ V3 + , and VO2 + ∕ VO2 + at Carbon Electrodes. *J. Electrochem. Soc.* **152**, A830–A836 (2005).
52. Nemani, V. P. & Smith, K. C. Analysis of Crossover-Induced Capacity Fade in Redox Flow Batteries with Non-Selective Separators. *J. Electrochem. Soc.* **165**, A3144–A3155 (2018).
53. Newman, J. & Thomas-Alyea, K. E. *Electrochemical Systems*. (John Wiley & Sons, 2012).
54. Darling, R., Gallagher, K., Xie, W., Su, L. & Brushett, F. Transport Property Requirements for Flow Battery Separators. *J. Electrochem. Soc.* **163**, A5029–A5040 (2016).
55. Dennison, C. R., Agar, E., Akuzum, B. & Kumbur, E. C. Enhancing Mass Transport in Redox Flow Batteries by Tailoring Flow Field and Electrode Design. *J. Electrochem. Soc.* **163**, A5163–A5169 (2016).
56. Chehayeb, K. M. & Lienhard, J. H. Entropy generation analysis of electrodialysis. *Desalination* **413**, 184–198 (2017).

CHAPTER 9: Summary

This thesis explains the ion transport mechanisms in electrochemical energy storage systems: li-ion batteries and redox flow batteries, by developing a 2D continuum model.

9.1 Major Contributions

Bi-tortuous Electrodes for Li-ion Batteries:

We design and optimize the use of electrolyte-rich macro-pores imprinted into anisotropic graphite electrodes favoring fast ion transport. This could enable manufacturing thick Li-ion battery electrodes without compromising the power density of such batteries. The key results from our work includes:

- Bi-tortuous electrode structures in anisotropic graphite anodes can enhance discharge capacity by two-fold over a homogeneous electrode containing the same average porosity.
- The macro-pores must be sized optimally and spaced at short intervals to realize maximum enhancement.
- The placement of a complementary macro-pore in the cathode, which is relatively more isotropic than the anode, provides a mild enhancement in discharge capacity.
- Our simulations suggest that bi-tortuous anodes are particularly useful at high cycling rates.
- A positive angle tapered macro-pores have slight improvements over straight macro-pores. Negative angled tapers degrade the performance.

Multi -Species Transport in Redox Flow Batteries

The 2D transient model we developed couples the transport of six different species with pore-scale redox reactions, and electron conduction in electrodes. We identify non-dimensional numbers governing the design and operation of RFBs. Major findings include:

- Mixing of electrolyte in the tanks leads to irreversible thermodynamic losses adding to cell polarization and capacity loss. This is particularly dominant at low flow rates.
- The pore-scale reaction current density is more uniformly spread at high flow rates resulting in lower polarization.
- The reaction current density resulting from crossover processes is at least one order of magnitude lower than the primary redox reactions.
- With the use of non-selective separators, the diffusion and migration mechanisms can either enhance or oppose each other during crossover depending upon the state-of-charge, charging/ discharging cycle and redox properties.
- A threshold amount of salt (at least 50% concentration of redox actives in either electrolyte) is needed to obtain 80% of discharge utilization capacity.
- Three different regimes dominated by ohmic-polarization, redox active shuttling and sufficient supporting electrolyte are identified in the 2D space of non-dimensional Damköhler numbers of the salt and the redox active species.
- The total cell polarization losses in RFBs have contributions from ohmic resistance, reaction kinetics of the redox species at the pore-scale, mass transfer resistance between the bulk electrolyte and the pore-scale, and irreversible electrolyte mixing in the tanks.

- To obtain a capacity retention of more than 99.5% for ten cycles, the fixed membrane charge should be at least twenty times larger than redox concentration.
- The pore-scale mass transport resistance is characterized by the pore-scale Damkohler number Da_p and the salt transport through the bulk of the electrolyte is represented by Da_s.
- A complete exergy destruction analysis is conducted to quantify energy losses associated with electronic conduction, pore-scale mass transport, bulk species transport, reaction kinetics and irreversible tank mixing.
- The sum of exergy destruction losses associated with the five processes mentioned above add up to the total energy loss within a single charge/ discharge cycle.
- Concentration polarization of the membrane counter-ion (when using IEM) is significant compared to the polarization due to pore-scale mass transfer at high current densities.

The significant contributions towards modeling of RFBs include:

- The use of Marcus-Hush-Chidsey kinetics over commonly used Butler-Volmer model. This is particularly relevant when operating RFBs with high cell potentials.
- A detailed chapter on the discrete equations used to solve the coupled partial differential equations for modeling RFBs using finite volume method and implicit time stepping is presented.
- The time step required for convergence is theoretically established using fixed point iteration convergence criteria.

- The ion-exchange membranes are modeled using Poisson equation. A fine layer mesh is used at the electrode-membrane interface to capture the steep electrolyte potential gradients at the interface.
- The solution for the concentration fields is presented as a logarithmic value to account for order of magnitude variation particularly during crossover.
- The electrochemical reactions are damped at very low redox species concentrations so as to achieve better numerical convergence.

9.2 Recommendations for Future Work

The model can be extended to 3D to model flow-by configurations such as serpentine flow field. This should go together with flow modeling using the Darcy-Brinkman equation to consider the boundary effects. Experimental validation of the results presented in this thesis will help identify fundamental mechanisms governing the performance of RFBs. The model presented in this thesis assumes dilute concentrations of the redox active species in the electrolyte where solute-solute interactions are not significant. The solute-solute interactions become significant when the electrolyte is concentrated as a result of which, the activity coefficients are not unity. Developing concentrated solution theory under such circumstances, where the solute-solute interactions are relevant (like transport within the ion exchange membranes) could be a possible direction to explore.